The Method of Fundamental Solutions for Helmholtz-type Problems

Bandar Abdullah Bin-Mohsin

Submitted in accordance with the requirements for the degree of Doctor of Philosophy

The University of Leeds
Department of Applied Mathematics

February 2013

The candidate confirms that the work submitted is his own, except where work which has formed part of jointly authored publications has been included. The contribution of the candidate and the other authors to this work has been explicitly indicated below. The candidate confirms that appropriate credit has been given within the thesis where reference has been made to the work of others.

Publications

This thesis is based on several publications detailed as follows:

► Some of the material of Chapter 3 is included in:

1. Bin-Mohsin, B. and Lesnic, D. (2011) The method of fundamental solutions for Helmholtz-type equations in composite materials, *Computers and Mathematics with Applications*, Vol.**62**, No.12, pp.4377-4390.

2. Bin-Mohsin, B. and Lesnic, D. (2011) The MFS for Helmholtz-type equations in layered materials, *Proceedings of the 8th UK Conference on Boundary Integral Methods*, (ed. D.Lesnic), Leeds University Press, pp.57-64.

► Some of the material of Chapter 4 is included in:

1. Bin-Mohsin, B. and Lesnic, D. (2012) Determination of inner boundaries in modified Helmholtz inverse geometric problems using the method of fundamental solutions, *Mathematics and Computers in Simulation*, Vol.**82**, pp.1445-1458.

► Some of the material of Chapter 5 is included in:

1. Lesnic, D. and Bin-Mohsin, B. (2012) Inverse shape and heat transfer coefficient identification, *Journal of Computational and Applied Mathematics*, Vol.**236**, No.7, pp.1876-1891.

► Some of the material Chapter 6 is included in:

1. Bin-Mohsin, B. and Lesnic, D. (2012) Identification of a corroded boundary and its Robin coefficient, *East Asia Journal on Applied Mathematics*, Vol.**2**, No.2, pp.126-149.

2. Bin-Mohsin, B. and Lesnic, D. (2013) A meshless numerical identification of a convective corroded boundary, *Proceedings of the 9th UK Conference on Boundary Integral Methods*, (ed. O. Menshykov), UniPrint, University of Aberdeen, pp.9-16.

▶ Some of the material of Chapter 7 is included in:

1. Bin-Mohsin, B. and Lesnic, D. (2013) Numerical reconstruction of an inhomogeneity in an elliptic equation, *Inverse Problems in Science and Engineering*, (accepted).

Acknowledgments

I would like to extend my great thanks to my supervisor Professor Daniel Lesnic for his great supervision, continuous support, helpful conversations, advice throughout the research of my PhD, sharing knowledge and expertise. In fact, words cannot express my heartfelt gratitude, appreciation and thanks for all the support, guidance and time he had provided during my stay in Leeds.

My gratitude extend to Professor Andreas Karageorghis for his valuable advice on my thesis during his visiting to the University of Leeds on November 2012.

My special thanks are due to my parents, my dear wife, Faten, and my children, Sarah; Lojain and Juwan, for their continuous love, tolerance, support, and praying. I dedicate this thesis to them.

Finaly, Many thanks go the Ministry of higher Education in Saudi Arabia for financially supporting my postgraduate studies.

Abstract

The purpose of this thesis is to extend the range of application of the method fundamental solutions (MFS) to solve direct and inverse geometric problems associated with two- or three-dimensional Helmholtz-type equations. Inverse problems have become more and more important in various fields of sicence and technology, and have certainly been one of the fastest growing areas in applied mathematics over the last three decades. However, as inverse geometric problems typically lead to mathematical models which are ill-posed, their solutions are unstable under data perturbations and classical numerical techniques fail to provide accurate and stable solutions.

The novel contribution of this thesis involves the developement of the MFS combined with standard techniques for composite bi-material problems, the determination of inner boundaries, inverse shape and heat transfer coefficient identification, identification of a corroded boundary and its Robin coefficient, as well as the numerical reconstruction of an inhomogeneity.

Based on the MFS, unknows are determined by imposing the available boundary conditions, this allows to obtain a system of linear/nonlinear algebraic equations. A well-conditioned system of linear algebraic equations is solved by using the Gaussian elimination method, whilst a highly ill-conditioned system of equations is solved by the regularised least-squares method using a standard NAG routine E04FCF.

The accuracy and convergence of the MFS numerical technique used in this thesis is investigated using certain test examples for various geometry domains. The stability of the numerical solutions is investigated by introducing random noise into the input data, this yields unstable results if no regularisation is used. The Tikhonov regularisation method is employed in order to reduce the influence of the measurement errors on the numerical results. The inverse numerical solutions are compared with their known analytical solution, where available, and with the corresponding direct numerical solution where no analytical solution is available.

Contents

List of Figures

List of Tables

Nomenclature

$\mathbb{A}$	operator
A	MFS matrix
$\mathbb{C}$	complex numbers
C^2	space of functions twice continuously differentiable
C^1	space of functions once continuously differentiable
$D, \overline{D}$	domain, closure of D
F	function
F_f	nonlinear operator
$G_{\pm}$	the fundamental solution of the Helmholtz-type equation
G_H	the fundamental solution of the Helmholtz equation
G_{MH}	the fundamental solution of the modified Helmholtz equation
H^1	Sobolev space
$H^{1/2}$	the space of traces of functions from H^1
$H^{-1/2}$	the dual space of $H^{1/2}$
$H_0^{(1)}, H_0^{(2)}$	Hankel function of first kind of order zero and one
J_0, J_1	the Bessel functions of first kind of order zero and one
K_0, K_1	the modified Bessel functions of first kind of order zero and one
$\mathbb{K}$	condition number
L^2	space of square integrable functions
L^∞	space of uniformly bounded functions
M	total number of boundary collocation points
N	total number of source points
$P^{(0)}, P^{(1)}, P^{(2)}$	zeroth-, first- and second-order Tikhonov regularisation matrices
P_n	Legendre function of degree n
$\mathbb{R}$	set of real numbers
$\mathbb{R}^2 = \mathbb{R} \times \mathbb{R}$	xy plane
S	diagonal matrix

T	nonlinear objective least-squares function
U, V	matrices of order $M \times M$and $N \times N$
h	convective heat transfer coefficient (Chapter 1) and given function (Chapter 4)
h_n, J_n	spherical Hankel and spherical Bessel functions of first kind of order n
i	imaginary part $\sqrt{-1}$
k, k_1, k_2	wave numbers
$\underline{n}$	outward unit normal to the boundary
p	pressure (Chapter 1)
p	precentage of noise in input data (other chapters)
(r, θ)	polar coordinates
(r, θ, ϕ)	spherical coordinates
x, y	Cartesian coordinates
u_i, v_i	ith columns of the orthogonal matrices $U$and V
u^{inc}, u^s	incident field and scattered wave
w	frequency

Greek letters

Ω	solution domain
α, η	Robin (impedance, surface heat transfer) coefficient
$\partial\Omega$	the boundary of domain Ω
$\partial\Omega_1, \Gamma_1$	part of the boundary of domain $\partial\Omega$
$\partial\Omega_2, \Gamma_2$	part of the boundary of domain $\partial\Omega$
ξ	source points
$\overline{\Omega} = \Omega \cup \partial\Omega$	closure of Ω
$\lambda, \lambda_1, \lambda_2$	regularisation parameters
σ	diagonal components (Chapter 1)
δ	estimate of the level of noise (Chapter 1)
δ	distance (Chapter 3)

ϵ, ϵ_i	Gaussian random perturbations
σ_i	standard deviation
κ	the ratio between the thermal conductivities of materials Ω_1 and Ω_2
θ, ϕ	angles

Superscripts

^{tr}	transpose of a matrix
$' = \frac{\partial}{\partial n}$	normal derivative
$^{-1}$	inversion of a matrix
$^{+}$	pseudo inversion of a matrix

Abbreviations

BEM	boundary element method
FDM	finite difference method
FEM	finite element method
MFS	method of fundamental solutions
O	order of
SVD	singular value decomposition
TSVD	truncated singular value decomposition
PDE(s)	partial differential equation(s)
EIT	electrical impedance tomography
GRET	gamma ray emission tomography
MRI	magneto-resonance imaging
Re, Im	real and imagnary parts

Chapter 1

Introduction

Helmholtz-type problems arise naturally in many physical and engineering applications. The research work presented in this thesis considers Helmholtz-type equations in a domain Ω.

► The modified Helmholtz equation, otherwise related to steady-state heat conduction governing the heat conduction in fins, see Kraus et al. (2001), is given by

$$\nabla^2 u - k^2 u = 0 \quad \text{in} \quad \Omega, \tag{1.1}$$

where u is the temperature, $k^2 = 2h/(\lambda\delta)$, h is the convective heat transfer coefficient, and λ and δ are the thermal conductivity and thickness of the fin, respectively.
► The Helmholtz (reduced wave) equation governing wave propagation in an acoustic medium, see Colton and Kress (1998), is given by

$$\nabla^2 u + k^2 u = 0 \quad \text{in} \quad \Omega, \tag{1.2}$$

where u is the space-dependent part of the velocity potential, $k = \frac{w}{c}$ is the wave number, w is the frequency and c is the speed of sound. Equation (1.2) is obtained from the wave equation

$$\frac{\partial^2 \Psi}{\partial t^2} - c^2 \nabla^2 \Psi = 0, \tag{1.3}$$

where Ψ is the velocity potential, assuming the solution to be time harmonic, i.e.

$$\Psi(\underline{X}, t) = e^{-\mathrm{i}wt} u(\underline{X}).$$

1.1 Motivation and background

Investigating the process of heat transfer and providing acceptable heat conditions occupy an important place in the design and development of production methods related to the heating and cooling of materials, for example, continuous steel casting, glassmaking, high temperature crystal growing out of melt, etc. Two heat transfer phenomena can be inferred as special features of heat condition of modern heat-loaded structures and production methods, namely the non-stationary state and non-linearity. These derive from the use of many traditional design, theoretical and experimental methods. Amongst them are methods based on a solution of inverse problem by measurements of the system or process state, to find one or more characteristics causing this state. An extensive list of references for inverse heat transfer problems can be found in Alifanov (1994). Referring to heat transfer, we assume that the temperature field u satisfies the modified Helmholtz equation (1.1) in a bounded domain Ω, which models the heat conduction in a fin.

Next, we refer to the scattering of time-harmonic waves by obstacles surrounded by a homogeneous medium, that is, an exterior problem for the Helmholtz equation (1.2).

There are two cases of impenetrable and penetrable objects in obstacle scattering. For sound-soft (impenetrable) obstacles, the pressure of the total wave $u = u^{inc} + u^s$, vanishes on the boundary of the obstacle D, where u^{inc} and u^s denote the incident field and the scattered wave, respectively. Similarly, the scattering from sound-hard obstacles leads to a homogeneous Neumann boundary condition $\frac{\partial u}{\partial n} = 0$ on ∂D. More generally, we can have a homogeneous Robin boundary condition $\frac{\partial u}{\partial n} + \mathrm{i}\alpha u = 0$ on ∂D, where α is the impedance. The scattering by a penetrable obstacle D with constant density ρ_D and speed of sound c_D differing from the density ρ and c of the surrounding medium $\mathbb{R}^3\backslash\overline{D}$ leads to a transmission problem. In this case, in addition to the total field $u = u^{inc} + u^s$ in $\mathbb{R}^3\backslash\overline{D}$ satisfying Helmholtz equation (1.2), we have also v in D satisfying the Helmholtz equation (1.2) with a different wave number $k_D = \frac{w}{c_D} \neq k$, and the transmission conditions $u = v$, $\frac{1}{\rho}\frac{\partial u}{\partial n} = \frac{1}{\rho_D}\frac{\partial v}{\partial n}$ on ∂D. In addition, the scattered wave u^s should satisfy the Sommerfeld radiation condition

$$\lim_{r\to\infty} r\Big(\frac{\partial u^s}{\partial r} - \mathrm{i}ku^s\Big) = 0, \quad r = |\underline{X}|, \tag{1.4}$$

where $|\underline{X}|$ is the Eucliden norm of a point $\underline{X}$ in $\mathbb{R}^3$.

The Helmholtz equation is also often used to explain the vibration of a structure in acoustics where the domain is divided into structural acoustics and aero acoustics. Structural acoustic deals with the occurrence of vibrations in structure, for example, the engine and propeller of a cruise ship cause distributing vibrations of the chairs

and tables in ship's restaurant. Aero acoustic mostly deals with the occurrence of vibrations in fluids and air, see Beskos (1997). It is used in the acoustic cavity problem which requires the domain of cavity, the wave number and the boundary conditions, see Chen and Wong (1998).

The aim of this thesis is to solve numerically direct and inverse geometric problems associated to two- or three-dimensional Helmholtz-type equations using the meshless method of fundamental solution (MFS). Whilst neverthelss direct problems have been previously solved using the more traditional finite and boundary elements methods, the application of the meshless MFS to solving inverse problems is of a rather more recent investigation, see for example the recent review by Karageorghis et al. (2011).

1.2 Direct problems

The major concern in a direct problem is to determine the unknown solution within a domain from the known initial and boundary conditions. Direct problems have been extensively studied over the last two centuries, resulting in a wealth of literature of procedures relating to their solution. Direct problems are in general well-posed. According to Hadamard (1923), a problem is well-posed if it satisfies the following properties:

- The solution exists for all data.
- The solution is unique for all data.
- The solution depends continuously on the data (stability), i.e. the inverse operator is continuous. In other words, continuous dependence on the data means that small errors in the input data cause only small errors in the output solution.

If one or more of the above properties is violated this leads to an ill-posed problem.

Let us make more clear the above concepts, as introduced in Colton and Kress (1998). Suppose that $\mathbb{A} : X \to Y$ is an operator from a normed space X to a normed space Y such that

$$\mathbb{A}x = y, \tag{1.5}$$

where $x \in X$ and $y \in Y$. Then the operator equation (1.5) is well-posed if $\mathbb{A}$ is bijective and the inverse operator $\mathbb{A}^{-1} : Y \to X$ is continuous; otherwise the equation (1.5) is ill-posed. According to the above definition, three types of ill-posedness can be classified in the following:

- If $\mathbb{A}$ is not surjective this means that the equation (1.5) is not solvable for all $y \in Y$ (non-existence).
- If $\mathbb{A}$ is not injective this means that the equation (1.5) may have more than one solution (non-uniqueness).
- If $\mathbb{A}^{-1}$ exists but is not continuous this means that the equation (1.5) does not continuously depend on the data y (instability).

Some information is required to be known in a direct problem formulation such as:

1. the boundary of the solution domain,
2. the governing equation in the domain,
3. the boundary conditions for the entire boundary and initial conditions if necessary,
4. the material properties,
5. the forces acting in the domain.

Direct problems for Helmholtz-type equations have been extensively studied in the literature, see for example Niwa et al. (1982). However, in many engineering problems certain quantities in the list above are not directly specified or measured and this leads to inverse problem formulations which are discussed in the next subsection.

1.3 Inverse problems

Inverse problems have been recently studied in various branches of science and engineering and medicine. Typical applications of inverse problems consider inverse scattering for constricting the potential energy from the phases of scattered waves, see Colton and Kress (1998), estimation of the component spectral curves from an unknown mixture spectra, electrocardiography for estimating epicardial potential distribution from that on the body surface, etc. Usually, the inverse problem implies identification of inputs from outputs. A definite and rational definition can be given by considering direct problems as the opposite to inverse problems, see Kubo (1988). When one or more of the conditions 1–5 of section 1.2 are either unknown, or not fully specified, this leads to an inverse problem. The unknown conditions are to be determined with the assistance of an over specified condition. Noise becomes an important concern in the solution of most inverse problems, as the over specified condition is usually provided by using experimental field data. In general, inverse

problems can be one of the following problems which correspond to the lack of one of the requisites or their combinations:

1. the determination of parts of the boundary of the solution domain;
2. the inference of the governing equations;
3. the identification of the boundary conditions and/or initial conditions;
4. the determination of the material properties involved,
5. the determination of the forces acting in the domain.

In practice, many experimental impediments may arise in measuring or enforcing certain conditions. The physical situation at the surface of a solid body may be unsuitable for attaching a sensor or the accuracy of the surface measurement may be seriously impaired by the presence of the sensor. The main feature in the interpretation of the experimental results for all these problems is what we have to derive the results by indirect manifestations of the object that can be measured experimentally. Thus we are dealing with problems where we need to determine the causes if we know the result of observations.

Science has been built by the accumulation of effort towards solving this kind of never-ending series of inverse problems. Direct analysis can be made only when inverse problem has been solved to determine the requisites for the direct problems. At the end, inverse problems can be recognised as the complement to direct problems and play one of the most important roles in science and engineering. Furthermore, they are also more difficult to solve both analytically and numerically than direct problems since they are non-linear and, in general, ill-posed as they do not fulfill the well-posedness criteria of Hadamard.

There are many inverse problems arising in several applications. Let us mention some of them as follows.

► Cauchy problems

In these problems, the boundary conditions on both the solution and its normal derivative (for second-order PDEs) are prescribed only on a part of the boundary of the solution domain, whilst on the remaining part of the boundary no condition is given, see, for example, the book by Fattorini (1984) on the Cauchy problem in which the list of references on the subject contains over 100 pages! The goal is to determine the missing solution and its normal derivative on this remaining part of the boundary. The practical situations that are modelled by such problems occur when due to either physical impossibility, or just inconvenience, for example there

are no available measurements of the pollutant concentration on some hostile parts of the boundary of the region that was polluted. However, the values of the concentrations are needed on those inaccessible parts and they are sought using some extra measurements that can be taken on the accessible boundary.

► **Source identification problems**
In these problems, one considers inhomogeneous equations where the boundary of the solution domain under consideration is known and on the part of the boundary conditions are over-specified. The unknown inhomogeneous source forcing term in the governing equation needs to be determined. Typical practical application arise in the case of water pollution caused by some point sources. A point source pollutant is one that enters the water from a pipe, channel, or some other confined and localised source. The most common example of a point source of pollutants is a pipe that discharge sewage into a stream or river. Inverse source identification problems have been described at length in the PhD thesis of Rap (2005).

► **Parameter identification problems**
In these problems, parameters in the governing PDE characterising the material properties are unknown. A typical example concerns the identification of an unknown thermal conductivity by means of temperature and heat flux measurements on the boundary, see Beck and Arnold (1977), and Beck et al. (1985).

► **Inverse geometric problems**
The research work in this thesis focuses on this type of inverse problems. Inverse geometric problems are an important class of inverse problems in which part of the domain or boundary needs to be identified. It can model defects such as obstacles, cavities, inclusions, flaws, faults, voids and cracks. In addition, they arise in typical medical application in detection of anomalies such as tumours inside or on the boundary of the body.

In these problems the location and shape of the part of the boundary of solution domain under consideration is unknown. On the known part of the boundary, conditions are over-specified. These problems are more difficult than the previous types of inverse problems because, in fact, the coordinates of points describing the the unknown part of the boundary display non-linearly and they produce a non-linear system of equations. In practice, inverse geometric problems are investigated using various imaging and tomography techniques such as electrical impedance tomography (EIT), see Vauhkonen (2004), gamma ray emission tomography (GRET), see Cattle (2005), magneto-resonance imaging (MRI), see Bertero and Boccacci (1998).

One of the most famous applications of an inverse geometric problem is the X-ray computed tomography, in which a tomographic image is reconstructed from X-ray shadow photographs taken from various direction.

The numerical solution of an initial/boundary value problem can be computed by direct or iterative solvers using a numerical method, such as the finite element method (FEM); the boundary element method (BEM); the finite difference method (FDM) or the method of fundamental solutions (MFS). It is the latter one that is employed in this thesis.

1.4 The Method of Fundamental Solutions (MFS)

The method of fundamental solutions (MFS) is a powerful meshfree method applicable to boundary value problems when a fundamental solution of the governing equation is explicitly defined. It was initially introduced by Kupradze and Aleksidze (1964), and it was firstly presented as a numerical method by Mathon and Johnston (1977). Over the past 30 years, the MFS has been widely used for the numerical approximation of a large variety of physical problems, see e.g the review by Fairweather and Karageorghis (1998). The general concept of the MFS is that the solution is approximated by a linear combination of fundamental solutions with respect to source points which are placed outside the solution domain. The MFS has all advantages of the BEM, for example, and does not require discretisation over the domain in contrast to discretisation methods such as the FDM and the FEM. In addition, integrations over the boundary are avoided, the solution in the interior of the domain is evaluated without additional quadratures, the derivatives are calculated directly from the MFS expansion representation, its implementation is very easy and only little data preparation is required. A couple of disadvantages are that the locations of the source points are preassigned (and this introduces some additional degree of arbitrariness) and also the resulting system of algebraic equations is ill-conditioned. Merits and drawbacks of the MFS compared with the BEM are discussed in Burgess and Mahajerin (1984), and Ahmed et al. (1989).

Now, let us consider Helmholtz-type equations in a bounded domain $\Omega \subset \mathbb{R}^n$, $n = 2, 3$, namely

$$\nabla^2 u(\underline{X}) \pm k^2 u(\underline{X}) = 0, \quad \text{in} \quad \Omega, \tag{1.6}$$

subject to the boundary conditions

$$C_1 u = f_1, \quad \text{on} \quad \partial\Omega_1 \tag{1.7}$$

and

$$C_2 u = f_2, \quad \text{on} \quad \partial\Omega_2, \tag{1.8}$$

where $\partial\Omega = \partial\Omega_1 \cup \partial\Omega_2$, $\partial\Omega_1 \cap \partial\Omega_2 = \emptyset$, C_1 and C_2 denote Dirichlet, Neumann or Robin boundary conditions/operators and f_1, f_2 are given functions. In the application of the MFS, the solution of problem (1.6) is approximated as a linear combination

$$u_N(\underline{X}) = \sum_{j=1}^{N} a_j G_{\pm}(\underline{X}, \underline{\xi}^j), \quad \underline{X} \in \overline{\Omega} = \Omega \cup \partial\Omega, \tag{1.9}$$

where $G_{\pm}(\underline{X}, \underline{\xi})$ is the fundamental solution of the Helmholtz-type equation (1.6), and $(\underline{\xi})_{j=\overline{1,N}}$ are sources ('singularities') located outside $\overline{\Omega}$. The locations of the source points are usually chosen by considering either the static scheme, in which the sources are preassigned, or the dynamic scheme, in which both the sources and unknown coefficients $(a_j)_{j=\overline{1,N}}$ are determined during the solution process, see for more details Fairweather and Karageorghis (1998).

In this thesis, in order to avoid additional nonlinearity caused by considering a dynamic scheme, we will consider only the static approach in which the locations of the source points to be preassigned and kept fixed on a pseudo-boundary $\partial\Omega'$, preferably taken to be a circle or a curve similar to the boundary $\partial\Omega$ containing $\overline{\Omega}$. The optimal location of this pseudo-boundary is one of the major challenges in the application of the MFS and this will be investigated thoroughly in Chapter 2.

1.5 Numerical solution of Helmholtz-type problems

1.5.1 The MFS for direct problems

The MFS unknown coefficients $\underline{a} = (a_j)_{j=\overline{1,N}}$ are determined by collocating the boundary conditions (1.7) and (1.8) at M points, in general, uniformly distributed over the entire the boundary $\partial\Omega$. This leads to a system of linear equations which can be written

$$A\underline{a} = \underline{b}, \tag{1.10}$$

where A is an $M \times N$ matrix, $\underline{a}$ is the $N \times 1$ vector of unknowns and $\underline{b}$ is an $M \times 1$ known vector.

In all situations, in order to obtain a unique solution for the system of equations (1.10) we require $M \geq N$. If $M = N$ the system of equations (1.10) can be solved using the Gaussian elimination method, whilst if $M > N$ one can employ the linear least-squares method which replaces the rectangular $M \times N$ overdetermined system

of equations (1.10) with the square $N \times N$ determined system

$$A^{tr} A\underline{a} = A^{tr}\underline{b}, \tag{1.11}$$

where ^{tr} denotes the transpose of a matrix/vector. It is well-known that the ill-conditioning of the MFS matrix A increases, as the distance between the source points $\left(\underline{\xi}^l\right)_{l=\overline{1,N}}$ and the boundary $\partial\Omega$ increases, see Chen et al. (2006). Thus if N is large, or if the input data (1.7) and (1.8) contain noisy errors, then the system of equations (1.11) needs to be regularised using, for example, the Tikhonov regularization method which gives

$$\underline{a}_\lambda = (A^{tr} A + \lambda \mathbb{I})^{-1} A^{tr}\underline{b}, \tag{1.12}$$

where $\mathbb{I}$ is the identity matrix and $\lambda > 0$ is a regularisation parameter to be prescribed according to some criterion, e.g. the discrepancy principle, see Morozov (1966), the L-curve criterion, see Hansen (1990) or the generalized cross validation principle, see Golub et al. (1979). Equation (1.12) imposes a continuity constraint onto the solution and is known as Tikhonov's regularisation of order zero. It is worth pointing out that the regularised solution (1.12) has been obtained from minimising the functional

$$T(\underline{a}) := \|A\underline{a} - \underline{b}\|^2 + \lambda \|\underline{a}\|^2. \tag{1.13}$$

Higher-order smoothness constraints can also be imposed by replacing the identity matrix in (1.12) with higher-order finite difference derivatives giving rise to higher-order regularisations, see Philips (1962). Alternatively, instead of the Tikhonov regularised solution one could employ the truncated singular value decomposition method (TSVD), see for more details Hansen (1990).

1.5.2 The MFS for inverse problems

In the application of the MFS to inverse problems, we distinguish between linear and nonlinear problems.

► Linear problems

Cauchy problems and source identification problems are linear. Typically, in such problems the boundary is known and the unknowns are the boundary data or the sources acting in the domain. By collocating the boundary conditions on part of the boundary and, in some cases, collocating the solution at some interior points this leads to a system of linear equations given by (1.10) which is ill-conditioned and requires the application of the Tikhonov regularisation method or the TSVD.

► **Non-linear problems**

Inverse geometric problems and parameter identification problems are nonlinear problems. The part of the boundary is unknown and needs to be determined by collocating the boundary conditions, in this case, this leads to a system of non-linear equations

$$F(\underline{a}, \underline{r}) = \underline{b}, \tag{1.14}$$

where $\underline{r}$ is a vector containing the geometric parameters describing the unknown part of the boundary. The system of non-linear equations (1.14) can be solved using the non-linear regularised least-squares which recasts into minimising the non-linear objective function

$$T(\underline{a}, \underline{r}) = \|F(\underline{a}, \underline{r}) - \underline{b}\|^2 + \lambda_1 \|\underline{a}\|^2 + \lambda_2 \|\underline{r}\|^2, \tag{1.15}$$

where λ_1 and λ_2 are positive regularisation parameters which can be chosen according to some criterion, e.g. the L-surface criterion, see Belge et al. (2002).

1.6 Condition number

For linear direct and inverse problems, the MFS implementation usually yields to a system of linear algebraic equations (1.10). The condition number of a matrix is defined as the ratio between the largest singular value to the smallest singular value. The basic concept of condition number is a measure of stability or sensitivity of the matrix. In other words, the condition number of matrix A measures the solution $\underline{a}$ to the errors in the data $\underline{b}$. It gives an indication of the accuracy of the results from the matrix inversion. If the inverse problem is ill-posed then, the known $\underline{b}$ contains measured information and the matrix A is ill-conditioned. The measured information always involves errors for a variety of different reasons. Thus, if the condition number is large, even a small error in $\underline{b}$, may caused a large error in the solution $\underline{a}$. On the other hand, if the condition number is small then the error in the solution $\underline{a}$ will not be bigger than the error in the data $\underline{b}$.

1.7 More on stable methods of regularisation

The MFS system of linear equations (1.10) is ill-conditioned due to the large condition number of the matrix A which increases as the number of boundary collocation and source points increases. Furthermore, inverse problems are in general ill-posed. This means that the systems of linear/non-linear equations (1.10) and (1.14) upon direct inversion will produce a highly unstable numerical solution. Regularisation

methods, which are described in more details below, are needed in order to achieve the stability of the numerical solution.

1.7.1 Tikhonov regularisation method

The Tikhonov regularised solution of the system of linear algebraic equations (1.10) is given by

$$\underline{a}_\lambda = \arg\min_{\underline{a}\in\mathbb{R}^N}\left\{\|A\underline{a}-\underline{b}\|^2+\lambda\|P^{(m)}\underline{a}\|^2\right\}, \tag{1.16}$$

where the matrix $P^{(m)} \in \mathbb{R}^{(N-m)\times N}$ induces a C^m-continuity constraint on the solution $\underline{a}_\lambda$ and $\lambda > 0$ is the regularisation parameter. When $\lambda = 0$ in (1.16), this reduces to the ordinary least-squares method which is unstable. In the case of the zeroth-, first- and second-order Tikhonov regularisation methods the matrix $P^{(m)}$, i.e. $m = 0, 1, 2$, is given by, see e.g. Marin and Lesnic (2005), $P^{(0)} = \mathbb{I} \in \mathbb{R}^{N\times N}$,

$$P^{(1)} = \begin{bmatrix} -1 & 1 & 0 & \cdots & 0 \\ 0 & -1 & 1 & \cdots & 0 \\ \vdots & \vdots & \ddots & \ddots & \vdots \\ 0 & 0 & \cdots & 1 & -1 \end{bmatrix} \in \mathbb{R}^{(N-1)\times N},$$

$$P^{(2)} = \begin{bmatrix} 1 & -2 & 1 & 0 & \cdots & 0 \\ 0 & 1 & -2 & 1 & \cdots & 0 \\ \vdots & \vdots & \ddots & \ddots & \vdots & \\ 0 & 0 & \cdots & 1 & -2 & 1 \end{bmatrix} \in \mathbb{R}^{(N-2)\times N}.$$

For the minimisation of (1.13), making its gradient equal to zero, the Tikhonov regularised solution (1.16) becomes

$$\underline{a}_\lambda = (A^{tr}A + \lambda P^{(m)tr}P^{(m)})^{-1}A^{tr}\underline{b}. \tag{1.17}$$

For the system of non-linear equations (1.14), the standard zeroth-order Tikhonov regularised term is added to the minimisation of the functional T as it appears in expression (1.15), whilst in the first-order Tikhonov regularised the term is $\lambda_2\|\underline{r}\|^2$ in (1.15) is replaced by $\lambda_2\|\underline{r}'\|^2$.

1.7.2 Truncated singular value decomposition (TSVD)

The singular value decomposition method (SVD) is a widely used technique in which the matrix A of the system of linear equations (1.10) is decomposed as, see e.g. Golub

and Van Loan (1989),

$$A = USV^{tr}, \tag{1.18}$$

where the columns of U are the orthonormal eigenvectors of AA^{tr}, the columns of V are the orthonormal eigenvectors of $A^{tr}A$, and S is a diagonal matrix containing the singular values $(\sigma_i)_{i=\overline{1,N}}$ in decreasing order

$$\sigma_1 \geqslant \sigma_2 \geqslant \cdots \geqslant \sigma_N \geqslant 0, \tag{1.19}$$

assuming that $M \geqslant N$. Then, the length of the vector $\underline{a}$ is minimised by

$$\|A\underline{a} - \underline{b}\| = \|USV^{tr}\underline{a} - \underline{b}\| = \|S\underline{y} - \underline{c}\|, \tag{1.20}$$

where $\underline{y} = V^{tr}\underline{a} = V^{-1}\underline{a}$, which has the same length as $\underline{a}$, and $\underline{c} = U^{tr}\underline{b}$. Hence, the optimal solution is $\tilde{\underline{y}} = S^{+}\underline{c}$, where S^{+} is an $N \times M$ pseudo-inverse of the diagonal matrix S defined by

$$S^{+} = diag(\sigma^{+}), \quad \sigma^{+} = \begin{cases} \sigma_i^{-1} & \text{if} \quad \sigma_i \neq 0 \\ 0 & \text{otherwise.} \end{cases} \tag{1.21}$$

This gives the compact solution

$$\tilde{\underline{a}} = V\tilde{\underline{y}} = VS^{+}U^{tr}\underline{b} = A^{+}\underline{b}, \tag{1.22}$$

where A^{+} denotes the pseudo (Moore-Penrose) inverse of the matrix A. Equation (1.20) can be rewritten in the spectral expression

$$\tilde{\underline{a}} = \sum_{i=1}^{N} \sigma_i^{+}(\underline{u}_i^{tr} \cdot \underline{b})\underline{v}_i. \tag{1.23}$$

In the TSVD, we drop the smallest singular values so that equation (1.23) becomes

$$\underline{a}_J = \sum_{i=1}^{J} \sigma_i^{-1}(\underline{u}_i^{tr} \cdot \underline{b})\underline{v}_i, \tag{1.24}$$

where $\underline{u}_i$ and $\underline{v}_i$ are the column vectors of the matrices U and V, respectively, and J is the truncation parameter, which can be determined according to some criterion, such as those briefly discussed in the next section.

1.7.3 Choice of regularisation parameters

Over the last four decades, many different methods for selecting regularisation parameters have been proposed. The proper choice of the regularisation/truncation parameters plays an important role in equations (1.17) and (1.24), respectively, for achieving accurate and stable numerical results of inverse problems. In the TSVD, it is mentioned in the previous section that the optimal choice of the truncation parameter J is based on discarding the smallest singular values of the matrix A in the system of linear equation (1.10), whilst in the Tikhonov regularisation method, the optimal choice of regularisation parameter λ is chosen based on L-curve, see Hansen (1990). Regularisation is necessary when solving ill-posed problems because the simple least-squares solution, i.e. $\lambda = 0$, is completely dominated by contributions from data and rounding errors. By adding regularisation we are able to damp out these contributions and maintain the norm $\|\underline{a}\|$ to be of reasonable size. If the regularisation parameter λ is chosen too small, then the regularized solution remains unstable and, conversely, if the regularisation parameter λ is chosen too large, then the regularised solution is oversmoothed and may deviate from the true solution.

The L-curve is one of the most convenient tools for the analysis of discrete ill-posed problems. It is actually a plot for many positive regularisation parameters of the norm $\|\underline{a}_\lambda\|$ of the regularised solution versus the corresponding residual norm $\|A\underline{a}_\lambda - \underline{b}\|$. In this way, the L-curve clearly displays the compromise between minimisation of these two quantities, which is the heart of any regularisation method.

The discrepancy principle is probably the most widely used technique for choosing the regularisation parameter, see Morozov (1966) and Tikhonov and Arsenin (1977). According to this principle the regularisation parameter λ should be chosen such as

$$\|A\underline{a} - \underline{b}\| \approx \delta, \tag{1.25}$$

where δ is an estimate of the level of noise present in the problem, i.e.

$$\delta = \|\underline{b} - \underline{b}^\epsilon\|, \tag{1.26}$$

where $\underline{b}^\epsilon$ is the perturbed value of the right-hand side of the system of equations (1.10).

1.8 Structure of the thesis

In this thesis, direct and inverse geometric problems are investigated. Based on the MFS, the direct and inverse problems are reduced to solving ill-conditioned

systems of linear/nonlinear equations. In direct problems, these systems of linear equations are then solved using the Gaussian elimination method and in some cases the Tikhonov regularisation method is needed, as in equation (1.12), whilst in inverse problems, these systems of nonlinear equations are solved by minimising the nonlinear regularised least-squares functional, as in equation (1.15). The choice of the regularisation parameters required in the Tikhonov regularisation and TSVD is based on the L-curve method, as well as on the discrepancy principle.

The accuracy of the numerical solution obtained by the MFS is investigated for several test examples using a varying number of boundary collocation and source points. The numerical results are compared with the analytical solutions, where available. Then, following the well-or ill-posed nature of the problems considered in this thesis, the stability of numerical solution is investigated by perturbing the input data in order to simulate the measurement errors inherently present in any measured data set of an actual engineering problem.

The present Chapter 1 provides the background of developing the MFS technique. Based on the MFS discretisation, the Helmholtz-type equations for both direct and inverse problems have been reduced to solving systems of linear/non-linear equations. Stable methods, such as Tikhonov regularisation and the TSVD, have been described in order to solve the resulting ill-conditioned system of equations due to increasing the condition number of MFS matrix or adding noise in the input data. The choice of the regularisation/truncation parameters have been highlighted.

In Chapter 2, several direct problems for Helmholtz-type elliptic partial differential equations (PDEs) in various geometries, such as circle; square; annulus; exterior of a circle; sphere and annular sphere, are investigated by employing the MFS. The convergence of the MFS numerical results is investigated and the numerical solutions are graphically illustrated both on the boundary and inside the solution domain.

In Chapter 3, we introduce and develop the MFS for solving Helmholtz-type PDEs in composite materials. Numerical results are presented and discussed for several examples involving both the modified Helmholtz and the Helmholtz equations in two- or three-dimensional, bounded or unbounded, smooth or non-smooth composite domains.

In Chapter 4, an inverse geometric problem for the modified Helmholtz equation arising in heat conduction in a fin, which consists of determining an unknown inner boundary (rigid inclusion or cavity) of an annular domain from a single pair of boundary Cauchy data is solved numerically using the MFS. A nonlinear minimisation of the objective function is regularised when noise is added into the input boundary data. The stability of numerical results is investigated for several test examples.

Chapter 5 extends the analysis of Chapter 4 for determining an unknown inner boundary of an annular domain and together with its surface heat transfer coefficient from one or two pairs of boundary Cauchy data.

In Chapter 6, an inverse geometric problem for two-dimensional Helmholtz-type equations arising in corrosion detection is considered. This problem which consists of determining an unknown corroded portion of the boundary of a two-dimensional domain and possibly its surface heat transfer (impedance) Robin coefficient from one or two pairs of boundary Cauchy data is solved numerically using the same numerical approach as in Chapters 4 and 5.

The method is further applied in Chapter 7 to solve an inverse geometric problem in a composite material which consists of reconstructing an unknown inner boundary of a domain from a single pair of boundary Cauchy data.

Finally, in Chapter 8, general conclusions and suggestions for possible futher work are given.

Chapter 2

Direct Problems for Helmholtz-type Equations

2.1 Introduction

In this chapter, we solve some direct problems for Helmholtz-type elliptic partial differential equations (PDEs) in various geometries by the method of fundamental solutions (MFS), which is an approximation technique introduced by Kupradze and Aleksidze (1964). In the first three decades of discovery, the MFS was mainly restricted to solving homogenous elliptic linear equations, for example, the Laplace and biharmonic equations. Sometimes, the MFS is also called as the desingularized method, or the charge simulation method in the mathematical and engineering literature, see Alves and Chen (2005).

The MFS is a powerful meshless technique and popular tool for solving various types of linear PDEs for which the fundamental solution is available explicitly. In addition, it also has the advantages of rapid convergence, see Xin (2005), Mitic and Rashed (2004), high accuracy, simple theory and convenience of implementation by programming, see Hui and Qinghua (2007). An excellent overview of the history of the MFS and its applications to elliptic linear PDEs has been given in Fairweather and Karageorghis (1998), and Golberg and Chen (1999).

The basic idea of the MFS is to approximate the solution by a linear combination of fundamental solutions of the governing equation with respect to source points which are placed outside the solution domain, see Bogomolny (1985). The MFS differs from the common well-known boundary element method (BEM) approach of discretising boundary integral equations in that the source points are located outside the solution domain. In particular, they are not on the boundary, and therefore there is no jump relation nor singularity of the fundamental solution kernel. Thus, an advantage over the BEM is that the solution may be simply and accurately

evaluated up to the boundary. There appear to be a few comparisons between the BEM and the MFS in the literature, notably Burgess and Mahajerin (1984) and Ahmed et al. (1989); however, our goal is not to undertake such task, but instead to show that the MFS may be competitive and hence deserves analysis in places where the BEM may become prohibitely computationally expensive and difficult to implement, e.g. in three-dimensional inverse problems.

The outline of this chapter is as follows. In section 2.2, we introduce the MFS for Helmholtz-type equations, namely the modified Helmholtz equation $\nabla^2 u - k^2 u = 0$ and the Helmholtz equation $\nabla^2 u + k^2 u = 0$. In section 2.3, we present a convergence analysis of the MFS. In section 2.4, we present and discuss the numerical results obtained for various benchmark test examples in some simple two- or three-dimensional geometries (circle, square, annulus, unbounded exterior of a circle, sphere, annular sphere, unbounded exterior of a sphere). Finally, in section 2.5 we give some conclusions.

2.2 The Method of Fundamental Solutions (MFS) for Helmholtz-type equations

2.2.1 The MFS for the modified Helmholtz equation

Let us consider the modified Helmholtz equation to be solved in a bounded domain $\Omega \subset \mathbb{R}^2$ or $\mathbb{R}^3$,

$$\nabla^2 u(\underline{X}) - k^2 u(\underline{X}) = 0, \qquad \underline{X} \in \Omega, \tag{2.1}$$

with boundary conditions

$$\text{Dirichlet:} \qquad u(\underline{X}) = f(\underline{X}), \qquad \underline{X} \in \Gamma_1, \tag{2.2}$$

$$\text{Neumann:} \qquad \frac{\partial u}{\partial n}(\underline{X}) = g(\underline{X}), \qquad \underline{X} \in \Gamma_2. \tag{2.3}$$

In the above, $k > 0$ is a given constant, $\underline{n}$ is the outward normal to the boundary $\partial\Omega$, f and g are given functions, the boundary $\partial\Omega = \Gamma_1 \cup \Gamma_2$ and $\Gamma_1 \cap \Gamma_2 = \emptyset$. The fundamental solution of equation (2.1), i.e. the free space Green function which satisfies equation (2.1) in the whole space except at $\underline{X} = \underline{Y}$ where it becomes infinite, is given by, see e.g. Balakrishnan and Ramachandran (2000),

$$G_-(\underline{X}, \underline{Y}) = \begin{cases} \frac{1}{2\pi} K_0(kr), & \text{in two-dimensions} \\ \\ \frac{e^{-kr}}{4\pi r}, & \text{in three-dimensions} \end{cases} \tag{2.4}$$

where $r = \| \underline{X} - \underline{Y} \|$ and K_0 is the modified Bessel function of the second kind of order zero. It is well-known that $K_0(kr)$ satisfies the modified Helmholtz equation (2.1) in $\mathbb{R}^2 \backslash \{(0,0)\}$ with a singularity at the origin $r = 0$.

In the MFS, we seek the solution of problem (2.1)-(2.3) as a linear combination of non-singular fundamental solutions (2.4), see e.g. Marin and Lesnic (2005), Marin (2005, 2010b),

$$u(\underline{X}) = \sum_{l=1}^{N} a_l G_-(\underline{X}, \underline{\xi}^l), \qquad \underline{X} \in \overline{\Omega}, \tag{2.5}$$

where $\left(\underline{\xi}^l\right)_{l=\overline{1,N}}$ are distinct source points ('singularities') located outside $\overline{\Omega}$, and $\left(a_l\right)_{l=\overline{1,N}}$ are unknown real coefficients to be determined by imposing the boundary conditions (2.2) and (2.3). In expression (2.5), the number of source points N represents the truncation number in an approximating series given by the denseness of the set $\left\{G_-\left(\cdot, \underline{\xi}^l\right) \mid l = 1, 2, \ldots, \infty, \ \underline{\xi}^l \notin \overline{\Omega}\right\}$ in $L^2(\Omega)$, see Bogomolny (1985). This denseness result constitutes the theoretical basis of the MFS for the modified Helmholtz equation.

Imposing the boundary conditions (2.2) and (2.3), equation (2.5) in two-dimensions gives

$$f(\underline{X}) = \sum_{l=1}^{N} a_l K_0\Big(k \parallel \underline{X} - \underline{\xi}^l \parallel \Big), \qquad \underline{X} \in \Gamma_1, \tag{2.6}$$

$$g(\underline{X}) = -k \sum_{l=1}^{N} \frac{a_l (\underline{X} - \underline{\xi}^l) \cdot \underline{n}}{\parallel \underline{X} - \underline{\xi}^l \parallel} K_1\Big(k \parallel \underline{X} - \underline{\xi}^l \parallel \Big), \qquad \underline{X} \in \Gamma_2, \tag{2.7}$$

where K_1 is the modified Bessel function of the second kind of order one and, for simplicity, the constant $\frac{1}{2\pi}$ has been embedded in the unknown coefficients $(a_l)_{l=\overline{1,N}}$. Taking $\underline{X} = \left(\underline{X}^j\right)_{j=\overline{1,M}} \in \partial\Omega$ boundary points such that $\underline{X} = \left(\underline{X}^j\right)_{j=\overline{1,M_1}} \in \Gamma_1$ and $\underline{X} = \left(\underline{X}^j\right)_{j=\overline{M_1+1,M}} \in \Gamma_2$, equations (2.6) and (2.7) are collocated as

$$f_j := f(\underline{X}^j) = \sum_{l=1}^{N} a_l K_0\Big(k \parallel \underline{X}^j - \underline{\xi}^l \parallel \Big), \qquad j = \overline{1, M_1}, \tag{2.8}$$

$$g_j := g(\underline{X}^j) = -k \sum_{l=1}^{N} \frac{a_l (\underline{X}^j - \underline{\xi}^l) \cdot \underline{n}}{\parallel \underline{X}^j - \underline{\xi}^l \parallel} K_1\Big(k \parallel \underline{X}^j - \underline{\xi}^l \parallel \Big), \qquad j = \overline{M_1 + 1, M}. \tag{2.9}$$

Equations (2.8) and (2.9) form a system of M linear algebraic equations with N unknowns which generically can be written as (1.10), where $\underline{a} = \left(a_1, ..., a_N\right)^{tr}$,

$\underline{b} = \big(f_1, ..., f_{M_1}, g_{M_1+1}, ..., g_M\big)^{tr}$,

$$A_{jl} = \begin{cases} K_0\Big(k \parallel \underline{X}^j - \underline{\xi}^l \parallel\Big), & j = \overline{1, M_1},\ l = \overline{1, N}, \\ -\frac{k(\underline{X}^j - \underline{\xi}^l)\cdot \underline{n}}{\|\underline{X}^j - \underline{\xi}^l\|} K_1\Big(k \parallel \underline{X}^j - \underline{\xi}^l \parallel\Big), & j = \overline{M_1+1, M},\ l = \overline{1, N}. \end{cases} \tag{2.10}$$

In three-dimensions the collocation of the boundary conditions (2.2) and (2.3) results in

$$f_j := f(\underline{X}^j) = \sum_{l=1}^{N^2} \frac{a_l e^{-k\|\underline{X}^j - \underline{\xi}^l\|}}{\parallel \underline{X}^j - \underline{\xi}^l \parallel}, \qquad j = \overline{1, M_1^2}, \tag{2.11}$$

$$g_j := g(\underline{X}^j) = -\sum_{l=1}^{N^2} \frac{a_l(k \parallel \underline{X}^j - \underline{\xi}^l \parallel +1)}{\parallel \underline{X}^j - \underline{\xi}^l \parallel^3} e^{-k\|\underline{X}^j - \underline{\xi}^l\|}(\underline{X}^j - \underline{\xi}^l)\cdot \underline{n},\ j = \overline{M_1^2+1, M^2}, \tag{2.12}$$

where again, for simplicity, the constant $\frac{1}{4\pi}$ has been embedded in the unknown coefficients $(a_l)_{l=\overline{1,N^2}}$.

2.2.2 The MFS for the Helmholtz equation

We also consider the Helmholtz equation

$$\nabla^2 u(\underline{X}) + k^2 u(\underline{X}) = 0, \qquad \underline{X} \in \Omega, \tag{2.13}$$

with the boundary conditions (2.2) and (2.3). In equation (2.13), $k > 0$ is called the wave number. Recall, see Colton and Kress (1998), that the problem (2.2), (2.3) and (2.13) is well-posed with solution $u \in H^1(\Omega)$ for $f \in H^{1/2}(\Gamma_1)$, $g \in H^{-1/2}(\Gamma_2)$ if $-k^2$ is not a mixed eigenvalue (of the Laplacian) for the bounded domain Ω. The fundamental solution of Helmholtz equation (2.16) is given by, see e.g. Barnett and Betcke (2008),

$$G_+(\underline{X}, \underline{Y}) = \begin{cases} \frac{\mathrm{i}}{4} H_0^{(1)}(kr), & \text{in two-dimensions} \\ \frac{e^{-\mathrm{i}kr}}{4\pi r}, & \text{in three-dimensions} \end{cases} \tag{2.14}$$

where $r = \parallel \underline{X} - \underline{Y} \parallel$, $\mathrm{i} = \sqrt{-1}$ and $H_0^{(1)} = J_0 + \mathrm{i}Y_0$ is the Hankel function of the first kind of order zero, J_0 is the Bessel function of the first kind of order zero, and Y_0 is the Bessel function of the second kind of order zero. It is well-known that $H_0^{(1)}(kr)$ satisfies the Helmholtz equation (2.13) in $\mathbb{C}\backslash\{\mathbf{0}\}$ with a singularity at $r = 0$. In three-dimensions, in equation (2.14) we took the fundamental solution $e^{-\mathrm{i}kr}/(4\pi r)$ instead of $e^{\mathrm{i}kr}/(4\pi r)$ since the former satisfies the Sommerfeld radiation condition

(1.4) at infinity.

In the MFS, we seek the solution of problem (2.2), (2.3) and (2.13) as a linear combination of non-singular fundamental solutions (2.14),

$$u(\underline{X}) = \sum_{l=1}^{N} a_l G_+(\underline{X}, \underline{\xi}^l), \qquad \underline{X} \in \overline{\Omega}, \tag{2.15}$$

where $(\underline{\xi}^l)_{l=\overline{1,N}}$ are distinct source points placed outside $\overline{\Omega}$, and $(a_l)_{l=\overline{1,N}}$ are unknown complex coefficients to be determined by imposing the boundary conditions (2.2) and (2.3). The denseness of the set $\left\{G_+\left(\cdot, \underline{\xi}^l\right) \mid l = 1, 2, \ldots, \infty, \ \underline{\xi}^l \notin \overline{\Omega}\right\}$ in $L^2(\Omega)$, see Bogomolny (1985), and Alves and Chen (2005), constitutes the theoretical basis of the MFS for the Helmholtz equation. Note that in two-dimensions the still singular functions Y_0 or $H_0^{(2)}$ may also be used instead of $H_0^{(1)}$ in the MFS approximation (2.15), see Ennenbach and Niemeyer (1996) and Karageorghis (2001). Some investigations, see Hon and Chen (2003) and Chen and Hon (2003), have even attempted to use the non-singular function J_0 in (2.15) giving rise to the so-called boundary knot method, but without much theoretical justification.

Imposing the boundary conditions (2.2) and (2.3), equation (2.15) in two-dimensions gives

$$f(\underline{X}) = \sum_{l=1}^{N} a_l H_0^{(1)}(k \parallel \underline{X} - \underline{\xi}^l \parallel), \qquad \underline{X} \in \Gamma_1, \tag{2.16}$$

$$g(\underline{X}) = -k \sum_{l=1}^{N} \frac{a_l (\underline{X} - \underline{\xi}^l) \cdot \underline{n}}{\parallel \underline{X} - \underline{\xi}^l \parallel} H_1^{(1)}\Big(k \parallel \underline{X} - \underline{\xi}^l \parallel \Big), \qquad \underline{X} \in \Gamma_2, \tag{2.17}$$

where $H_1^{(1)}$ is the Hankel function of the first kind of order one and, for simplicity, the constant $\frac{\mathrm{i}}{4}$ has been embedded in the unknown complex coefficients $(a_l)_{l=\overline{1,N}}$. Using that

$$H_j^{(1)}(kr) = J_j(kr) + \mathrm{i} Y_j(kr), \qquad j = 0, 1, \tag{2.18}$$

where J_1 is the Bessel function of first kind of order one, and Y_1 is the Bessel function of second kind of order one, equations (2.15) with $G_+(\underline{X}, \underline{\xi}^l)$ replaced by $H_0^{(1)}(k \parallel \underline{X} - \underline{\xi}^l \parallel)$ can be rewritten as (viz $a_l = \alpha_l + \mathrm{i}\beta_l$ for $l = \overline{1, N}$)

$$u(\underline{X}) = \sum_{l=1}^{N} \Bigg[\alpha_l J_0\Big(k \parallel \underline{X} - \underline{\xi}^l \parallel \Big) - \beta_l Y_0\Big(k \parallel \underline{X} - \underline{\xi}^l \parallel \Big)$$
$$+\mathrm{i}\Bigg(\alpha_l Y_0\Big(k \parallel \underline{X} - \underline{\xi}^l \parallel \Big) + \beta_l J_0\Big(k \parallel \underline{X} - \underline{\xi}^l \parallel \Big)\Bigg)\Bigg], \qquad \underline{X} \in \overline{\Omega}. \tag{2.19}$$

Also, equations (2.16) and (2.17) when collocated at the boundary points $(\underline{X}^j)_{j=\overline{1,M}}$ result in

$$f_j := f(\underline{X}^j) = \sum_{l=1}^{N} \left[\alpha_l J_0\Big(k \parallel \underline{X}^j - \underline{\xi}^l \parallel\Big) - \beta_l Y_0\Big(k \parallel \underline{X}^j - \underline{\xi}^l \parallel\Big) \right.$$
$$\left. +\mathrm{i}\left(\alpha_l Y_0\Big(k \parallel \underline{X}^j - \underline{\xi}^l \parallel\Big) + \beta_l J_0\Big(k \parallel \underline{X}^j - \underline{\xi}^l \parallel\Big)\right)\right], \qquad j = \overline{1, M_1}, \tag{2.20}$$

$$g_j := g(\underline{X}^j) = -k \sum_{l=1}^{N} \frac{(\underline{X} - \underline{\xi}^l) \cdot \underline{n}}{\parallel \underline{X} - \underline{\xi}^l \parallel} \left[\alpha_l J_1\Big(k \parallel \underline{X}^j - \underline{\xi}^l \parallel\Big) - \beta_l Y_1\Big(k \parallel \underline{X}^j - \underline{\xi}^l \parallel\Big) \right.$$
$$\left. +\mathrm{i}\left(\alpha_l Y_1\Big(k \parallel \underline{X}^j - \underline{\xi}^l \parallel\Big) + \beta_l J_1\Big(k \parallel \underline{X}^j - \underline{\xi}^l \parallel\Big)\right)\right], \; j = \overline{M_1 + 1, M} \tag{2.21}$$

Separating the real and imaginary parts, equations (2.20) and (2.21) form a system of $2M$ linear algebraic equations with $2N$ unknowns which can be written as (1.10), where $\underline{a} = (\alpha_1 \dots \alpha_N, \beta_1 \dots \beta_N)^{tr}$, $\underline{b} = (f_1, \dots, f_{M_1}, g_{M_1+1}, \dots, g_M, 0 \dots, 0)^{tr}$, and

$$A_{jl} = \begin{cases} J_0(k \parallel \underline{X}^j - \underline{\xi}^l \parallel), & j = \overline{1, M_1},\ l = \overline{1, N} \\ -Y_0(k \parallel \underline{X}^j - \underline{\xi}^{l-N} \parallel), & j = \overline{1, M_1},\ l = \overline{N+1, 2N} \\ J_1(k \parallel \underline{X}^j - \underline{\xi}^l \parallel), & j = \overline{M_1+1, M},\ l = \overline{1, N} \\ -Y_1(k \parallel \underline{X}^j - \underline{\xi}^{l-N} \parallel), & j = \overline{M_1+1, M},\ l = \overline{N+1, 2N} \\ Y_0(k \parallel \underline{X}^{j-M} - \underline{\xi}^l \parallel), & j = \overline{M+1, M+M_1},\ l = \overline{1, N} \\ J_0(k \parallel \underline{X}^{j-M} - \underline{\xi}^{l-N} \parallel), & j = \overline{M+1, M+M_1},\ l = \overline{N+1, 2N} \\ Y_1(k \parallel \underline{X}^{j-M} - \underline{\xi}^l \parallel), & j = \overline{M+M_1+1, 2M},\ l = \overline{1, N} \\ J_1(k \parallel \underline{X}^{j-M} - \underline{\xi}^{l-N} \parallel), & j = \overline{M+M_1+1, 2M},\ l = \overline{N+1, 2N} \end{cases} \tag{2.22}$$

In three-dimensions the collocation of the boundary conditions (2.2) and (2.3)

gives,

$$f_j := f(\underline{X}^j) = \sum_{l=1}^{N^2} \frac{1}{\parallel \underline{X}^j - \underline{\xi}^l \parallel} \Big[\alpha_l \cos(k \parallel \underline{X}^j - \underline{\xi}^l \parallel) + \beta_l \sin(k \parallel \underline{X}^j - \underline{\xi}^l \parallel) + \mathrm{i}\Big(- \alpha_l \sin(k \parallel \underline{X}^j - \underline{\xi}^l \parallel) + \beta_l \cos(k \parallel \underline{X}^j - \underline{\xi}^l \parallel)\Big)\Big], \; j = \overline{1, M_1^2}, \tag{2.23}$$

$$g_j := g(\underline{X}^j) = -\sum_{l=1}^{N^2} \frac{(\underline{X}^j - \underline{\xi}^l) \cdot \underline{n}}{\parallel \underline{X}^j - \underline{\xi}^l \parallel^3} \Bigg\{ \alpha_l \Big[\cos(k \parallel \underline{X}^j - \underline{\xi}^l \parallel) + k \parallel \underline{X}^j - \underline{\xi}^l \parallel \sin(k \parallel \underline{X}^j - \underline{\xi}^l \parallel)\Big] + \beta_l \Big[\sin(k \parallel \underline{X}^j - \underline{\xi}^l \parallel) - k \parallel \underline{X}^j - \underline{\xi}^l \parallel \cos(k \parallel \underline{X}^j - \underline{\xi}^l \parallel)\Big] + \mathrm{i}\Big\{\alpha_l \Big[- \sin(k \parallel \underline{X}^j - \underline{\xi}^l \parallel) + k \parallel \underline{X}^j - \underline{\xi}^l \parallel \cos(k \parallel \underline{X}^j - \underline{\xi}^l \parallel)\Big] + \beta_l \Big[\cos(k \parallel \underline{X}^j - \underline{\xi}^l \parallel) + k \parallel \underline{X}^j - \underline{\xi}^l \parallel \sin(k \parallel \underline{X}^j - \underline{\xi}^l \parallel)\Big]\Big\}\Bigg\}, \quad j = \overline{M_1^2 + 1, M^2}. \tag{2.24}$$

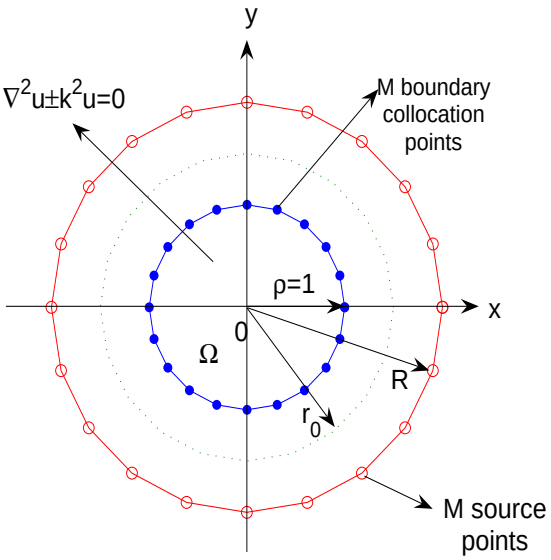

Figure 2.1: Sketch of the MFS with $M = N$ boundary collocation and source points.

2.3 Convergence analysis of the MFS

In order to analyse the convergence of the numerical results obtained, we introduce two approximation errors given by

$$\text{absolute error} = |u(\underline{X}) - u_M(\underline{X})|, \quad \text{relative error} = \left|\frac{u(\underline{X}) - u_M(\underline{X})}{u(\underline{X})}\right|,$$

where $u(\underline{X})$ is the exact solution and $u_M(\underline{X})$ is the MFS numerical solution with $M = N$ source and boundary collocation points, as shown in Figure 2.1.

In Katsurada and Okamoto (1996), and Fairweather and Karageorghis (1998), for the Dirichlet problem for the Laplace equation $\nabla^2 u = 0$ in Ω, $u\,|_{\partial\Omega} = f$ on $\partial\Omega$, it was given that if $\Omega = B(\mathbf{0};\rho)$ is a circle of radius $\rho > 0$, f is analytical, and if u is analytically harmonic continuable to the whole plane $\mathbb{R}^2$, then the maximum (supremum) of local error at any point $(x_0, y_0) \in \Omega$ obeys, for sufficiently large M,

$$\begin{aligned}|u_M(x_0,y_0) - u(x_0,y_0)| \le \|u_M - u\|_{L^\infty(\Omega)} &= \sup_{(x,y)\in\Omega} |u_M(x,y) - u(x,y)| \\ &\le C\Big(\frac{\rho}{R}\Big)^M, \quad (2.25)\end{aligned}$$

where $C > 0$ is a positive constant which may depend on f and R, but not on M, and $R > \rho$ is the radius of the exterior circle where the M sources are positioned. This shows that the MFS is exponentially convergent with respect to increasing M, or R. The same result holds for the Helmholtz operator $\nabla^2 + k^2 I$, see Barnett and Betcke (2008), and for the modified Helmholtz operator $\nabla^2 - k^2 I$, by accommodating the proofs of [Balakrishnan and Ramachandran (2000); Barnett and Betcke (2008); Bogomolny (1985)] related to the Laplace equation.

The estimate (2.25) was proved by Katsurada (1989, 1990) for $\partial\Omega$ a circle and an analytical Jordan curve, respectively. In the case that u is not analytically continuable to the whole plane $\mathbb{R}^2$, but rather only up to an extension $B(\mathbf{0}; r_0)$ with $r_0 > \rho$ then the error estimate (2.25) modifies as, see Kitagawa (1988, 1991), for sufficient large M,

$$\|u_M - u\|_{L^\infty(\Omega)} \le \|u\|_{L^\infty(\partial B(\mathbf{0};r_0))}\Big(\frac{2}{1-\frac{\rho}{r_0}}\Big)\left\{[1 + A(R,\rho)]\Big(\frac{\rho}{r_0}\Big)^{M/3} + 4\Big(\frac{\rho}{R}\Big)^{M/3}\right\}, \quad (2.26)$$

where $A(R,\rho)$ is some constant between 1 and 2. The price to pay for this excellent exponential convergence is that the condition number of the coefficient matrix of the resulting MFS system of equations grows exponentially with respect to M, and

can be estimated by

$$\mathbb{K}(M,R) \sim \frac{\ln(R)}{2} M \Big(\frac{R}{\rho}\Big)^{M/2}. \tag{2.27}$$

2.4 Numerical results and discussion

In this section, we present and discuss numerical results obtained in different geometries, see Figure 2.2, namely,

$$\Omega = \begin{cases} \{(x,y) \in \mathbb{R}^2 \mid x^2+y^2 < 1\}, & \text{(circle) Examples 1 and 4,} \\ \{(x,y) \in \mathbb{R}^2 \mid x,y \in (-1/2,1/2)\}, & \text{(square) Example 2,} \\ \{(x,y) \in \mathbb{R}^2 \mid 1 < x^2+y^2 < 4\}, & \text{(annulus) Examples 3 and 5} \\ \{(x,y) \in \mathbb{R}^2 \mid x^2+y^2 > 1\}, & \text{(unbounded exterior circle) Example 6} \\ \{(x,y,z) \in \mathbb{R}^3 \mid x^2+y^2+z^2 < 1\}, & \text{(sphere) Examples 7 and 9} \\ \{(x,y,z) \in \mathbb{R}^3 \mid 1 < x^2+y^2+z^2 < 4\}, & \text{(annular sphere) Example 8} \\ \{(x,y,z) \in \mathbb{R}^3 \mid x^2+y^2+z^2 > 1\}, & \text{(unbounded exterior sphere) Example 10} \end{cases} \tag{2.28}$$

1. (a) For the analytical solution of the modified Helmholtz equation (2.1) in two-dimensions we take

$$u(\underline{X}) = e^{x+y}, \qquad \underline{X} = (x,y) \in \Omega, \tag{2.29}$$

which satisfies it with $k = \sqrt{2}$. The various geometries (2.28) are considered in Examples 1-3 in order to illustrate the applicability of the MFS to deal with smooth, non-smooth and multiply-connected domains.

For simplicity, we consider Dirichlet boundary conditions only, i.e. $\Gamma_2 = \emptyset$, $\Gamma_1 = \partial\Omega$ namely

$$u(x,y) = f(x,y) = e^{x+y}, \qquad (x,y) \in \partial\Omega. \tag{2.30}$$

Corresponding to (2.29), the normal derivative is given by

$$\frac{\partial u}{\partial n}(x,y) = e^{x+y}(n_x + n_y), \qquad (x,y) \in \partial\Omega, \tag{2.31}$$

where $\underline{n} = (n_x, n_y)$.

(b) For the analytical solution of the modified Helmholtz equation (2.1) in three-dimensions we take

$$u(\underline{X}) = e^{x+y+z}, \qquad \underline{X} = (x,y,z) \in \Omega, \tag{2.32}$$

which satisfies it with $k = \sqrt{3}$. The unit sphere and annular spherical geometries (2.28) are considered in Examples 7 and 8 in order to illustrate the applicability of the MFS to deal with smooth simply and multiply-connected domains. For simplicity, we consider Dirichlet boundary conditions only, i.e. $\Gamma_2 = \emptyset$, $\Gamma_1 = \partial\Omega$, namely

$$u(x, y, z) = f(x, y, z) = e^{x+y+z}, \qquad (x, y, z) \in \partial\Omega. \tag{2.33}$$

Corresponding to (2.32), the normal derivative is given by

$$\frac{\partial u}{\partial n}(x, y, z) = e^{x+y+z}(n_x + n_y + n_z), \qquad (x, y, z) \in \partial\Omega, \tag{2.34}$$

where $\underline{n} = (n_x, n_y, n_z)$.

2. (a) For the analytical solution of the Helmholtz equation (2.13) in two-dimensions we take

$$u(\underline{X}) = \sin(x + y), \qquad \underline{X} = (x, y) \in \Omega \tag{2.35}$$

which satisfies it with $k = \sqrt{2}$. The circle and annulus geometries are considered in Examples 4 - 6 in order to illustrate the applicability of the MFS to deal with smooth simply-connected, multiply-connected and unbounded domains. For simplicity, we consider Dirichlet boundary conditions only, i.e. $\Gamma_2 = \emptyset$, $\Gamma_1 = \partial\Omega$, namely

$$u(x, y) = f(x, y) = \sin(x + y), \qquad (x, y) \in \partial\Omega. \tag{2.36}$$

Corresponding to (2.35), the normal derivative is given by

$$\frac{\partial u}{\partial n}(x, y) = (n_x + n_y)\cos(x + y), \qquad (x, y) \in \partial\Omega. \tag{2.37}$$

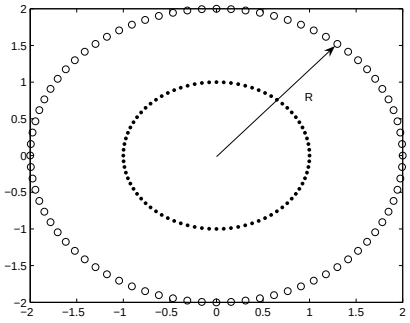

(a) Examples 1 and 4

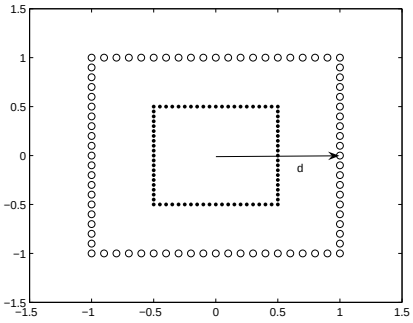

(b) Example 2(a)

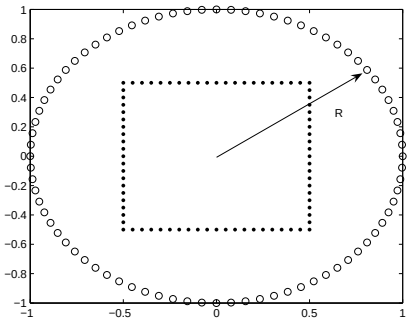

(c) Example 2(b)

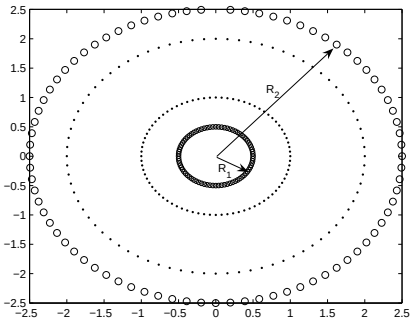

(d) Examples 3 and 5

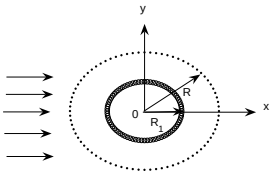

(e) Example 6

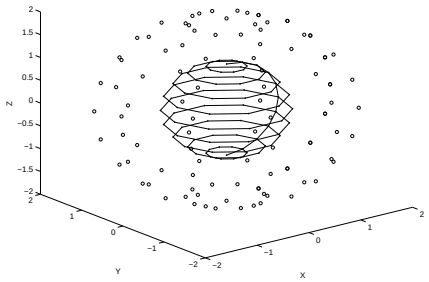

(f) Examples 7 and 9

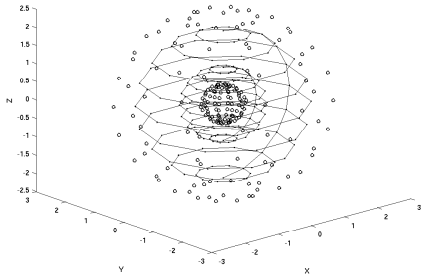

(g) Example 8

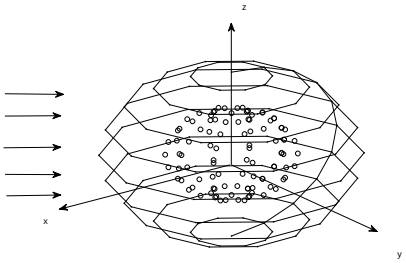

(h) Example 10

Figure 2.2: The distributions of source (○) and boundary collocation (●) points.

(b) For the analytical solution of the Helmholtz equation (2.13) in three-dimensions we take

$$u(\underline{X}) = \sin(x + y + z), \qquad \underline{X} = (x, y, z) \in \Omega, \tag{2.38}$$

which satisfies it with $k = \sqrt{3}$. The geometries (2.28) of Examples 9 and 10 are considered in order to illustrate the applicability of the MFS to deal with smooth bounded and unbounded domains. For simplicity, we consider Dirichlet boundary conditions only, i.e. $\Gamma_2 = \emptyset$, $\Gamma_1 = \partial\Omega$, namely

$$u(x, y, z) = f(x, y, z) = \sin(x + y + z), \qquad (x, y, z) \in \partial\Omega. \tag{2.39}$$

Corresponding to (2.38), the normal derivative is given by

$$\frac{\partial u}{\partial n}(x, y, z) = (n_x + n_y + n_z)\cos(x + y + z), \qquad (x, y, z) \in \partial\Omega. \tag{2.40}$$

The MFS is also applicable to other types of boundary conditions, e.g. Neumann, oblique, mixed, Robin, radiative, see Golberg and Chen (1999).

In all the computations, performed in FORTRAN and MATLAB, we take, for simplicity, $M = N$ uniformly distributed points and we investigate the convergence of the numerical solution with respect to increasing the number of source/boundary collocation points $M = N$ from 20 to 40, and then to 80 in two-dimensions, and from 5×5 to 10×10, and then to 20×20 in three-dimensions.

2.4.1 Example 1 (Modified Helmholtz equation, circle)

For the unit circle geometry $\Omega = B(\mathbf{0}; 1)$, the source points are located on a circle of radius $R > 1$ centred at the origin, and we investigate various values of $R \in \{1.5, 2, 2.5\}$. The distributions of source and boundary collocation points are shown in Figure 2.2(a). The numerical interior solutions for $u(0.5, 0.5)$ obtained with $M = N \in \{20, 40, 80\}$ and $R \in \{1.5, 2, 2.5\}$ are shown in Table 2.1. From Table 2.1 it can be seen that as $M = N$ increases, or R increases the numerical solution for $u(0.5, 0.5)$ converges toward its exact value of $e^{1.0} \simeq 2.718282$. The numerical solutions for normal derivative $\partial u/\partial n(1, \theta)$ obtained with $R = 2$ and various values of $M = N \in \{20, 40, 80\}$ are shown in Figure 2.3 in comparison with the analytical solution (2.31) given by

$$\frac{\partial u}{\partial n}(1, \theta) = (\cos(\theta) + \sin(\theta))e^{\cos(\theta)+\sin(\theta)}, \qquad \theta \in [0, 2\pi). \tag{2.41}$$

From this figure it can be seen that the numerical solution converges to the analytical solution (2.41) as $M = N$ increases. Overall from Table 2.1 and Figure 2.3 it can be concluded that the MFS provides a convergent and accurate numerical solution for solving the Dirichlet problem for the modified Helmholtz equation in smooth geometries.

In order to investigate the influence of the number M of source and boundary collocation points and the radius R on the convergence of the numerical results obtained, we set $M \in \{10, 20, 40, 60, 80, 160, 320\}$, $R \in \{1.5, 2, 2.5\}$. Figure 2.4 shows the logarithm of the local absolute error at the interior point $(0.5, 0.5) \in \Omega$. From this figure it can be seen that this error decreases exponentially as the number M of source/collocation points increases to 40, 60, and 80.

Table 2.1: The numerical solution for $u(0.5, 0.5)$ in Example 1 for various values of $M = N \in \{20, 40, 80\}$ and $R \in \{1.5, 2, 2.5\}$. The exact value is $e^{1.0} \simeq 2.718282$.

$M = N$	R	$u(0.5, 0.5)$	R	$u(0.5, 0.5)$	R	$u(0.5, 0.5)$
20	1.5	2.717843	2	2.718277	2.5	2.718282
40	1.5	2.718282	2	2.718282	2.5	2.718282
80	1.5	2.718282	2	2.718282	2.5	2.718282

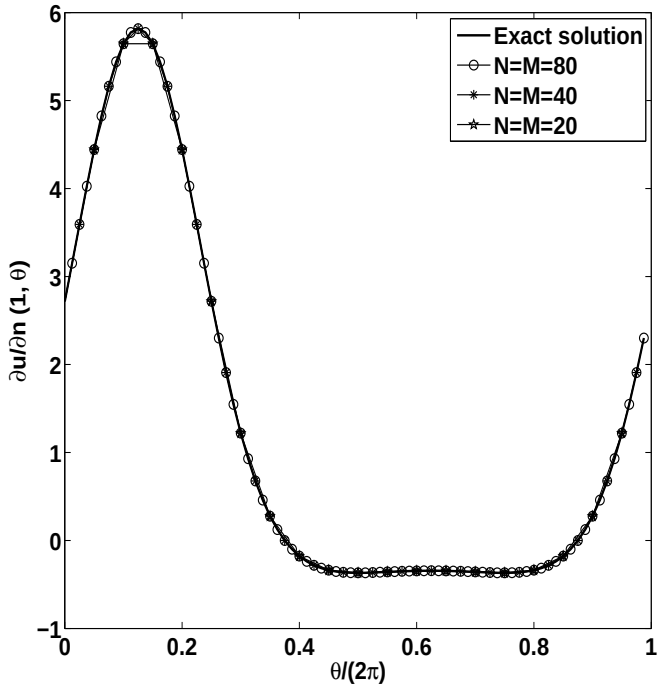

Figure 2.3: The analytical and the MFS solutions for the normal derivative $\partial u/\partial n(1,\theta)$ for various values of $M = N \in \{20, 40, 80\}$ and $R = 2$, for Example 1.

This can be estimated by the equations $\log|u_M(0.5, 0.5) - e| = -0.4M + 1.4$, $-0.7M + 3$, and $-M + 5$ when $R = 1.5, 2$, and 2.5, respectively. This is expected since from (2.25) with $\rho = 1$ we have

$$\log|u_M(x_0, y_0) - u(x_0, y_0)| \leq \log C - M \log R, \tag{2.42}$$

where C is a positive constant which may depend on k, R and f, but not on M. However, this error increases slightly for $M > 160$, $M > 60$, and $M > 40$ for $R = 1.5, 2$ and 2.5, respectively, due to the round-off machine's double precision of $\mathbf{O}(10^{-16})$ being reached.

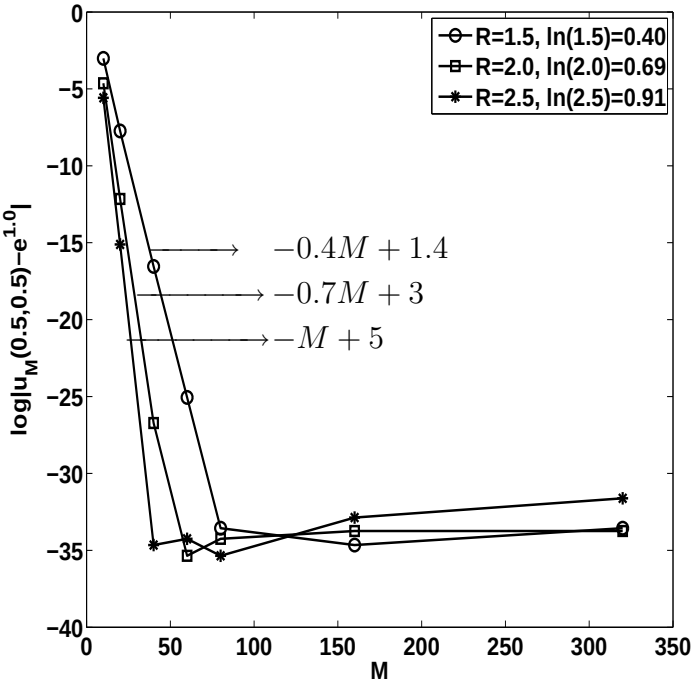

Figure 2.4: Logarithm of the local absolute error at the interior point $(0.5, 0.5) \in \Omega$ versus M, for various R.

Figure 2.5 shows the global error for the interior numerical solution given by

$$\|u_M(x,y) - u(x,y)\|_{L^2(\Omega)} \simeq \sqrt{\frac{1}{10}\sum_{i=1}^{10}\frac{2\pi}{5}\sum_{j=1}^{5}\left|u_M(r_i,\widetilde{\theta}_j) - u(r_i,\widetilde{\theta}_j)\right|^2}, \qquad (2.43)$$

where $r_i = i/11$ for $i = \overline{1,10}$, and $\widetilde{\theta}_j = 2\pi j/5$ for $j = \overline{1,5}$. It can be seen that error decreases exponentially as the number M of source/collocation points increases to 40, 60, and 80. This can be estimated by the equations $\log \|u_M(x,y) - e^{x+y}\|_{L^2(\Omega)} = -0.4M + 3$, $-0.5M + 0.8$, and $-0.9M + 3.3$ when $R = 1.5, 2$, and 2.5, respectively. However, this error increases slightly for $M > 160$, $M > 60$, and $M > 40$, respectively. This is expected since from (2.1) we have

$$\frac{1}{\sqrt{\pi}}\|u_M(x,y) - u(x,y)\|_{L^2(\Omega)} \leq \sup_{(x,y)\in\Omega}|u_M(x,y) - u(x,y)| \leq \frac{C}{R^M}, \qquad (2.44)$$

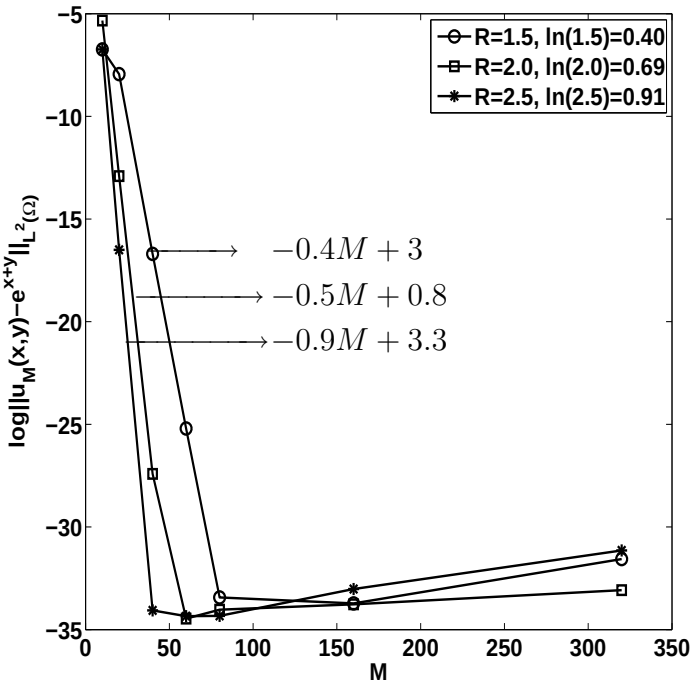

Figure 2.5: Logarithm of the global $L^2(\Omega)$ error for the numerical interior solution $u|_\Omega$ versus M, for various R.

Figure 2.6 shows the global error for the numerical normal derivative given by

$$\left\| \frac{\partial u_M}{\partial n}(x,y) - \frac{\partial u}{\partial n}(x,y) \right\|_{L^2(\partial\Omega)} = \left(\frac{2\pi}{10} \sum_{i=1}^{10} \left| \frac{\partial u_M}{\partial n}(\cos(\theta_i), \sin(\theta_i)) - \frac{\partial u}{\partial n}(\cos(\theta_i), \sin(\theta_i)) \right|^2 \right)^{\frac{1}{2}}, \tag{2.45}$$

where $\theta_i = 2\pi i/10$ for $i = \overline{1,10}$, and $\frac{\partial u}{\partial n}(x,y) = (\cos(\theta) + \sin(\theta))e^{\cos(\theta)+\sin(\theta)}$, for $(x,y) \in \partial\Omega$. It can be seen that error decreases exponentially as the number M of source/collocation points increases to 40, 60, and 80. This can be estimated by the equations $\log \|\frac{\partial u_M}{\partial n}(x,y) - \frac{\partial u}{\partial n}(x,y)\|_{L^2(\partial\Omega)} = -0.4M + 3$, $-0.6M + 0.8$, and $-0.8M + 4.6$ when $R = 1.5, 2$, and 2.5, respectively.

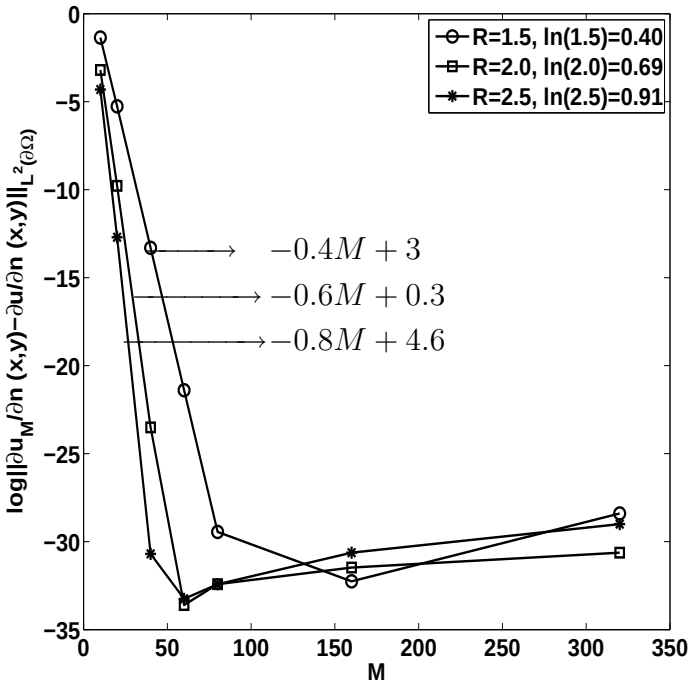

Figure 2.6: Logarithm of the global $L^2(\partial\Omega)$ error for the numerical normal derivative $\frac{\partial u}{\partial n}|_{\partial\Omega}$ versus M, for various R.

Figure 2.7 shows the global error for the boundary numerical solution given by

$$\|u_M(x,y) - e^{x+y}\|_{L^2(\partial\Omega)} \simeq \sqrt{\frac{2\pi}{10}\sum_{i=1}^{10}\left|u_M(\cos(\theta_i),\sin(\theta_i)) - e^{\cos(\theta_i)+\sin(\theta_i)}\right|^2}, \quad (2.46)$$

It can be seen that error decreases exponentially as the number M of source/ collocation points increases to 40, 60, and 80. This can be estimated by the equations $\log\|u_M(x,y)-e^{x+y}\|_{L^2(\partial\Omega)} = -0.4M+2.2$, $-0.6M+2$, and $-M+6$ when $R = 1.5, 2,$ and 2.5, respectively. The error can be used efficiently for the Dirichlet boundary value problem if no exact solution is available explicitly. Then, by the maximum principle for elliptic partial differential equations, the error inside Ω will be bounded from above by the error on the boundary $\partial\Omega$. Hence, the error (2.46) quantifies the maximum error obtainable throughout $\overline{\Omega} = \Omega \cup \partial\Omega$.

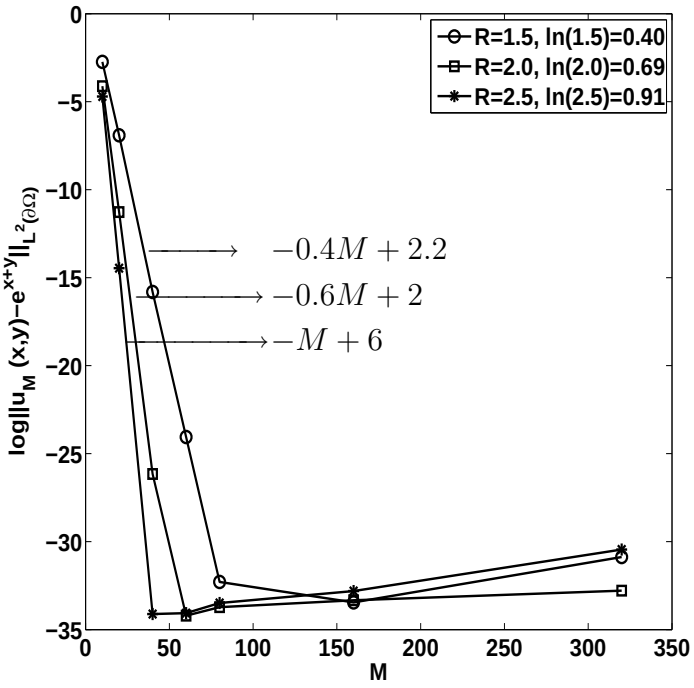

Figure 2.7: Logarithm of the global $L^2(\partial\Omega)$ error for the numerical boundary solution $u\,|_{\partial\Omega}$ versus M, for various R.

2.4.2 Example 2 (Modified Helmholtz equation, square)

In order to illustrate how the MFS performs in non-smooth domains with corners we consider the solution domain to be the square $\Omega = (-1/2, 1/2) \times (-1/2, 1/2)$. Again we investigate the convergence of the numerical solution as $M = N$ increases. The source points are located on an outside square at a distance $d \in \{1, 1.5, 2\}$ from the origin, see Figure 2.2(b).

Example 2. The numerical interior solutions for $u(0.2, 0.2)$ obtained with $M = N \in \{20, 40, 80\}$ and $d \in \{1, 1.5, 2\}$ are shown in Table 2.2. From this table it can be seen that as $M = N$ increases, or d increases the numerical solution for $u(0.2, 0.2)$ converges toward its exact value of $e^{0.4} \simeq 1.4918247$. The numerical solutions for normal derivative $\partial u/\partial n(S)$, where S is the arclength measured counterclockwise along the perimeter starting from the corner $(-1/2, -1/2)$ obtained with $d = 1$ and various values of $M = N \in \{20, 40, 80\}$ are shown in Figure 2.8 in comparison with

the analytical solution (2.31) given by

$$\frac{\partial u}{\partial n}(x,y) = \begin{cases} -e^{x-1/2}, & x \in (-\frac{1}{2},\frac{1}{2}), y = -\frac{1}{2} \\ e^{1/2+y}, & y \in (-\frac{1}{2},\frac{1}{2}), x = \frac{1}{2} \\ e^{1/2+x}, & x \in (-\frac{1}{2},\frac{1}{2}), y = \frac{1}{2} \\ -e^{y-1/2}, & y \in (-\frac{1}{2},\frac{1}{2}), x = -\frac{1}{2} \end{cases} \tag{2.47}$$

From this figure it can be seen that the numerical solution converges to the analytical solution (2.47) as $M = N$ increases. Similar results have been obtained when the source points were located on an outside circle of radius $R = \{1, 1.5, 2\}$ centred at the origin, see Figure 2.2(c), and therefore they are presented.

Table 2.2: The numerical solution for $u(0.2, 0.2)$ in Example 2 for various values of $M = N \in \{20, 40, 80\}$ and $d \in \{1, 1.5, 2\}$. The exact value is $e^{0.4} \simeq 1.4918247$.

$M = N$	d	$u(0.2, 0.2)$	d	$u(0.2, 0.2)$	d	$u(0.2, 0.2)$
20	1	1.49182876	1.5	1.49182469	2	1.4918247
40	1	1.4918247	1.5	1.4918247	2	1.4918247
80	1	1.4918247	1.5	1.4918247	2	1.4918247

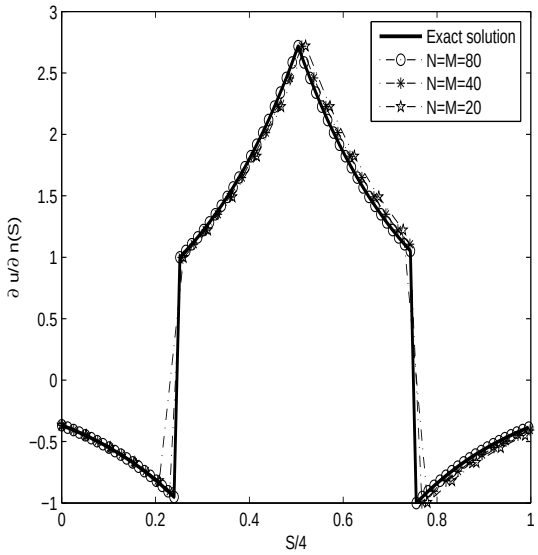

Figure 2.8: The analytical and the MFS solutions for the normal derivative $\partial u/\partial n(S)$, as a function of the arclength S for various values of $M = N \in \{20, 40, 80\}$ and $d = 1$, for Example 2.

2.4.3 Example 3 (Modified Helmholtz equation, annulus)

In order to illustrate how the MFS performs in multiply-connected domains we consider the solution domain to be the annulus $\Omega = \{\underline{X} = (x, y) \in \mathbb{R}^2 | 1 < x^2 + y^2 < 4\}$, and, as in the previous section, we investigate the convergence of the numerical solution as $M = N$ increases. In the case of annulus, the source points are located on an outside circle of radius $R = 2.5$ and on an inside circle of radius $R = 0.5$, see Figure 2.2(d). The numerical interior solutions for $u(1.5, \theta)$ obtained with $M = N \in \{20, 40, 80\}$ are shown in Figure 2.9. Form Figure 2.9 it can be seen that as $M = N$ increases the numerical solution for $u(1.5, \theta)$ converges toward the analytical solution (2.29). The numerical solutions for the normal derivatives $\partial u/\partial n(1, \theta)$ and $\partial u/\partial n(2, \theta)$, for various values of $M = N \in \{20, 40, 80\}$ are shown in Figure 2.10 in comparison with the analytical solutions (2.31) given by

$$\begin{aligned} \frac{\partial u}{\partial n}(1, \theta) &= -(\cos(\theta) + \sin(\theta)) e^{\cos(\theta)+\sin(\theta)}, \\ \frac{\partial u}{\partial n}(2, \theta) &= (\cos(\theta) + \sin(\theta)) e^{2(\cos(\theta)+\sin(\theta))}, \quad \theta \in [0, 2\pi). \end{aligned} \tag{2.48}$$

From Figure 2.10 it can be seen that the numerical solution converges to the analytical solution (2.40) as $M = N$ increases. Overall from Figures 2.9 and 2.10 it can be concluded that the MFS provides a convergent and accurate numerical solution for solving the Dirichlet problem for the modified Helmholtz equation in multiply-connected geometries.

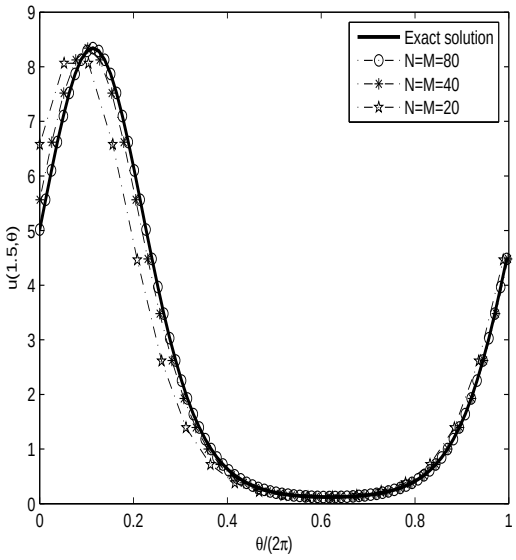

Figure 2.9: The analytical and the MFS solutions for $u(1.5, \theta)$ for various values of $M = N \in \{20, 40, 80\}$, for Example 3.

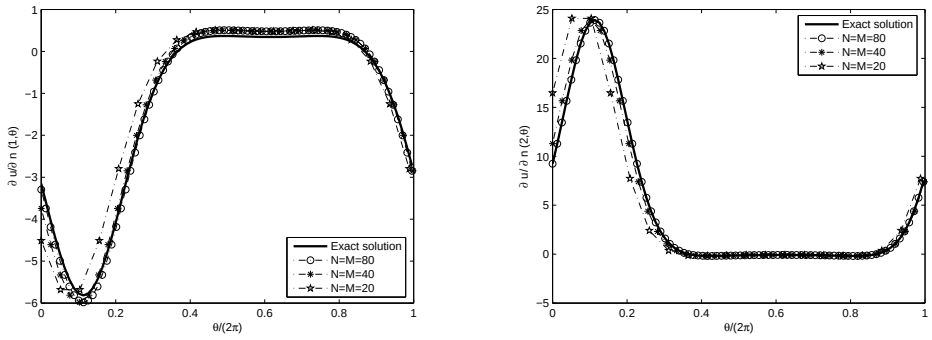

(a) (b)

Figure 2.10: The analytical and the MFS solutions for the normal derivatives (a) $\partial u/\partial n(1, \theta)$ and (b) $\partial u/\partial n(2, \theta)$, for various values of $M = N \in \{20, 40, 80\}$, for Example 3.

2.4.4 Example 4 (Helmholtz equation, circle)

As in Example 1, for the unit circle geometry $\Omega = B(\mathbf{0}; 1)$, the source points are located on a circle of radius $R > 1$ centred at the origin, and we investigate various values of $R \in \{1.5, 2, 2.5\}$. The distributions of source and boundary collocation points are shown in Figure 2.2(a). The numerical interior solutions for $u(0.7, 0.5)$ obtained with $M = N \in \{20, 40, 80\}$ and $R = \{1.5, 2, 2.5\}$ are shown in Table 2.3. From this

table it can be seen that as $M = N$ increases, or as R increases the numerical solution for $u(0.7, 0.5)$ converges toward its exact value of $\sin(1.2) = 0.93203909$. For solutions with no singularities outside $\overline{\Omega}$ the estimate (2.25) holds and the value of R can be increased until a very ill-conditioned matrix would eventually fail a Gaussian elimination inversion. Figure 2.11 shows the numerical solutions for normal derivative $\partial u/\partial n(1, \theta)$ obtained with $R = 2$ and various values of $M = N \in \{20, 40, 80\}$ in comparison with the analytical solution (2.37) given by

$$\frac{\partial u}{\partial n}(1, \theta) = (\cos(\theta) + \sin(\theta)) \cos(\cos(\theta) + \sin(\theta)), \qquad \theta \in [0, 2\pi). \tag{2.49}$$

From this figure it can be seen that the numerical solution converges to the analytical solution (2.49) as $M = N$ increases. Overall form Table 2.3 and Figure 2.11 it can be concluded that the MFS solution is a convergent and accurate numerical solution for solving the Dirichlet problem for the Helmholtz equation in smooth geometries.

Table 2.3: The numerical solution for $u(0.7, 0.5)$ in Example 4 for various values of $M = N \in \{20, 40, 80\}$ and $R \in \{1.5, 2, 2.5\}$. The exact value is $\sin(1.2) \simeq 0.93203909$.

$M = N$	R	$u(0.7, 0.5)$	R	$u(0.7, 0.5)$	R	$u(0.7, 0.5)$
20	1.5	0.93205434	2	0.93203926	2.5	0.93203909
40	1.5	0.93203909	2	0.93203909	2.5	0.93203909
80	1.5	0.93203909	2	0.93203909	2.5	0.93203909

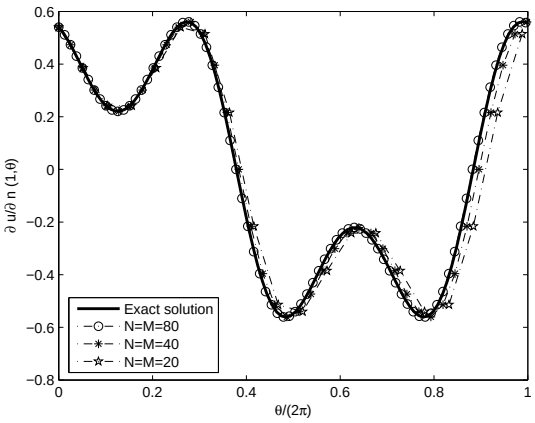

Figure 2.11: The analytical and the MFS solutions for the normal derivative $\partial u/\partial n(1, \theta)$ for various values of $M = N \in \{20, 40, 80\}$ and $R = 2$, for Example 4.

2.4.5 Example 5 (Helmholtz equation, annulus)

As in Example 3, the annular geometry is $\Omega = \{\underline{X} = (x, y) \in \mathbb{R}^2 | 1 < x^2 + y^2 < 4\}$, and we investigate the convergence of the numerical solution as $M = N$ increases. The source points are located on an outside circle of radius $R_2 = 2.5$ and on an inside circle of radius $R_1 = 0.5$, see Figure 2.2(d). The numerical interior solutions for $u(1.5, \theta)$ obtained with $M = N \in \{20, 40, 80\}$ are shown in Figure 2.12. Form this figure it can be seen that as $M = N$ increases the numerical solution for $u(1.5, \theta)$ converges towards the analytical solution (2.35). This concludes that the MFS provides a convergent and accurate numerical solution for solving the Dirichlet problem for the Helmholtz equation in multiply-connected geometries.

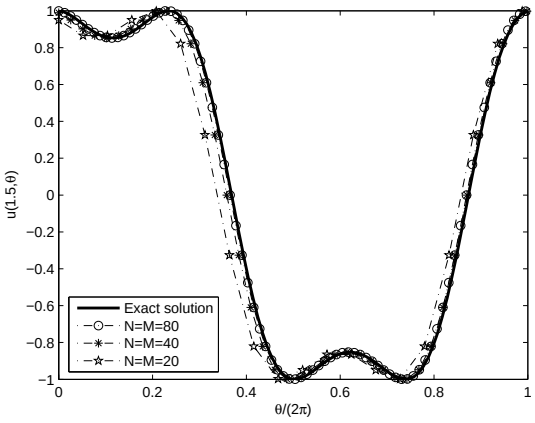

Figure 2.12: The analytical and the MFS solutions for $u(1.5, \theta)$ for various values of $M = N \in \{20, 40, 80\}$, for Example 5.

2.4.6 Example 6 (Helmholtz equation, unbounded exterior of a circle)

In the direct scattering problem, let $\Omega \subset \mathbb{R}^2$ be a bounded planar domain with boundary $\partial\Omega \in C^2$ such that the exterior $\mathbb{R}^2 \backslash \overline{\Omega}$ of $\overline{\Omega}$ is connected. We are given the wave number $k > 0$, and an incident field given by a plane wave moving in the unit direction $\widehat{\underline{d}} \in S^1 = \{\underline{d} \in \mathbb{R}^2 : |\underline{d}| = 1\}$, namely

$$u^{inc}(\underline{X}) = e^{\mathrm{i}k\underline{X}.\widehat{\underline{d}}}, \qquad \underline{X} \in \mathbb{R}^2. \tag{2.50}$$

Then the scattering of u^{inc} by Ω produces a scattered wave u^s with corresponding total field $u = u^s + u^{inc}$, where $u^s \in C^2(\mathbb{R}^2 \backslash \overline{\Omega}) \cap C^1(\mathbb{R}^2 \backslash \Omega)$ which satisfies the

Helmholtz equation

$$\Delta u^s(\underline{X}) + k^2 u^s(\underline{X}) = 0, \qquad \underline{X} \in \mathbb{R}^2 \backslash \overline{\Omega} \tag{2.51}$$

and the Sommerfeld radiation condition at infinity

$$\lim_{r\to\infty} \sqrt{r}\Big(\frac{\partial u^s}{\partial r}(\underline{X}) - \mathrm{i}k u^s(\underline{X})\Big) = 0 \quad \text{(uniformly with respect to } \widehat{\underline{X}} = \underline{X}/|\underline{X}|), \tag{2.52}$$

where $r = |\underline{X}|$, and the boundary conditions corresponding to:

(a) the Dirichlet boundary condition (sound-soft obstacle)

$$u(\underline{X}) = 0, \quad \underline{X} \in \partial\Omega \iff u^s(\underline{X}) = -u^{inc}(\underline{X}) = -e^{\mathrm{i}k\underline{X}.\widehat{\underline{d}}}, \quad \underline{X} \in \partial\Omega \tag{2.53}$$

or

(b) the Neumann boundary condition (sound-hard obstacle)

$$\frac{\partial u}{\partial n}(\underline{X}) = 0, \quad \underline{X} \in \partial\Omega \iff \tfrac{\partial u^s}{\partial n}(\underline{X}) = -\tfrac{\partial u^{inc}}{\partial n}(\underline{X}) = -\tfrac{\partial (e^{\mathrm{i}k\underline{X}.\widehat{\underline{d}}})}{\partial n}(\underline{X}), \quad \underline{X} \in \partial\Omega. \tag{2.54}$$

In the scattering problem from an obstacle Ω, say the unit circle, the solution domain is exterior and unbounded hence, the MFS source points are located on an inside circle of radius $R_1 < 1$, say $R_1 = 1/2$, centred at the origin. The distributions of source and boundary collocation points are shown in Figure 2.2(e). The analytical solution for the direct scattering from a sound-soft circular obstacle $B(\mathbf{0}; a)$ of radius a centred at the origin by an incident plane wave in the $x-$direction is given by, see Colton and Kress (1983),

$$u(r,\theta) = J_0(kr) - \frac{J_0(ka)H_0^{(1)}(kr)}{H_0^{(1)}(ka)} + 2\sum_{n=1}^{\infty} \mathrm{i}^n \cos(n\theta) \quad \Big[J_n(kr) - \tfrac{J_n(ka)H_n^{(1)}(kr)}{H_n^{(1)}(ka)}\Big], \quad (r,\theta) \in \mathbb{R}^2 \backslash B(\mathbf{0}; a) = \{r \geq a, \theta \in [0, 2\pi)\} \tag{2.55}$$

where $H_n^{(1)}$ and J_n are the Hankel and Bessel functions of first kind of order n, respectively. For simplicity, we consider the Dirichlet sound-soft boundary condition (2.53). In what follows we take $a = k = 1$.

The connection between the Rayleigh hypothesis, i.e. the region of the convergence of the series (2.55), and the MFS has been pointed out recently by Martin (2012). In particular, in the MFS the radius $R_1 < 1$ should be chosen such that

there are no singularities of the analytic continuation of the solution in the annulus $B(\mathbf{0}; a)\backslash B(\mathbf{0}; R_1)$.

We investigate the convergence of the numerical solution as $M = N$ increases. The numerical exterior solutions for the real and imaginary parts of $u^s(2, \theta)$ obtained with $M = N \in \{20, 40, 80\}$ are shown in Figure 2.13. From this figure it can be seen that the numerical solution converges towards the analytical solution (2.55) on $\partial B(\mathbf{0}, 2)$, as $M = N$ increases.

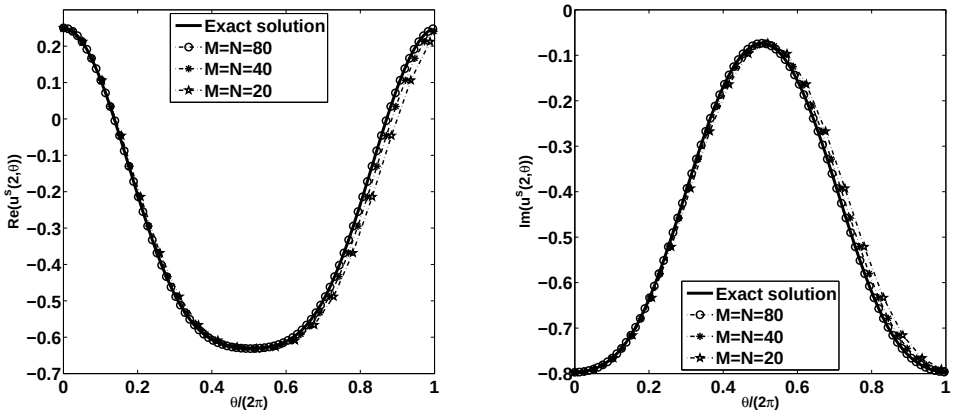

(a) (b)

Figure 2.13: The analytical and the MFS solutions of: (a) real, and (b) imaginary parts of $u^s(2, \theta)$ for various values of $M = N \in \{20, 40, 80\}$, for Example 6.

The numerical solutions for the real and imaginary parts of the normal derivative $\partial u^s/\partial n(1, \theta)$, for various values of $M = N \in \{20, 40, 80\}$ are shown in Figure 2.14 in comparison with the analytical solution

$$\frac{\partial u^s}{\partial n}(1, \theta) = \frac{\partial u}{\partial n}(1, \theta) - \frac{\partial u^{inc}}{\partial n}(1, \theta) \qquad \theta \in [0, 2\pi), \tag{2.56}$$

where from (2.55),

$$\frac{\partial u}{\partial n}(1, \theta) = \frac{\partial u}{\partial r}(1, \theta) = \frac{kJ_0(k)H_1^{(1)}(k)}{H_0^{(1)}(k)} - kJ_1(k) + 2k\sum_{n=1}^{\infty} \mathrm{i}^n \cos(n\theta)$$
$$\Big[J_{n-1}(k) - \frac{n}{k}J_n(k) - \frac{J_n(k)(\frac{n}{k}H_n^{(1)}(k) - H_{n+1}^{(1)}(k))}{H_n^{(1)}(k)}\Big], \quad \theta \in [0, 2\pi). \tag{2.57}$$

We also have that

$$\frac{\partial u^{inc}}{\partial n}(1, \theta) = \frac{\partial(e^{\mathrm{i}kr\cos(\theta)})}{\partial r}(1, \theta) = \mathrm{i}k\cos(\theta)e^{\mathrm{i}k\cos(\theta)}. \tag{2.58}$$

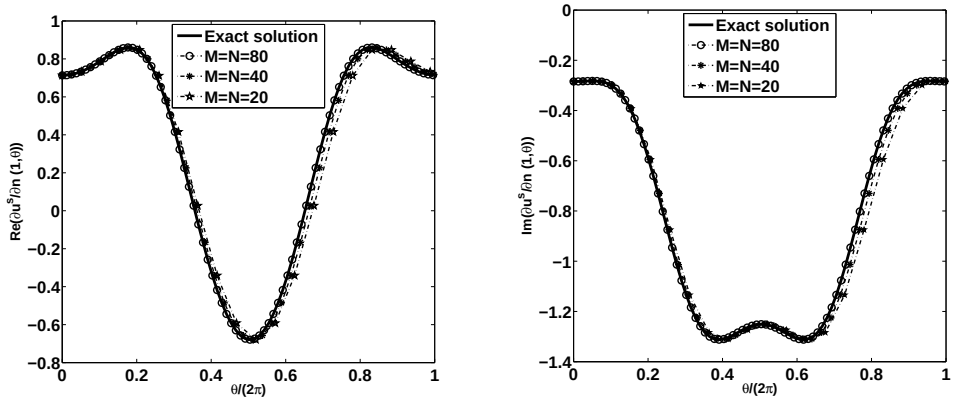

(a) (b)

Figure 2.14: The analytical and the MFS solutions of: (a) real, and (b) imaginary parts of $\partial u^s/\partial n(1,\theta)$ for various values of $M = N \in \{20, 40, 80\}$, for Example 6.

From Figure 2.14 it can be seen that the numerical solution for the normal derivative converges to the analytical solution (2.56) as $M = N$ increases. We have also investigated the numerical results for various values of $R_1 \in (0, 1)$ and, although not illustrated, we report that the numerical MFS solutions become more accurate as R_1 decreases from 1 to about 0.1, after which ill-conditioning takes over and regularization would be required. Overall from Figures 2.13 and 2.14 it can be concluded that the MFS provides a convergent and accurate numerical solution for solving direct scattering problems in exterior unbounded domains. In the next examples we extend the MFS analysis to three-dimensions.

2.4.7 Example 7 (Modified Helmholtz equation, sphere)

In this example in which the domain Ω is a sphere, a standard equiangular spherical coordinates distribution is used for the boundary collocation and source points given by

$$\begin{cases} x = r\cos(\theta_j)\sin(\phi_i), \\ y = r\sin(\theta_j)\sin(\phi_i), \\ z = r\cos(\phi_i), \end{cases} \tag{2.59}$$

where $\theta_j = \frac{2\pi j}{M}$, $\phi_i = \frac{\pi i}{M}$, for $i, j = \overline{1, M}$. This was introduced only for convenience and is not optimal as it concentrates points near the poles. More sophisticated knot distributions are also possible, see Alves and Valtchev (2005).

In order to illustrate how the MFS performs in a typical three-dimensional smooth geometry we consider the solution domain to be the unit sphere $\Omega = \{\underline{X} = (x, y, z) \in \mathbb{R}^3 | x^2 + y^2 + z^2 < 1\}$, with the source points located on a sphere of radius

$R > 1$, centred at the origin. We investigate various values of $R \in \{1.5, 2, 2.3\}$, and also the convergence of the numerical solution as M^2 increases. The distributions of source and boundary collocation points are shown in Figure 2.2(f). The numerical interior solutions for $u(0.5, \theta, \pi/2)$ and $u(0.5, \pi/4, \phi)$ obtained with $M \in \{5, 10, 20\}$ and $R \in \{1.5, 2, 2.3\}$ are shown in Figures 2.15 and 2.16, respectively. From these figures it can be seen that as M increases, or the radius R increases the numerical solutions for $u(0.5, \theta, \pi/2)$ and $u(0.5, \pi/4, \phi)$ converge toward the analytical solution (2.32).

The numerical solution for the normal derivative $\partial u/\partial n(1, \theta, \phi)$ obtained with $R = 2$ and $M^2 = 20 \times 20$ is shown in Figure 2.17 in comparison with the analytical solution (2.34) given by

$$\frac{\partial u}{\partial n}(1, \theta, \phi) = (\cos(\theta)\sin(\phi) + \sin(\theta)\sin(\phi) + \cos(\phi))e^{\cos(\theta)\sin(\phi)+\sin(\theta)\sin(\phi)+\cos(\phi)}, \quad \theta \in [0, 2\pi), \phi \in [0, \pi). \tag{2.60}$$

From this figure it can be seen that the numerical solution converges to the analytical solution (2.60) as increases. Overall from Figures 2.15-2.17 it can be concluded that the MFS provides a convergent and accurate numerical solution for solving the Dirichlet problem for the modified Helmholtz equation in a smooth simply-connected three-dimensional geometry such as a sphere.

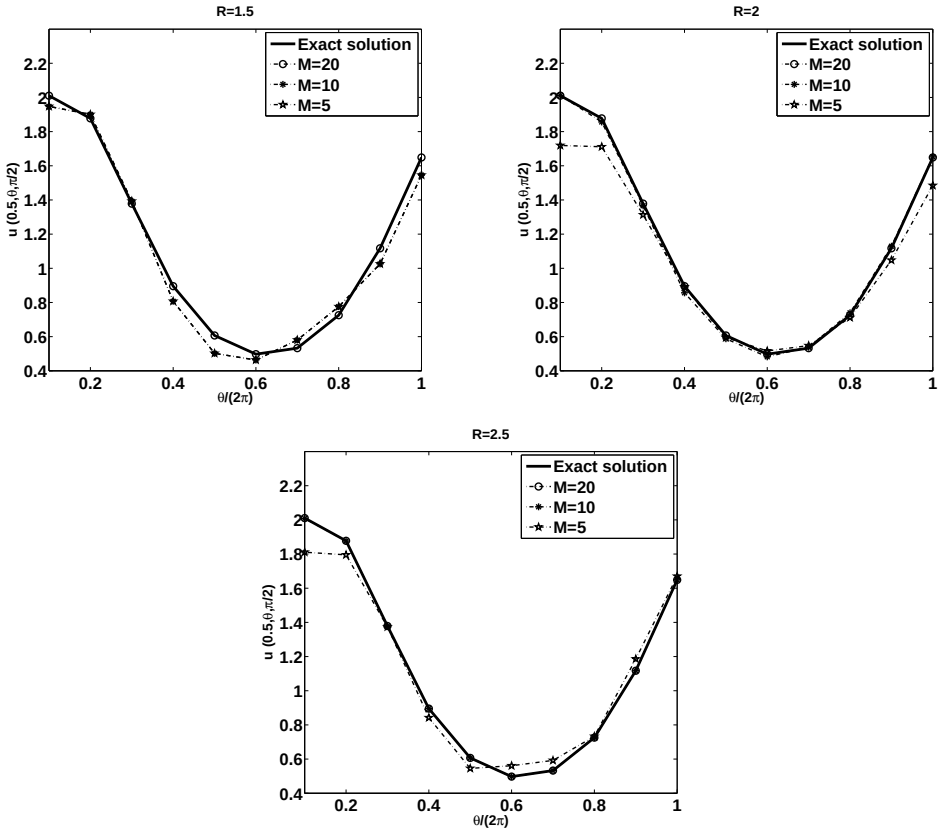

Figure 2.15: The analytical and the MFS solutions for $u(0.5, \theta, \pi/2)$ for various $M \in \{5, 10, 20\}$ and $R \in \{1.5, 2, 2.3\}$, for Example 7.

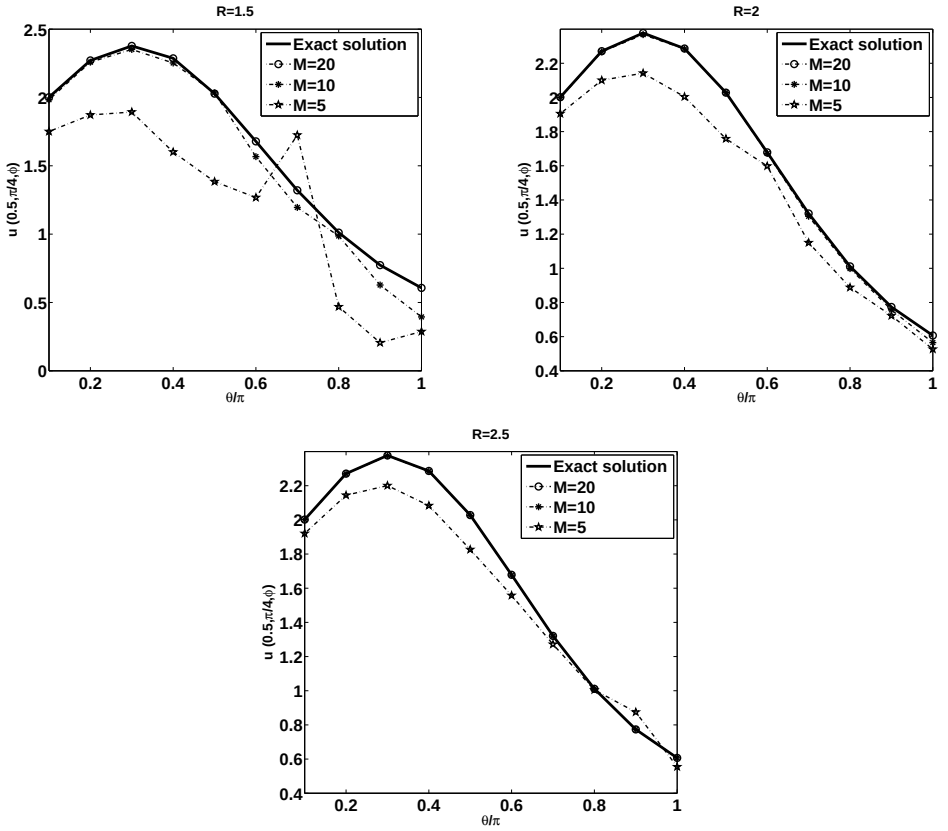

Figure 2.16: The analytical and the MFS solutions for $u(0.5, \pi/4, \phi)$ for various $M \in \{5, 10, 20\}$ and $R \in \{1.5, 2, 2.3\}$, for Example 7.

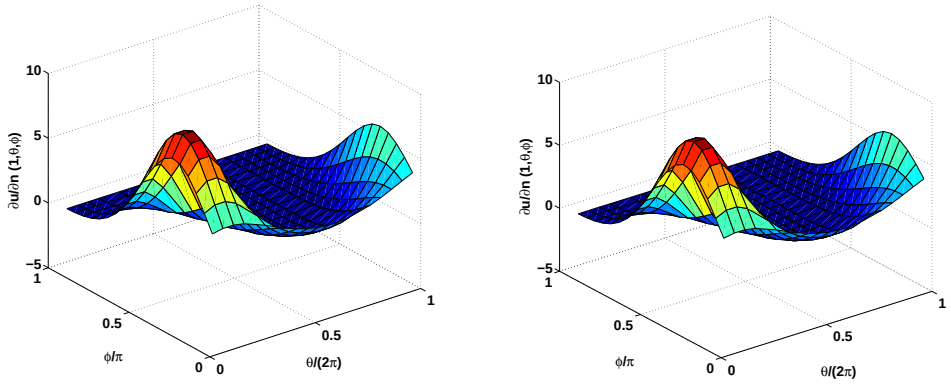

(a) Exact solution (b) MFS solution

Figure 2.17: (a) The analytical, and (b) the MFS solution for the normal derivative $\partial u/\partial n(1, \theta, \phi)$ for $M = 20$ and $R = 2$, for Example 7.

In order to investigate the influence of the number M of source and boundary collocation points and the radius R on the convergence of the numerical results

obtained, we set $M \in \{10, 15, 20, 30, 40, 50, 60, 80\}$, $R \in \{1.5, 2, 2.5\}$. Figure 2.18 shows the logarithm of the local absolute error at the interior point $(0.5, 0, 0) \in \Omega$. From this figure it can be seen that this error decreases exponentially as the number M of source/collocation points increases to 40, 50, and 80. This can be estimated by the equations $\log|u_M(0.5,0,0) - e^{0.5}| = -0.4M + 2.8$, $-0.7M + 2$, and $-0.8M + 2$ when $R = 1.5, 2$, and 2.5, respectively. This is expected since from (2.25) we have

$$\log|u_M(x_0, y_0, z_0) - u(x_0, y_0, z_0)| \leq C - M \log R. \tag{2.61}$$

However, this error increases slightly for $M > 80$, $M > 50$, and $M > 40$ for $R = 1.2, 2$ and 2.5, respectively, the reason of increasing error is the same reason of ill-conditioning as in the two-dimensional case.

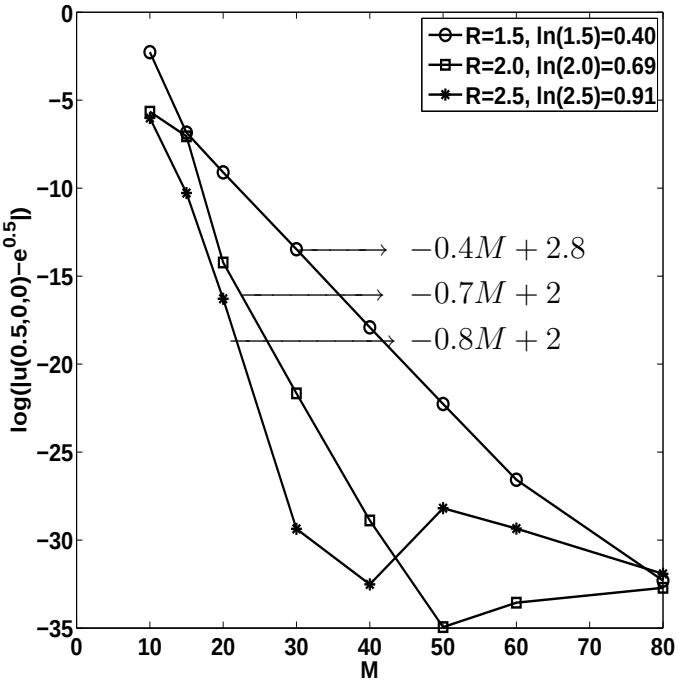

Figure 2.18: Logarithm of the local absolute error at the interior point $(0.5, 0, 0) \in \Omega$ versus M, for various R.

Figure 2.19 shows the global error for the interior numerical solution given by

$$\|u_M(x,y,z) - u(x,y,z)\|_{L^2(\Omega)} \simeq$$
$$\sqrt{\sum_{k=1}^{4}\sum_{i=1}^{10}\sum_{j=1}^{10}\left(\frac{1}{5}\right)\left(\frac{2\pi}{10}\right)\left(\frac{\pi}{10}\right) r_k^2 \sin(\phi_j)\left|u_M(r_k,\theta_i,\phi_j) - u(r_k,\theta_i,\phi_j)\right|^2}, \tag{2.62}$$

where $r_k = k/5$ for $k = \overline{1,4}$, $\theta_i = 2\pi i/10$ for $i = \overline{1,10}$, and $\phi_j = \pi j/10$ for $j = \overline{1,10}$. It can be seen that error decreases exponentially as M increases to 40, 50, and 80. This can be estimated by the equations $\log \|u_M(x,y,z) - e^{x+y+z}\|_{L^2(\Omega)} = -0.4M + 2$, $-0.7M + 4$, and $-0.8M + 3$ when $R = 1.5, 2$, and 2.5, respectively. This is expected since from (2.25) we have

$$\frac{\sqrt{3}}{2\sqrt{\pi}} \|u_M(x,y,z) - u(x,y,z)\|_{L^2(\Omega)} \leq \sup_{(x,y,z)\in\Omega} |u_M(x,y,z) - u(x,y,z)| \leq \frac{C}{R^M}. \quad (2.63)$$

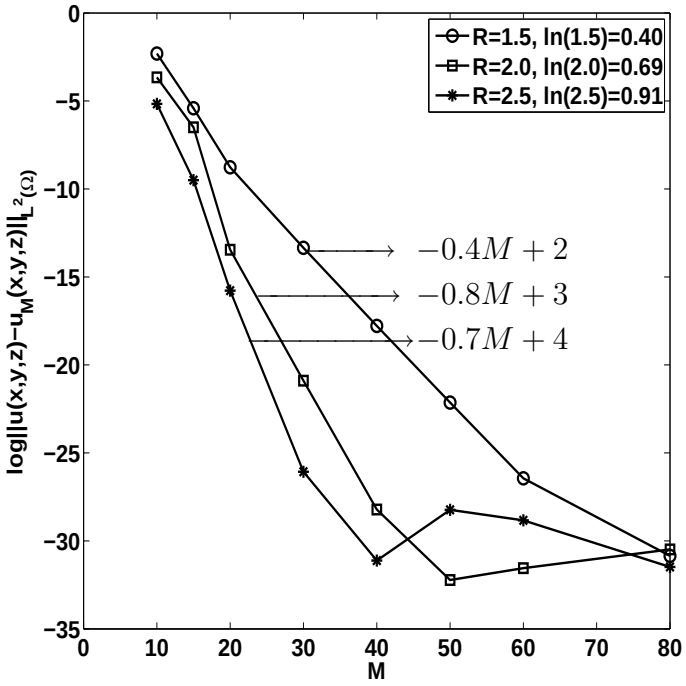

Figure 2.19: Logarithm of the global $L^2(\Omega)$ error for the numerical interior solution $u|_\Omega$ versus M, for various R.

However, the error increases slightly for $M > 80$, $M > 50$, and $M > 40$, respectively, as a result of ill-conditioning. Overall from Figures 2.18 and 2.19 it can be concluded that the rate of convergence of the MFS approximation in two- or three-dimensions for Helmholtz-type equations satisfy equation (2.25) which shows that the error is exponentially decreasing as $M \to \infty$. However, as given by equation (2.27), the condition number also increases exponentially as $M \to \infty$.

2.4.8 Example 8 (Modified Helmholtz equation, annular sphere)

In order to illustrate how the MFS performs in multiply-connected three-dimensional domains we consider the solution domain to be the annular sphere $\Omega = \{\underline{X} = (x, y, z) \in \mathbb{R}^3 | 1 < x^2 + y^2 + z^2 < 4\}$. We investigate the convergence of the numerical solution as the $2M^2$ increases. In the case of the annular sphere between the concentric circles of radii 1 and 2, the source points are located on an outside sphere of radius $R = 2.5$ and on an inside sphere of radius $R = 0.5$, see Figure 2.2(g). The numerical interior solutions for $u(1.5, \theta, \pi/2)$ and $u(1.5, \pi/4, \phi)$ obtained for various $M \in \{5, 10, 20\}$ are shown in Figure 2.20. From this figure it can be seen that as M increases the numerical solution for $u(1.5, \theta, \pi/2)$ and $u(1.5, \pi/4, \phi)$ converge toward the analytical solution (2.32). The numerical solutions for the normal derivatives $\partial u/\partial n(1, \theta, \phi)$ and $\partial u/\partial n(2, \theta, \phi)$, for $M = 20$ are shown in Figures 2.21 and 2.22 in comparison with the analytical solutions (2.34) given by

$$\begin{aligned}
\frac{\partial u}{\partial n}(1, \theta, \phi) &= -(\cos(\theta)\sin(\phi) + \sin(\theta)\sin(\phi) + \cos(\phi))e^{\cos(\theta)\sin(\phi)+\sin(\theta)\sin(\phi)+\cos(\phi)}, \\
\frac{\partial u}{\partial n}(2, \theta, \phi) &= (\cos(\theta)\sin(\phi) + \sin(\theta)\sin(\phi) + \cos(\phi))e^{2(\cos(\theta)\sin(\phi)+\sin(\theta)\sin(\phi)+\cos(\phi))}, \\
&\qquad \theta \in [0, 2\pi), \phi \in [0, \pi). \qquad (2.64)
\end{aligned}$$

From Figures 2.21 and 2.22 it can be seen that the numerical solutions for the normal derivatives are in good agreement with the analytical solutions (2.64). Overall from Figures 2.20-2.22 it can be concluded that the MFS provides a convergent and accurate numerical solution for solving the Dirichlet problem for the modified Helmholtz equation in multiply-connected three-dimensional smooth geometries such as an annular sphere.

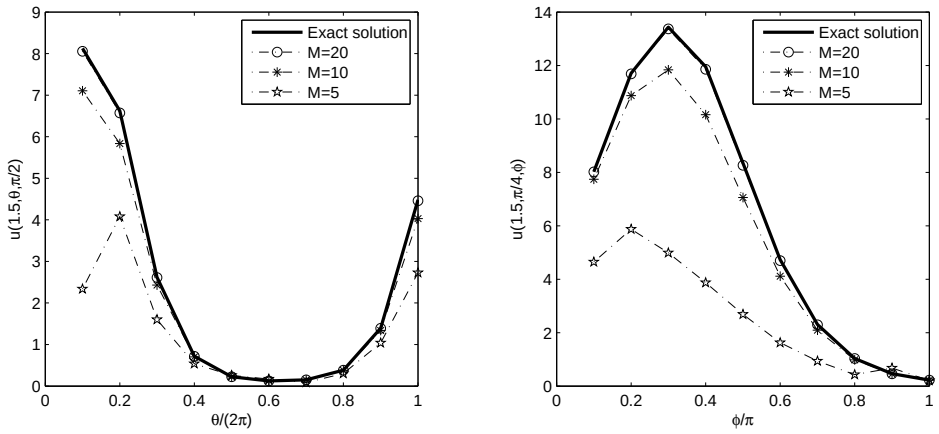

(a) (b)

Figure 2.20: The analytical and the MFS solutions for: (a) $u(1.5, \theta, \pi/2)$, and (b) $u(1.5, \pi/4, \phi)$ for various $M \in \{5, 10, 20\}$, for Example 8.

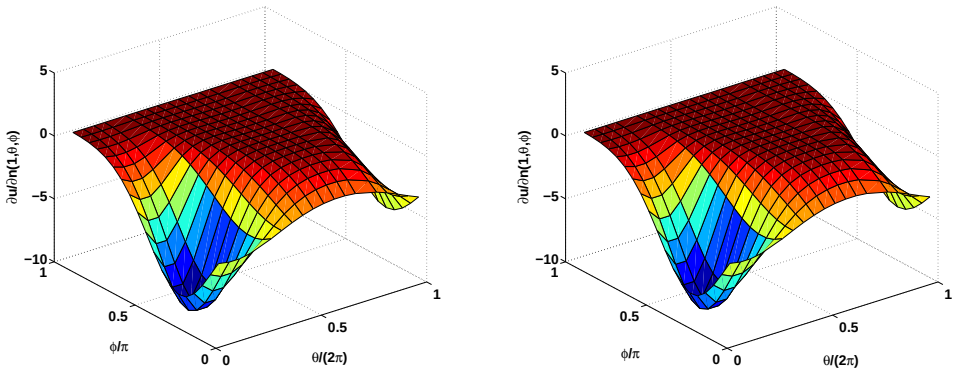

(a) Exact solution (b) MFS solution

Figure 2.21: (a) The analytical, and (b) the MFS solutions for the normal derivative $\partial u/\partial n(1, \theta, \phi)$, for $M = 20$, for Example 8.

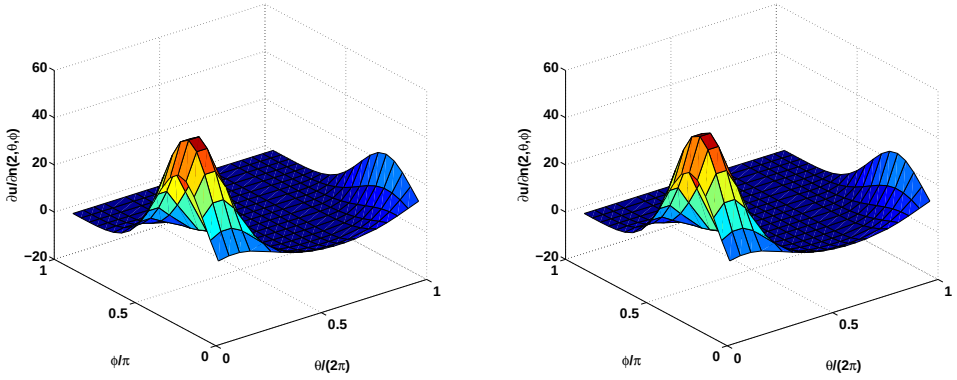

(a) Exact solution (b) MFS solution

Figure 2.22: (a) The analytical, and (b) the MFS solutions for the normal derivative $\partial u/\partial n(2,\theta,\phi)$, for $M = 20$, for Example 8.

2.4.9 Example 9 (Helmholtz equation, sphere)

As in Example 7, a standard equiangular spherical coordinates distribution for the boundary collocation and source points are used. In order to illustrate how the MFS performs in a typical three-dimensional smooth geometry we consider the solution domain to be the unit sphere $\Omega = \{\underline{X} = (x, y, z) \in \mathbb{R}^3 | x^2 + y^2 + z^2 < 1\}$, with the source points located on a sphere of radius $R > 1$, centred at the origin. We investigate various values of $R \in \{1.5, 2, 2.5\}$, and also the convergence of the numerical solution as M^2 increases. The distributions of source and boundary collocation points are shown in Figure 2.2(f). The numerical interior solutions for $u(0.5, \theta, \pi/2)$ and $u(0.5, \pi/4, \phi)$ obtained with $M \in \{5, 10, 20\}$ and $R \in \{1.5, 2, 2.5\}$ are shown in Figures 2.23 and 2.24, respectively. From these figures it can be seen that as M increases, or the radius R increases the numerical solutions for $u(0.5, \theta, \pi/2)$ and $u(0.5, \pi/4, \phi)$ converge toward the analytical solution (2.38).

The numerical solution for the normal derivative $\partial u/\partial n(1, \theta, \phi)$ obtained with $R = 2$ and $M^2 = 20 \times 20$ is shown in Figure 2.25 in comparison with the analytical solution (2.40) given by

$$\frac{\partial u}{\partial n}(1,\theta,\phi) = [\cos(\theta)\sin(\phi) + \sin(\theta)\sin(\phi) + \cos(\phi)]\cos(\cos(\theta)\sin(\phi) + \sin(\theta)\sin(\phi) + \cos(\phi)), \qquad \theta \in [0, 2\pi), \phi \in [0, \pi). \tag{2.65}$$

From this figure it can be seen that the numerical solution converges to the analytical solution (2.65) as M increases. Overall from Figures 2.23-2.25 it can be concluded that the MFS provides a convergent and accurate numerical solution for solving

the Dirichlet problem for the Helmholtz equation in a smooth simply-connected three-dimensional geometry such as a sphere.

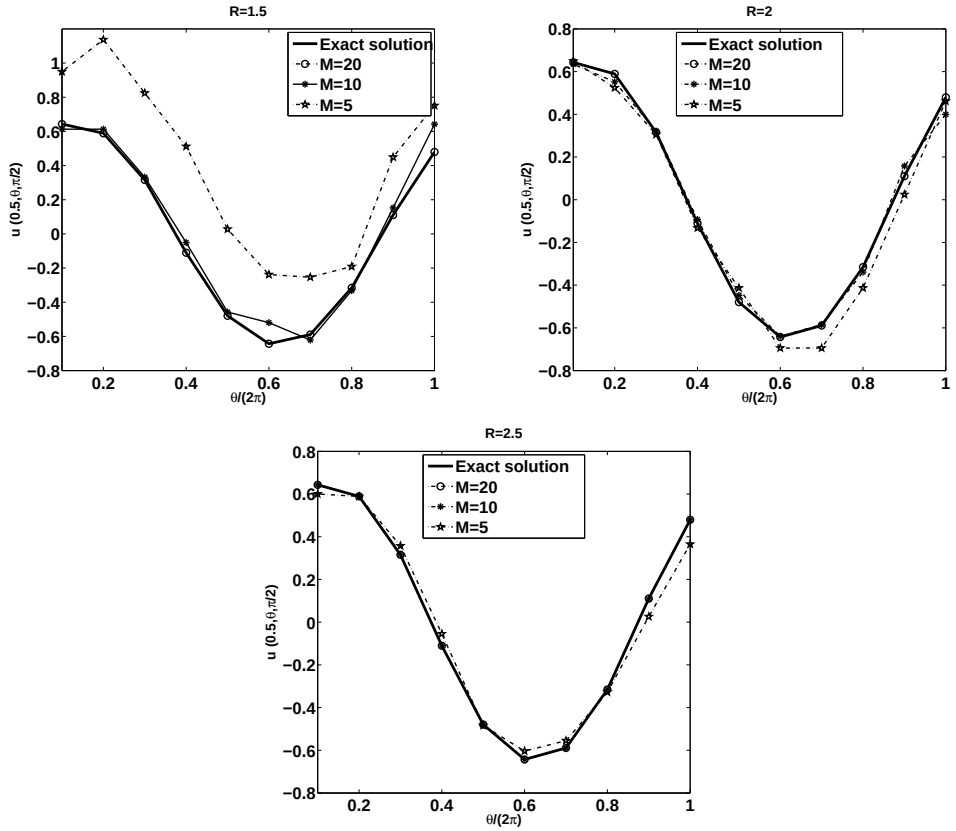

Figure 2.23: The analytical and the MFS solutions for $u(0.5, \theta, \pi/2)$ for various $M \in \{5, 10, 20\}$ and $R \in \{1.5, 2, 2.5\}$, for Example 9.

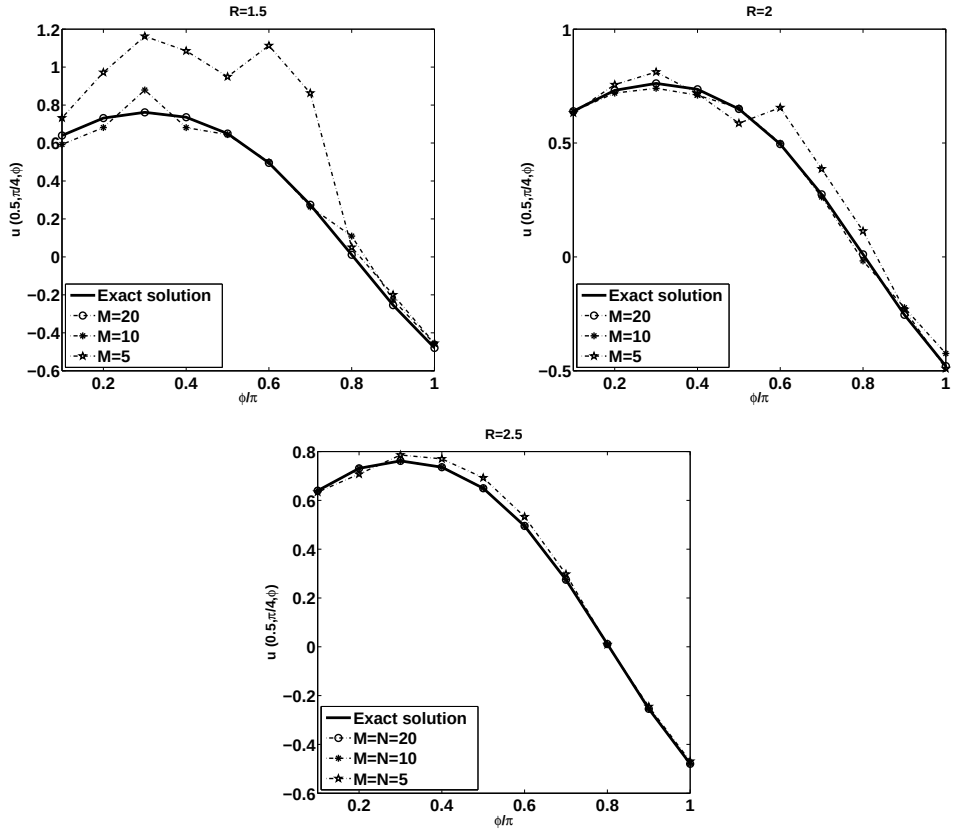

Figure 2.24: The analytical and the MFS solutions for $u(0.5, \pi/4, \phi)$ for various $M \in \{5, 10, 20\}$ and $R \in \{1.5, 2, 2.5\}$, for Example 9.

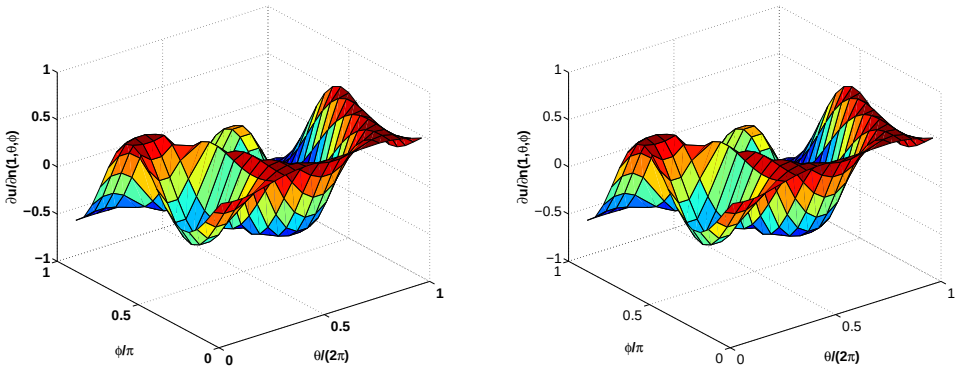

(a) (b)

Figure 2.25: (a) The analytical, and (b) the MFS solution for the normal derivative $\partial u/\partial n(1, \theta, \phi)$ for $M = 20$ and $R = 2$, for Example 9.

2.4.10 Example 10 (Helmholtz equation, unbounded exterior of a sphere)

For the direct scattering problem in three-dimensions, let $\Omega \subset \mathbb{R}^3$ be a bounded planar domain with boundary $\partial\Omega \in C^2$ such that the exterior $\mathbb{R}^3\backslash\overline{\Omega}$ of $\overline{\Omega}$ is connected. We are given the wave number $k > 0$, and an incident field given by a plane wave moving in the unit direction $\widehat{\underline{d}} \in S^2 = \{\underline{d} \in \mathbb{R}^3 : |\underline{d}| = 1\}$, namely

$$u^{inc}(\underline{X}) = e^{\mathrm{i}k\underline{X}.\widehat{\underline{d}}}, \qquad \underline{X} \in \mathbb{R}^3. \tag{2.66}$$

Then the scattering of u^{inc} by Ω produces a scattered wave u^s with corresponding total field $u = u^s + u^{inc}$, where $u^s \in C^2(\mathbb{R}^3\backslash\overline{\Omega}) \cap C^1(\mathbb{R}^3\backslash\Omega)$ which satisfies the Helmholtz equation

$$\Delta u^s(\underline{X}) + k^2 u^s(\underline{X}) = 0, \qquad \underline{X} \in \mathbb{R}^3\backslash\overline{\Omega} \tag{2.67}$$

and the Sommerfeld radiation condition at infinity

$$\lim_{r\to\infty} r\Big(\frac{\partial u^s}{\partial r}(\underline{X}) - \mathrm{i}ku^s(\underline{X})\Big) = 0 \qquad \text{(uniformly with respect to } \widehat{\underline{X}} = \underline{X}/|\underline{X}|), \tag{2.68}$$

where $r = |\underline{X}|$, and the boundary conditions corresponding to (2.53) and (2.54).

As in Example 6, in the scattering problem from an obstacle Ω, say the unit sphere, the solution domain is exterior and unbounded hence, the MFS source points are located on an inside sphere of radius $R_1 < 1$, say $R_1 = 1/2$, centred at the origin. The distributions of source and boundary collocation points are shown in Figure 2.2(h). The analytical solution for the direct scattering from a sound-soft spherical obstacle $B(\mathbf{0}; a)$ of radius a centred at the origin by an incident plane wave in the $x-$direction is given by, see Colton and Kress (1998),

$$\begin{aligned} u^s(r,\theta,\phi) &= -\frac{j_0(ka)}{h_0^{(1)}(ka)} h_0^{(1)}(kr) P_0(\cos(\phi)) \\ &- \sum_{n=1}^{\infty} \mathrm{i}^n (2n+1) \frac{j_n(ka)}{h_n^{(1)}(ka)} h_n^{(1)}(kr) P_n(\cos(\phi)), \\ (r,\phi) &\in \mathbb{R}^3\backslash B(\mathbf{0}; a) = \{r \geq a, \phi \in [0,\pi)\} \end{aligned} \tag{2.69}$$

where $h_n^{(1)}$ and j_n are the spherical Hankel and spherical Bessel functions of first kind of order n, respectively, P_n is the Legendre function of degree n. For simplicity, we consider the Dirichlet sound-soft boundary condition (2.53). Corresponding to

(2.69), the normal derivative is given by

$$\frac{\partial u^s(a,\theta,\phi)}{\partial n} = \frac{kj_0(ka)P_0(\cos(\phi))h_1^{(1)}(ka)}{h_0^{(1)}(ka)} - \frac{k}{2}\sum_{n=1}^{\infty} \mathrm{i}^n(2n+1)\frac{j_n(ka)P_n(\cos(\phi))}{h_n^{(1)}(ka)} \Big[h_{n-1}^{(1)}(ka) - \frac{h_n^{(1)}(ka)+kah_{n+1}^{(1)}(ka)}{ka}\Big], \qquad \phi\in[0,\pi). \tag{2.70}$$

In what follows we take $a = k = 1$. We investigate the convergence of the numerical solution as $M = N$ increases. The numerical exterior solutions for real and imaginary parts of $u^s(2,\pi/4,\phi)$ obtained with $M = N \in \{8,16,32\}$ are shown in Figure 2.26. From this figure it can be seen that the numerical solution converges towards the analytical solution (2.69) on $\partial B(\mathbf{0},2)$, as $M = N$ increases.

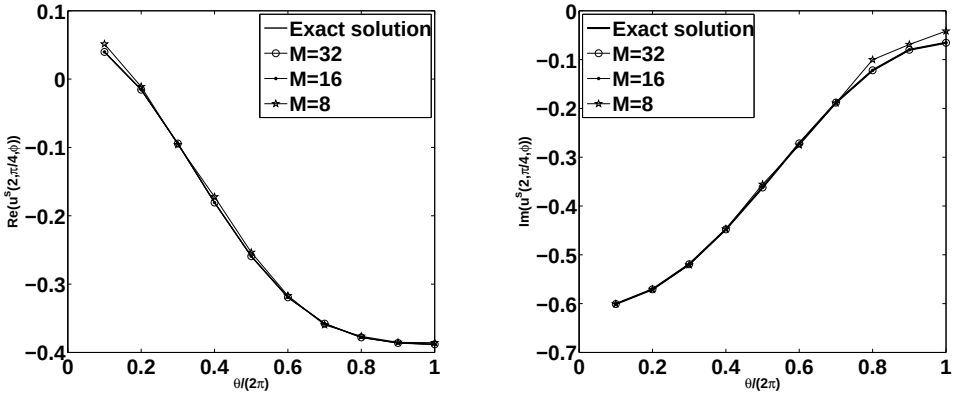

(a) (b)

Figure 2.26: The analytical and the MFS solutions of: (a) real, and (b) imaginary parts of $u^s(2,\pi/4,\phi)$ for various values of $M = N \in \{8,16,32\}$, for Example 10.

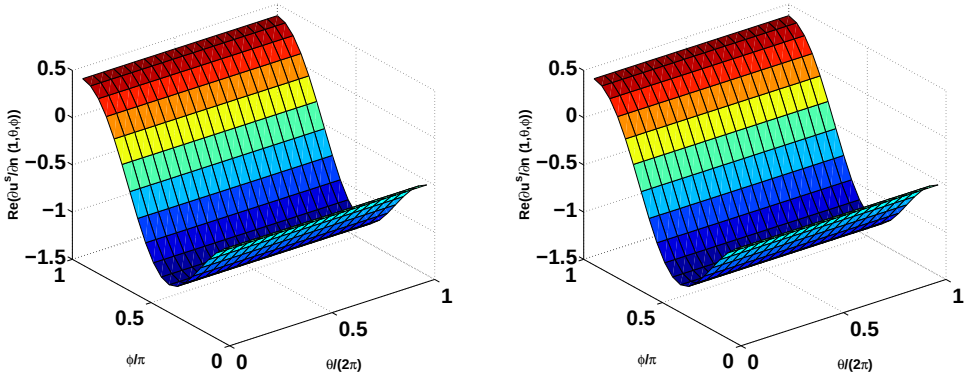

(a) Exact solution (b) MFS solution

Figure 2.27: (a) The analytical and (b) the MFS solutions of real part of $\partial u^s/\partial n(1,\theta,\phi)$ for various values of $M = N = 20$, for Example 10.

The numerical solutions for the real and imaginary parts of the normal derivative $\partial u^s/\partial n(1,\theta,\phi)$, for various values of $M = N = 20$ are shown in Figures 2.27 and 2.28 in comparison with the analytical solution (2.70). From these figures it can be seen that the numerical solution for the normal derivative converges to the analytical solution (2.70) as $M = N$ increases. Overall from Figures 2.26-2.28 it can be concluded that the MFS provides a convergent and accurate numerical solution for solving direct scattering problems in exterior unbounded domains.

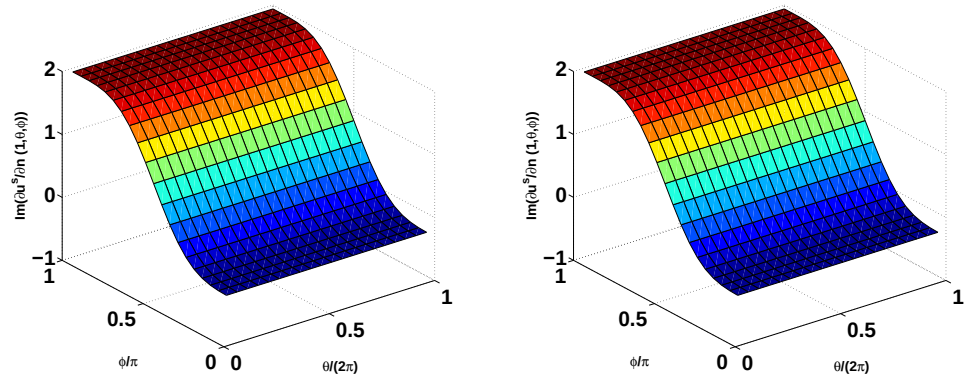

(a) Exact solution (b) MFS solution

Figure 2.28: (a) The analytical and (b) the MFS solutions of imaginary part of $\partial u^s/\partial n(1,\theta,\phi)$ for various values of $M = N = 20$, for Example 10.

2.5 Conclusions

In this chapter, Helmholtz-type equations in two- or three-dimensions, subject to (Dirichlet) boundary conditions, have been investigated by employing the MFS. Ten examples involving various geometries (circle, square, annulus, exterior unbounded of a circle, sphere, annular sphere) have been analysed. The numerical results obtained show that the convergence of the MFS depend on increasing the number of source and collocation points and the distance from the source points to the boundary of the solution domain. The application of the MFS for Helmholtz-type equations in composite materials will be presented in the next chapter.

Chapter 3

The method of fundamental solutions for Helmholtz-type equations in composite materials

3.1 Introduction

The composite bi-material problems under consideration in this chapter are solved by using a domain decomposition MFS technique developed in Berger and Karageorghis (1999, 2001); Marin and Lesnic (2007); Karageorghis and Lesnic (2008). The bi-material is decomposed into two subdomains and the solution is approximated by an MFS-type expansion in each subdomain. At the interface, the continuity conditions for the solution and its normal derivative are imposed.

The outline of this chapter is as follows. In section 3.2 we introduce the mathematical formulation, whilst in section 3.3 we present the MFS for Helmholtz-type equations in composite bi-materials. In section 3.4 we present and discuss the numerically obtained results for each case considered. In section 3.5 we give some conclusions and possible future work.

3.2 Mathematical formulation

We consider a bi-material composed of two subdomains Ω_1 and Ω_2, with boundaries $\partial\Omega_1$ and $\partial\Omega_2$, respectively. Referring to the fields of heat conduction and acoustics, the two homogeneous materials in Ω_1 and Ω_2 are characterized by the constant heat transfer coefficients (wavenumbers) k_1 and k_2, respectively. The temperature (acous-

tic pressure) distribution in each subdomain satisfies the Helmholtz-type equations

$$\nabla^2 u_1 \pm k_1^2 u_1 = 0 \qquad \text{in} \quad \Omega_1, \tag{3.1}$$

$$\nabla^2 u_2 \pm k_2^2 u_2 = 0 \qquad \text{in} \quad \Omega_2. \tag{3.2}$$

(a) In the first case we consider the modified Helmholtz equation with a minus sign in (3.1) and (3.2) subject to the boundary conditions

$$u_1 = f_1 \qquad \text{on } \partial\Omega_1 \backslash \Gamma_{12}, \tag{3.3}$$

$$u_2 = f_2 \qquad \text{on } \partial\Omega_2 \backslash \Gamma_{12}, \tag{3.4}$$

and on the interface $\Gamma_{12} = \partial\Omega_1 \cap \partial\Omega_2$ we have the continuity of solution and its normal derivative, namely

$$u_1 = u_2, \qquad \text{on } \Gamma_{12}, \tag{3.5}$$

$$-\kappa \frac{\partial u_1}{\partial n_1} = \frac{\partial u_2}{\partial n_2} \qquad \text{on } \Gamma_{12}, \tag{3.6}$$

where $\underline{n}_1$ and $\underline{n}_2$ are the outward unit normal vectors to the domains Ω_1 and Ω_2, respectively, and κ represents the ratio between the thermal conductivities of the materials Ω_1 and Ω_2.

(b) In the second case we consider the direct scattering problem from a penetrable bounded obstacle Ω_1 with mixed transmission conditions. This is given by the Helmholtz equation with plus sign in (3.1) and (3.2) when Ω_1 is a bounded obstacle and $\Omega_2 = \mathbb{R}^n \backslash \Omega_1$, where $n = 2, 3$, is its exterior unbounded complement which is assumed connected. The mixed transmission conditions on the interface $\partial\Omega_1$ are given by

$$u_1 - (u_2 + u^{inc}) = 0 \qquad \text{on } \Gamma_1, \tag{3.7}$$

$$u_1 - (u_2 + u^{inc}) = \text{-i}\eta \frac{\partial (u_2 + u^{inc})}{\partial n_2} \qquad \text{on } \Gamma_2, \tag{3.8}$$

$$\kappa \frac{\partial u_1}{\partial n_1} + \frac{\partial (u_2 + u^{inc})}{\partial n_2} = 0 \qquad \text{on } \partial\Omega_1, \tag{3.9}$$

where κ represents the ratio between the electric permittivities of the materials Ω_1 and Ω_2, Γ_1 and Γ_2 are two disjoint portions of the boundary $\partial\Omega_1$ such that $\Gamma_1 \cap \Gamma_2 = \emptyset$ and $\Gamma_1 \cup \Gamma_2 = \partial\Omega_1$, η is the impedance coefficient allowing for non-perfect contact, and u^{inc} is the incident field given by a plane wave moving in the unit direction $\widehat{\underline{d}} \in S^{n-1} = \{\underline{d} \in \mathbb{R}^n : |\underline{d}| = 1\}$, namely $u^{inc}(\underline{X}) = e^{\text{i}k_2 \underline{X}.\widehat{\underline{d}}}$. The Sommerfeld infinity

condition is given by

$$\lim_{|\underline{X}|\to\infty}\sqrt{|\underline{X}|^{n-1}}\Big(\frac{\partial u_2}{\partial|\underline{X}|}(\underline{X})-\mathrm{i}k_2u_2(\underline{X})\Big)=0$$
$$\text{(uniformly with respect to } \widehat{\underline{X}}=\underline{X}/|\underline{X}|). \tag{3.10}$$

3.3 The Method of Fundamental Solutions (MFS)

3.3.1 The MFS for the modified Helmholtz equation

Example 1. Let us first consider the case when the governing equation is the modified Helmholtz equation, namely

$$\nabla^2u_1-k_1^2u_1=0 \qquad \text{in} \quad \Omega_1, \tag{3.11}$$
$$\nabla^2u_2-k_2^2u_2=0 \qquad \text{in} \quad \Omega_2, \tag{3.12}$$

where Ω_1 and Ω_2 occupy the rectangular regions, see Figure 3.1(a), $\Omega_1=(-1/2,1/2)\times(0,1/2)$ and $\Omega_2=(-1/2,1/2)\times(-1/2,0)$. Now, we treat the two subdomains separately: in $\overline{\Omega}_1$, the solution u_1 is approximated by

$$u_{1,N}(\underline{X}_1)=\sum_{j=1}^{N}a_jG_-(\underline{X}_1,\underline{\xi_1}^j;k_1), \qquad \underline{X}_1\in\overline{\Omega}_1, \tag{3.13}$$

and in $\overline{\Omega}_2$, the solution u_2 is approximated by

$$u_{2,N}(\underline{X}_2)=\sum_{j=1}^{N}b_jG_-(\underline{X}_2,\underline{\xi_2}^j;k_2), \qquad \underline{X}_2\in\overline{\Omega}_2, \tag{3.14}$$

where the $2N$ vectors $(\underline{\xi_1}^j)_{j=\overline{1,N}}$ and $(\underline{\xi_2}^j)_{j=\overline{1,N}}$ contain the sources which are located uniformly distributed outside $\overline{\Omega}_1$ and $\overline{\Omega}_2$, respectively, at a distance $\delta>0$ from them, see Figure 3.1(a). The fundamental solutions G_- of modified Helmholtz equations (3.11) and (3.12) are given by, see Balakrishnan and Ramachandran (2000),

$$G_-(\underline{X},\underline{Y};k_i)=\begin{cases}K_0(k_ir), & \text{in two-dimensions}\\ \frac{e^{-k_ir}}{r}, & \text{in three-dimensions}\end{cases} \tag{3.15}$$

where $r=\|\ \underline{X}-\underline{Y}\ \|, i=1,2$, and, for simplicity, the constants $\frac{1}{2\pi}$ in two-dimensions and $\frac{1}{4\pi}$ in three-dimensions have been embedded in the unknown coefficients $(a_j)_{j=\overline{1,N}}$ and $(b_j)_{j=\overline{1,N}}$ in (3.13) and (3.14), respectively. Imposing the boundary conditions (3.3) and (3.4), and the interface conditions (3.5) and (3.6),

yield

$$\begin{cases} \sum_{j=1}^{N} a_j G_-(\underline{X_1}(i), \underline{\xi_1}^j; k_1) = f_1(\underline{X_1}(i)), & i = \overline{1, 2M/3} \\ \sum_{j=1}^{N} a_j G_-(\underline{X_1}(i), \underline{\xi_1}^j; k_1) - \sum_{j=1}^{N} b_j G_-(\underline{X_2}(i), \underline{\xi_2}^j; k_2) = 0, & i = \overline{2M/3+1, M} \\ \sum_{j=1}^{N} b_j G_-(\underline{X_2}(i-M), \underline{\xi_2}^j; k_2) = f_2(\underline{X_2}(i-M)), & i = \overline{M+1, 5M/3} \\ -\kappa \sum_{j=1}^{N} a_j \frac{\partial G_-}{\partial y}(\underline{X_1}(i-M), \underline{\xi_1}^j; k_1) + \sum_{j=1}^{N} b_j \frac{\partial G_-}{\partial y}(\underline{X_2}(i-M), \underline{\xi_2}^j; k_2) = 0, & \\ \qquad\qquad i = \overline{5M/3+1, 2M} \end{cases} \tag{3.16}$$

where $(\underline{X_1}(i))_{i=\overline{1,M}}$ and $(\underline{X_2}(i))_{i=\overline{1,M}}$ are boundary collocation points uniformly distributed (as midpoints) on $\partial\Omega_1$ (starting from the point $(-\frac{1}{2}, 0)$ in a clockwise direction) and on $\partial\Omega_2$ (starting from the point $(-\frac{1}{2}, 0)$ in a counterclockwise direction), see Figure 3.1(a). We have chosen midpoints in order to avoid collocating at the corners of the rectangles where the normal derivative is undefined. In (3.16)

$$\frac{\partial G_-}{\partial y}(\underline{X_l}(i-M), \underline{\xi_l}^j; k_l) = -k_l \frac{(\underline{X_l}(i-M) - \underline{\xi_l}) \cdot (0,1)}{\parallel \underline{X_l}(i-M) - \underline{\xi_l}^j \parallel} K_1\Big(k_l \parallel \underline{X_l}(i-M) - \underline{\xi_l}^j \parallel\Big), \quad l = 1, 2, \tag{3.17}$$

Equations (3.16) form a system of $2M$ linear algebraic equations with $2N$ unknowns which generically can be written as

$$A\underline{c} = \underline{d}, \tag{3.18}$$

where $\underline{c} = \big(a_1, \cdots, a_N, b_1, \cdots, b_N\big)^{tr}$, $\underline{d} = \begin{pmatrix} f_1(\underline{X_1}(i))_{i=\overline{1,2M/3}} \\ (0)_{i=\overline{2M/3+1,M}} \\ f_2(\underline{X_2}(i-M))_{i=\overline{M+1,5M/3}} \\ (0)_{i=\overline{5M/3+1,2M}} \end{pmatrix}$, and

$$A_{ij}=\begin{cases} K_0(k_1 \parallel \underline{X_1}(i)-\underline{\xi_1}^j \parallel), & i=\overline{1,2M/3},\ j=\overline{1,N} \\ 0, & i=\overline{1,2M/3},\ j=\overline{N+1,2N} \\ K_0(k_1 \parallel \underline{X_1}(i)-\underline{\xi_1}^j \parallel), & i=\overline{2M/3+1,M},\ j=\overline{1,N} \\ -K_0(k_2 \parallel \underline{X_2}(i)-\underline{\xi_2}^j \parallel), & i=\overline{2M/3+1,M},\ j=\overline{N+1,2N} \\ 0, & i=\overline{M+1,5M/3},\ j=\overline{1,N} \\ K_0(k_2 \parallel \underline{X_2}(i-M)-\underline{\xi_2}^j \parallel), & i=\overline{M+1,5M/3}, j=\overline{N+1,2N} \\ \frac{\kappa k_1(\underline{X_1}(i-M)-\underline{\xi_1}^j)\cdot(0,1)}{\|\underline{X_1}(i-M)-\underline{\xi_1}^j\|}K_1\Big(k_1 \parallel \underline{X_1}(i-M)-\underline{\xi_1}^j \parallel\Big), & i=\overline{5M/3+1,2M},\ j=\overline{1,N} \\ \frac{-k_2(\underline{X_2}(i-M)-\underline{\xi_2}^j)\cdot(0,1)}{\|\underline{X_2}(i-M)-\underline{\xi_2}^j\|}K_1\Big(k_2 \parallel \underline{X_2}(i-M)-\underline{\xi_2}^j \parallel\Big), & i=\overline{5M/3+1,2M},\ j=\overline{N+1,2N} \end{cases} \tag{3.19}$$

Example 2. Secondly, we consider the case when the domain Ω_1 occupies the concentric annular region $\Omega_1=\{(x,y)\in\mathbb{R}^2|R_1^2<x^2+y^2<R_2^2\}$, and the domain Ω_2 occupies the circular region $\Omega_2=\{(x,y)\in\mathbb{R}^2|x^2+y^2<R_1^2\}$, see Figure 3.1(b). Using the MFS we treat the two subdomains separately: in $\overline{\Omega}_1$, the solution u_1 can be approximated by

$$u_{1,2N}(\underline{X})=\sum_{j=1}^{2N}a_jG_-(\underline{X},\underline{\xi}^j;k_1),\qquad \underline{X}\in\overline{\Omega}_1, \tag{3.20}$$

and in $\overline{\Omega}_2$, the solution u_2 can be approximated by

$$u_{2,N}(\underline{X})=\sum_{j=1}^{N}b_jG_-(\underline{X},\underline{\eta}^j;k_2),\qquad \underline{X}\in\overline{\Omega}_2, \tag{3.21}$$

where the $2N$ vectors $(\underline{\xi}^j)_{j=\overline{1,2N}}$ and the N vectors $(\underline{\eta}^j)_{j=\overline{1,N}}$ contain the sources which are located outside $\overline{\Omega}_1$ and $\overline{\Omega}_2$, respectively. In particular, $(\underline{\xi}^j)_{j=\overline{1,N}}$, $(\underline{\xi}^j)_{j=\overline{N+1,2N}}$ and $(\underline{\eta}^j)_{j=\overline{1,N}}$ are uniformly distributed on concentric circles of radii $R_3\in(0,R_1)$, $R_4\in(R_2,\infty)$ and $R_5\in(R_1,\infty)$, respectively, see Figure 3.1(b). Imposing the boundary condition (3.3) and the interface continuity conditions (3.5)

and (3.6), yield

$$\begin{cases} \sum_{j=1}^{2N} a_j G_-(\underline{X}(i),\underline{\xi}^j;k_1) = f_1(\underline{X}(i)), & i=\overline{1,M} \\ \sum_{j=1}^{2N} a_j G_-(\underline{X}(i),\underline{\xi}^j;k_1) - \sum_{j=1}^{N} b_j G_-(\underline{X}(i),\underline{\eta}^j;k_2) = 0, & i=\overline{M+1,2M} \\ -\kappa\sum_{j=1}^{2N} a_j \frac{\partial G_-}{\partial r}(\underline{X}(i-M),\underline{\xi}^j;k_1) + \sum_{j=1}^{N} b_j \frac{\partial G_-}{\partial r}(\underline{X}(i-M),\underline{\eta}^j;k_2) = 0, & \\ & i=\overline{2M+1,3M} \end{cases} \tag{3.22}$$

where $(\underline{X}(i))_{i=\overline{1,M}}$ and $(\underline{X}(i))_{i=\overline{M+1,2M}}$ are boundary collocation points uniformly distributed on the circles of radii R_2 and R_1, respectively, and

$$\begin{cases} \frac{\partial G_-}{\partial r}(\underline{X}(i-M),\underline{\xi}^j;k_1) = -k_1 \frac{(\underline{X}(i-M)-\underline{\xi}^j)\cdot\underline{X}(i-M)}{\|\underline{X}(i-M)-\underline{\xi}^j\|R_1} K_1\Big(k_1 \parallel \underline{X}(i-M)-\underline{\xi}^j \parallel\Big) \\ \\ \frac{\partial G_-}{\partial r}(\underline{X}(i-M),\underline{\eta}^j;k_2) = -k_2 \frac{(\underline{X}(i-M)-\underline{\eta}^j)\cdot\underline{X}(i-M)}{\|\underline{X}(i-M)-\underline{\eta}^j\|R_2} K_1\Big(k_2 \parallel \underline{X}(i-M)-\underline{\eta}^j \parallel\Big) \end{cases} \tag{3.23}$$

Equations (3.22) form a system of $3M$ linear algebraic equations with $3N$ unknowns which generically can be written as (3.18), where

$\underline{c} = \big(a_1,\cdots,a_{2N},b_1,\cdots,b_N\big)^{tr}$, $\underline{d} = \begin{pmatrix} f_1(\underline{X}(i))_{i=\overline{1,M}} \\ (0)_{i=\overline{M+1,2M}} \\ (0)_{i=\overline{2M+1,3M}} \end{pmatrix}$ and

$$A_{ij} = \begin{cases} K_0(k_1 \parallel \underline{X}(i)-\underline{\xi}^j \parallel), & i=\overline{1,M},\ j=\overline{1,2N} \\ 0, & i=\overline{1,M},\ j=\overline{2N+1,3N} \\ K_0(k_1 \parallel \underline{X}(i)-\underline{\xi}^j \parallel), & i=\overline{M+1,2M},\ j=\overline{1,2N} \\ -K_0(k_2 \parallel \underline{X}(i)-\underline{\eta}^j \parallel), & i=\overline{M+1,2M},\ j=\overline{2N+1,3N} \\ \frac{\kappa k_1(\underline{X}(i-M)-\underline{\xi}^j)\cdot\underline{X}(i-M)}{\|\underline{X}(i-M)-\underline{\xi}^j\|R_1} K_1\Big(k_1 \parallel \underline{X}(i-M)-\underline{\xi}^j \parallel\Big), & \\ & i=\overline{2M+1,3M},\ j=\overline{1,2N} \\ \frac{-k_2(\underline{X}(i-M)-\underline{\eta}^j)\cdot\underline{X}(i-M)}{\|\underline{X}(i-M)-\underline{\eta}^j\|R_2} K_1\Big(k_2 \parallel \underline{X}(i-M)-\underline{\eta}^j \parallel\Big), & \\ & i=\overline{2M+1,3M}, j=\overline{2N+1,3N} \end{cases} \tag{3.24}$$

Example 3. Finaly, we consider the case when the domains Ω_1 and Ω_2 are the three-dimensional cubes presented in Figure 3.1(c), where $\Omega_1 = (0,1)\times(0,1)\times(0,1)$ and $\Omega_2 = (0,1)\times(0,1)\times(-1,0)$. We treat the two subdomains separately: in $\overline{\Omega}_1$, the

solution u_1 is approximated by

$$u_{1,6N^2}(\underline{X_1}) = \sum_{j=1}^{6N^2} a_j G_-(\underline{X_1}, \underline{\xi_1}^j; k_1), \qquad \underline{X_1} \in \overline{\Omega}_1, \tag{3.25}$$

and in $\overline{\Omega}_2$, the solution u_2 is approximated by

$$u_{2,6N^2}(\underline{X_2}) = \sum_{j=1}^{6N^2} b_j G_-(\underline{X_2}, \underline{\xi_2}^j; k_2), \qquad \underline{X_2} \in \overline{\Omega}_2, \tag{3.26}$$

where the $12N^2$ vectors $(\underline{\xi_1}^j)_{j=\overline{1,6N^2}}$ and $(\underline{\xi_2}^j)_{j=\overline{1,6N^2}}$ contain the sources which are located outside $\overline{\Omega}_1$ and $\overline{\Omega}_2$, respectively, at a distance $\delta > 0$ from them. More precisely, we take

$$\xi_l^1 = \left(-\delta, -\delta + \frac{(1+2\delta)(i-1)}{M-1}, -\delta + \frac{(1+2\delta)(j-1)}{M-1} \right),$$

$$\xi_{N^2+l}^1 = \left(1+\delta, -\delta + \frac{(1+2\delta)(i-1)}{M-1}, -\delta + \frac{(1+2\delta)(j-1)}{M-1} \right),$$

$$\xi_{2N^2+l}^1 = \left(-\delta + \frac{(1+2\delta)i}{M+1}, -\delta, -\delta + \frac{(1+2\delta)(j-1)}{M-1} \right),$$

$$\xi_{3N^2+l}^1 = \left(-\delta + \frac{(1+2\delta)i}{M+1}, 1+\delta, -\delta + \frac{(1+2\delta)(j-1)}{M-1} \right),$$

$$\xi_{4N^2+l}^1 = \left(-\delta + \frac{(1+2\delta)i}{M+1}, -\delta + \frac{(1+2\delta)j}{M+1}, 1+\delta \right),$$

$$\xi_{5N^2+l}^1 = \left(-\delta + \frac{(1+2\delta)i}{M+1}, -\delta + \frac{(1+2\delta)j}{M+1}, -\delta \right),$$

and

$$\xi_l^2 = \left(-\delta, -\delta + \frac{(1+2\delta)(i-1)}{M-1}, -1-\delta + \frac{(1+2\delta)(j-1)}{M-1} \right),$$

$$\xi_{N^2+l}^2 = \left(1+\delta, -\delta + \frac{(1+2\delta)(i-1)}{M-1}, -1-\delta + \frac{(1+2\delta)(j-1)}{M-1} \right),$$

$$\xi_{2N^2+l}^2 = \left(-\delta + \frac{(1+2\delta)i}{M+1}, -\delta, -1-\delta + \frac{(1+2\delta)(j-1)}{M-1} \right),$$

$$\xi^2_{3N^2+l} = \left(-\delta + \frac{(1+2\delta)i}{M+1}, 1+\delta, -1-\delta + \frac{(1+2\delta)(j-1)}{M-1} \right),$$

$$\xi^2_{4N^2+l} = \left(-\delta + \frac{(1+2\delta)i}{M+1}, -\delta + \frac{(1+2\delta)j}{M+1}, -1-\delta \right),$$

$$\xi^2_{5N^2+l} = \left(-\delta + \frac{(1+2\delta)i}{M+1}, -\delta + \frac{(1+2\delta)j}{M+1}, \delta \right), \quad i,j = \overline{1,M},\ l = (i-1)M + j.$$

Imposing the boundary conditions (3.3) and (3.4), and the interface conditions (3.5) and (3.6), yield

$$\begin{cases} \displaystyle\sum_{j=1}^{6N^2} a_j G_-(\underline{X_1}(i), \underline{\xi_1}^j; k_1) = f_1(\underline{X_1}(i)), & i = \overline{1, 5M^2} \\ \displaystyle\sum_{j=1}^{6N^2} a_j G_-(\underline{X_1}(i), \underline{\xi_1}^j; k_1) - \sum_{j=1}^{6N^2} b_j G_-(\underline{X_2}(i), \underline{\xi_2}^j; k_2) = 0, & i = \overline{5M^2+1, 6M^2} \\ \displaystyle\sum_{j=1}^{6N^2} b_j G_-(\underline{X_2}(i-6M^2), \underline{\xi_2}^j; k_2) = f_2(\underline{X_2}(i-6M^2)), & i = \overline{6M^2+1, 11M^2} \\ \displaystyle\kappa \sum_{j=1}^{6N^2} a_j \frac{\partial G_-}{\partial z}(\underline{X_1}(i-6M^2), \underline{\xi_1}^j; k_1) - \sum_{j=1}^{6N^2} b_j \frac{\partial G_-}{\partial z}(\underline{X_2}(i-6M^2), \underline{\xi_2}^j; k_2) = 0, & \\ \qquad\qquad i = \overline{11M^2+1, 12M^2} \end{cases} \tag{3.27}$$

where $(\underline{X_1}(i))_{i=\overline{1,6M^2}}$ and $(\underline{X_2}(i))_{i=\overline{1,6M^2}}$ are boundary collocation points uniformly distributed on $\partial\Omega_1$ and $\partial\Omega_2$, see Figure 3.1(c). More precisely, we take

$$X^1_l = \left(0, \frac{(i-1)}{M-1}, \frac{(j-1)}{M-1}\right), \quad X^2_l = \left(0, \frac{(i-1)}{M-1}, -1 + \frac{(j-1)}{M-1}\right),$$

$$X^1_{M^2+l} = \left(1, \frac{(i-1)}{M-1}, \frac{(j-1)}{M-1}\right), \quad X^2_{M^2+l} = \left(1, \frac{(i-1)}{M-1}, -1 + \frac{(j-1)}{M-1}\right),$$

$$X^1_{2M^2+l} = \left(\frac{i}{M+1}, 0, \frac{(j-1)}{M-1}\right), \quad X^2_{2M^2+l} = \left(\frac{i}{M+1}, 0, -1 + \frac{(j-1)}{M-1}\right),$$

$$X^1_{3M^2+l} = \left(\frac{i}{M+1}, 1, \frac{(j-1)}{M-1}\right), \quad X^2_{3M^2+l} = \left(\frac{i}{M+1}, 1, -1 + \frac{(j-1)}{M-1}\right),$$

$$X^1_{4M^2+l} = \left(\frac{i}{M+1}, \frac{j}{M+1}, 1\right), \quad X^2_{4M^2+l} = \left(\frac{i}{M+1}, \frac{j}{M+1}, -1\right),$$

$$X^{1,2}_{5M^2+l} = \left(\frac{i}{M+1}, \frac{j}{M+1}, 0\right), \quad i,j = \overline{1,M},\ l = (i-1)M + j.$$

In (3.27)

$$\frac{\partial G_-}{\partial z}\Big(\underline{X_l}(i-6M^2),\underline{\xi_l}^j;k_l\Big)=\Big(k_l+\frac{1}{\|\underline{X_l}(i-6M^2)-\underline{\xi_l}^j\|}\Big)\\ \frac{(\zeta_l^j-z_l(i-6M^2))}{\|\underline{X_l}(i-6M^2)-\underline{\xi_l}^j\|^2}e^{-k_l\|\underline{X_l}(i-6M^2)-\underline{\xi_l}^j\|},\qquad l=1,2, \tag{3.28}$$

where z_l and ζ_l^j are the third component of $\underline{X_l}$ and $\underline{\xi_l}^j$, respectively. Equations (3.27) form a system of $12M^2$ linear algebraic equations with $12N^2$ unknowns which generically can be written in the form of system (3.18), where

$$\underline{c}=\big(a_1,\cdots,a_{6N^2},b_1,\cdots,b_{6N^2}\big)^{tr},\ \underline{d}=\begin{pmatrix} f_1(\underline{X_1}(i))_{i=\overline{1,5M^2}}\\ (0)_{i=\overline{5M^2+1,6M^2}}\\ f_2(\underline{X_2}(i-6M^2))_{i=\overline{6M^2+1,11M^2}}\\ (0)_{i=\overline{11M^2+1,12M^2}}\end{pmatrix},\text{ and}$$

$$A_{ij}=\begin{cases} \frac{e^{-k_1\|\underline{X_1}(i)-\underline{\xi_1}^j\|}}{\|\underline{X_1}(i)-\underline{\xi_1}^j\|}, & i=\overline{1,5M^2},\ j=\overline{1,6N^2}\\ 0, & i=\overline{1,5M^2},\ j=\overline{6N^2+1,12N^2}\\ \frac{e^{-k_1\|\underline{X_1}(i)-\underline{\xi_1}^j\|}}{\|\underline{X_1}(i)-\underline{\xi_1}^j\|}, & i=\overline{5M^2+1,6M^2},\ j=\overline{1,6N^2}\\ -\frac{e^{-k_2\|\underline{X_2}(i)-\underline{\xi_2}^j\|}}{\|\underline{X_2}(i)-\underline{\xi_2}^j\|}, & i=\overline{5M^2+1,6M^2},\ j=\overline{6N^2+1,12N^2}\\ 0, & i=\overline{6M^2+1,11M^2},\ j=\overline{1,6N^2}\\ \frac{e^{-k_2\|\underline{X_2}(i-6M^2)-\underline{\xi_2}^j\|}}{\|\underline{X_2}(i-6M^2)-\underline{\xi_2}^j\|}, & i=\overline{6M^2+1,11M^2},\ j=\overline{6N^2+1,12N^2}\\ \kappa\Big(k_1+\frac{1}{\|\underline{X_1}(i-6M^2)-\underline{\xi_1}^j\|}\Big)\frac{(\zeta_1^j-z_1(i-6M^2))}{\|\underline{X_1}(i-6M^2)-\underline{\xi_1}^j\|^2}e^{-k_1\|\underline{X_1}(i-6M^2)-\underline{\xi_1}^j\|}, & i=\overline{11M^2+1,12M^2},\ j=\overline{1,6N^2}\\ -\Big(k_2+\frac{1}{\|\underline{X_2}(i-6M^2)-\underline{\xi_2}^j\|}\Big)\frac{(\zeta_2^j-z_2(i-6M^2))}{\|\underline{X_2}(i-6M^2)-\underline{\xi_2}^j\|^2}e^{-k_2\|\underline{X_2}(i-6M^2)-\underline{\xi_2}^j\|}, & i=\overline{11M^2+1,12M^2},\ j=\overline{6N^2+1,12N^2}\end{cases} \tag{3.29}$$

In all situations, in order to obtain a unique solution for the system of equations (3.18) we require $M \geq N$. The underdetermined case $M < N$ with the MFS has been recently considered in Smyrlis and Karageorghis (2010), but it will not be investigated herein. If $M = N$ the system of linear equations (3.18) can be solved using the Gaussian elimination method, whilst if $M > N$ one can employ an ordinary linear least-squares method which replaces the rectangular over determined system of equations (3.18) with the square determined system

$$A^{tr}A\underline{c}=A^{tr}\underline{d}. \tag{3.30}$$

The MFS resulting matrix A is often ill-conditioned, see Chen et al. (2006), hence, if N is large, then the system of equations (3.30) needs to be regularized using, for

example, the Tikhonov regularization method which gives

$$(A^{tr}A + \lambda \mathbb{I})\underline{c} = A^{tr}\underline{d}, \tag{3.31}$$

where $\mathbb{I}$ is the identity matrix and $\lambda > 0$ is a regularization parameter to be prescribed according to some selection criterion such as the discrepancy principle, the L-curve, or the generalized cross validation.

3.3.2 The MFS for the Helmholtz equation

Example 4. Let us now consider the case when the governing equation is the Helmholtz equation, namely

$$\nabla^2 u_1 + k_1^2 u_1 = 0 \qquad \text{in} \quad \Omega_1, \tag{3.32}$$

$$\nabla^2 u_2 + k_2^2 u_2 = 0 \qquad \text{in} \quad \Omega_2, \tag{3.33}$$

where Ω_1 occupies the circular region $\Omega_1 = \{(x, y) \in \mathbb{R}^2 | x^2 + y^2 < R_1^2\}$, and Ω_2 occupies its complement, i.e. the unbounded exterior region of the circle, namely $\Omega_2 = \{(x, y) \in \mathbb{R}^2 | x^2 + y^2 > R_1^2\}$, see Figure 3.1(d). Using the MFS we treat the two subdomains separately: in $\overline{\Omega}_1$, the solution u_1 can be approximated by

$$u_{1,N}(\underline{X}) = \sum_{j=1}^{N} a_j G_+(\underline{X}, \underline{\xi_1}^j; k_1), \qquad \underline{X} \in \overline{\Omega}_1, \tag{3.34}$$

and in $\overline{\Omega}_2$, the solution u_2 can be approximated by

$$u_{2,N}(\underline{X}) = \sum_{j=1}^{N} b_j G_+(\underline{X}, \underline{\xi_2}^j; k_2), \qquad \underline{X} \in \overline{\Omega}_2, \tag{3.35}$$

where the $2N$ vectors $(\underline{\xi_1}^j)_{j=\overline{1,N}}$ and$(\underline{\xi_2}^j)_{j=\overline{1,N}}$ contain the sources which are located outside $\overline{\Omega}_1$ and $\overline{\Omega}_2$, respectively. In particular, $(\underline{\xi_1}^j)_{j=\overline{1,N}}$ and $(\underline{\xi_2}^j)_{j=\overline{1,N}}$ are uniformly distributed on concentric circles of radii $R_3 \in (0, R_1)$ and $R_2 \in (R_1, \infty)$, respectively, see Figure 3.1(d).

The fundamental solution G_+ of Helmholtz equations (3.32) and (3.33), in the two-dimensional case are given by, see Fairweather and Karageorghis (1998),

$$G_+(\underline{X}, \underline{Y}; k_l) = H_0^{(1)}(k_l r), \qquad l = 1, 2, \tag{3.36}$$

where for simplicity, the constant $\frac{\mathrm{i}}{4}$, which does not appear in (3.36), has been embedded in unknown complex coefficients $(a_j)_{j=\overline{1,N}}$ and $(b_j)_{j=\overline{1,N}}$ in (3.34) and

(3.35), respectively. The convergence, stability and error estimates of the MFS for the Helmholtz equation have been investigated in Barnett and Betcke (2008), and Ushijima and Chiba (2003). Equations (3.34) and (3.35) with $G_+(\underline{X},\underline{Y},k_l),\ l=1,2$, replaced by $H_0^{(1)}(k_l\|\underline{X}-\underline{\xi_l}^j\|)$ can be rewritten as

$$u_{1,N}(\underline{X})=\sum_{j=1}^{N}a_jH_0^{(1)}(k_1\|\underline{X}-\underline{\xi_1}^j\|),\qquad \underline{X}\in\overline{\Omega}_1, \tag{3.37a}$$

$$u_{2,N}(\underline{X})=\sum_{j=1}^{N}b_jH_0^{(1)}(k_2\|\underline{X}-\underline{\xi_2}^j\|),\qquad \underline{X}\in\overline{\Omega}_2. \tag{3.37b}$$

Collocating the mixed transmission conditions (3.7)-(3.9) at the points $\Big(\underline{X}(\ell)\Big)_{\ell=1,M}$ uniformly distributed (as midpoints) on the interface $\Gamma_{12}=\partial\Omega_1=\{(x,y)\in\mathbb{R}^2|\ x^2+y^2=R_1^2\}=\Gamma_1\cup\Gamma_2=\{(x,y)\in\Gamma_{12}|\ y\geq 0\}\cup\{(x,y)\in\Gamma_{12}|\ y<0\}$ yield

$$\sum_{j=1}^{N}\left[a_jH_0^{(1)}\Big(k_1\|\underline{X}(\ell)-\underline{\xi_1}^j\|\Big)-b_jH_0^{(1)}\Big(k_2\|\underline{X}(\ell)-\underline{\xi_2}^j\|\Big)\right]=e^{\mathrm{i}k_2\underline{X}(\ell)\cdot\widehat{\underline{d}}},$$
$$\ell=\overline{1,M/2}, \tag{3.38}$$

$$\begin{aligned}&\sum_{j=1}^{N}\left[a_jH_0^{(1)}\Big(k_1\|\underline{X}(\ell)-\underline{\xi_1}^j\|\Big)-b_jH_0^{(1)}\Big(k_2\|\underline{X}(\ell)-\underline{\xi_2}^j\|\Big)\right]\\ &+\frac{\mathrm{i}k_2\eta(\underline{X}(\ell))}{R_1}\sum_{j=1}^{N}\frac{(\underline{X}(\ell)-\underline{\xi_2}^j)\cdot\underline{X}(\ell)}{\|\underline{X}(\ell)-\underline{\xi_2}^j\|}b_jH_1^{(1)}\Big(k_2\|\underline{X}(\ell)-\underline{\xi_2}^j\|\Big)\\ &=e^{\mathrm{i}k_2\underline{X}(\ell)\cdot\widehat{\underline{d}}}\left(1-k_2\eta(\underline{X}(\ell))\frac{\Big(\underline{X}(\ell)\cdot\widehat{\underline{d}}\Big)}{R_1}\right),\quad \ell=\overline{M/2+1,M},\end{aligned} \tag{3.39}$$

$$\begin{aligned}&-k_1\kappa\sum_{j=1}^{N}a_jH_1^{(1)}\Big(k_1\|\underline{X}(\ell-M)-\underline{\xi_1}^j\|\Big)\frac{(\underline{X}(\ell-M)-\underline{\xi_1}^j)\cdot\underline{X}(\ell-M)}{\|\underline{X}(\ell-M)-\underline{\xi_1}^j\|}\\ &+k_2\sum_{j=1}^{N}b_jH_1^{(1)}\Big(k_2\|\underline{X}(\ell-M)-\underline{\xi_2}^j\|\Big)\frac{(\underline{X}(\ell-M)-\underline{\xi_2}^j)\cdot\underline{X}(\ell-M)}{\|\underline{X}(\ell-M)-\underline{\xi_2}^j\|}\\ &=-\mathrm{i}k_2e^{\mathrm{i}k_2\underline{X}(\ell-M)\cdot\widehat{\underline{d}}}\ \frac{\Big(\underline{X}(\ell-M)\cdot\widehat{\underline{d}}\Big)}{R_1},\quad \ell=\overline{M+1,2M}.\end{aligned} \tag{3.40}$$

Separating the real and imaginary parts, equations (3.38)-(3.40) form a system of $4M$ linear algebraic equations with $4N$ unknowns which generically can be written as (3.18) for the unknown coefficients

$\underline{c} = \big(Re(a_1), \cdots, Re(a_N), Im(a_1), \cdots, Im(a_N), Re(b_1), \cdots, Re(b_N), Im(b_1), \cdots, Im(b_N)\big)^{tr}$.

Calculation of the condition number of the matrix A reveals that this matrix is highly ill-conditioned. As such, the resulting MFS system cannot be solved by a direct method, such as the Gaussian elimination method which would produce a highly oscillatory and unstable numerical solution. Therefore, in order to deal with this instability issue we employ the Tikhonov regularization method (3.31).

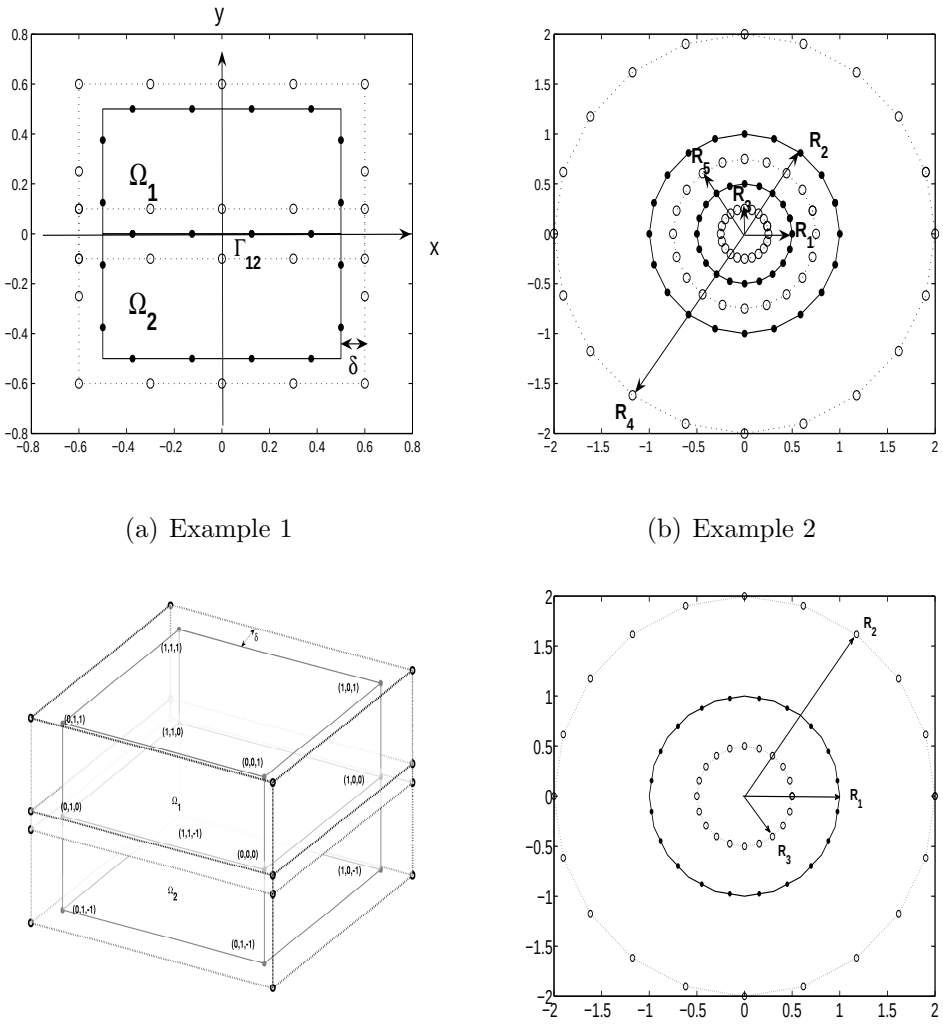

(a) Example 1

(b) Example 2

(c) Example 3

(d) Example 4

Figure 3.1: The distributions of source (∘) and boundary collocation (•) points.

3.4 Numerical results and discussion

In the Fortran computations we have used the NAG routines S18ACF, S18ADF, S17AEF, S17AFF, S17ACF and S17ADF for implementing the special functions

K_0, K_1, J_0, J_1, Y_0 and Y_1, respectively. For Examples 1-3 regularization was not needed and the linear least-squares method was employed for solving the system of equations (3.30). However, for Example 4 regularization, as given by expression (3.31), was found necessary in order to obtain a stable solution.

3.4.1 Modified Helmholtz equation

It is the purpose of this subsection to present and discuss numerical results obtained for the modified Helmholtz equations (3.11) and (3.12) in different composite geometries, see Figure 3.1.

$$\text{Example 1:} \begin{cases} \Omega_1 = (-1/2, 1/2) \times (0, 1/2), & \text{(rectangle)} \\ \Omega_2 = (-1/2, 1/2) \times (-1/2, 0), & \text{(rectangle)} \end{cases} \tag{3.41}$$

$$\text{Example 2:} \begin{cases} \Omega_1 = \{(x, y) \in \mathbb{R}^2 |\ 0.25 = R_1^2 < x^2 + y^2 < R_2^2 = 1\}, & \text{(annulus)} \\ \Omega_2 = \{(x, y) \in \mathbb{R}^2 |\ x^2 + y^2 < R_1^2 = 0.25\}, & \text{(circle)} \end{cases} \tag{3.42}$$

$$\text{Example 3:} \begin{cases} \Omega_1 = (0, 1) \times (0, 1) \times (0, 1), & \text{(cube)} \\ \Omega_2 = (0, 1) \times (0, 1) \times (-1, 0), & \text{(cube)} \end{cases} \tag{3.43}$$

We present results for $M = N$ uniformly distributed points and $\delta = 0.1$ for Example 1 and $\delta = 0.5$ for Example 3 which is three-dimensional. Other values of δ between $\mathbf{O}(10^{-1})$ and $\mathbf{O}(1)$ did not significantly affect the accuracy of the numerical results and practical experience indicates that δ should be chosen neither too small nor too large.

Example 1. We take the Dirichlet data (3.3) and (3.4) given by

$$u_1(x, y) = f_1(x, y) = e^{x+y}, \qquad (x, y) \in \partial\Omega_1 \backslash \Gamma_{12} \tag{3.44}$$

$$u_2(x, y) = f_2(x, y) = e^x(1 + y), \qquad (x, y) \in \partial\Omega_2 \backslash \Gamma_{12} \tag{3.45}$$

We also take $k_1 = \sqrt{2}$, $k_2 = 1$ and $\kappa = 1$. We can realize $\kappa = 1$ and still have composite different heat conductors by taking two materials with the same thermal conductivity, but with different heat capacities. For example, the thermal property measurements performed by the company *Hukse flux Thermal Sensors* indicate that, at 20° Celsius, quartz and marble have both the same thermal conductivity $3W/(m \cdot K)$, but their volumetric heat capacities are different, namely, 2.130 $J/(cm^3 \cdot K)$ and 2.376 $J/(cm^3 \cdot K)$, respectively. This implies that their thermal diffusivities are also different and equal to 0.0141 cm^2/s for quartz and 0.0126 cm^2/s for marble. The bi-material (3.41) is considered in order to show the applicability of the MFS to deal

with non-smooth composite domains, see Figure 3.1(a). This example possesses an analytical solution which is given by

$$u_1(x,y) = e^{x+y}, \qquad (x,y) \in \overline{\Omega}_1 \tag{3.46}$$

$$u_2(x,y) = e^{x}(1+y), \qquad (x,y) \in \overline{\Omega}_2 \tag{3.47}$$

Corresponding to (3.46) and (3.47), the normal derivatives at the interface $\Gamma_{12} = (-1/2, 1/2) \times \{0\}$ are given by

$$-\frac{\partial u_1}{\partial y}(x,0) = -e^x, \quad \frac{\partial u_2}{\partial y}(x,0) = e^x, \qquad (x,y) \in \Gamma_{12}. \tag{3.48}$$

Figures 3.2(a) and 3.2(b) show the logarithm of the L^2-errors for the solution u_1 and its normal derivative $\partial u_1/\partial y$ along the interface Γ_{12} given by

$$\|u_1 - u_{1,N}\|_{L^2(\Gamma_{12})} \approx \sqrt{\frac{1}{M_1}\sum_{i=1}^{M_1}\Big|u_1(x_1(i),0) - u_{1,N}(x_1(i),0)\Big|^2}, \tag{3.49}$$

$$\Big\|\frac{\partial u_1}{\partial y} - \frac{\partial u_{1,N}}{\partial y}\Big\|_{L^2(\Gamma_{12})} \approx \sqrt{\frac{1}{M_1}\sum_{i=1}^{M_1}\Big|\frac{\partial u_1}{\partial y}(x_1(i),0) - \frac{\partial u_{1,N}}{\partial y}(x_1(i),0)\Big|^2}, \tag{3.50}$$

where $x_1(i) = (2i-1)/(2M_1)$ for $i = \overline{1, M_1}$, and $M_1 = 99$. The value of M_1 is irrelevant as we only wish to calculate the solution at points on the boundary different from the boundary collocation points.

Although not illustrated, we report that for $M = 30$ to 60 the errors are large because there are not enough points to approximate a complicated geometry. From Figures 3.2(a) and 3.2(b) it can be seen that the errors (3.49) and (3.50) decrease exponentially as the number M of source/collocation points increases to 90, 120, and 150. The numerical and analytical interior solutions for u_1 and u_2 obtained with $M = 90$ are shown in Figures 3.3(a) and 3.3(b), respectively. From these figures it can be seen that the agreement between the MFS numerical solution and the analytical solution is excellent.

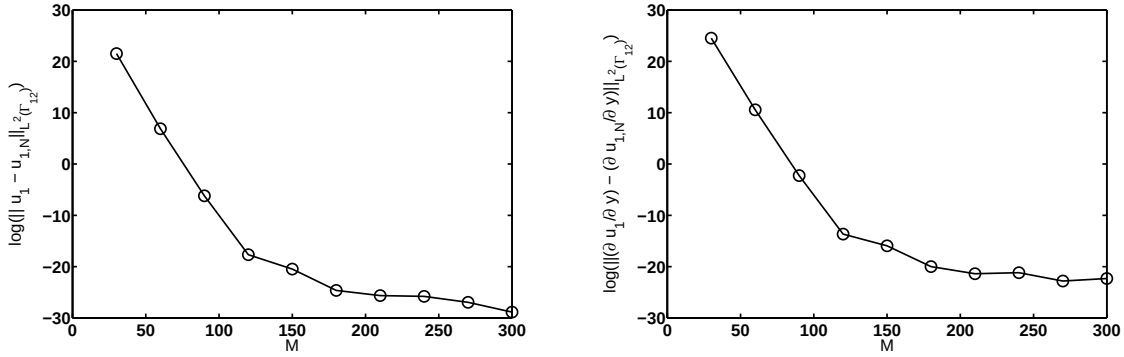

(a) (b)

Figure 3.2: Logarithm of the errors (3.49) and (3.50).

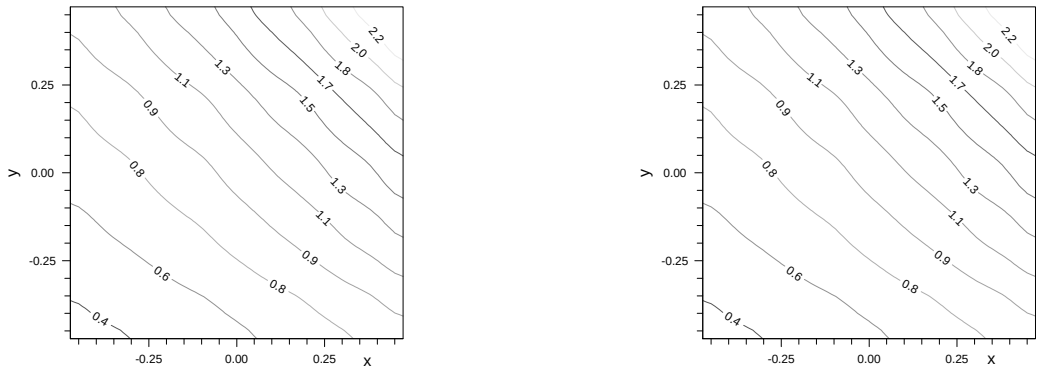

(a) (b)

Figure 3.3: (a) The MFS solution for $u_1,\ u_2$ and (b) the analytical solutions (3.46) and (3.47) with $M = 90$.

Example 2. We take $k_1 = \sqrt{2}$, $k_2 = \sqrt{5}$, a high contrast bi-material with $\kappa = 5$, and the Dirichlet data (3.3) given by

$$u_1(x, y) = f_1(x, y) = e^{x-y}, \qquad (x, y) \in \partial\Omega_1 \backslash \Gamma_{12}. \tag{3.51}$$

Note that this example does not possess an explicit analytical solution to compare with the numerical results. Further, the bi-material (3.42) is considered in order to show the applicability of the MFS to deal with smooth composite domains which may not be simply connected, see Figure 3.1(b).

Figure 3.4 shows the logarithm of the error for the numerical solution u_1 on the

boundary $\partial\Omega_1$ given by

$$\|u_{1,2N} - f_1\|_{L^2(\partial\Omega_1)} \approx \sqrt{\frac{2\pi}{M_1}\sum_{i=1}^{M_1}\left|u_{1,2N}(1,\theta_i) - f_1(1,\theta_i)\right|^2}, \tag{3.52}$$

where $\theta_i = \frac{2\pi i}{M_1}$ for $i = \overline{1, M_1}$, and $M_1 = 99$. From this figure it can be seen that the error (3.52) decreases exponentially as the number M of source/collocation points increases to 40, 60, and 80. However, this error increases slightly for $M > 160$. As in the previous example, the reason for this increase in the error is that the system of linear equations (3.18) becomes ill-conditioned.

The numerical solutions for the normal derivatives $\partial u_1/\partial n(1,\theta)$ and $\partial u_1/\partial n(0.5,\theta)$ for $M = 40$ are shown in Figures 3.5(a) and 3.5(b), respectively. The numerical interior solutions for $u_1(0.75,\theta)$ and $u_2(0.25,\theta)$ obtained with $M = N \in \{20, 40, 80\}$ are shown in Figures 3.5(d) and 3.5(c), respectively. Although Example 2 does not possesses an analytical solution available explicitly, the convergence illustrated, as M increases, in Figures 3.5(d) and 3.5(c) shows that an accurate numerical MFS solution has been obtained.

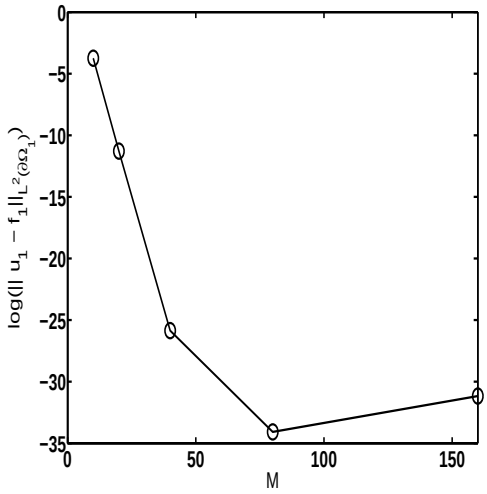

Figure 3.4: Logarithm of the error (3.52).

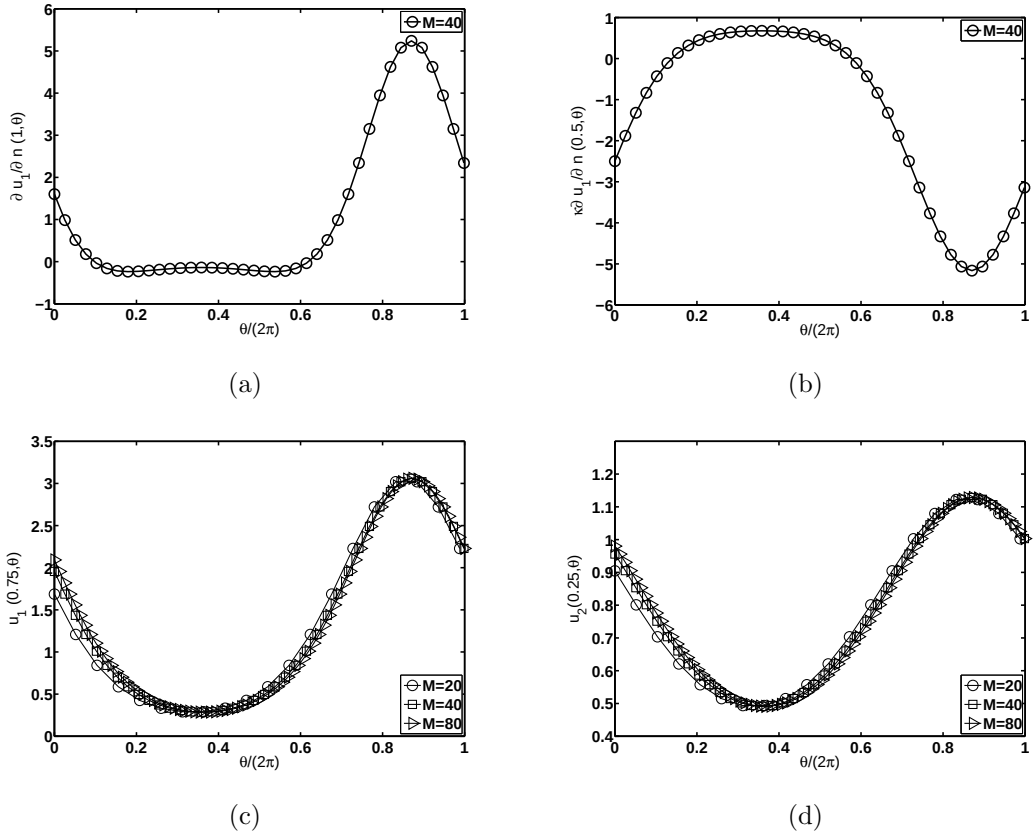

Figure 3.5: The MFS solutions for: (a) $\partial u_1/\partial n(1,\theta)$, (b) $\partial u_1/\partial n(0.5,\theta)$, (c) $u_1(0.75,\theta)$, and (d) $u_2(0.25,\theta)$.

Example 3. We take the Dirichlet data (3.3) and (3.4) given by

$$u_1(x,y,z) = f_1(x,y,z) = e^{x+y+z}, \qquad (x,y,z) \in \partial\Omega_1 \backslash \Gamma_{12} \tag{3.53}$$

$$u_2(x,y,z) = f_2(x,y,z) = e^{x+y}(1+z), \qquad (x,y,z) \in \partial\Omega_2 \backslash \Gamma_{12} \tag{3.54}$$

We also take $k_1 = \sqrt{3}$, $k_2 = \sqrt{2}$ and $\kappa = 1$. The bi-material (3.43) is considered in order to show the applicability of the MFS to three-dimensional non-smooth composite domains, see Figure 3.1(c). This example possesses an analytical solution given by

$$u_1(x,y,z) = e^{x+y+z}, \qquad (x,y,z) \in \overline{\Omega}_1 \tag{3.55}$$

$$u_2(x,y,z) = e^{x+y}(1+z), \qquad (x,y,z) \in \overline{\Omega}_2 \tag{3.56}$$

Corresponding to (3.55) and (3.56), the normal derivatives at the planar interface

$\Gamma_{12} = (0,1) \times (0,1) \times \{0\}$ are given by

$$-\frac{\partial u_1}{\partial z}(x,y,0) = -e^{x+y}, \qquad \frac{\partial u_2}{\partial z}(x,y,0) = e^{x+y}, \qquad (x,y,z) \in \Gamma_{12}. \tag{3.57}$$

Figures 3.6(a) and 3.6(b) show the logarithm of the L^2-errors for the solution u_k and its normal derivative $\partial u_k/\partial z$ along the interface Γ_{12} given by

$$\|u_k - u_{k,6N^2}\|_{L^2(\Gamma_{12})} \approx \sqrt{\frac{1}{M_1^2}\sum_{i,j=1}^{M_1}\left|u_k(x_k(i),y_k(j),0) - u_{k,6N^2}(x_k(i),y_k(j),0)\right|^2}, \tag{3.58}$$

$$\left\|\frac{\partial u_k}{\partial z} - \frac{\partial u_{k,6N^2}}{\partial z}\right\|_{L^2(\Gamma_{12})} \approx \sqrt{\frac{1}{M_1^2}\sum_{i,j=1}^{M_1}\left|\frac{\partial u_k}{\partial z}(x_k(i),y_k(j),0) - \frac{\partial u_{k,6N^2}}{\partial z}(x_k(i),y_k(j),0)\right|^2}, \tag{3.59}$$

for $k = 1, 2$, where $x_k(i) = i/(M_1+1)$ for $i = \overline{1, M_1}$, $y_k(j) = j/(M_1+1)$ for $j = \overline{1, M_1}$, and $M_1 = 99$. From Figures 3.6(a) and 3.6(b) it can be seen that the errors (3.58) and (3.59) decrease exponentially as the number M of source/collocation points increases.

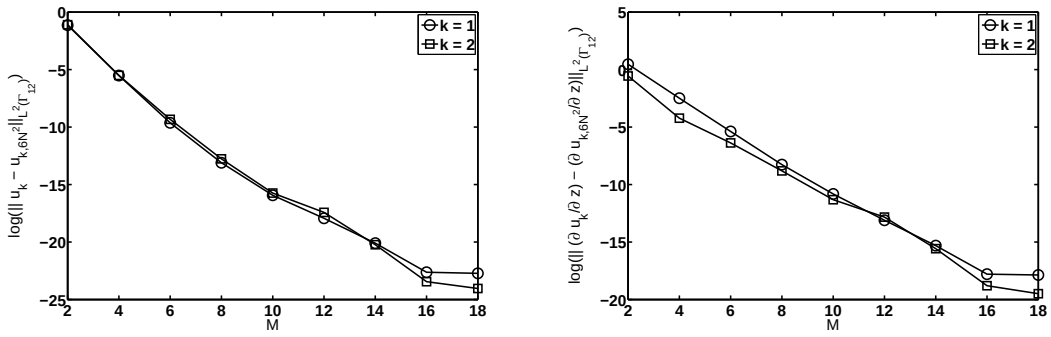

(a) (b)

Figure 3.6: Logarithm of the errors (3.58) and (3.59).

3.4.2 Helmholtz equation

It is the purpose of this subsection to present and discuss numerical results obtained for the Helmholtz equations (3.32) and (3.33) in the composite geometry

$$\begin{cases} \Omega_1 = \{(x,y) \in \mathbb{R}^2 |\ x^2 + y^2 < R_1^2 = 1\}, & \text{(circle)} \\ \Omega_2 = \{(x,y) \in \mathbb{R}^2 |\ 1 = R_1^2 < x^2 + y^2\}, & \text{(unbounded exterior circle)} \end{cases} \tag{3.60}$$

This can be viewed as a bi-material composed of a bounded domain material Ω_1 and its unbounded complement domain material $\Omega_2 = \mathbb{R}^2 \backslash \overline{\Omega}_1$.

Example 4. In this example we take $k_1 = 1/2$, $k_2 = 1$, $\kappa = 2$ and the positive impedance function $\eta(\underline{X}) = 1$. The bi-material (3.60) is considered in order to show the applicability of the MFS to deal with unbounded domains, see Figure 3.1(d). Taking the direction of scattering $\widehat{\underline{d}} = (1,0)$ along the x-axis, the incident field is given by

$$u^{inc}(\underline{X}) = \cos(k_2 x) + \mathrm{i}\sin(k_2 x), \qquad \underline{X} = (x,y) \in \mathbb{R}^2. \tag{3.61}$$

Corresponding to (3.61), the normal derivative of the incident field along the interface $\Gamma_{12} = \partial\Omega_1$ is given by

$$\frac{\partial u^{inc}}{\partial r}(\underline{X}) = \frac{k_2 x}{R_1}\Big(-\sin(k_2 x) + \mathrm{i}\cos(k_2 x)\Big), \qquad \underline{X} = (x,y) \in \Gamma_{12}. \tag{3.62}$$

The numerical solutions for the real and imaginary parts of the difference $u_1(1,\theta) - u_2(1,\theta)$ on the portion $\Gamma_1 = \{(x,y) \in \mathbb{R}^2 |\ x^2 + y^2 = R_1^2 = 1, y \geq 0\}$ of the interface $\Gamma_{12} = \partial\Omega_1$ obtained with various values of $M = N \in \{20, 40, 80\}$ and $\lambda = 0$, and with various values of the regularization parameter $\lambda \in \{0, 10^{-6}, 10^{-3}\}$ and $M = N = 80$ are shown in Figures 3.7 and 3.8, respectively, in comparison with the exact incident field

$$u^{inc}(1,\theta) = e^{\mathrm{i}k_2\cos(\theta)}, \qquad \theta \in [0,\pi]. \tag{3.63}$$

These were calculated at $M_1 = 19$ uniformly distributed points on Γ_1 different from the boundary collocation points. From Figure 3.7 it can be seen for relatively low values of $M = N \in \{20, 40\}$ the numerical MFS solution obtained with no regularization is in good agreement with the exact incident field (3.63), but as $M = N$ increases to 80 the numerical solution without regularization starts to manifest instabilities, see Figure 3.7(a). This is consistent with the findings of Ramachandran (2002) who suggested the use of regularization in order to obtain a stable MFS

solution. Therefore, in Figure 3.8 we present the results obtained with regularization included in (3.31) and it can be seen that smoother and more stable numerical results are obtained.

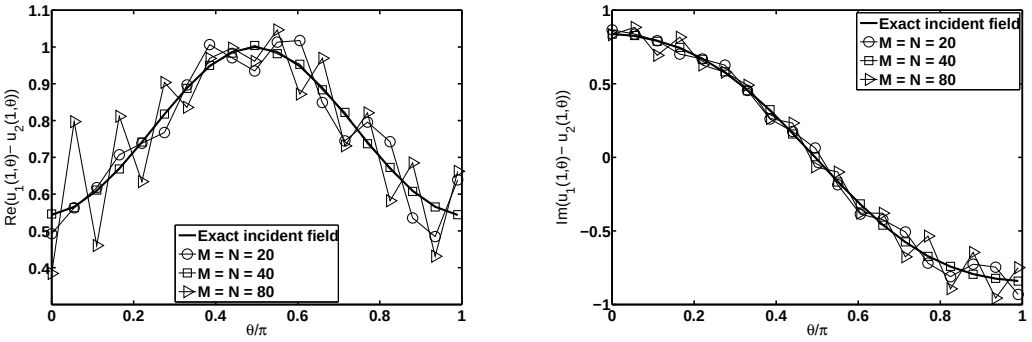

(a) (b)

Figure 3.7: (a) Real and (b) imaginary parts of $u_1(1,\theta) - u_2(1,\theta)$ for $\lambda = 0$ and various values of $M = N \in \{20, 40, 80\}$ in comparison with the exact incident field (3.63).

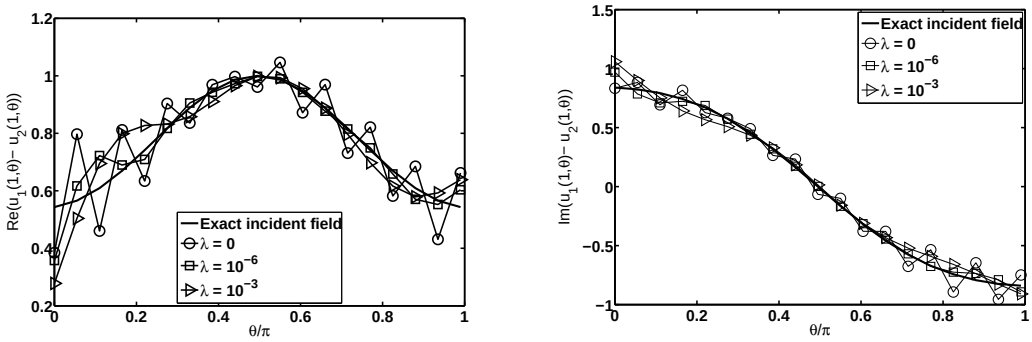

(a) (b)

Figure 3.8: (a) Real and (b) imaginary parts of $u_1(1,\theta) - u_2(1,\theta)$ for $M = N = 80$ and various values of $\lambda \in \{0, 10^{-6}, 10^{-3}\}$ in comparison with the exact incident field (3.63).

3.5 Conclusions

In this chapter, Helmholtz-type equations in both two- and three-dimensional composite materials subject to boundary conditions and interface continuity conditions have been investigated by the MFS. Four examples involving the Helmholtz-type equations in composite materials have been analysed. The numerical results obtained by the MFS are accurate and in good agreement with the exact solution, where available (Examples 1 and 3). Future work will concern developing the MFS for inverse geometric problems associated to Helmholtz-type equations in which the interfaces between the composite materials are considered unknown, see Cakoni et al. (2010b), Carpio and Rapun (2010), and the next chapter.

Chapter 4

Determination of inner boundaries in modified Helmholtz inverse geometric problems

4.1 Introduction

In this chapter, we consider the application of the MFS for solving the inverse problem which consists of determining an unknown defect D compactly contained in a simply-connected bounded domain Ω assuming that the temperature u satisfies the modified Helmholtz equation governing the heat conduction in a fin, see e.g. Marin et al. (2004),

$$\nabla^2 u - k^2 u = 0 \qquad \text{in } \Omega \setminus \overline{D}, \tag{4.1}$$

where $k^2 = 2h/(\lambda\delta)$, h is the convective heat transfer coefficient, λ and δ are the thermal conductivity and fin thickness, respectively, from the knowledge of the Dirichlet temperature data u and the Neumann heat flux data $\partial u/\partial n$ on the boundary $\partial\Omega$ of Ω, where $\underline{n}$ is the outward unit normal at $\partial\Omega$, and a boundary condition (Dirichlet, Neumann or Robin) on the boundary ∂D of D.

In earlier chapters we have found that the MFS produces an accurate approximation to the solution of the direct problem in both two- and three-dimensions, and in this chapter we extend it to solve numerically the inverse problem of identifying the unknown inner boundary ∂D of a defect D compactly contained in Ω. More concretely, the inverse nonlinear ill-posed problem of determining the inner boundary is approached based on a regularized optimization procedure which uses the MFS solver at each iteration. This chapter, which is a variant of the Kirsch-Kress idea for inverse scattering, see Kirsch and Kress (1987), builds upon the previous recent applications of the MFS for solving inverse geometric problems governed by

the Laplace equation, see Borman et al. (2009) and Karageorghis and Lesnic (2009), the Helmholtz equation, see Karageorghis and Lesnic (2011), the biharmonic equation, see Karageorghis and Lesnic (2010b), the Lamé system in elasticity, see Alves and Martins (2009), and the Stokes system in slow viscous flow, see Martins and Silvestre (2008). A related inverse geometric problem when the unknown defect, e.g. a crack, is at the boundary of $\partial\Omega$, known as the inverse boundary determination has been investigated using the MFS in Mera and Lesnic (2005), Marin et al. (2011), Marin (2009), Marin and Munteanu (2010) for the isotropic, anisotropic and functionally graded Laplace equation, in Marin and Karageorghis (2009) for Helmholtz-type equations, in Zeb et al. (2008) for the biharmonic equation, and in Marin (2010a) for the Lamé system in elasticity.

The outline of this chapter is as follows. In section 4.2 we introduce the mathematical formulation, whilst in section 4.3 we present the MFS for the inverse geometric problem. In section 4.4 we present and discuss the numerically obtained results. In section 4.5 we give some conclusions and possible future work.

4.2 Mathematical formulation

We consider a bounded simply-connected domain Ω with smooth boundary and a smooth subdomain D of Ω such that $\overline{D} \subset \Omega$, and $\Omega \setminus D$ is connected. The steady-state temperature u in a fin satisfies the modified Helmholtz equation (4.1) subject to the boundary conditions

$$u = f \qquad \text{on} \quad \partial\Omega, \tag{4.2}$$

and

$$u = h \qquad \text{on} \quad \partial D, \tag{4.3}$$

or

$$\frac{\partial u}{\partial n} = h \qquad \text{on} \quad \partial D, \tag{4.4}$$

where $f \in H^{1/2}(\partial\Omega)$ non-constant, and h are given functions. It is well-known that the direct Dirichlet problem given by equations (4.1)-(4.3) has a unique solution $u \in H^1(\Omega \setminus D)$, when D is known and $h \in H^{1/2}(\partial D)$. Also the direct mixed problem given by equations (4.1), (4.2) and (4.4) has a unique solution $u \in H^1(\Omega \setminus D)$ when D is known and $h \in H^{-1/2}(\partial D)$. Here $H^{1/2}(\partial\Omega)$ denotes the space of traces of functions $u \in H^1(\Omega)$ restricted to the boundary $\partial\Omega$, and $H^{-1/2}(\partial\Omega)$ denotes the dual space of $H^{1/2}(\partial\Omega)$. We can then define a nonlinear operator $F_f(\partial D)$, which maps from the set of admissible Lipschitz boundaries ∂D to the data space of Neumann heat flux

(measured) data in $H^{-1/2}(\partial\Omega)$, as follows:

$$F_f(\partial D) := \frac{\partial u}{\partial n}\Big|_{\partial\Omega} = g \in H^{-1/2}(\partial\Omega). \tag{4.5}$$

Then the inverse problem under consideration consists of extracting some information about the boundary ∂D from the data $g = F_f(\partial D)$. The data (4.5) may also be only partial, i.e. the flux being measured on a non-zero measure portion $\Gamma \subset \partial\Omega$, instead on the whole boundary $\partial\Omega$. It is well-known that the inverse problem is nonlinear and ill-posed as opposed to the direct problem which is linear and well-posed. Although one can show, see Isakov (2009), that the solution of the inverse problem given by equations (4.1)-(4.3) and (4.5), or (4.1), (4.2), (4.4) and (4.5), is unique, this solution does not depend continuously upon errors in the input Cauchy data (4.2) and (4.5). Usually, one has $h = 0$ in (4.3), i.e. D is a rigid inclusion (impenetrable soft obstacle), or in (4.4), i.e. D is a cavity (impenetrable hard obstacle). The general composite case in which in D we have another material with different heat transfer coefficient $k'^2 \neq k^2$ and the unknown interface ∂D is to be identified, i.e. D is a penetrable, or transparent obstacle, is deferred to a future work, see Karageorghis and Lesnic (2010a) for the corresponding inverse transmission problem for the Laplace equation arising in electrical impedance tomography (EIT) in electrostatics.

We finally note that the uniqueness of solution of the inverse problem is not guaranteed if the Dirichlet or Neumann boundary condition (4.3) or (4.4) is replaced by a Robin boundary condition of the form

$$\frac{\partial u}{\partial n} + \alpha u = h \qquad \text{on} \quad \partial D, \tag{4.6}$$

with $\alpha > 0$ the surface heat transfer coefficient. In such a situation, in fact, one can determine both D and α, but from two, instead of one, linearly independent pairs of Cauchy data (4.2) and (4.5), see Isakov (2009), and Chapters 5 and 6.

4.3 The Method of Fundamental Solutions (MFS)

Based on the density results of Bogomolny (1985) and Smyrlis (2009) for the MFS for the modified Helmholtz equation, we approximate the solution of equation (4.1) by a linear combination of fundamental solutions with respect to source points which are placed outside the solution domain, namely

$$u(\underline{X}) = \sum_{j=1}^{M+N} a_j G_-(\underline{X}, \underline{\xi}^j), \qquad \underline{X} \in \overline{\Omega} \setminus D, \tag{4.7}$$

where the $M+N$ vectors $(\underline{\xi}^j)_{j=\overline{1,M+N}}$ are distinct source points ('singularities') located outside domain $\overline{\Omega}$ and inside domain D, and G_- is the fundamental solution of the modified Helmholtz equation (4.2). In two-dimensions it is given by, see equation (2.4),

$$G_-(\underline{X},\underline{Y}) = K_0(kr), \tag{4.8}$$

where for simplicity, the constant $\frac{1}{2\pi}$, which does not appear in (4.8), has been embedded in the unknown coefficients $(a_j)_{j=\overline{1,M+N}}$ in (4.8).

For simplicity, we assume that Ω is the unit disk $B(\mathbf{0};1)$; otherwise, we first conformally map the simply-connected domain Ω onto the unit disk. We also assume that the unknown domain D is star-shaped with respect to origin, i.e. $\partial D = \{(r(\theta)\cos(\theta), r(\theta)\sin(\theta))|\ \theta \in [0,2\pi)\}$, where $r(\theta)$ is a 2π-periodic smooth function with values in the interval (0,1). We take

$$\underline{X}_i = (\cos(\tilde{\theta}_i), \sin(\tilde{\theta}_i)), \qquad i = \overline{1,M} \tag{4.9}$$

boundary collocation points uniformly distributed on $\partial\Omega = \partial B(\mathbf{0};1)$, where $\tilde{\theta}_i = 2\pi i/M$ for $i = \overline{1,M}$, and

$$\underline{X}_{i+M} = (r_i\cos(\theta_i), r_i\sin(\theta_i)), \qquad i = \overline{1,N} \tag{4.10}$$

boundary collocation points on ∂D where $\theta_i = 2\pi i/N$, $r_i := r(\theta_i)$ for $i = \overline{1,N}$. The $(M+N)$ source points $(\underline{\xi}^j)_{j=\overline{1,M+N}}$ in $(\mathbb{R}^2 \setminus \overline{\Omega}) \cup D$ are taken as

$$\underline{\xi}^j = (R\cos(\tilde{\theta}_j), R\sin(\tilde{\theta}_j)), \qquad j = \overline{1,M}, \tag{4.11}$$

$$\underline{\xi}^{j+M} = (\frac{r_j}{s}\cos(\theta_j), \frac{r_j}{s}\sin(\theta_j)), \qquad j = \overline{1,N}, \tag{4.12}$$

where $s > 1$ and $R > 1$. Note that taking only the source points (4.11) outside $\overline{\Omega}$ is not enough because the solution domain is $\overline{\Omega} \setminus D$ which is doubly-connected. Hence, we also need the source points (4.12) located inside D. The distributions of the boundary collocation points (4.9) and (4.10), and of the source points (4.11) and (4.12) are schematically shown in Figure 4.1. Then the coefficients $(a_j)_{j=\overline{1,M+N}}$ and the radii $(r_i)_{i=\overline{1,N}}$ can be determined by imposing the boundary conditions (4.2), (4.3) and (4.5) in a least-squares sense which recasts into minimising the objective function

$$T(\underline{a},\underline{r}) := \|u-f\|^2_{L^2(\partial\Omega)} + \left\|\frac{\partial u}{\partial n} - g\right\|^2_{L^2(\partial\Omega)} + \|u-h\|^2_{L^2(\partial D)}. \tag{4.13}$$

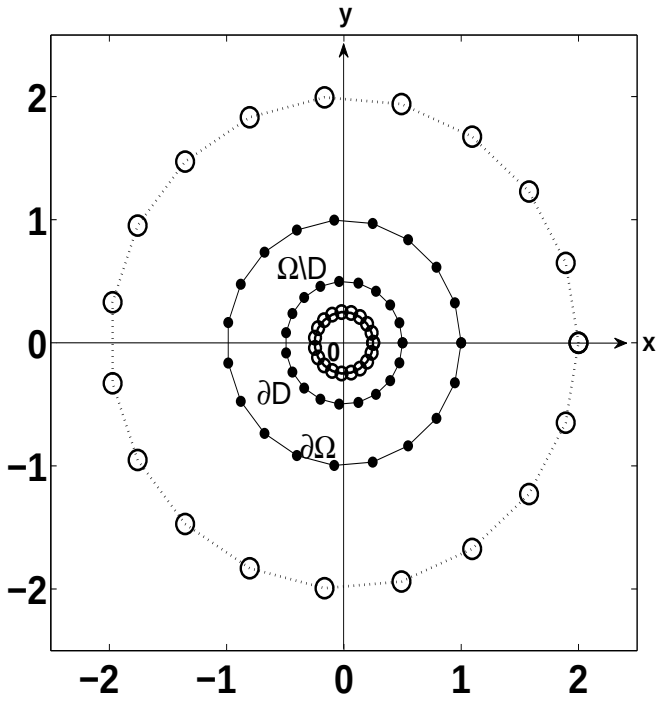

Figure 4.1: Schematic distribution of source (∘) and boundary collocation (•) points.

In the case when the Neumann condition (4.4) applies instead of the Dirichlet condition (4.3) on ∂D, the last term in (4.13) is replaced by $\left\| \frac{\partial u}{\partial n} - h \right\|^2_{L^2(\partial D)}$. Upon discretization, equation (4.13) yields

$$T(\underline{a},\underline{r}) = \sum_{i=1}^{M} \Big[\sum_{j=1}^{M+N} a_j G_-(\underline{X}_i, \underline{\xi}^j) - f(X_i) \Big]^2 + \sum_{i=M+1}^{2M} \Big[\sum_{j=1}^{M+N} a_j \frac{\partial G_-}{\partial n}(\underline{X}_{i-M}, \underline{\xi}^j) - g(\underline{X}_{i-M}) \Big]^2 + \sum_{i=2M+1}^{2M+N} \Big[\sum_{j=1}^{M+N} a_j G_-(\underline{X}_{i-M}, \underline{\xi}^j) - h(\underline{X}_{i-M}) \Big]^2 \quad (4.14)$$

The minimisation of (4.14) imposes $2M + N$ nonlinear equations in the $2N + M$ unknowns $(\underline{a}, \underline{r})$, and for a unique solution it is necessary that $M \geq N$. If there is noise in the measured data (4.5), we replace g in (4.14) by g^ε, namely,

$$g^\epsilon(\underline{X}_i) = g(\underline{X}_i) + \epsilon_i, \qquad i = \overline{1, M}, \quad (4.15)$$

where ϵ_i are random variables generated using the NAG routine D05DDF from a Gaussian normal distribution with mean zero and standard deviation

$$\sigma = p \times \max_{\partial\Omega} |g|, \quad (4.16)$$

where p represents the percentage of noise. In equation (4.14), the normal derivative of G_- is given by

$$\frac{\partial G_-}{\partial n}(\underline{X},\underline{\xi}) = -k\frac{(\underline{X}-\underline{\xi})\cdot\underline{n}}{\|\underline{X}-\underline{\xi}\|}K_1\Big(k\|\underline{X}-\underline{\xi}\|\Big), \tag{4.17}$$

The minimisation of the objective function (4.14) is accomplished computationally using the NAG routine E04FCF, which is a comprehensive algorithm for minimising an unconstrained sum of squares of nonlinear functions. The method of minimisation is based on combined Gauss-Newton and modified Newton algorithm using function values only; for more details see Gill and Murray (1978). Although the gradient of the function (4.14) can be calculated analytically, the NAG routine E04FCF does not require the user to supply it. If required, the constraints $0 < r_i < 1$ for $i = \overline{1,N}$ can be imposed manually during the iterative procedure by adjustment at each iteration. The minimisation process usually terminates when either a user-specified tolerance is achieved, or when a user-specified maximum number of iterations is reached.

We finally remark that the process of minimisation of the nonlinear functional (4.14) is an iterative method for finding simultaneously both the MFS coefficients $\underline{a}$ and the inner boundary radial vector $\underline{r}$. Alternatively, one could have used a decomposition approach to take care of the ill-posedness and the nonlinearity of the inverse problem separately. In this latter approach one would first determine the MFS coefficients $\underline{a}$ by imposing the Cauchy data (4.2) and (4.5), and after that find the boundary ∂D by looking for the Dirichlet level set (4.3). However, the reconstructions obtained by decomposition methods are not as accurate as those obtained by iterative minimisation methods, see Serranho (2007). In addition, if the Neumann condition (4.4) is to be satisfied then the nonlinear step of a decomposition approach becomes impractical.

4.4 Numerical results and discussion

In this section numerical results are presented for the MFS parameters $R = s = 2$ and $M = N$. The initial guess for the vector $\underline{a}$ is arbitrary, say all components equal to 0.1. The initial guess for the inner boundary is arbitrary and is taken, say to be a circle located at the origin with radius 0.5. Actually, in the next section we will also investigate a different initial guess.

4.4.1 Example 1

We consider first a simple two-dimensional detection of an unknown circular (rigid inclusion) inner boundary $D = B(\mathbf{0}; r_0)$ of radius $r_0 = 0.7$ within the unit circle $\Omega = B(\mathbf{0}; 1)$. We take $u(1, \theta) = f(\theta) = e^{\cos(\theta)+\sin(\theta)}$ on $\partial\Omega$ and $u(r(\theta), \theta) = h(\theta) = e^{0.7(\cos(\theta)+\sin(\theta))}$ on ∂D, as the Dirichlet data given by equations (4.2) and (4.3), respectively. We also take $k = \sqrt{2}$. We take the normal derivative on $\partial\Omega$ given by $\frac{\partial u}{\partial n}(1, \theta) = g(\theta) = (\cos(\theta) + \sin(\theta))e^{\cos(\theta)+\sin(\theta)}$. For this input data, the analytical solution is $u(r, \theta) = e^{r(\cos(\theta)+\sin(\theta))}$.

No noise

Let us consider first the case of exact data when there is no noise $p = 0$ in the measured data (4.5). Figure 4.2 shows the objective function (4.14), as a function of the number of iterations for various $M = N = \{5, 10, 20\}$. From this figure it can be seen that the objective function (4.14) converges to zero within few iterations as $M = N$ increases. In Figure 4.3 we present the results obtained from the minimisation routine following a series of 7 iterations when $M = N = 20$. It can be seen that at the final iteration 7 one locates the inner circular boundary of radius $r_0 = 0.7$ with a high accuracy.

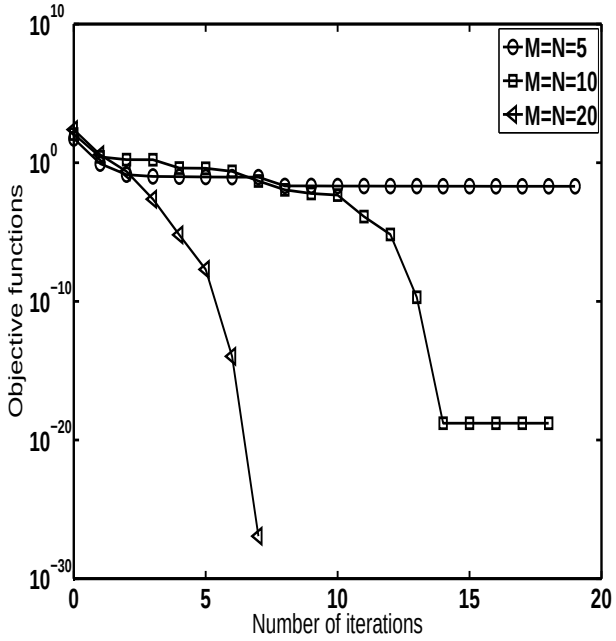

Figure 4.2: The objective function (4.14), as a function of the number of iterations, (no noise), for various $M = N \in \{5, 10, 20\}$ for Example 1. Initial guess is a circle of radius 0.5.

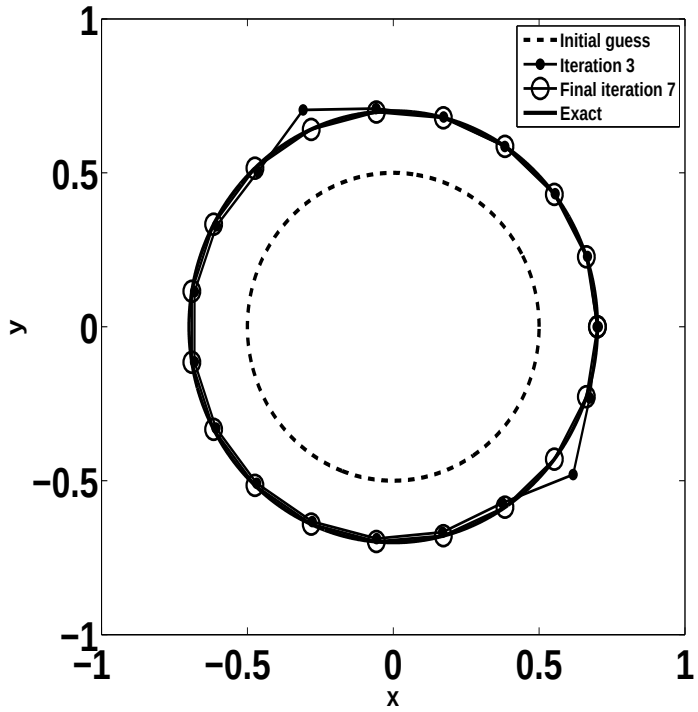

Figure 4.3: The reconstructed boundary for Example 1 when searching for a circular inner boundary located at the origin of radius $r_0 = 0.7$, (no noise), and $M = N = 20$. Initial guess is a circle of radius 0.5.

Robustness with respect to the initial guess

In order to highlight the influence of the initial guess on the numerical results we take a different guess from the previous computation of Figures 4.2 and 4.3 which used as initial guess for the inner boundary a circle of radius 0.5 centred at the origin.

We therefore consider an ellipse of semiaxes 0.5 and 0.4 in the x- and y-directions, respectively, as an initial guess. The corresponding results to Figures 4.2 and 4.3 are presented in Figures 4.4 and 4.5, respectively. First, from Figure 4.5 it can be seen that the circular inclusion is accurately identified after 12 iterations (for $M = N = 20$). Secondly, by comparing Figures 4.2 and 4.4 it can be seen that, as expected, it takes a larger number of iterations to achieve convergence in the latter case than in the former one for all the degrees of freedom $M = N \in \{5, 10, 20\}$. From this analysis it can be concluded that the iterative NAG routine E04FCF is rather robust with respect to a reasonable choice of the initial guess.

In the reminder of this chapter we select as initial guess the former choice of a circle of radius 0.5 centred at the origin.

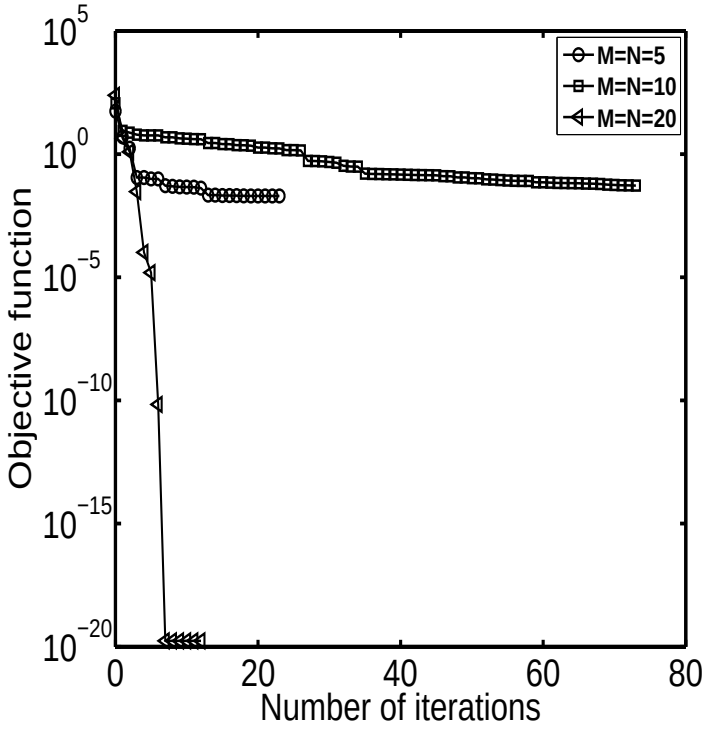

Figure 4.4: The objective function (4.14), as a function of the number of iterations, (no noise), for various $M = N \in \{5, 10, 20\}$ for Example 1. Initial guess is an ellipse of semiaxes 0.5 and 0.4.

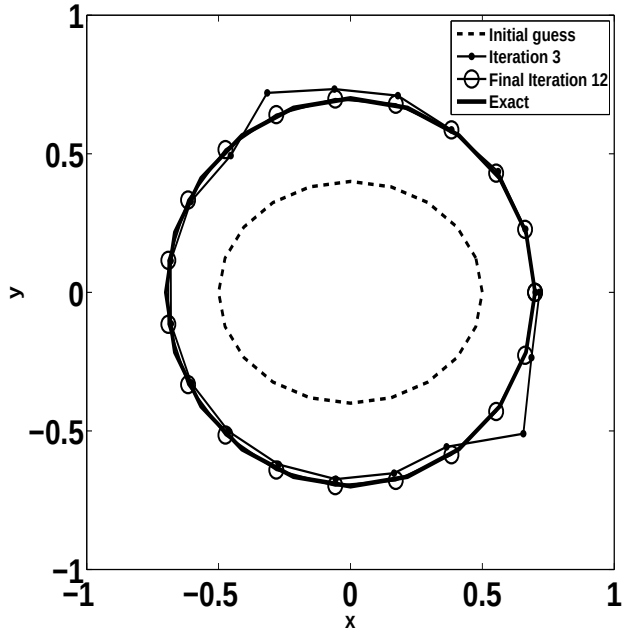

Figure 4.5: The reconstructed boundary for Example 1 when searching for a circular inner boundary located at the origin of radius $r_0 = 0.7$, (no noise), and $M = N = 20$. Initial guess is an ellipse of semiaxes 0.5 and 0.4.

Adding noise to the boundary data

In order to investigate the stability of the numerical solution, we add noise into the Neumann boundary data g as g^ϵ given by expression (4.15). In this case the total amount of noise is

$$\epsilon = \|g - g^\epsilon\|^2_{L^2(\partial\Omega)} = \sum_{i=1}^{M} \epsilon_i^2. \tag{4.18}$$

In Figure 4.6(a) we present the objective function (4.14), as a function of the number of iterations for the noise level $p = 1\%$ when $M = N = 20$. For this level of noise the value of ϵ in (4.18) is 0.0357. Figure 4.6(b) shows the results obtained from the minimisation routine at various iterations. From this figure it can be seen that if the minimisation process is let to run until the final convergence illustrated in Figure 4.6(a) is reached, i.e. for 2878 iterations, then it produces an unstable inner boundary solution. If the minimisation procedure would have a regularising character then one way to stabilize the solution is to employ some discrepancy-type criterion, namely terminate the minimisation process of (4.14) at the first iteration for which the objective function $T(\underline{a}, \underline{r})$ becomes less than the amount of error ϵ. According to Figure 4.6(a) for $\epsilon = 0.0357$ this yields the iteration number 1267. However, the numerical results presented in Figure 4.6(b) at this iteration number

are still unstable. This is somewhat expected since the NAG routine E04FCF used is unlikely to have a regularising character. An alternative way to regularise the least-squares functional (4.14), and obtain a stable solution, is to add to it penalizing terms which impose additional smoothness on the solution.

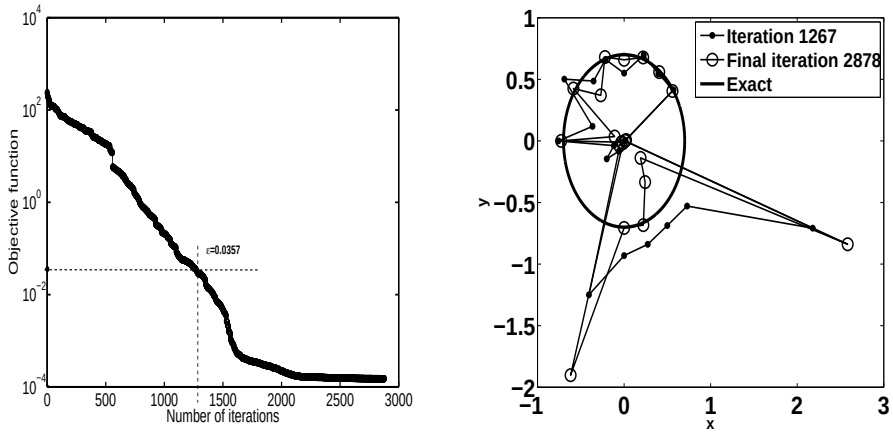

(a) (b)

Figure 4.6: (a) The objective function (4.14), as a function of the number of iterations, ($p = 1\%$ noise) for Example 1. (b) The reconstructed boundary for Example 1 when searching for a circular inner boundary located at the origin of radius $r_0 = 0.7$, when there is $p = 1\%$ noise in the data (4.5), and $M = N = 20$.

Incorporating a regularising term

In order to overcome the instablility of the numerical solution illustrated in Figure 4.6(b), we add standard zeroth- and first-order Tikhonov's regularisation terms to the functional T given by equation (4.14), namely,

$$Reg(\underline{a},\underline{r}) = \sum_{j=2M+N+1}^{3M+2N} \left(\sqrt{\lambda_1}a_{j-2M-N}\right)^2 + \sum_{j=3M+2N+1}^{3M+3N-1} \Big[\sqrt{\lambda_2}\Big(r_{j-3M-2N+1} - r_{j-3M-2N}\Big)\Big]^2, \quad (4.19)$$

where $\lambda_1, \lambda_2 \geq 0$ are regularisation parameters. The first term in (4.19) penalises the norm of $\|\underline{a}\|^2$, whilst the second term penalises the norm of the derivative $\|\underline{r}'\|^2$. Penalising the norm of the function $\|\underline{r}\|^2$ has also been tried and the results were less accurate.

Choice of regularisation parameters

Clearly, the rigorous choice of the regularisation two-parameter family λ_1 and λ_2 in the nonlinear Tikhonov functional (4.19) is very challenging. One can attempt the usual discrepancy principle or, the more recent L-surface criterion, Belge et al. (2002), but the calculations are very expensive and close to being prohibitive. In our study, we have investigated by trial and error several values for λ_1 and λ_2, and although we are not optimal in their difficult choice, at least we can discard the unstable solutions (those highly oscillatory and unbounded) and provide some nearly-optimal plausible stable condidates. Currently, the regularisation parameters are chosen based on experience by first choosing some small values and gradually increasing them until the numerical oscillations in the unknown inner boundary are removed. Nevertheless, more work should be undertaken on the subject of multiple regularisation in the future.

Results with regularisation

We fix $M = N = 20$ and show the results when $\lambda_1 = 0$, $\lambda_2 \in \{10^{-6}, 10^{-3}, 10^{-1}\}$ and $\lambda_1 \in \{10^{-6}, 10^{-3}, 10^{-1}\}$, $\lambda_2 = 0$ for $p = 1\%$ noise.

Figures 4.7 and 4.8 show the regularised objective function and the retrieved inner boundary, respectively, for $p = 1\%$ noise and various regularisation parameters. Comparison between Figure 4.6(b) and Figure 4.8(a) shows that the results when $\lambda_1 = 0$, $\lambda_2 = \{10^{-3}, 10^{-1}\}$ become slightly better than the results with $\lambda_2 = 0$ or 10^{-6} though they appear still unstable. Much improved stable results can be seen if one regularises with $\lambda_1 \in \{10^{-3}, 10^{-1}\}$, $\lambda_2 = 0$, compare Figures 4.6(b) and 4.8(b).

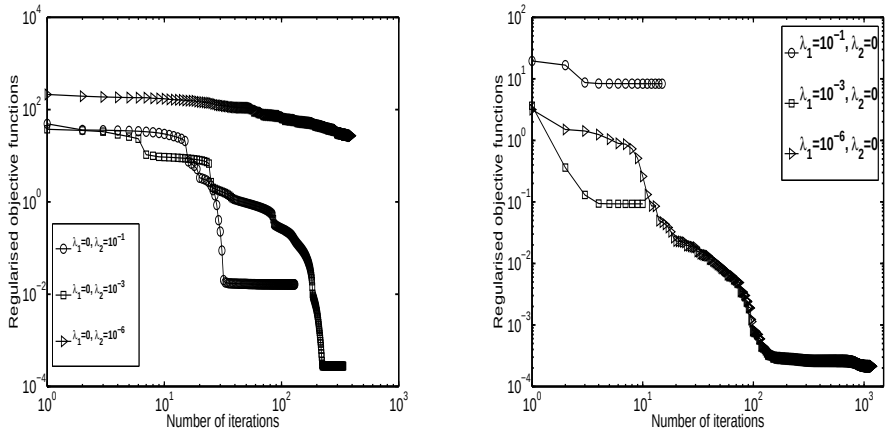

(a) (b)

Figure 4.7: The regularised objective function for: (a) $\lambda_1 = 0$, $\lambda_2 \in \{10^{-6}, 10^{-3}, 10^{-1}\}$, and (b) $\lambda_1 \in \{10^{-6}, 10^{-3}, 10^{-1}\}$, $\lambda_2 = 0$, as a function of the number of iterations, ($p = 1\%$ noise) for Example 1.

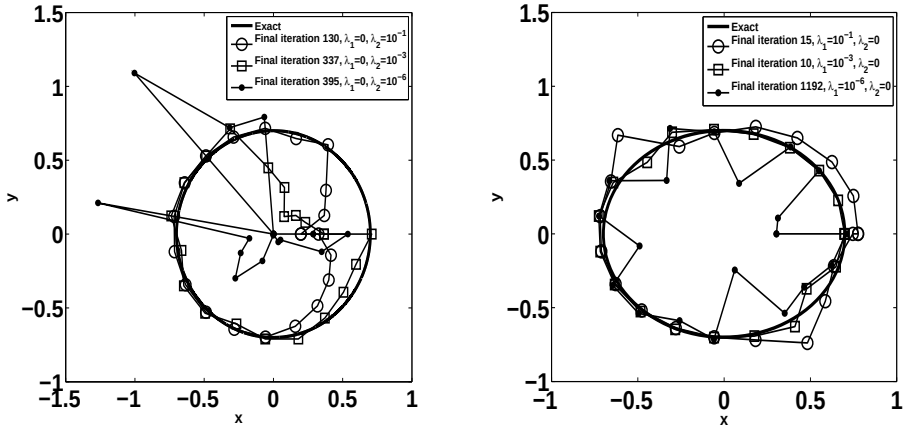

(a) (b)

Figure 4.8: The reconstructed boundary for: (a) $\lambda_1 = 0$, $\lambda_2 \in \{10^{-6}, 10^{-3}, 10^{-1}\}$, and (b) $\lambda_1 \in \{10^{-6}, 10^{-3}, 10^{-1}\}$, $\lambda_2 = 0$, for Example 1 when searching for a circular inner boundary located at the origin of radius $r_0 = 0.7$, when there is $p = 1\%$ noise in the data (4.5).

Discussion on the objective function

We find it useful to finish this example with a discussion about the objective function (4.14) which is illustrated in Figures 4.2 (no noise, no regularisation), 4.6(a) (1% noise, no regularisation) and 4.7 (1% noise, with regularisation (4.19)). First

in the case of no noise, the rapid decreasing behaviour of the objective function (4.14) shows that the minimisation process is convergent. If this would not have happened then this could have indicated that the minimisation process is divergent or, more likely that the computational code contains errors. Next, when noise is included in the data (4.15), Figure 4.6(a) is also useful because it illustrates the semi-convergent behaviour of the unregularised objective function (4.14). That is, although the objective function appears convergent, the solution obtained after 2878 iterations, and illustrated in Figure 4.6(b), is in fact unstable. This is a well-known phenomenon present in iterative methods for solving ill-posed problems, see e.g. Engl et al. (2000). In order to restore stability, one can try the so-called discrepancy principle which ceases the iterative process at the iteration number for which the residual becomes comparable with the level of noise ε, as illustrated in Figure 4.6(a). This yields a stopping iteration number 1267, and the numerical results shown in Figure 4.6(b) although yet unstable they are better than the results obtained after the final 2878 iterations. A reason why the results obtained with this stopping criterion happens to be yet unstable may be that the NAG routine E04FCF used does not have a regularizing character, as that shown by more classical minimisation schemes, e.g. Levenberg-Marquardt, conjugate gradient, etc. An alternative to the difficult challenge of obtaining a stable and accurate reconstruction could be to augment the least-squares functional (4.14) with the regularisation terms (4.19). Then the iterative algorithm based on minimising (4.14)+(4.19) does not have to be terminated, and it can be run until convergence is achieved, as illustrated in Figure 4.7. The price to pay is that including (4.19) it introduces additional regularisation parameters whose prescription is also difficult, as described in a previous section on the choice of the regularisation parameters.

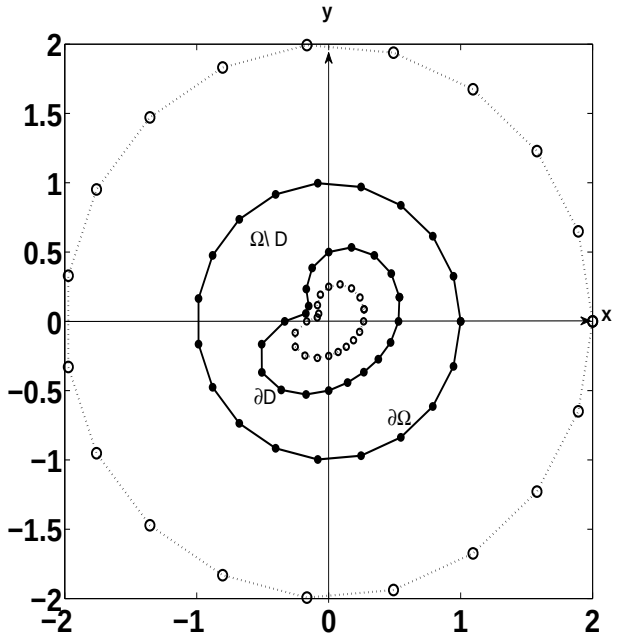

Figure 4.9: Distribution of source (∘) and boundary collocation (•) points for the direct problem associated to Example 2.

4.4.2 Example 2

In this example, we consider the more complicated bean shaped inner boundary ∂D given by the radial parameterization

$$r(\theta) = \frac{0.5 + 0.4\cos(\theta) + 0.1\sin(2\theta)}{1 + 0.7\cos(\theta)}, \qquad \theta \in (0, 2\pi] \tag{4.20}$$

within the unit circle $\Omega = B(\mathbf{0}, 1)$. The Dirichlet data (4.2) on $\partial\Omega$ was taken to be the same as in Example 1. In this case, since no analytical solution is available, the Neumann data (4.5) is simulated numerically by solving, using the MFS, the direct Dirichlet problem (4.1), with $k = \sqrt{2}$, $u = 0$ on ∂D and $u(1, \theta) = f(\theta) = e^{\cos(\theta)+\sin(\theta)}$ on $\partial\Omega$, when ∂D is given by (4.20), see Figure 4.9. The numerical solutions for the normal derivative $\partial u/\partial n(1, \theta)$ on $\partial\Omega$, obtained with $R = s = 2$ for various values of $M = N \in \{10, 20, 40\}$ with no regularisation, and with some little regularisation such as $\lambda = 10^{-9}$ when $M = N = 40$, are shown in Figure 4.10. From the first three curves on this figure it can be seen that when no regularisation is employed the numerical results obtained for $M = N = 10$ and 20 are close to each other; however, as $M = N$ increases to 40 the numerical solution departs and becomes slightly oscillatory indicating that ill-conditioning starts to manifest. This is consistent with the truncated singular value decomposition analysis of Ramachandran (2002)

regarding the use of regularisation to circumvent the ill-conditioning of the MFS. We were able to deal with this instability by including a small regularisation parameter $\lambda = 10^{-9}$, and then stable results could be achieved, see the close agreement between the curve for $M = N = 20$ and the curve for $M = N = 40$ and $\lambda = 10^{-9}$. Twenty evenly spread points out of the forty data points of this last curve are chosen as input Neumann numerically simulated data (4.5) in order to avoid committing an inverse crime. That is to say that the inverse solver is applied with $M = N = 20$ which is different from the direct problem $M = N = 40$ and $\lambda = 10^{-9}$.

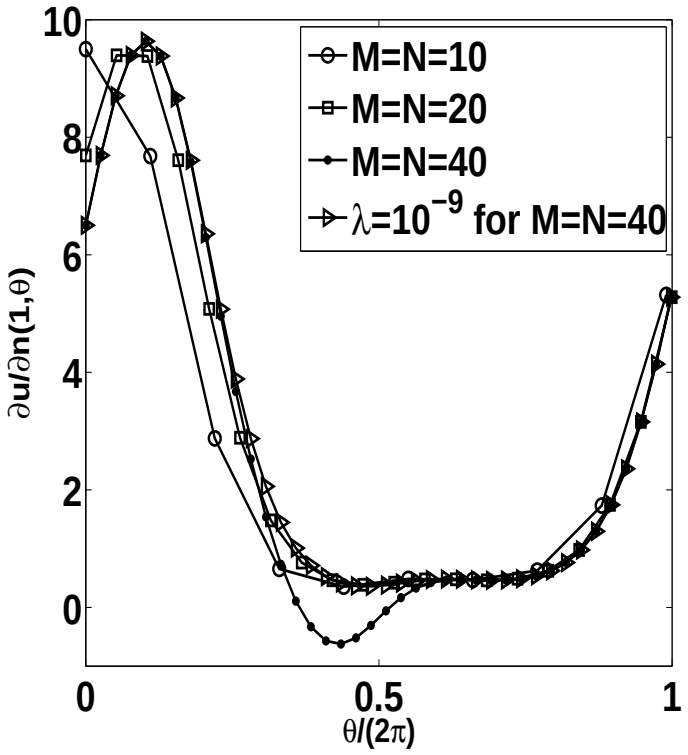

Figure 4.10: The numerical solutions for the normal derivative $\partial u/\partial n(1, \theta)$, obtained with $R = s = 2$ for various values of $M = N \in \{10, 20, 40\}$ with no regularisation, and the regularised solution $\lambda = 10^{-9}$ when $M = N = 40$, for the direct problem associated to Example 2.

In Figure 4.11(a), we present the reconstructed and the exact shape obtained with no noise and no regularisation. From this figure it can be seen that the reconstructed shape fails to determine the exact shape of the inner boundary. In order to obtain the reconstructed shape stable and in reasonable good agreement with the exact shape we apply the regularisation with $\lambda_1 = 10^{-6}, \lambda_2 = 0$, as shown in Figure 4.11(b).

Figures 4.12 and 4.13 show the regularised objective function and the retrieved

inner boundary, respectively, for $p = 1\%$ noise and various regularisation parameters. From Figure 4.13 it can be seen that, except for the case $\lambda_1 = 0, \lambda_2 = 10^{-1}$, the results are quite inaccurate even if regularisation is employed. The reason for this is that the numerical solution depends strongly on the proper choice of the regularisation parameters which in this paper are based on trial and error. And, in fact, slightly improved stable results can be obtained if regularisation with $\lambda_1 = \lambda_2 = 10^{-1}$ is used, see Figure 4.14.

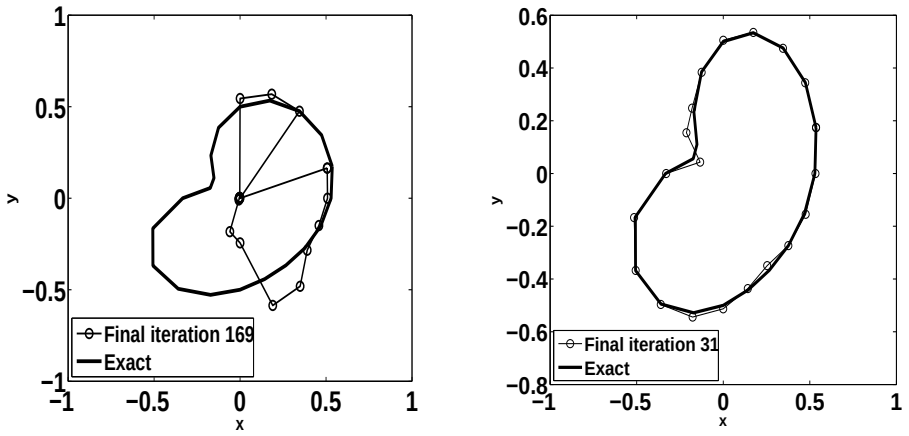

(a) (b)

Figure 4.11: The reconstructed boundary for Example 2 when searching for a bean-shaped inner boundary located at the origin of radius $r(\theta)$ in (4.20), when there is no noise in the data and (a) no regularisation, and (b) regularisation with $\lambda_1 = 10^{-6}$, $\lambda_2 = 0$.

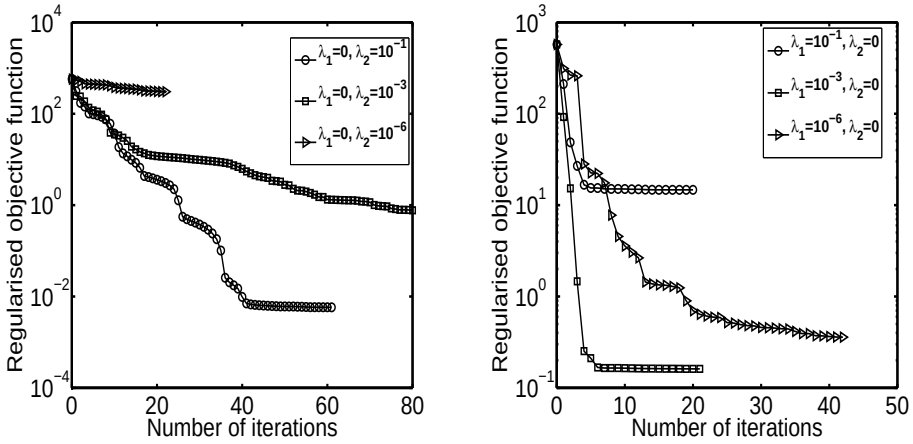

(a) (b)

Figure 4.12: The regularised objective function for: (a) $\lambda_1 = 0$, $\lambda_2 \in \{10^{-6}, 10^{-3}, 10^{-1}\}$, and (b) $\lambda_1 \in \{10^{-6}, 10^{-3}, 10^{-1}\}$, $\lambda_2 = 0$, as a function of the number of iterations, ($p = 1\%$ noise) for Example 2.

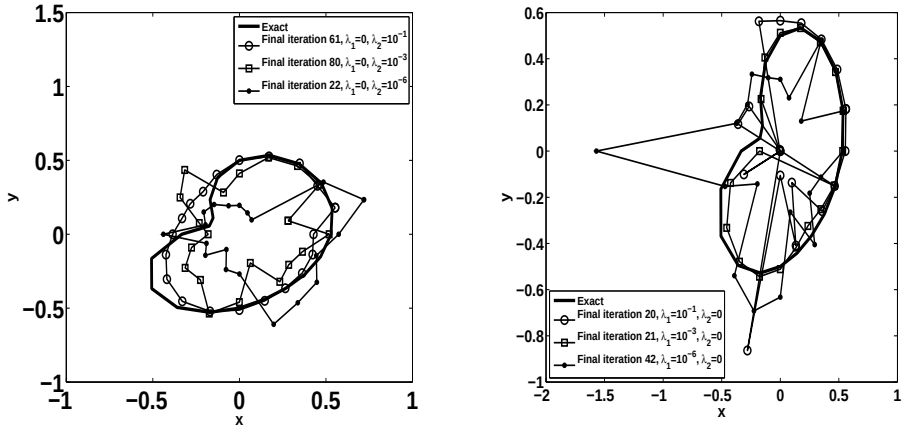

(a) (b)

Figure 4.13: The reconstructed boundary for: (a) $\lambda_1 = 0$, $\lambda_2 \in \{10^{-6}, 10^{-3}, 10^{-1}\}$, and (b) $\lambda_1 \in \{10^{-6}, 10^{-3}, 10^{-1}\}$, $\lambda_2 = 0$, for Example 2 when searching for a bean-shaped inner boundary located at the origin of radius $r(\theta)$ in (4.20), when there is $p = 1\%$ noise in the data (4.5).

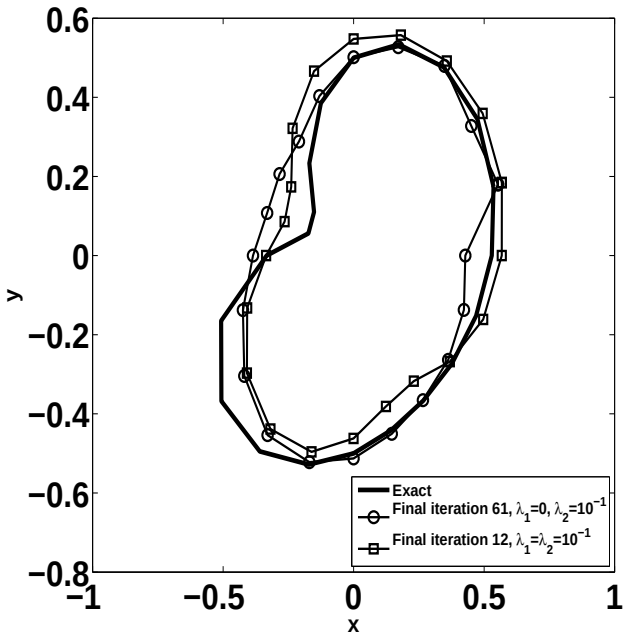

Figure 4.14: The reconstructed boundary for $\lambda_1 = 0$, $\lambda_2 = 10^{-1}$, and $\lambda_1 = \lambda_2 = 10^{-1}$, for Example 2 when searching for a bean-shaped inner boundary located at the origin of radius $r(\theta)$ in (4.20), when there is $p = 1\%$ noise in the data (4.5).

4.4.3 Example 3

So far, the previous two examples have been concerned with the reconstruction of an inclusion (simple, such as a circle, or complicated, such as a bean-shaped) on which the Dirichlet boundary condition (4.3) was enforced. In this example, we consider reconstructing a complicated peanut-shaped cavity given by the radial parameterization

$$r(\theta) = \frac{3}{4}\sqrt{\cos^2(\theta) + 0.25\sin^2(\theta)}, \qquad \theta \in (0, 2\pi], \tag{4.21}$$

on which the homogeneous Neumann boundary condition (4.4) applies. We take $k = 1$, and the Dirichlet data (4.2) on $\partial\Omega = \partial B(\mathbf{0}, 1)$ given as in Ivanyshyn and Kress (2006),

$$u(1, \theta) = f(\theta) = e^{-\cos^2(\theta)}, \quad \theta \in [0, 2\pi). \tag{4.22}$$

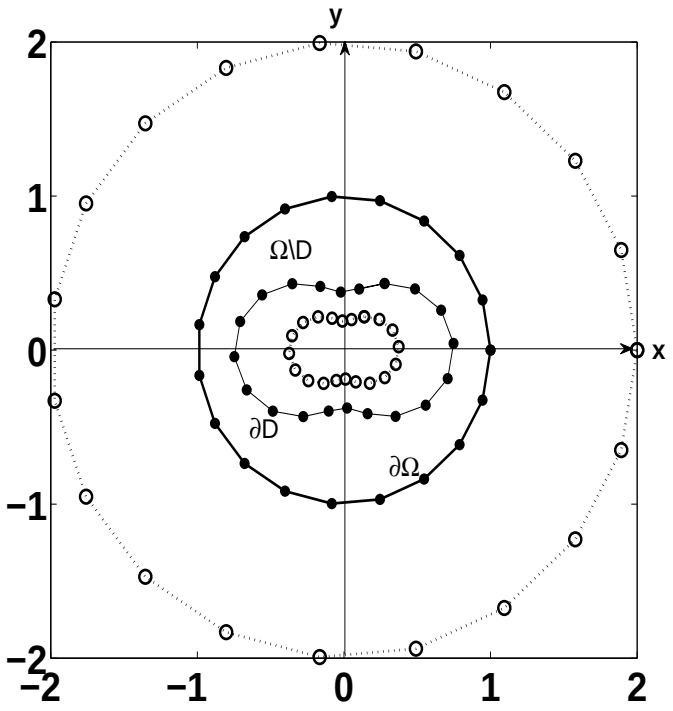

Figure 4.15: Distribution of source (∘) and boundary collocation (•) points for the direct problem associated to Example 3.

As in Example 2, since no analytical solution is available, the Neumann data (4.5) is simulated numerically by solving, using the MFS, the direct mixed problem (4.1), with $k = 1$, $\partial u/\partial n = 0$ on ∂D, and (4.22), when ∂D is given by (4.21), see Figure 4.15. In imposing the homogeneous Neumann boundary condition on the (insulated) cavity ∂D given by equation (4.21), one needs to use expression (4.17) with the (inward) normal to ∂D given by

$$\underline{n} = \frac{1}{\sqrt{r^2(\theta) + r'^2(\theta)}}[-(r'(\theta)\sin(\theta) + r(\theta)\cos(\theta))\underline{i} + (r'(\theta)\cos(\theta) - r(\theta)\sin(\theta))\underline{j}], \tag{4.23}$$

where $\underline{i} = (1, 0)$ and $\underline{j} = (0, 1)$. For the peanut-shaped cavity (4.21), the expression for the normal (4.23) becomes

$$\underline{n} = \frac{1}{\sqrt{(cos^2(\theta) + 0.25\sin^2(\theta))^2 + 0.5625\sin^2(\theta)\cos^2(\theta)}}\Big[n_1\underline{i} + n_2\underline{j}\Big], \tag{4.24}$$

where

$$n_1 = \cos(\theta)\big(0.5\sin^2(\theta) - \cos^2(\theta)\big), \quad n_2 = -\sin(\theta)\big(0.25\sin^2(\theta) + 1.75\cos^2(\theta)\big).$$

The numerical solutions for the normal derivative $\partial u/\partial n(1,\theta)$ on $\partial\Omega$, obtained with $R = s = 2$ for various values of $M = N \in \{20, 40, 80\}$ with no regularisation, and with regularisation $\lambda = 10^{-6}$, are shown in Figure 4.16. The same conclusion about the need of including regularisation when the dimension of the matrix of the system of linear algebraic equations increases, as that obtained in Figure 4.10 can be drawn. This is consistent with the comments made by Chen et al. (2006) regarding the ill-conditioning of the MFS for direct problems with exact boundary conditions. The inverse solver is applied with $M = N = 20$ and the input data (4.5) is chosen out of the curves with $M = N = 40$ from Figure 4.16 as explained for Example 2. For the cavity identification problem given by equations (4.1), (4.2), (4.4) and (4.5) with $h = 0$, the last term in (4.14) is replaced by

$$\sum_{i=2M+1}^{2M+N} \Big[\sum_{j=1}^{M+N} a_j \frac{\partial G_-}{\partial n}(\underline{X}_{i-M}, \underline{\xi}^j) \Big]^2. \tag{4.25}$$

In expressing this term one needs to use (4.17) with the (inward) normal to ∂D given by (4.23), where, in discretised form, the derivative r' is approximated using simple backward finite differences as

$$r'(\theta) \approx \frac{r_i - r_{i-1}}{\theta_i - \theta_{i-1}}, \qquad i = \overline{1, N} \tag{4.26}$$

with the convention that $r_0 = r_N$ and $\theta_0 = 0$. Central finite differences can also be used, see Karageorghis and Lesnic (2010a).

Similar results to those presented for Example 2 have been obtained and, for brevity, we only illustrate Figure 4.17 which shows the reconstructed boundary for $p = 1\%$ noise and regularisation parameters $\lambda_1 = \lambda_2 \in \{10^{-5}, 10^{-3}\}$. From this figure it can be seen that reasonable accurate and stable numerical results are obtained.

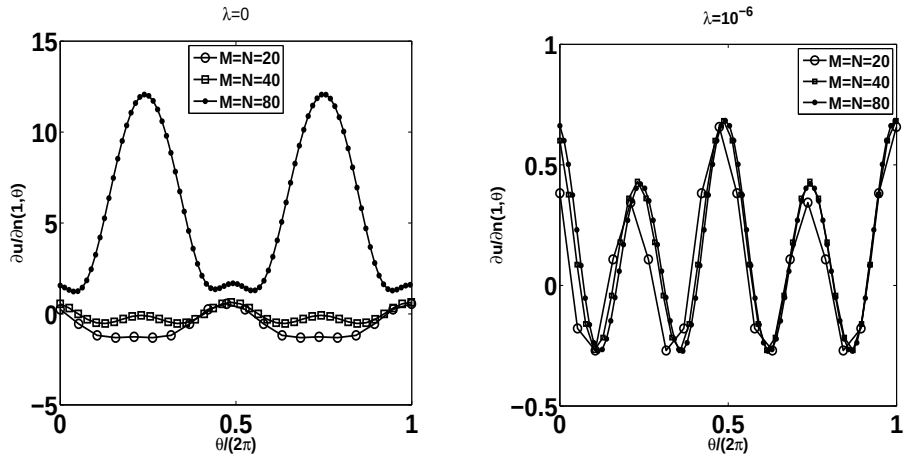

(a) (b)

Figure 4.16: The numerical solutions for the normal derivative $\partial u/\partial n(1,\theta)$ for various values of $M = N \in \{20, 40, 80\}$ with (a) no regularisation, and (b) with regularisation $\lambda = 10^{-6}$, for the direct problem associated to Example 3.

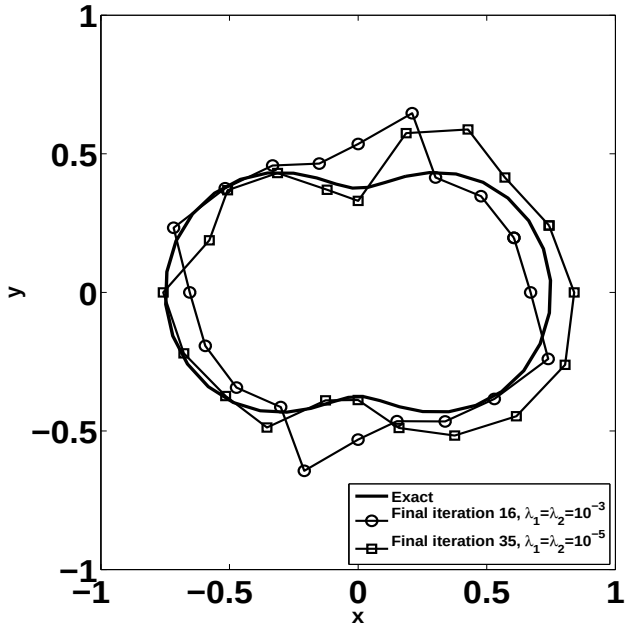

Figure 4.17: The reconstructed boundary for $\lambda_1 = \lambda_2 \in \{10^{-3}, 10^{-5}\}$ for Example 3 when searching for a peanut-shaped inner boundary located at the origin of radius $r(\theta)$ in (4.21), when there is $p = 1\%$ noise in the data (4.5).

4.5 Conclusions

In this chapter, the modified Helmholtz inverse geometric problem, which consists of determining an unknown inner boundary of an annular domain from a single pair of outer boundary Cauchy data has been investigated by the MFS. Several examples for two-dimensional simple, bean and peanut-shaped inner boundaries have been considered. The numerical results show that the MFS is well-suited for the solution of inverse geometric problems and is very accurate for exact data. When 1% noise was added into the Neumann data this yields unstable results if no regularisation was employed. Regularisation terms were added in order to obtain a stable solution. The model presented here has potential for extension to thermography since the modified Helmholtz equation can be obtained from the time-dependent heat equation through the θ-scheme associated with the time finite-difference discretization and averaging of the transient fields.

Chapter 5

Inverse shape and surface heat transfer coefficient identification

5.1 Introduction

The identification of unknown obstacles and their resistive characteristics is very important in inverse problems, design and optimisation. Similarly as in chapter 4, consider the inverse problem which consists of determining an unknown defect D compactly contained in a simply-connected bounded domain Ω assuming that the steady-state temperature u satisfies the modified Helmholtz equation (4.1) from the knowledge of the Dirichlet temperature data u and the Neumann heat flux data $\partial u/\partial n$ on the boundary $\partial\Omega$, and a Robin boundary condition on ∂D.

The inverse nonlinear ill-posed problem of determining the inner boundary ∂D and possibly its surface heat transfer coefficient is approached using a regularised minimisation procedure which employs an MFS solver at each iteration. We mention that there also exists an extensive literature on using the boundary element method (BEM) instead of the MFS for internal boundary identification, see e.g. Duraiswami et al. (1997) and Lesnic (2001) for the Laplace equation in electrical impedance tomography (EIT), Marin et al. (2003) for the Lame system in elasticity, and Marin et al. (2004) for the modified Helmholtz equation. However, there are clear methodological differences between the MFS and the BEM, see e.g. Ahmed et al. (1989) for a comparison between the two methods. In summary, although the MFS formulation may introduce some extra ill-conditioning, by avoiding the numerical integration it is considerably easier to use, especially in higher dimensional problems.

The outline of this chapter is as follows. In section 5.2 we introduce the mathematical formulation, whilst in section 5.3 we present the MFS for the modified Helmholtz equation. In section 5.4 we present and discuss the numerically obtained

results. In section 5.5 we give some conclusions and possible future work.

5.2 Mathematical formulation

Consider a bounded simply-connected domain Ω with smooth boundary such as $\overline{D} \subset \Omega$, and $\Omega \setminus D$ is connected. The steady-state temperature u satisfies the modified Helmholtz equation (4.1) subject to the boundary conditions

$$u = f \qquad \text{on} \quad \partial\Omega, \tag{5.1}$$

and

$$\frac{\partial u}{\partial n} + \alpha u = 0 \qquad \text{on} \quad \partial D, \tag{5.2}$$

where $f \in H^{1/2}(\partial\Omega)$ is non-constant and $L^{\infty}(\partial D) \ni \alpha \geqslant 0$ is the surface heat transfer coefficient. In equation (5.2), $\underline{n}$ denotes the outward normal to the domain $\Omega \setminus D$, i.e. pointing inwards with respect to D. It is well-known that the direct Robin problem given by equations (4.1), (5.1) and (5.2) has a unique solution $u \in H^1(\Omega \backslash D)$, when D is known. We can then define the nonlinear operator $F_f(\partial D)$ given by equation (4.5). Then the inverse problem under consideration consists of extracting some information about the boundary ∂D from the data $g = F_f(\partial D)$. The Robin boundary condition (5.2) models Newton's law of cooling which gives a linear relationship between the heat flux and the surface temperature through a surface heat transfer coefficient of proportionality α. The simpler extreme case when $\alpha = 0$, i.e. the obstacle D is a hard cavity on whose boundary ∂D the homogeneous Neumann condition $\partial u/\partial n = 0$ applies, possesses a unique solution, see Isakov (2009), Theorem 3.1). Uniqueness also holds for $\alpha = \infty$, i.e. the obstacle D is a soft rigid inclusion on whose boundary ∂D the homogeneous Dirichlet condition $u = 0$ applies, see Lesnic and Bin-Mohsin (2012).

Although the uniqueness of solution holds for the simpler extreme cases $\alpha \in \{0, \infty\}$, this solution, in general, does not depend continuously on the input Cauchy data (5.1) and (4.5). Special corrective procedures are necessary in order to obtain a stable solution, see Yang et al. (2010), Bin-Mohsin and Lesnic (2012).

In the general case $\alpha \in (0, \infty)$ there are counterexamples for which the obstacle D cannot be uniquely retrieved, see Pagani and Pierotti (2009) for the case of Laplace's equation, i.e. $k = 0$ in (4.1).

We briefly note that the situation regarding the uniqueness/non-uniqueness of solution is much more settled in the case of a boundary determination in corrosion detection, see Cakoni et al. (2010a), and Isakov (2009). However, in many obstacle problems it is not always physically realistic to assume that the boundary condition

on the obstacle is known, in which situation the coefficient α in (5.2) together with the obstacle D are to be simultaneously determined. Then, clearly one set of Cauchy boundary measurements (5.1) and (4.5) is not sufficient to simultaneously recover the shape and the heat transfer coefficient. However, it turns out that two linearly independent boundary temperatures measurements f_1 and f_2, one of which is positive, inducing, via (4.5), two corresponding heat flux measurements g_1 and g_2, are sufficient to provide a unique solution for the pair (D, α), see Pagani and Pierotti (2009, Theorem 4.5). Similar uniqueness, see Rundell (2008) and Bacchelli (2009), as well as stability, see Sincich (2010), results have been obtained recently in the more established case of identifying on unknown corroded boundary and its impedance.

We finally note that the mathematical heat conduction fin model given by equations (4.1), (5.1), (5.2) and (4.5) also arises in electrostatics (with $k = 0$), where u represents the electric potential, f is the voltage, g is the current flux and α corresponds to the impedance which is the reciprocal of the resistance. Also, if in equations (4.1) and (5.2), the real quantities k and α become purely imaginar we have the corresponding situation in acoustics.

5.3 The Method of Fundamental Solutions (MFS)

The MFS is applied as described in Section 4.3. When α is known, the MFS coefficient vector $\underline{a} = (a_j)_{j=\overline{1,M+N}}$ and the radii vector $\underline{r} = (r_i)_{i=\overline{1,N}}$ characterising the star-shaped inner boundary ∂D can be determined by imposing the boundary conditions (5.1), (5.2) and (4.5) in a least-squares sense which recasts into minimising the nonlinear objective function

$$T(\underline{a}, \underline{r}) := \Big\| u - f \Big\|^2_{L^2(\partial\Omega)} + \Big\| \frac{\partial u}{\partial n} - g \Big\|^2_{L^2(\partial\Omega)} + \Big\| \frac{\partial u}{\partial n} + \alpha u \Big\|^2_{L^2(\partial D)} + \lambda_1 \|\underline{a}\|^2 + \lambda_2 \|\underline{r}'\|^2, \quad (5.3)$$

where $\lambda_1, \lambda_2 \geq 0$ are regularisation parameters to be prescribed. The last term in (5.3) contains a C^1-smoothing constraint on the sought shape ∂D. Introducing the MFS approximation (4.7) into (5.3) yields

$$\begin{aligned} T(\underline{a}, \underline{r}) = \sum_{i=1}^{M} \Big[\sum_{j=1}^{M+N} a_j G_-(\underline{X}_i, \underline{\xi}^j) - f(\underline{X}_i) \Big]^2 + \sum_{i=M+1}^{2M} \Big[\sum_{j=1}^{M+N} a_j \frac{\partial G_-}{\partial n}(\underline{X}_{i-M}, \underline{\xi}^j) \\ - g(\underline{X}_{i-M}) \Big]^2 + \sum_{i=2M+1}^{2M+N} \Big[\sum_{j=1}^{M+N} a_j \Big(\frac{\partial G_-}{\partial n}(\underline{X}_{i-M}, \underline{\xi}^j) + \alpha(\underline{X}_{i-M}) G_-(\underline{X}_{i-M}, \underline{\xi}^j) \Big) \Big]^2 \\ + \lambda_1 \sum_{j=1}^{M+N} a_j^2 + \lambda_2 \sum_{j=1}^{N-1} (r_{j+1} - r_j)^2. \quad (5.4) \end{aligned}$$

The minimisation of (5.4) imposes $2M + N$ nonlinear equations in the $2N + M$ unknowns $(\underline{a}, \underline{r})$, and for a unique solution it is necessary that $M \geq N$. If there is noise in the measured data (4.5), we replace g in (5.4) by g^{ε} given by (4.15).

The minimisation of the objective function (5.4) is accomplished computationally using the NAG routine E04FCF. In Chapter 4, the physical constraints $0 < r_i < 1$ for $i = \overline{1, N}$ that the defect D stays within the host domain Ω during the iteration proccess were imposed manually during the iterative procedure by adjustment at each iteration. However, in this chapter we impose this physical constraint by changing to the new variables $\underline{q} = (q_i)_{i=\overline{1,N}}$ defined by $r_i = 1 - \frac{1}{1+e^{2q_i}}$ for $i = \overline{1, N}$. This way the minimisation of (5.4) with respect to the new variables $(\underline{a}, \underline{q})$ becomes unconstrained because the function $\mathbb{R} \ni q \mapsto 1 - \frac{1}{1+e^{2q}} = \frac{1}{2}(1 + \tanh(q)) \in (0, 1)$ is a bijection.

Finally, we observe that the form of the functional (5.3) contains a single measurement of the heat flux g for a prescribed temperature f, via the operatorial relation (4.5). However, in some cases, as discussed in Section 5.2, one may need to use two measurements of the heat flux g_1 and g_2 for two prescribed linearly independent temperatures f_1 and f_2, via the operatorial relation (4.5). This means that we double up the number of measurements in equation (5.3) which now reads as

$$\begin{aligned} T(\underline{a}^{(1)}, \underline{a}^{(2)}, \underline{r}) := & \left\| u_1 - f_1 \right\|^2_{L^2(\partial\Omega)} + \left\| u_2 - f_2 \right\|^2_{L^2(\partial\Omega)} + \left\| \frac{\partial u_1}{\partial n} - g_1 \right\|^2_{L^2(\partial\Omega)} \\ & + \left\| \frac{\partial u_2}{\partial n} - g_2 \right\|^2_{L^2(\partial\Omega)} + \left\| \frac{\partial u_1}{\partial n} + \alpha u_1 \right\|^2_{L^2(\partial D)} + \left\| \frac{\partial u_2}{\partial n} + \alpha u_2 \right\|^2_{L^2(\partial D)} \\ & + \lambda_1 \Big(\|\underline{a}^{(1)}\|^2 + \|\underline{a}^{(2)}\|^2 \Big) + \lambda_2 \|\underline{r}'\|^2, \end{aligned} \tag{5.5}$$

where $\underline{a}^{(1)}$ and $\underline{a}^{(2)}$ are the corresponding unknown coefficients in the MFS expansion (4.7) for approximating the solutions of the inverse problems with the Dirichlet data f_1 and f_2, respectively.

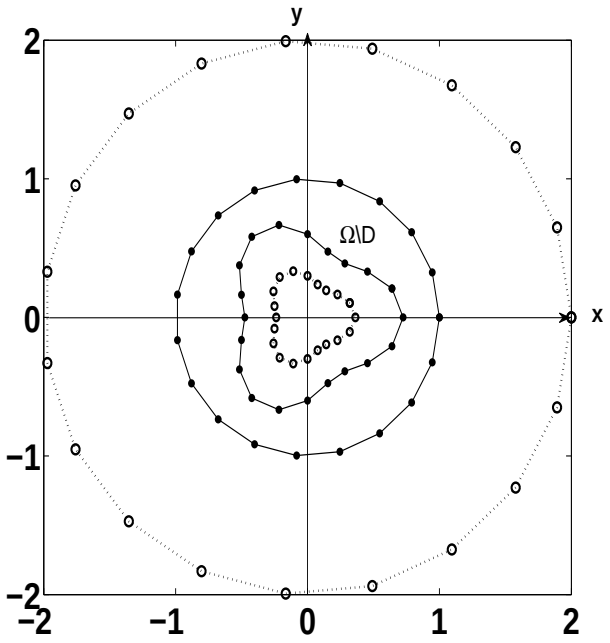

Figure 5.1: Distribution of source (∘) and boundary collocation (•) points for the direct problem associated to the pear-shape (5.6).

5.4 Numerical results and discussion

In this section numerical results are presented for $k = 1$ and the MFS parameters $R = s = 2$ and $M = N$. We consider reconstructing a complicated pear-shaped inner boundary ∂D given by the radial parametrization, see Qin and Cakoni (2011),

$$r(\theta) = 0.6 + 0.125\cos(3\theta), \qquad \theta \in (0, 2\pi], \tag{5.6}$$

and we initially take the Dirichlet data (5.1) on $\partial\Omega = \partial B(\mathbf{0}; 1)$ given by (4.22) Since no analytical solution is available, the Neumann data (4.5) on $\partial\Omega$ is simulated numerically by solving, using the MFS, the direct mixed problem given by the modified Helmholtz equation (4.1), the homogeneous Robin boundary condition (5.2) on ∂D, and the Dirichlet boundary condition (4.22) on $\partial\Omega$, when ∂D is known and given by (5.6). The arrangement of the source and boundary collocation points are shown in Figure 5.1. For the pear-shaped cavity (5.6), the expression for the inward normal (4.23) is given by

$$\underline{n} = \frac{1}{\sqrt{(0.6 + 0.125\cos(3\theta))^2 + 0.140625\sin^2(3\theta)}}\Big[n_1\underline{i} + n_2\underline{j}\Big],$$

where

$$n_1 = 0.375\sin(3\theta)\sin(\theta) - \cos(\theta)\Big(0.6 + 0.125\cos(3\theta)\Big),$$
$$n_2 = -0.375\sin(3\theta)\cos(\theta) - \sin(\theta)\Big(0.6 + 0.125\cos(3\theta)\Big).$$

The numerical solutions for the normal derivative $\partial u/\partial n(1,\theta)$ on $\partial\Omega$, obtained for various values of $M = N \in \{20, 40, 80\}$ for Example 1 below (with $\alpha = 0$) are shown in Figure 5.2. From this figure it can be seen that the numerical results are convergent as the number of degrees of freedom increases. Twenty evenly spread points out of the curve $M = N = 40$ of Figure 5.2 are chosen as input Neumann numerically simulated data (4.5) in the inverse problem next in order to avoid committing an inverse crime. That is to say, the inverse solver is applied with $M = N = 20$ which is different from that of the direct problem $M = N = 40$. Observe that by this procedure we already have introduced some numerical noise into the data (4.5), even when there is no additional random noise in equation (4.15), i.e. $p = 0$ in equation (4.16). This procedure of fabricating heat flux input data (4.5), in the absence of an analytical solution being available, has been applied in all the examples of this section.

The initial guess for the vector $\underline{a}$ is $\underline{0.1}$, and for the vector $\underline{q}$ is $\underline{0}$, i.e. the initial guess for the inner boundary is taken a circle located at the origin with radius 0.5. In our computational program execution of the NAG routine E04FCF, we initially set a user-specified maximum number of calls of function evaluations, MAXCAL, to be equal to 400 $\times$ (number of unknowns), as suggested by the NAG Fortran library manual. The minimisation process terminates when either the MAXCAL number is reached, or when unbounded values of $\underline{q}$, e.g. the absolute value of a component of $\underline{q}$ is greater than 10^{10}, are recorded. In this latter situation, we re-choose MAXCAL as the last number of calls before the program execution halted and re-run the program.

5.4.1 Example 1 ($\alpha = 0$)

We consider first the case when the obstacle D is a cavity, i.e. $\alpha = 0$ in equation (5.2). From Isakov (2009, Theorem 3.1), we know that for $\alpha = 0$ the solution of the inverse problem is unique.

We consider first the case when there is no noise, i.e. $p = 0$, in the input flux data (4.5). Figure 5.3(a) shows the objective function (5.4) with $\lambda_1 = \lambda_2 = 10^{-4}$, as a function of the number of iterations. From this figure it can be seen that the objective cost functional decreases rapidly to a low stationary level of $\mathbf{O}(10^{-3})$ in about 20 iterations. In Figure 5.3(b), we present the exact shape (5.6) and the

reconstructed shape obtained from the regularised minimisation of the objective function illustrated in Figure 5.3(a). From this figure it can be seen that the numerically reconstructed shape is stable and reasonably accurate in comparison with the exact shape (5.6). Although not illustrated, it is reported that the numerical results obtained with no regularisation imposed in the nonlinear least-squares functional (5.4), i.e. $\lambda_1 = \lambda_2 = 0$, were found unstable and inaccurate. This is to be expected since the inverse problem under investigation is ill-posed and therefore some sort of regularisation is needed in order to obtain stable solutions.

Figures 5.4-5.6 show the regularised objective function and the retrieved inner boundary when there is $p = 1\%$ noise in the input flux data (4.5), generated as in (4.15), for various regularisation parameters. As expected, from Figure 5.5 it can be seen that if the regularisation parameters λ_1 and λ_2 are too small (say 10^{-6}) then oscillating unstable solutions are obtained. However, reasonably stable numerical solutions are obtained for $\lambda_1 = 0$, $\lambda_2 = 10^{-3}$, and $\lambda_1 = \lambda_2 = 10^{-4}$.

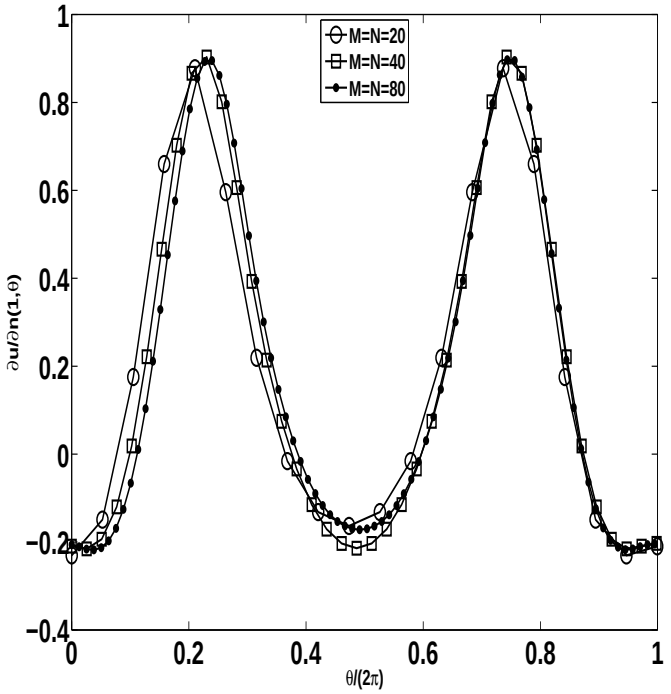

Figure 5.2: The numerical solutions for the normal derivative $\partial u/\partial n(1, \theta)$, obtained by solving the direct problem with various values of $M = N \in \{20, 40, 80\}$, for Example 1.

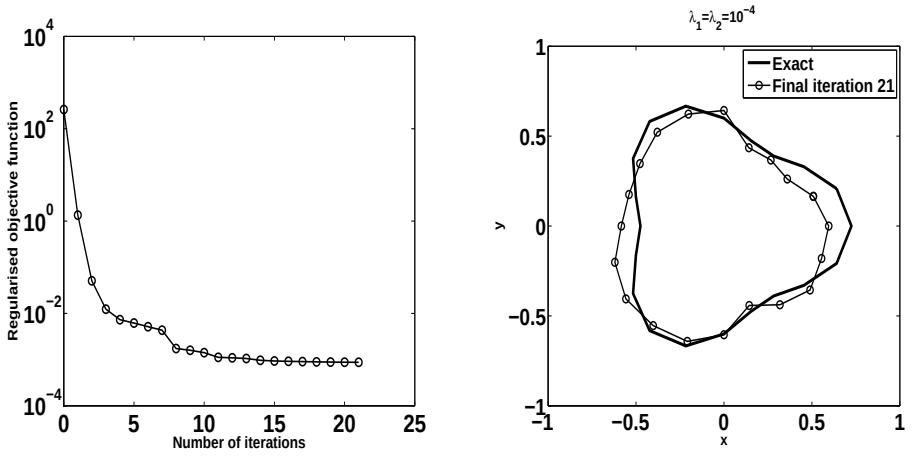

(a) (b)

Figure 5.3: (a) The regularised objective function, as a function of the number of iterations, and (b) the reconstructed boundary for $\lambda_1 = \lambda_2 = 10^{-4}$, for Example 1 when there is no noise in the data (4.5).

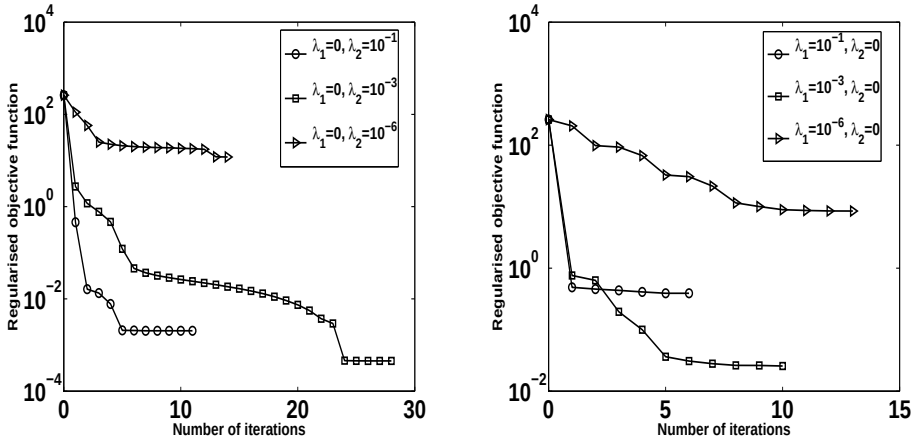

(a) (b)

Figure 5.4: The regularised objective function (5.4) for: (a) $\lambda_1 = 0$, $\lambda_2 \in \{10^{-6}, 10^{-3}, 10^{-1}\}$, and (b) $\lambda_1 \in \{10^{-6}, 10^{-3}, 10^{-1}\}$, $\lambda_2 = 0$, as a function of the number of iterations, ($p = 1\%$ noise) for Example 1.

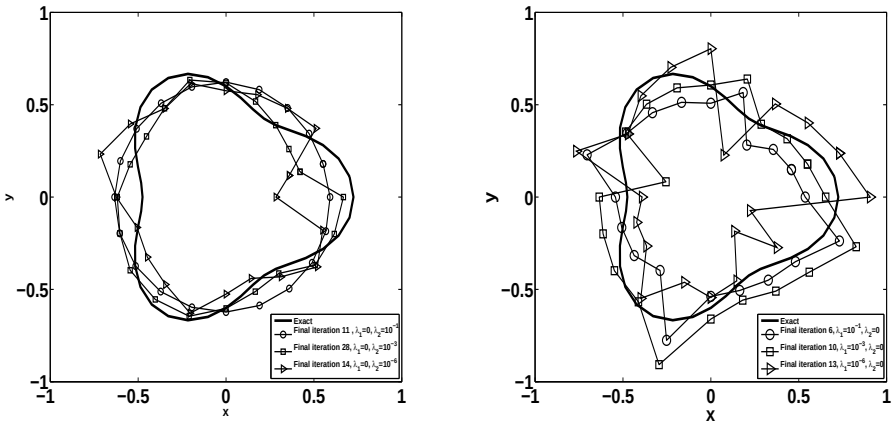

(a) (b)

Figure 5.5: The reconstructed boundary for: (a) $\lambda_1 = 0$, $\lambda_2 \in \{10^{-6}, 10^{-3}, 10^{-1}\}$, and (b) $\lambda_1 \in \{10^{-6}, 10^{-3}, 10^{-1}\}$, $\lambda_2 = 0$, for Example 1 when there is $p = 1\%$ noise in the data (4.5).

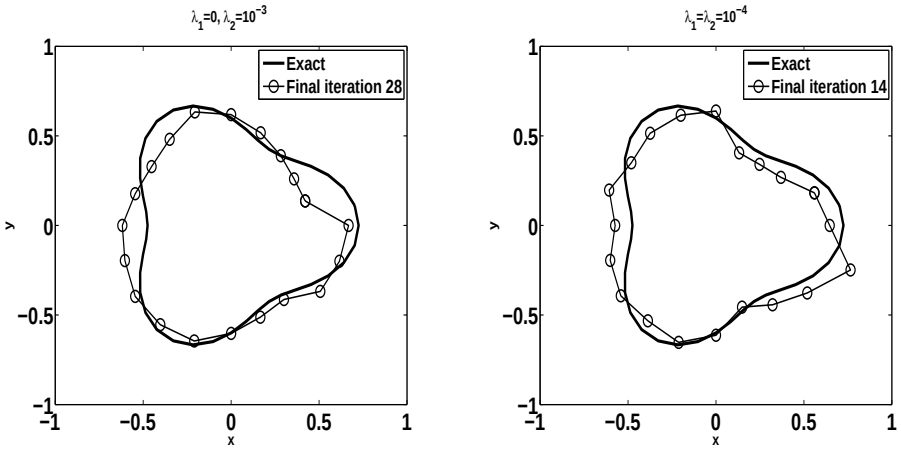

(a) (b)

Figure 5.6: The reconstructed boundary for: (a) $\lambda_1 = 0$, $\lambda_2 = 10^{-3}$, and (b) $\lambda_1 = \lambda_2 = 10^{-4}$, for Example 1 when there is $p = 1\%$ noise in the data (4.5).

5.4.2 Example $1'$ ($\alpha = 10$)

In this related example we change the heat transfer coefficient α from 0 to a large value such as 10 in order to mimic a rigid inclusion, i.e. as $\alpha \to \infty$ the Robin condition (5.2) recasts as the homogeneous Dirichlet boundary condition $u = 0$. Note that, although from Theorem 1 we know that for $\alpha = \infty$ the solution of the inverse problem is unique, from the counterexample presented in Appendix A, the

solution of the inverse problem with $\alpha \in (0, \infty)$ may not be unique.

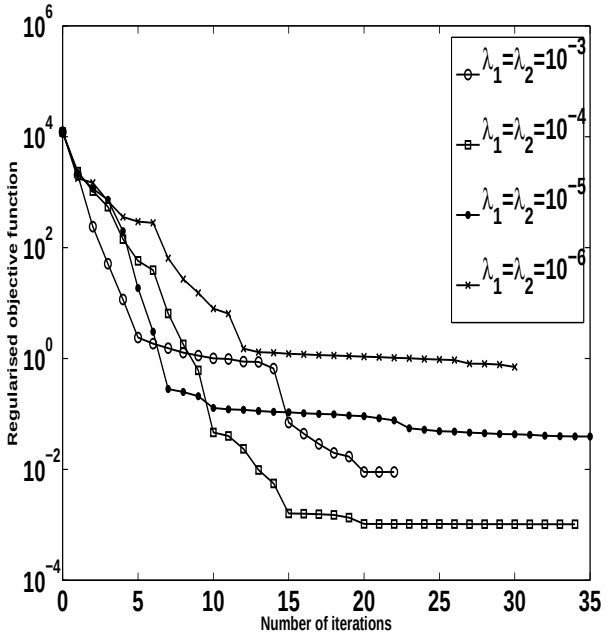

Figure 5.7: The regularised objective function (5.4) for $\lambda_1 = \lambda_2 \in \{10^{-k} | \ k = \overline{3,6}\}$, as a function of the number of iterations, for Example $1^{'}$ when there is no noise in the data (4.5).

Figure 5.7 shows the objective function (5.4) obtained with $\lambda_1 = \lambda_2 \in \{10^{-k} | \ k = \overline{3,6}\}$, as a function of the number of iterations. The exact shape (5.6) and the reconstructed shape obtained, when there is no noise in the input data (4.5), are presented in Figure 5.8. From Figure 5.8 it can be seen that there is some improvement in the numerically reconstructed shape which is stable and accurate for $\lambda_1 = \lambda_2 = 10^{-4}$ in comparison with Figure 5.3(b).

When $p = 1\%$ noise is added to the input data (4.5), Figure 5.9 shows the regularised objective function for various values of $\lambda_1 = \lambda_2 \in \{10^{-k} | \ k = \overline{3,6}\}$, whilst Figure 5.10 shows the corresponding reconstructed shapes. From these plots it can be seen that there is improvement in the numerical results, particularly for $\lambda_1 = \lambda_2 = 10^{-4}$ comparing to Figures 5.5 and 5.6.

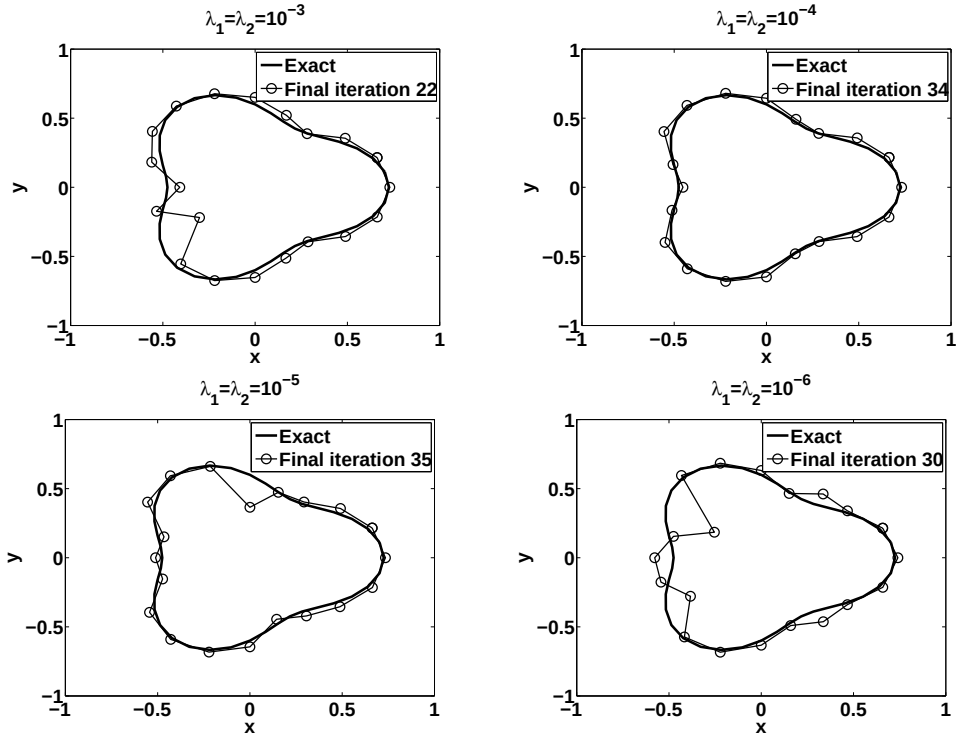

Figure 5.8: The reconstructed boundary for $\lambda_1 = \lambda_2 \in \{10^{-k} | \ k = \overline{3,6}\}$, for Example $1^{'}$ when there is no noise in the data (4.5).

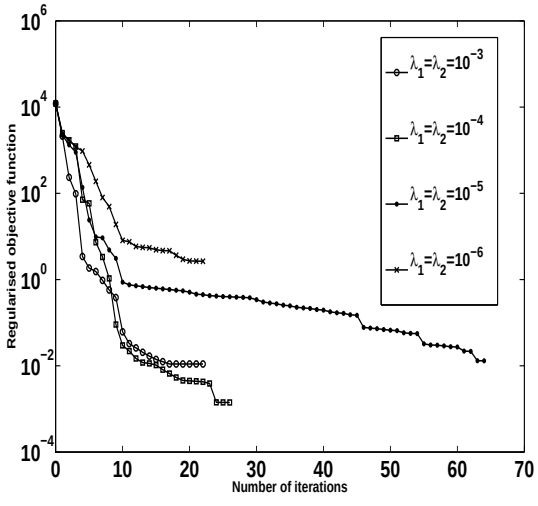

Figure 5.9: The regularised objective function (5.3) for $\lambda_1 = \lambda_2 \in \{10^{-k} | \ k = \overline{3,6}\}$, as a function of the number of iterations, for Example $1^{'}$ when there is $p = 1\%$ noise in the data (4.5).

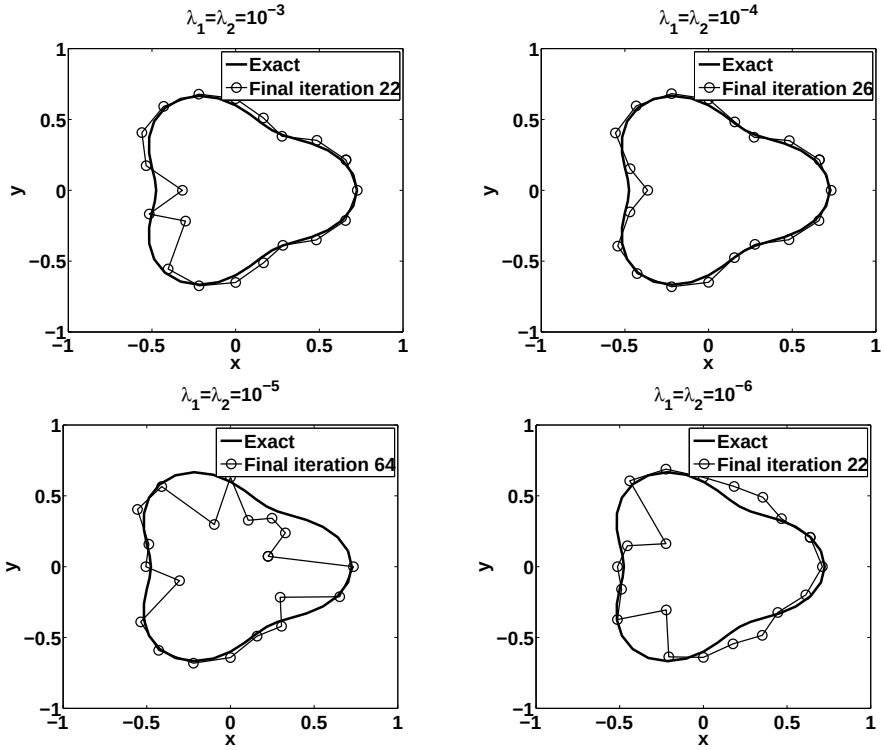

Figure 5.10: The reconstructed boundary for $\lambda_1 = \lambda_2 \in \{10^{-k} | \ k = \overline{3,6}\}$, for Example $1^{'}$ when there is $p = 1\%$ noise in the data (4.5).

5.4.3 Example 2

In this example, we consider reconstructing the same pear-shaped inner boundary given by expression (5.6) on which the homogeneous Robin boundary condition (5.2) applies with the positive heat transfer coefficient given by, see Serranho (2006),

$$\alpha(\theta) = 1.5 - \cos(\theta) + 0.5\sin(2\theta), \quad \theta \in [0, 2\pi). \tag{5.7}$$

We also take the same Dirichlet data (5.1) on $\partial\Omega = \partial B(\mathbf{0}, 1)$ given by (4.22). Figure 5.11 shows the objective function (5.4) obtained with $\lambda_1 = \lambda_2 \in \{10^{-k} | \ k = \overline{3,6}\}$, as a function of the number of iterations. In Figure 5.12, we present the exact shape (4.23) and the reconstructed shapes obtained when there is no noise in the input data (4.5). From Figure 5.12 it can be seen that the numerically reconstructed shapes are stable and reasonable accurate in comparison with the exact shape (5.6).

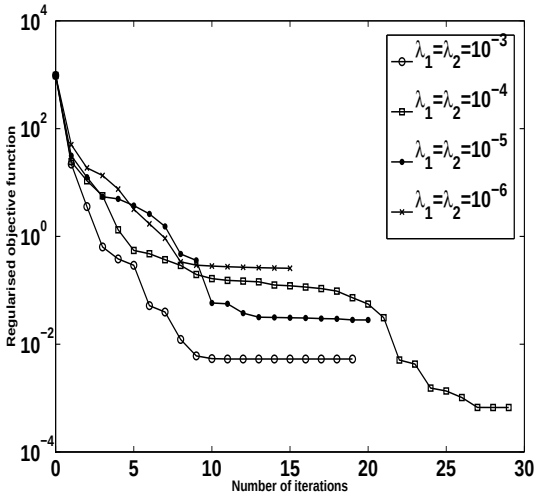

Figure 5.11: The regularised objective function (5.4) for $\lambda_1 = \lambda_2 \in \{10^{-k} | \ k = \overline{3,6}\}$, as a function of the number of iterations, for Example 2 when there is no noise in the data (4.5).

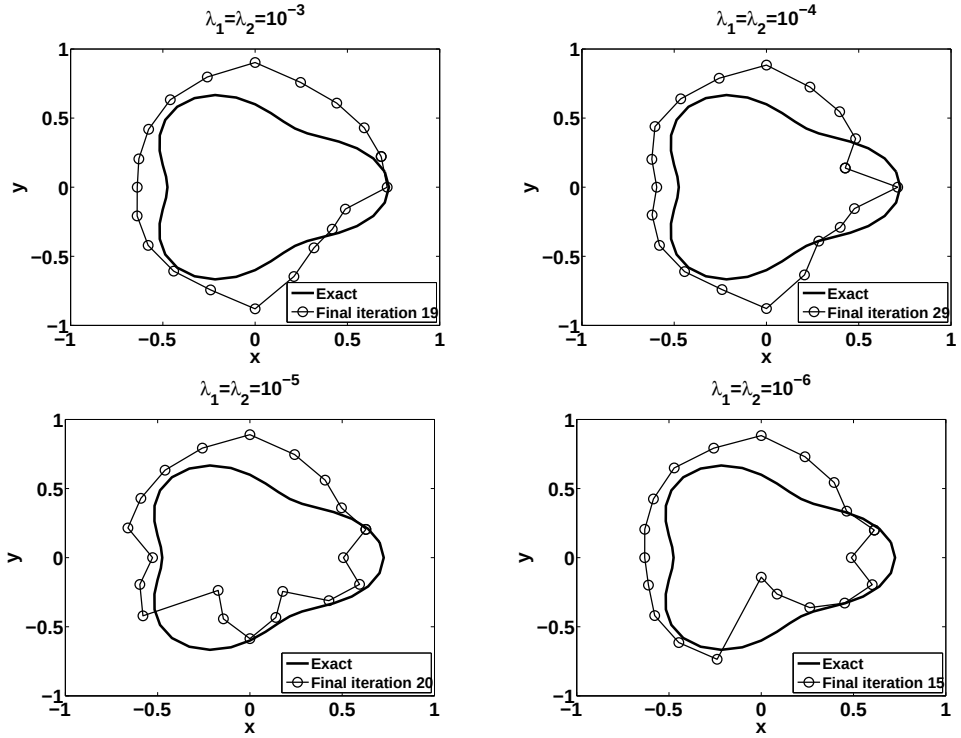

Figure 5.12: The reconstructed boundary for $\lambda_1 = \lambda_2 \in \{10^{-k} | \ k = \overline{3,6}\}$, for Example 2 when there is no noise in the data (4.5).

5.4.4 Example $2^{'}$.

Next, we change the Dirichlet data (4.22) on $\partial\Omega = \partial B(\mathbf{0}, 1)$ to

$$u(1, \theta) = f(\theta) = \sin(\theta), \quad \theta \in [0, 2\pi). \tag{5.8}$$

and reconsider Example 2. We shall call this Example $2^{'}$.

Figure 5.13 shows the objective function (5.4) with various regularisation parameters $\lambda_1 = \lambda_2 \in \{10^{-k} | \ k = \overline{3, 6}\}$, as a function of the number of iterations. The resulting shapes obtained for different values of the regularisation parameters $\lambda_1 = \lambda_2$ are presented in Figure 5.14. From these plots, it can be seen that reasonable results are obtained for $\lambda_1 = \lambda_2 = 10^{-4}$.

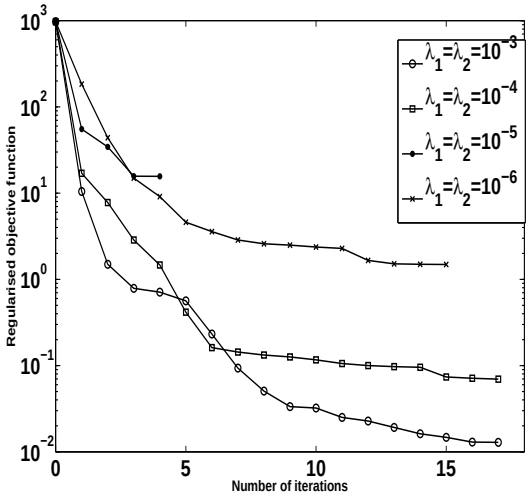

Figure 5.13: The regularised objective function (5.4) for $\lambda_1 = \lambda_2 \in \{10^{-k} | \ k = \overline{3, 6}\}$, as a function of the number of iterations, for Example $2^{'}$ when there is no noise in the data (4.5).

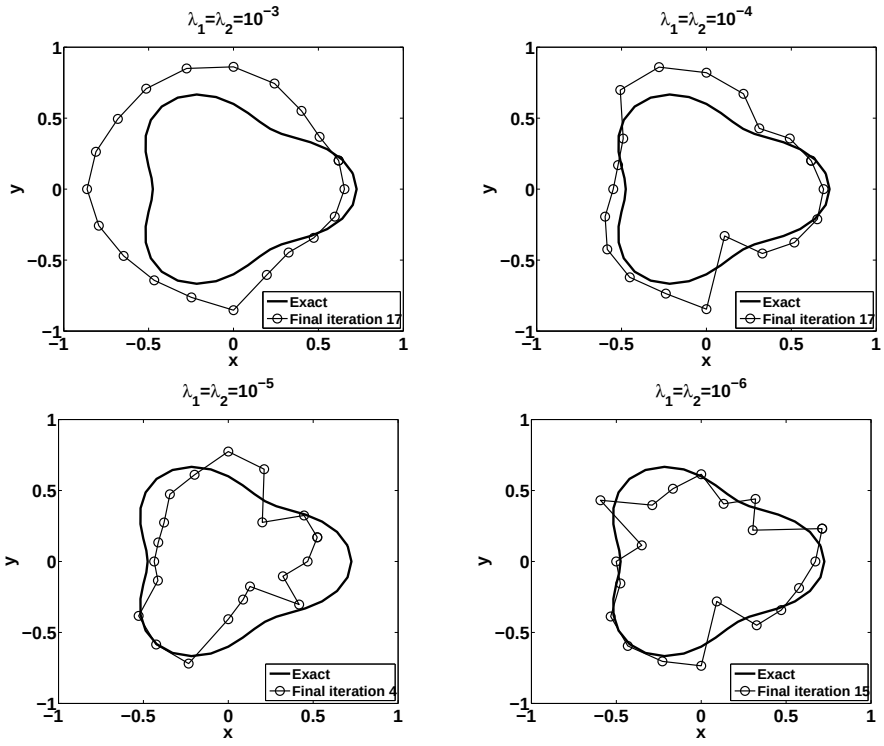

Figure 5.14: The reconstructed boundary for $\lambda_1 = \lambda_2 \in \{10^{-k} |\ k = \overline{3,6}\}$, for Example $2^{'}$ when there is no noise in the data (4.5).

5.4.5 Example $2^{''}$.

In the previous two Examples 2 and $2^{'}$, as given in the counterexample of Lesnic and Bin-Mohsin (2012), solution may not be unique since we are using a single set of data (4.22) or (5.8). This is one possible reason why the results of Figures 5.12 and 5.14 are inaccurate even for exact data. In order to ensure the uniqueness of solution we combine the Dirichlet data (4.22) and (5.6) on $\partial\Omega = \partial B(\mathbf{0}, 1)$ as

$$u_1(1,\theta) = f_1(\theta) = e^{-\cos^2(\theta)}, \quad u_2(1,\theta) = f_2(\theta) = \sin(\theta), \quad \theta \in [0, 2\pi). \tag{5.9}$$

These boundary temperature data are linearly independent and they induce the heat fluxes g_1 and g_2 via the operatorial relation (4.5).

Figure 5.15 shows the regularised objective function (5.5) with various values of $\lambda_1 = \lambda_2 \in \{10^{-k} |\ k = \overline{3,6}\}$, whilst Figure 5.16 shows the corresponding reconstructed shapes. From these plots it can be seen that there are improvements for $\lambda_1 = \lambda_2 \in \{10^{-4}, 10^{-3}\}$ when using more data compared to the single data inversion previously illustrated in Figures 5.12 and 5.14.

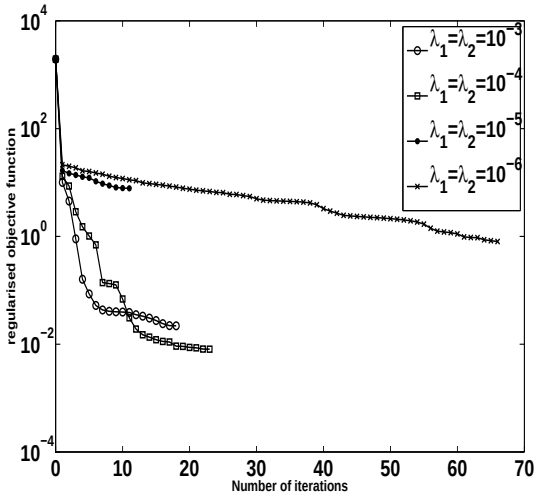

Figure 5.15: The regularised objective function for $\lambda_1 = \lambda_2 \in \{10^{-k} | \ k = \overline{3,6}\}$, as a function of the number of iterations, for Example $2''$ when there is no noise in the data (4.5).

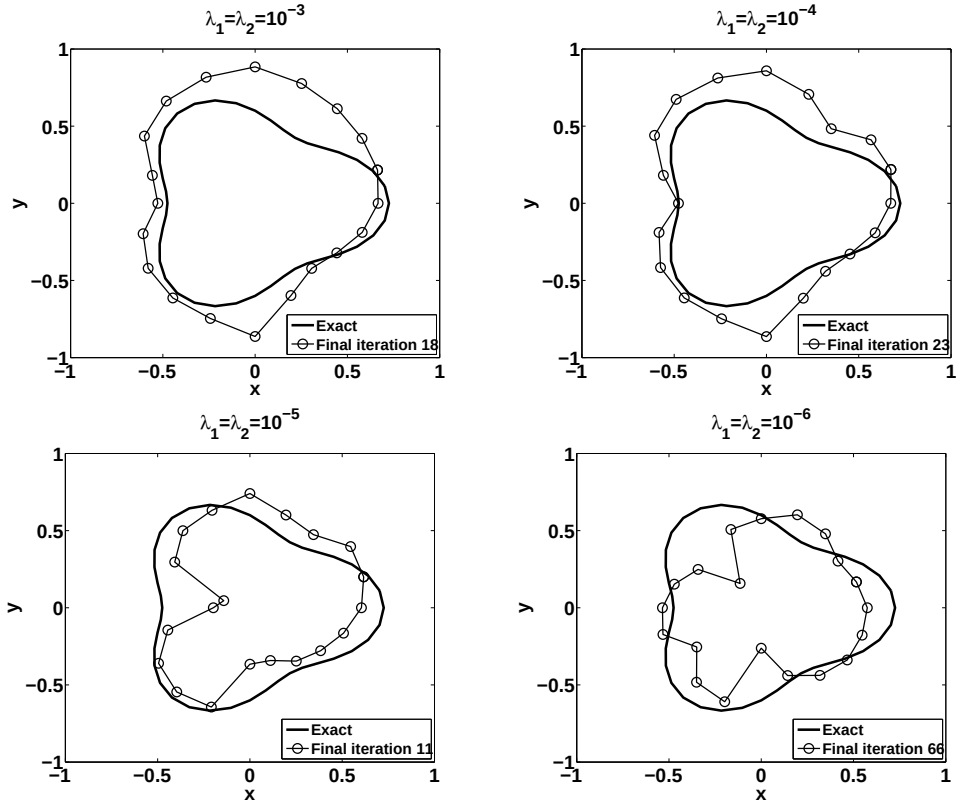

Figure 5.16: The reconstructed boundary for $\lambda_1 = \lambda_2 \in \{10^{-k} | \ k = \overline{3,6}\}$, for Example $2''$ when there is no noise in the data (4.5).

5.4.6 Example 3

We finally consider the case when both ∂D and α are unknown. In this case, two linearly independent Dirichlet data (5.1), with at least one of them positive, ensure a unique solution for the pair $(\partial D, \alpha)$, see Pagani and Pierotti (2009) and Isakov (2009). As in Example $2''$, the two Dirichlet data (5.9) on $\partial\Omega = \partial B(\mathbf{0}; 1)$ are considered. Since now the heat transfer coefficient α is also unknown, i.e. the functional T appearing in the left-hand side of (5.5) also depends on α, as $T(\underline{a}^{(1)}, \underline{a}^{(2)}, \underline{r}, \underline{\alpha})$, we add to it yet another regularisation term $\lambda_3 \|\underline{\alpha}\|^2$. As expected, the numerical results cannot be better than those from Figure 5.16, because we use the same two pieces of information, but there are more unknowns in Example 3 than in Example $2''$.

Figure 5.17 shows the reconstructed shapes for various regularisation parameters λ_1, λ_2 and λ_3, whilst Figure 5.18 shows the correspondingly retrieved heat transfer coefficient α. From Figure 5.17 it can be seen that reasonable stable results are achieved although the accuracy is rather limited. Furthermore, from Figure 5.18 it can be seen that the inclusion of regularisation for α, i.e. $\lambda_3 > 0$, improves the stability and accuracy of the numerical results.

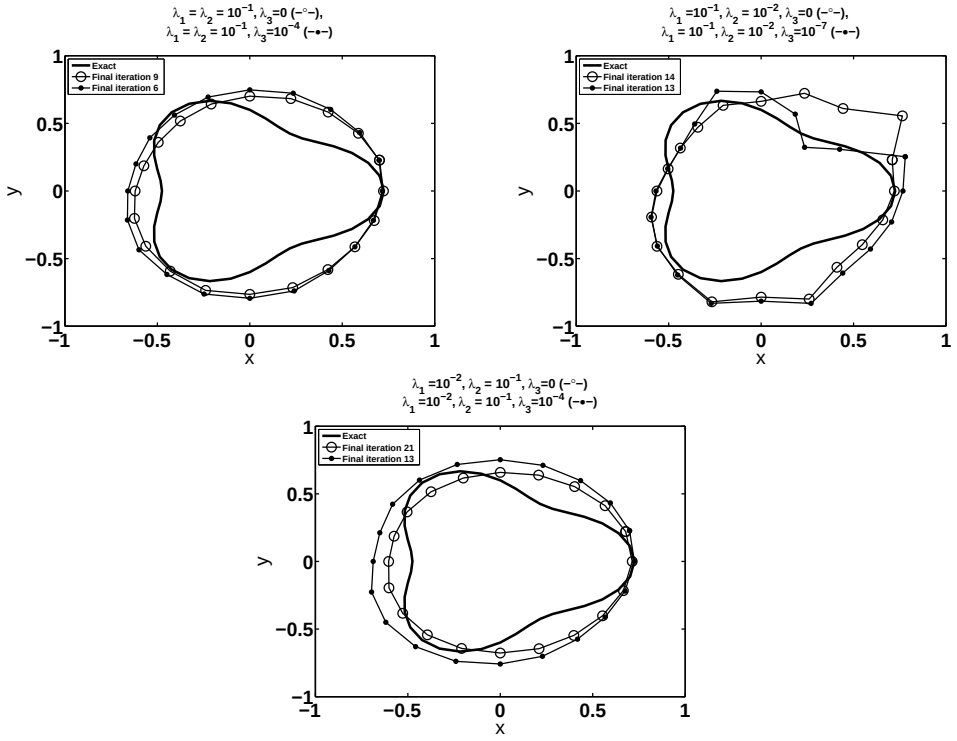

Figure 5.17: The reconstructed boundary for various regularisation parameters, for Example 3 when there is no noise in the data (4.5).

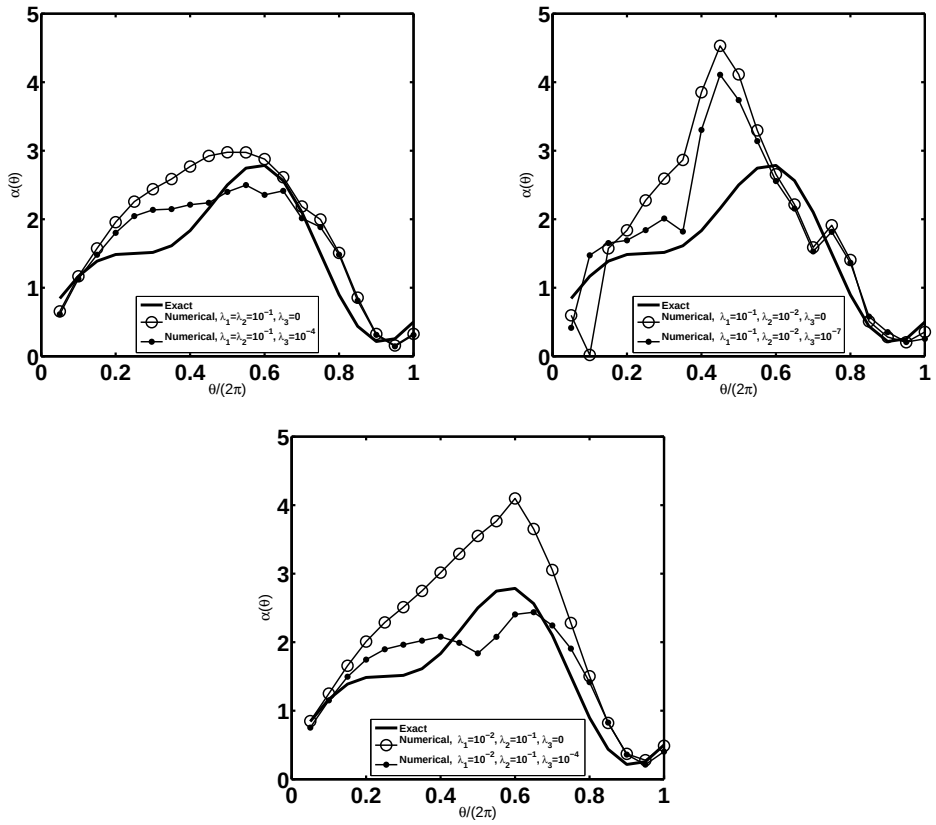

Figure 5.18: The numerical and exact solutions for α obtained with various regularisation parameters, for Example 3 when there is no noise in the data (4.5).

5.5 Conclusions

In this chapter, the modified Helmholtz inverse geometric problem, which consists of determining an unknown inner boundary and its surface heat transfer coefficient in an annular domain from one or two linearly independent pairs of outer boundary Cauchy data, has been investigated by the MFS. Further, regularization terms were added in order to obtain stable and accurate numerical results. Of course, one possible disadvantage of the formulation is the introduction of these additional regularisation parameters. The choice of one single parameter is already highly non-trivial, and the choice of two or three parameters can be very expensive and difficult to justify. Other than by trial and error, as it has been performed in our preliminary investigation, one could employ the concept of the L-(hyper) surface criterion, see Belge *et al.* (2002), but this is deferred to a future study.

The numerical results show satisfactory reconstructions for the homogeneous Robin condition ($\alpha = 0$, $\alpha = 10$ and $\alpha(\theta)$) with reasonable stability against noisy data. Although overall from the figures illustrated in Section 5.4 the accuracy of the

numerical results seems rather limited, we believe that more accurate results can be obtained if one uses more sophisticated NAG routines which allow for simple bounds on the variables to be imposed directly. This, however, would require the gradient to be supplied by the user, and this computational implementation is deferred to a future work.

In the next chapter, we allow for the defect D to occur at the boundary $\partial\Omega$.

Chapter 6

Identification of a corroded boundary and its Robin coefficient

6.1 Introduction

Inverse geometric problems arise in analysing various imaging and tomography techniques such as electrical impedance tomography (EIT), gamma ray emission tomography (GRET), magneto-resonance imaging (MRI), etc. In this chapter, we consider the application of the MFS to solving numerically the inverse geometric problem which consists of determining an unknown part of the boundary $\Gamma_2 \subset \partial\Omega$ assuming that the dependent variable u satisfies the Helmholtz (or the modified Helmholtz) equation in a simply-connected bounded domain $\Omega \subset \mathbb{R}^2$, namely

$$\nabla^2 u \pm k^2 u = 0 \qquad \text{in } \Omega, \tag{6.1}$$

where $k > 0$, from the knowledge of the Dirichlet boundary data $u|_{\Gamma_1}$ and the Neumann flux data $\partial u/\partial n$, i.e. Cauchy data, on the known part of the boundary $\Gamma_1 = \partial\Omega \setminus \Gamma_2$, together with a boundary condition (Dirichlet, Neumann or Robin) on the unknown part of the boundary Γ_2. Equation (6.1) with minus sign is the modified Helmholtz equation and it models the heat conduction in a fin, whilst equation (6.1) with plus sign is the Helmholtz equation and it models the wave propagation in acoustics.

The inverse, nonlinear and ill-posed problem of determining the unknown (inaccessible) corroded portion of the boundary Γ_2 and possibly its surface heat transfer coefficient, if a Robin condition is prescribed on Γ_2, is approached using a regularised minimisation procedure which employs an MFS solver at each iteration. This study is general and builds upon the previous recent applications of the MFS to solving similar boundary determination corrosion problems in Marin (2009); Marin et al.

(2011); Marin and Munteanu (2010); Mera and Lesnic (2005); Yang et al. (2009) for the isotropic, anisotropic and functionally graded Laplace equation, in Marin and Karageorghis (2009) for Helmholtz-type equations, in Zeb et al. (2008) for the biharmonic equation, in Marin (2010a) for the Lamé system in elasticity, and in Hon and Li (2008) for the heat equation. For more details about the MFS, as applied to inverse problems in general, see the recent review by Karageorghis et al. (2011). We finally mention that there also exists an extensive literature on using the BEM instead of the MFS for the corrosion boundary identification, see e.g. Lesnic et al. (2002) for the Laplace equation in EIT, Marin and Lesnic (2003) for the Lamé system in elasticity, and Marin (2006) for Helmholtz-type equations.

The outline of this chapter is as follows. In section 6.2 we introduce and discuss the mathematical formulation, whilst in section 6.3 we present the MFS for the Helmholtz-type equations. In section 6.4 we present and discuss the numerically obtained results for several test examples. In section 6.5 we give some conclusions and possible future work.

6.2 Mathematical formulation

We consider that the solution domain Ω is a simply-connected bounded by a smooth or a piecewise smooth curve $\partial\Omega$, such that $\partial\Omega = \Gamma_1 \cup \Gamma_2$, $\Gamma_1 \cap \Gamma_2 = \emptyset$, and Γ_1 and Γ_2 are of positive measure. The function u satisfies the Helmholtz (or the modified Helmholtz) equation (6.1) subject to the boundary conditions

$$u = f \qquad \text{on} \quad \Gamma_1, \tag{6.2}$$

and

$$\frac{\partial u}{\partial n} + \alpha u = h \qquad \text{on} \quad \Gamma_2, \tag{6.3}$$

where $f \in H^{1/2}(\partial\Omega)$ non-constant and $h \in H^{-1/2}(\partial\Omega)$ are given functions, and $\alpha \in L^{\infty}(\Gamma_2)$ is the non-negative impedance (surface heat transfer) Robin coefficient. In equation (6.3), h is usually zero in which case (6.3) represents a homogeneous Robin boundary condition. In the case of the Helmholtz equation we also assume that k^2 is not an eigenvalue for the negative of the Laplacian $-\nabla^2$ in the domain Ω with the homogeneous form of the mixed boundary conditions (6.2) and (6.3) on $\partial\Omega$. It is well-known that the direct Robin problem given by equations (6.1)-(6.3) has a unique solution $u \in H^1(\Omega)$, when Γ_2 is known. We can then define a nonlinear operator $F_f(\Gamma_2)$, which maps the set of admissible Lipschitz boundaries Γ_2 to the

data space of Neumann flux data in $H^{-1/2}(\Gamma_1)$, as follows:

$$F_f(\Gamma_2) := \frac{\partial u}{\partial n}\Big|_{\Gamma_1} = g \in H^{-1/2}(\Gamma_1). \tag{6.4}$$

Then the inverse problem under consideration consists of extracting some information about the boundary Γ_2 from the data $g = F_f(\Gamma_2)$. The data (6.4) may also be only partial, i.e. the flux being measured on a non-zero measure portion $\Gamma \subset \Gamma_1$, instead of the whole boundary Γ_1. It is well-known that this inverse problem is nonlinear and ill-posed, as opposed to the direct problem which is linear and well-posed.

We briefly note that the situation regarding the uniqueness/non-uniqueness of solution is much more settled in the case of the inverse shape boundary determination of Γ_2 when α is known, see Cabib et al. (2011); Cakoni and Kress (2007); Cakoni et al. (2010a); Inglese and Mariani (2004); Isakov (2009), or in the case of the inverse impedance determination of α when Γ_2 is known, see Inglese (1997); Chaabane and Jaoua (1999); Ivanyshyn and Kress (2011). However, in corrosion problems it is not always physically realistic to assume that the boundary condition on the corroded boundary is known, in which situation the coefficient α in (6.3) together with the obstacle Γ_2 are to be simultaneously determined. Then, clearly one set of Cauchy boundary measurements (6.2) and (6.4) is not sufficient to simultaneously recover Γ_2 and α. However, it turns out that two linearly independent boundary data f_1 and f_2, one of which is positive, inducing, via (6.4), two corresponding flux measurements g_1 and g_2, are sufficient to provide a unique solution for the pair (Γ_2, α), see Pagani and Pierotti (2009); Rundell (2008); Bacchelli (2009). The stability issue has also been recently addressed in Sincich (2010).

We finally note that the case when Ω is a doubly-connected annular domain with outer boundary Γ_1 and inner unknown boundary Γ_2 has been investigated in Chapter 5.

Even when α is known, one set of Cauchy data (6.2) and (6.4) may not be enough to determine uniquely the corroded boundary Γ_2, as it can be seen from the following counterexample.

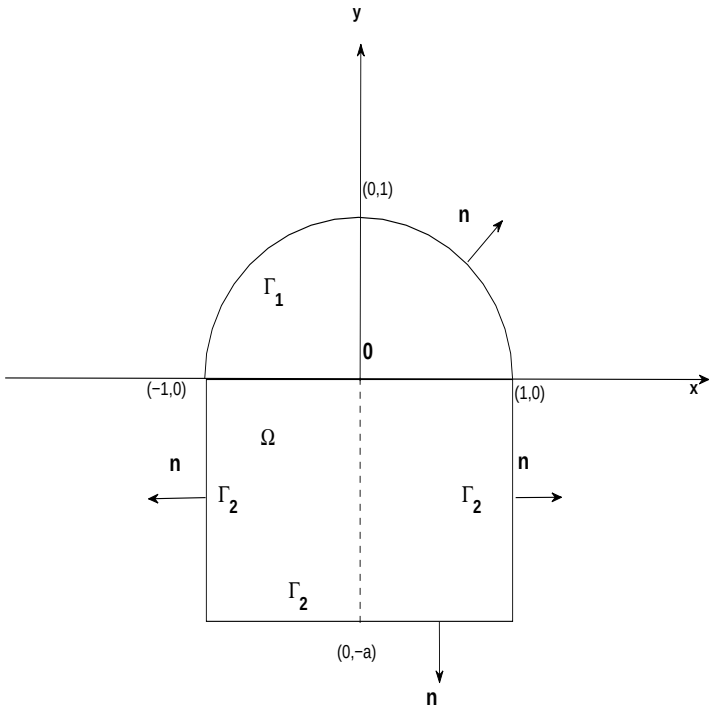

Figure 6.1: Geometry for the counterexample.

6.2.1 Counterexample

We follow the analysis of Cakoni and Kress (2007) for the Laplace equation, i.e. $k = 0$, and consider the geometrical configuration for the solution domain Ω sketched in Figure 6.1, where $a > 0$ is a constant parameter.

Let the solution domain be

$$\Omega = \{(x, y) \in \mathbb{R}^2 |\ x^2+y^2 < 1, y > 0\} \cup \{(x, y) \in \mathbb{R}^2 |\ x \in (-1, 1), y \in (-a, 0)\}, \quad (6.5)$$

consisting of a semicircle and a rectangle. Consider the following function

$$u(x, y) = \sqrt{2}e^{\gamma y} \sin\Big(\frac{\pi}{4}(\beta x + \beta + 1)\Big), \qquad (x, y) \in \Omega, \quad (6.6)$$

where β and γ are some constants to be prescribed.

(a) *The modified Helmholtz equation*
Consider first the case of the modified Helmholtz equation

$$\nabla^2 u - k^2 u = 0 \qquad \text{in } \Omega. \quad (6.7)$$

It can be seen that (6.6) satisfies the modified Helmholtz equation (6.7) if $\gamma^2 = k^2 + \frac{\beta^2\pi^2}{16}$. Let us try now to satisfy the homogeneous form of the Robin boundary condition (6.3) on Γ_2. On the left vertical boundary of Γ_2 we have $u(-1,y) = e^{\gamma y}$, $\frac{\partial u}{\partial n}(-1,y) = -\frac{\partial u}{\partial x}(-1,y) = -\frac{\pi\beta}{4}e^{\gamma y}$, $y \in (-a,0)$, and we can take

$$\alpha(-1,y) = \frac{\beta\pi}{4}, \qquad y \in (-a,0). \tag{6.8}$$

We can make this non-negative by requiring that $\beta \geq 0$. On the right vertical boundary of Γ_2 we have $u(1,y) = \sqrt{2}e^{\gamma y}\sin\left(\frac{\pi(2\beta+1)}{4}\right)$, $\frac{\partial u}{\partial n}(1,y) = \frac{\partial u}{\partial x}(1,y) = \frac{\pi\beta\sqrt{2}}{4}e^{\gamma y}\cos\left(\frac{\pi(2\beta+1)}{4}\right)$, $y \in (-a,0)$, and we can take

$$\alpha(1,y) = -\frac{\beta\pi}{4}\cot\left(\frac{\pi(2\beta+1)}{4}\right) = \frac{\beta\pi}{4}\tan\left(\frac{\pi(2\beta-1)}{4}\right), \qquad y \in (-a,0). \tag{6.9}$$

We can make this non-negative by requiring that

$$\beta \in \left[\frac{1}{2},\frac{3}{2}\right] \cup \left[\frac{5}{2},\frac{7}{2}\right]. \tag{6.10}$$

Finally, on the horizontal boundary of Γ_2 we have $u(x,-a) = \sqrt{2}e^{-a\gamma}\sin\left(\frac{\pi}{4}(\beta x + \beta + 1)\right)$, $\frac{\partial u}{\partial n}(x,-a) = -\frac{\partial u}{\partial y}(x,-a) = -\gamma\sqrt{2}e^{-a\gamma}\sin\left(\frac{\pi}{4}(\beta x+\beta+1)\right)$, $x \in (-1,1)$, and we can take

$$\alpha(x,-a) = \gamma, \qquad x \in (-1,1). \tag{6.11}$$

We can make this non-negative by taking

$$\gamma = \sqrt{k^2 + \frac{\beta^2\pi^2}{16}}. \tag{6.12}$$

To summarize, one can observe that by taking γ given by (6.12) and β in the intervals given in (6.10), we can satisfy the homogeneous form of the Robin boundary condition (6.3) on Γ_2, independent of the constant positive parameter a. In addition, the solution (6.6) does not depend on a and so it will be independent of the Cauchy data (6.2) and (6.4) on $\Gamma_1 = \{(x,y) \in \mathbb{R}^2 |\ x^2+y^2 = 1,\ y \geq 0\}$. In conclusion, $a > 0$ cannot be identified from equations (6.2)-(6.4) and (6.6) only, and therefore this is a counterexample to the uniqueness of solution.

We now perform a similar analysis for the Helmholtz equation.

(b) *The Helmholtz equation*
Consider now the case of the Helmholtz equation

$$\nabla^2 u + k^2 u = 0 \qquad \text{in } \Omega. \tag{6.13}$$

It can be seen that (6.6) satisfies the Helmholtz equation (6.13) if $\gamma^2 = \frac{\beta^2\pi^2}{16} - k^2$, and we immediately require that $\beta^2 \geq \frac{16k^2}{\pi^2}$.

On trying to satisfy the homogeneous form of the Robin boundary condition (6.3) on Γ_2, as before, one obtains $\alpha(-1, y) = \frac{\beta\pi}{4}$, $\alpha(1, y) = \frac{\beta\pi}{4} \tan\left(\frac{\pi(2\beta-1)}{4}\right)$, $y \in (-a, 0)$, $\alpha(x, -a) = \gamma$. If we take, for example, β to be an odd integer greater or equal than $4k/\pi$ and $\gamma = \sqrt{\frac{\beta^2\pi^2}{16} - k^2}$ then, $\alpha(1, y) = \frac{\beta\pi}{4}$ and we satisfy that $\alpha \geq 0$ everywhere on Γ_2. Again the non-uniqueness of solution follows because $a > 0$ cannot be determined.

6.3 The Method of Fundamental Solutions (MFS)

In the MFS for Helmholtz (or modified Helmholtz) elliptic equation, we can approximate the solution of equation (6.1) by a linear combination of fundamental solutions with respect to source points which are placed outside the solution domain, namely

$$u(\underline{X}) = \sum_{j=1}^{N} a_j G_{\pm}(\underline{X}, \underline{\xi}^j), \qquad \underline{X} \in \overline{\Omega}, \tag{6.14}$$

where the N vectors $(\underline{\xi}^j)_{j=\overline{1,N}}$ are distinct source points located outside the domain $\overline{\Omega}$, and $G_{\pm}$ is the fundamental solutions of Helmholtz (or modified Helmholtz) equation (6.1). The fundamental solutions of the Helmholtz and the modified Helmholtz in two-dimensions are given by

$$G_+(\underline{X}, \underline{Y}) = H_0^{(1)}(kr), \tag{6.15}$$

and

$$G_-(\underline{X}, \underline{Y}) = K_0(kr), \tag{6.16}$$

respectively, where for simplicity, the constants $\frac{i}{4}$ and $\frac{1}{2\pi}$, which do not appear in (6.15) and (6.16), respectively, have been embedded in the unknown coefficients $(a_j)_{j=\overline{1,N}}$ in (6.14). These coefficients are real for the modified Helmholtz equation and complex for the Helmholtz equation.

Assume for simplicity that $\Gamma_1 = \{(r, \theta) |\ r = 1,\ \theta \in [0, \pi]\}$ is the upper-half of

the unit circle. Consider

$$\underline{X}_i = (\cos(\tilde{\theta}_i), \sin(\tilde{\theta}_i)), \qquad i = \overline{1, M+1}, \tag{6.17}$$

to be boundary collocation points uniformly distributed on the known boundary Γ_1, where $\tilde{\theta}_i = \pi(i-1)/M$ for $i = \overline{1, M+1}$. Assume also that the corroded solution domain Ω is star-shaped with respect to the origin such that Γ_2 can be parametrised by

$$\Gamma_2 = \{(r(\theta)\cos(\theta), r(\theta)\sin(\theta))|\ \theta \in (\pi, 2\pi), r(\theta) > 0\}. \tag{6.18}$$

Consider

$$\underline{X}_i = (r_{i-M}\cos(\tilde{\theta}_i), r_{i-M}\sin(\tilde{\theta}_i)), \qquad i = \overline{M+2, 2M}, \tag{6.19}$$

to be boundary collocation points on the unknown boundary Γ_2, where $r_{i-M} = r(\tilde{\theta}_i)$ and $\tilde{\theta}_i = \pi(i-1)/M$ for $i = \overline{M+2, 2M}$. The source points $(\underline{\xi}^j)_{j=\overline{1,N}}$ in $\mathbb{R}^2 \setminus \overline{\Omega}$ are taken as

$$\underline{\xi}^j = (R\cos(\hat{\theta}_j), R\sin(\hat{\theta}_j)), \qquad j = \overline{1, N}, \tag{6.20}$$

where $R > 1$ and $\hat{\theta}_j = 2\pi(j-1)/N$ for $j = \overline{1, N}$. Typical distributions of the boundary collocation points (6.17) and (6.19), and of the source points (6.20) are schematically shown in Figure 6.2.

When α is known, the MFS coefficient vector $\underline{a} = (a_j)_{j=\overline{1,N}}$ and the radii vector $\underline{r} = (r_i)_{i=\overline{2,M}}$ characterising the star-shaped unknown boundary Γ_2 can be determined by imposing the boundary conditions (6.2)-(6.4) in a least-squares sense which recasts the problem into minimising the nonlinear objective function

$$T(\underline{a}, \underline{r}) := \left\| u - f \right\|^2_{L^2(\Gamma_1)} + \left\| \frac{\partial u}{\partial n} - g \right\|^2_{L^2(\Gamma_1)} + \left\| \left(\frac{\partial u}{\partial n} + \alpha u \right) - h \right\|^2_{L^2(\Gamma_2)} + \lambda_1 \|\underline{a}\|^2 + \lambda_2 \|\underline{r}'\|^2, \tag{6.21}$$

where $\lambda_1, \lambda_2 \geq 0$ are regularisation parameters which are introduced in order to stabilise the numerical solution. The last term in (6.21) contains a C^1-smoothing constraint on the sought shape Γ_2. Introducing the MFS approximation (6.14) into (6.21) yields

$$\begin{aligned} T(\underline{a}, \underline{r}) = \sum_{i=1}^{M+1} \left| \sum_{j=1}^{N} a_j G_{\pm}(\underline{X}_i, \underline{\xi}^j) - f(\underline{X}_i) \right|^2 + \sum_{i=M+2}^{2M+2} \left| \sum_{j=1}^{N} a_j \frac{\partial G_{\pm}}{\partial n}(\underline{X}_{i-M-1}, \underline{\xi}^j) \right. \\ \left. - g(\underline{X}_{i-M-1}) \right|^2 + \sum_{i=2M+3}^{3M+1} \left| \sum_{j=1}^{N} a_j \Big(\frac{\partial G_{\pm}}{\partial n}(\underline{X}_{i-M-1}, \underline{\xi}^j) + \alpha(\underline{X}_{i-M-1}) G_{\pm}(\underline{X}_{i-M-1}, \underline{\xi}^j) \Big) \right. \\ \left. - h(\underline{X}_{i-M-1}) \right|^2 + \lambda_1 \sum_{j=1}^{N} |a_j|^2 + \lambda_2 \sum_{j=2}^{M-1} (r_{j+1} - r_j)^2. \end{aligned} \tag{6.22}$$

In the real case, for the modified Helmholtz equation (6.7) the minimisation of (6.22) imposes $3M+1$ nonlinear equations in the $N+M-1$ unknowns $(\underline{a},\underline{r})$, and for a unique solution it is necessary that $2M \geq N-2$. In the complex case, for the Helmholtz equation (6.13) the minimisation of (6.22) imposes $6M+2$ nonlinear equations in the $2N+M-1$ unknowns $(\underline{a},\underline{r})$ and for a unique solution it is necessary that $5M \geq 2N-3$.

If there is noise in the measured data (6.4), we replace g in (6.22) by g^{ε}, namely,

$$g^{\epsilon}(\underline{X}_i) = g(\underline{X}_i) + \epsilon_i, \qquad i = \overline{1, M+1}, \tag{6.23}$$

where ϵ_i are random variables generated using the NAG routine D05DDF from a Gaussian normal distribution with mean zero and standard deviation

$$\sigma = p \times \max_{\Gamma_1} |g|, \tag{6.24}$$

where p represents the percentage of noise.

In equation (6.22), the normal derivatives of the fundamental solution $G_{\pm}$, via (6.15) and (6.16), are given by

$$\frac{\partial G_+}{\partial n}(\underline{X},\underline{\xi}) = -k\frac{(\underline{X}-\underline{\xi})\cdot\underline{n}}{\|\underline{X}-\underline{\xi}\|}H_1^{(1)}\Big(k\|\underline{X}-\underline{\xi}\|\Big), \tag{6.25}$$

and

$$\frac{\partial G_-}{\partial n}(\underline{X},\underline{\xi}) = -k\frac{(\underline{X}-\underline{\xi})\cdot\underline{n}}{\|\underline{X}-\underline{\xi}\|}K_1\Big(k\|\underline{X}-\underline{\xi}\|\Big), \tag{6.26}$$

and

$$\underline{n}(\underline{X}) = \begin{cases} \cos(\theta)\underline{i} + \sin(\theta)\underline{j}, & \text{if} \quad \underline{X} \in \Gamma_1, \\ \frac{1}{\sqrt{r^2(\theta)+r'^2(\theta)}}\Big[(r'(\theta)\sin(\theta) + r(\theta)\cos(\theta))\underline{i} + (-r'(\theta)\cos(\theta) \\ +r(\theta)\sin(\theta))\underline{j}\Big], & \text{if} \quad \underline{X} \in \Gamma_2, \end{cases} \tag{6.27}$$

where $\underline{i} = (1,0)$ and $\underline{j} = (0,1)$. In (6.27), the derivative r' is approximated using backward finite differences as

$$r'(\widetilde{\theta}_{i+M}) \approx \frac{r_i - r_{i-1}}{\pi/M}, \qquad i = \overline{2, M}, \tag{6.28}$$

with the convention that $r_1 = 1$.

The minimisation of the objective function (6.22) is accomplished computationally using the NAG routine E04FCF. If required, the constraints $r_i > 0$ for $i = \overline{2, M}$

can be imposed manually during the iterative procedure by adjustment at each iteration. The minimisation process usually terminates when either a user-specified tolerance is achieved, or when a user-specified maximum number of iterations is reached.

Finally, we observe that the form of the functional (6.21) contains a single measurement of the Neumann flux g for a prescribed Dirichlet boundary data f, via the relation (6.4). However, in some cases, one may need to use two measured fluxes g_1 and g_2 for two prescribed linearly independent boundary data f_1 and f_2, via the operatorial relation (6.4). This means that we double up the number of equations in (6.21) which now reads as

$$T(\underline{a}^{(1)}, \underline{a}^{(2)}, \underline{r}) := \left\| u_1 - f_1 \right\|^2_{L^2(\Gamma_1)} + \left\| u_2 - f_2 \right\|^2_{L^2(\Gamma_1)} + \left\| \frac{\partial u_1}{\partial n} - g_1 \right\|^2_{L^2(\Gamma_1)}$$
$$+ \left\| \frac{\partial u_2}{\partial n} - g_2 \right\|^2_{L^2(\Gamma_1)} + \left\| \left(\frac{\partial u_1}{\partial n} + \alpha u_1 \right) - h \right\|^2_{L^2(\Gamma_2)} + \left\| \left(\frac{\partial u_2}{\partial n} + \alpha u_2 \right) - h \right\|^2_{L^2(\Gamma_2)}$$
$$+ \lambda_1 \left(\|\underline{a}^{(1)}\|^2 + \|\underline{a}^{(2)}\|^2 \right) + \lambda_2 \|\underline{r}'\|^2, \quad (6.29)$$

where $\underline{a}^{(1)}$ and $\underline{a}^{(2)}$ are the corresponding unknown coefficients in the MFS expansion (6.14) for approximating the solutions of the inverse problems with the Dirichlet data f_1 and f_2, respectively.

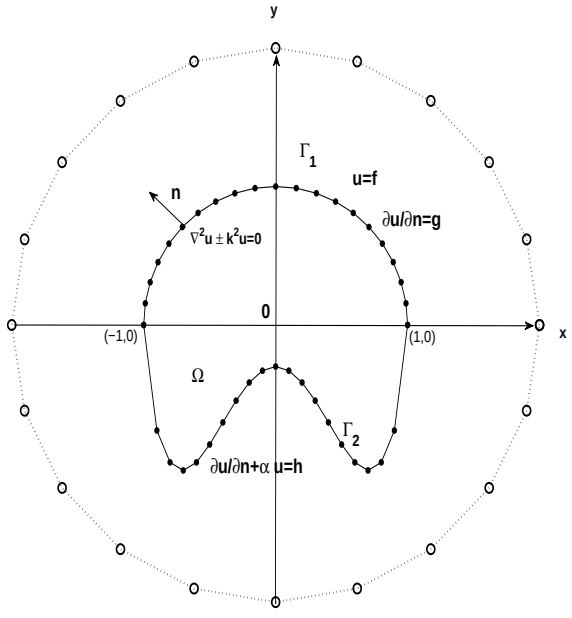

Figure 6.2: Typical distribution of source (∘) and boundary collocation (•) points.

6.4 Numerical results and discussion

In this section numerical results are presented for $R = 2$ for Examples 1 and 2, $R = 3$ for Examples 3–6, $2M = N = 28$ for Examples 1–5 and $2M = N = 40$ for Example 6. The use of higher MFS parameters M and N did not improve the accuracy of the numerical results, but it may become computationally expensive. Moreover, the initial guess for the vector $\underline{a}$ is $\underline{1.0}$ and the initial guess for the unknown part of the boundary Γ_2 is taken as the lower-half of the circle located at the origin with radius 0.5 for the first five examples and 1 for the sixth example. In all numerical experiments, as required by the NAG routine E04FCF used, the tolerance, XTol was set to 10^{-6}, and the maximum number of function evaluations, MAXCAL, was set to $400(N + M - 1)$ for the first four and final examples, and to $800(N + M - 1)$ for the fifth example. In all examples the corroded boundary Γ_2 is unknown. Also, in the first four and final examples the Robin coefficient α is known, whilst in the fifth example α is unknown. In comparison with the numerical MFS investigations concerning sound-soft (Dirichlet boundary condition applies on Γ_2) or sound-hard (Neumann boundary condition applies on Γ_2) boundary identification of Marin and Karageorghis (2009), the novelty of this section consists of solving different inverse problems to determine an unknown absorbing boundary Γ_2 on which the Robin boundary condition (6.3) applies. In addition, the Robin surface coefficient α can also be considered unknown, see Example 5. For the Helmholtz equation (6.13) the main difficulty for solving either the direct or inverse problem is in the case when k is large. Nevertheless, there are studies, see e.g. Chandler-Wilde et al. (2004), which deal with this high frequency case, but this issue will not be pursuit herein. Indeed, for simplicity, only numerical results for the modified Helmholtz equation (6.7) which is free of any such difficulty for large wavenumbers are illustrated.

6.4.1 Example 1

Consider the unit disk domain $\Omega = \{(x, y) \in \mathbb{R}^2 |\ x^2 + y^2 < r = 1\}$, whose boundary is divided into two parts, namely

$$\Gamma_1 = \{(x, y) \in \mathbb{R}^2 |\ x = \cos(\theta);\ y = \sin(\theta);\ \theta \in [0, \pi]\}, \tag{6.30}$$

and

$$\Gamma_2 = \{(x, y) \in \mathbb{R}^2 |\ x = r(\theta)\cos(\theta);\ y = r(\theta)\sin(\theta);\ \theta \in (\pi, 2\pi), r(\theta) = 1\}. \tag{6.31}$$

We take the Dirichlet data (6.2) on Γ_1 given by

$$u(1,\theta) = f(\theta) = e^{\cos(\theta)+\sin(\theta)}, \qquad \theta \in [0,\pi], \tag{6.32}$$

the Neumann data (6.4) on Γ_1 given by

$$\frac{\partial u}{\partial n}(1,\theta) = g(\theta) = (\cos(\theta)+\sin(\theta))e^{\cos(\theta)+\sin(\theta)}, \qquad \theta \in [0,\pi], \tag{6.33}$$

and the inhomogeneous Robin boundary condition (6.3) on Γ_2, given by

$$\frac{\partial u}{\partial n}(r(\theta),\theta) + \alpha(\theta)u(r(\theta),\theta) = h(\theta) = (\cos(\theta)+\sin(\theta)+\alpha(\theta))e^{\cos(\theta)+\sin(\theta)}, \quad \theta \in (\pi, 2\pi), \tag{6.34}$$

where $\alpha(\theta)$ is a given non-negative function.

In this example, assuming that α is known, the analytical solution for the modified Helmholtz equation (6.7) for $k = \sqrt{2}$ satisfying (6.32)-(6.34) is given by

$$u(x,y) = e^{x+y}, \qquad (x,y) \in \overline{\Omega}, \tag{6.35}$$

and Γ_2 given by expression (6.31)

6.4.2 Example 2

Also consider a more complicated geometric shape whose boundary is divided into two parts, namely Γ_1 is the upper-half of the circle given by expression (6.30) and Γ_2 is the lower-half of a peanut shape parametrised by

$$\Gamma_2 = \Big\{(x,y) \in \mathbb{R}^2 |\ x = r(\theta)\cos(\theta);\ y = r(\theta)\sin(\theta);\ \theta \in (\pi, 2\pi), \\ r(\theta) = \sqrt{\cos^2(\theta) + \frac{1}{4}\sin^2(\theta)}\Big\}. \tag{6.36}$$

The Dirichlet data (6.2) on Γ_1 is given by (6.32), the Neumann data (6.4) on Γ_1 is given by (6.33) and the inhomogeneous Robin boundary condition on Γ_2 is given by

$$\frac{\partial u}{\partial n}(r(\theta),\theta) + \alpha(\theta)u(r(\theta),\theta) = h(\theta) = e^{r(\theta)(\cos(\theta)+\sin(\theta))}\Big(\alpha(\theta) + (1,1)\cdot \underline{n}(\theta)\Big), \quad \theta \in (\pi, 2\pi), \tag{6.37}$$

where $\underline{n}$ is given by the second branch of expression (6.27), $r(\theta)$ is given by (6.36) and $r'(\theta) = -3\sin(2\theta)/(8r(\theta))$. Assuming that α is known, the analytical solution for the modified Helmholtz equation (6.7) for $k = \sqrt{2}$ satisfying (6.32)-(6.33) and

(6.37) is given by (6.35) and Γ_2 is given by expression (6.36).

(a) Case I (Dirichlet boundary condition)

Consider first the case when the Dirichlet boundary condition applies on Γ_2. This means that the first term in equation (6.3) is ignored ($\frac{\partial u}{\partial n} = 0$ and we take $\alpha = 1$). Thus we consider the Dirichlet boundary condition on Γ_2 given by

$$u(1, \theta) = h(\theta) = e^{\cos(\theta)+sin(\theta)}, \qquad \theta \in (\pi, 2\pi). \tag{6.38}$$

No noise. Here, consider the case when there is no noise, i.e. $p = 0$, in the input flux data (6.33). Figures 6.3(a) and 6.4(a) show the objective function (6.22) without regularisation, i.e. $\lambda_1 = \lambda_2 = 0$, as a function of the number of iterations, for Examples 1 and 2, respectively. From these figures it can be seen that the objective function decreases rapidly to a very low stationary level of $\mathbf{O}(10^{-15})$ in about 26 and 31 iterations, respectively. The corresponding exact and reconstructed shapes of the boundary Γ_2 are presented in Figures 6.3(b) and 6.4(b). From these figures it can be clearly seen that the numerically reconstructed shapes are stable and accurate in comparison with the exact shapes (6.31) and (6.36).

Adding noise. Consider now the case when there is $p = \{1\%, 3\%, 5\%\}$ noise in the input flux data (6.33) added as in (6.23). Although not illustrated, it is reported that the numerical results obtained with no regularisation imposed in the nonlinear least-squares functional (6.22) were found unstable and highly inaccurate. This is to be expected since the inverse problem under investigation is ill-posed and therefore regularisation is needed in order to obtain stable solutions.

Figures 6.5 and 6.6 show the regularised objective function and the retrieved boundary Γ_2 obtained with the regularisation parameters $\lambda_1 = 10^{-5}, \lambda_2 = 10^{-1}$ for Example 1 and $\lambda_1 = \lambda_2 = 10^{-2}$ for Example 2. From the computational experiments, it is noted that if the regularisation parameters λ_1 and λ_2 are too small then oscillating unstable solutions are obtained. However, from Figures 6.5(b) and 6.6(b) it can be seen that reasonably stable numerical solutions can be obtained if the regularisation parameters λ_1 and λ_2 are properly tuned. In our work, we chose them based on trial and error though one can also try the L-surface framework proposed by Belge et al. (2002). From these figures it can also be seen that the numerical solutions become more accurate as the amount of noise p, included in the input data, decreases.

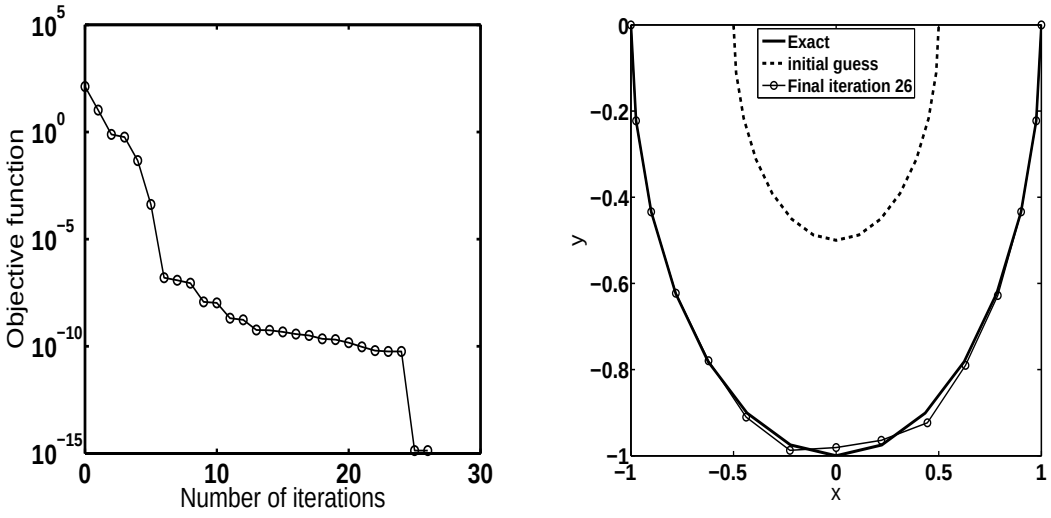

(a) (b)

Figure 6.3: (a) The objective function and (b) Initial guess, exact and numerically reconstructed shapes of the boundary Γ_2, for Example 1, *Case I*, when there is no noise in the data (6.33) and no regularisation.

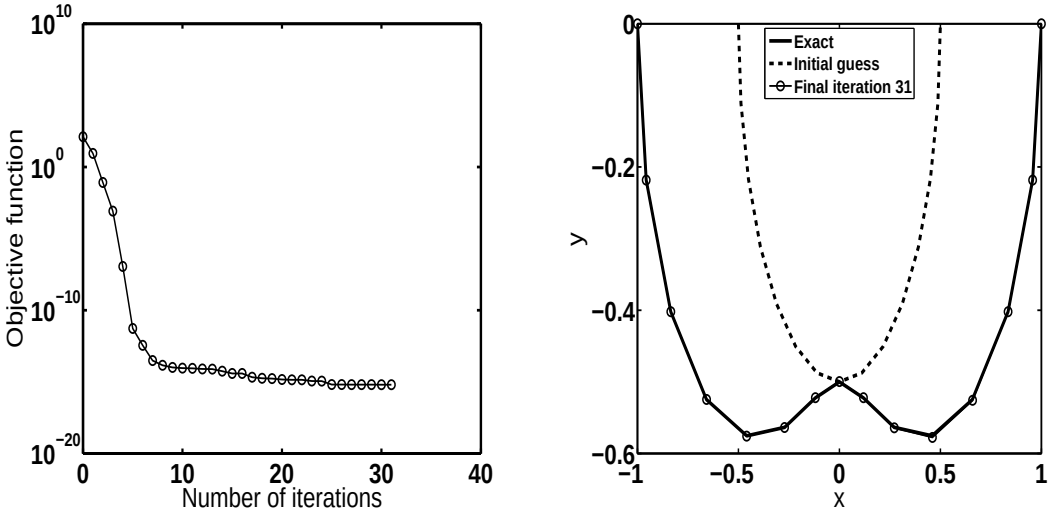

(a) (b)

Figure 6.4: (a) The objective function and (b) Initial guess, exact and numerically reconstructed shapes of the boundary Γ_2, for Example 2, *Case I*, when there is no noise in the data (6.33) and no regularisation.

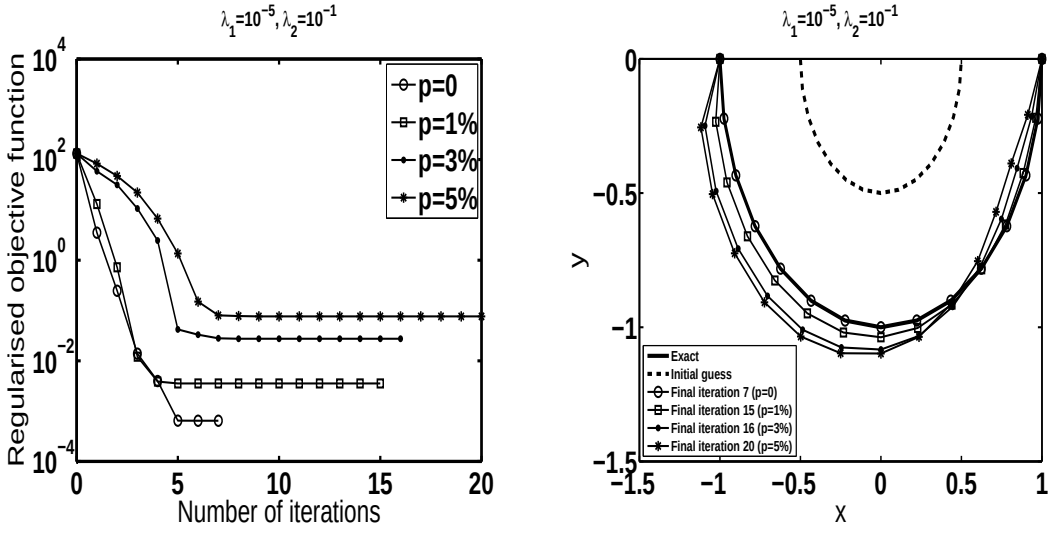

(a) (b)

Figure 6.5: (a) The regularised objective function and (b) Initial guess, exact and numerically reconstructed shapes of the boundary Γ_2, for Example 1, *Case I*, when there is $p = \{0, 1, 3, 5\}\%$ noise in the data (6.33) and $\lambda_1 = 10^{-5}, \lambda_2 = 10^{-1}$.

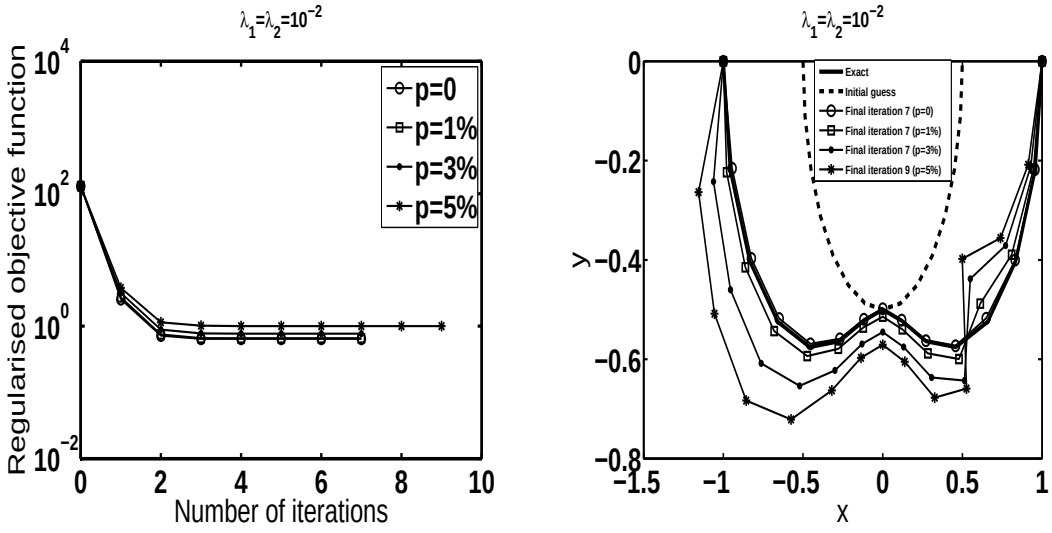

(a) (b)

Figure 6.6: (a) The regularised objective function and (b) Initial guess, exact and numerically reconstructed shapes of the boundary Γ_2, for Example 2, *Case I*, when there is $p = \{0, 1, 3, 5\}\%$ noise in the data (6.33) and $\lambda_1 = \lambda_2 = 10^{-2}$.

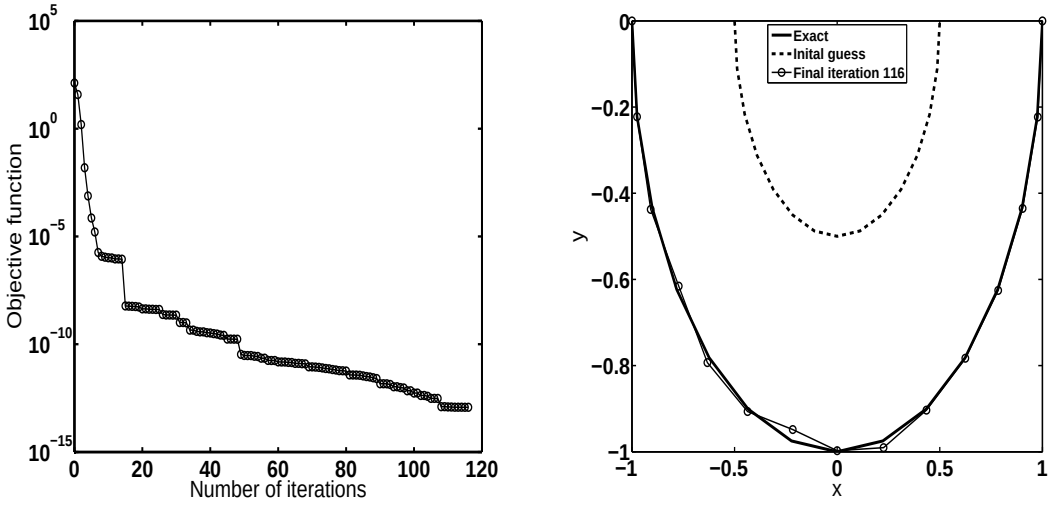

(a) (b)

Figure 6.7: (a) The objective function and (b) Initial guess, exact and numerically reconstructed shapes of the boundary Γ_2, for Example 1, *Case II*, when there is no noise in the data (6.33) and no regularisation.

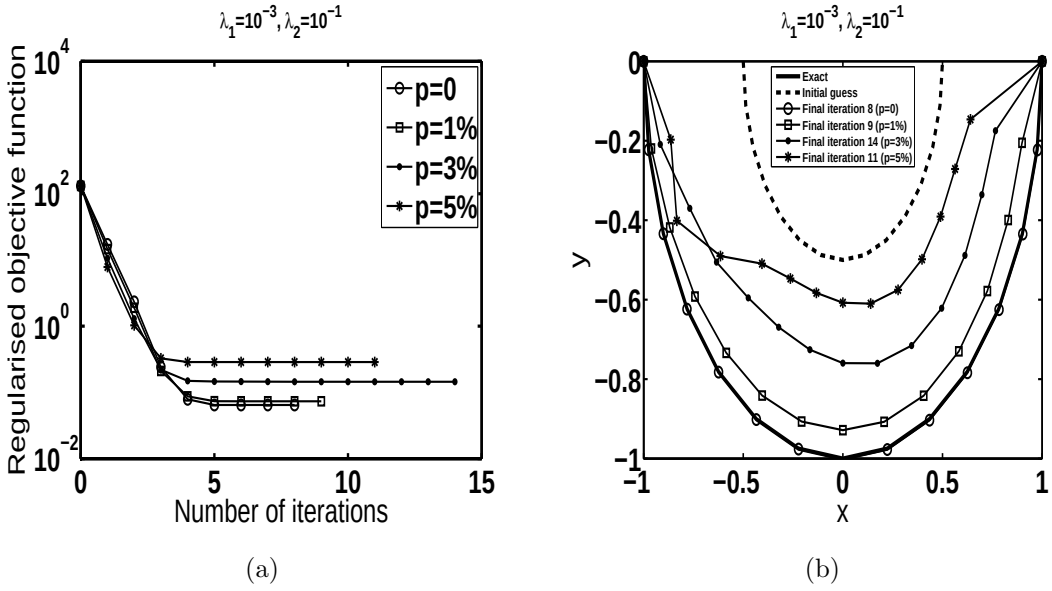

(a) (b)

Figure 6.8: (a) The regularised objective function and (b) Initial guess, exact and numerically reconstructed shapes of the boundary Γ_2, for Example 1, *Case II*, when there is $p = \{0, 1, 3, 5\}\%$ noise in the data (6.33) and $\lambda_1 = 10^{-3},\ \lambda_2 = 10^{-1}$.

(b) Case II (Neumann boundary condition)

We consider a second case when the Neumann boundary condition, i.e. $\alpha = 0$, applies on Γ_2, this means that the second term in equation (6.3) is ignored ($\alpha u = 0$).

Thus we consider the Neumann boundary condition on Γ_2 given by

$$\frac{\partial u}{\partial n}(1,\theta) = h(\theta) = \Big(\cos(\theta)+\sin(\theta)\Big)e^{\cos(\theta)+\sin(\theta)}, \qquad \theta \in (\pi, 2\pi). \tag{6.39}$$

The numerical results for Example 1 obtained for *Case II* illustrated in Figures 6.7 and 6.8 are similar to those obtained in Figures 6.3 and 6.5 for *Case I*. We finally report that the accuracy and stability numerical results presented in Figures 6.3-6.8 for the *Cases I* and *II* are similar to those obtained in Marin and Karageorghis (2009). However, in Marin and Karageorghis (2009) a different NAG routine was used and some of the computational details are different.

In the remaining of this section, the numerical investigation now departs from the analysis of Marin and Karageorghis (2009). For the sake of our preliminary investigation into an ill-posed problem which may lack the uniqueness of solution, see the discussion in Section 6.2, we consider next only the determination of the semicircular boundary (6.31). The retrieval of more complicated shapes such as the lower-half of the peanut shape (6.36) under the Robin boundary condition (6.3) is deferred to a future numerical investigation.

(c) Case III (Robin boundary condition)

Consider now the third case when the Robin boundary condition (6.34) with $\alpha = 1$ applies on Γ_2. Unlike the previous Dirichlet and Neumann *Cases I* and *II*, see Figures 6.3 and 6.7, Figure 6.9 shows that in the Robin *Case III* the numerical results appear unstable even for exact data, i.e.$p = 0$, if no regularisation is imposed on (6.22). In this case, a slight amount of regularisation is needed in order to obtain stable solutions and these stable and accurate numerical results are also illustrated in Figure 6.9. For noisy data, the numerical results obtained for *Case III* illustrated in Figure 6.10 are similar to those obtained in Figure 6.5 for *Case I* and in Figure 6.8 for *Case II*.

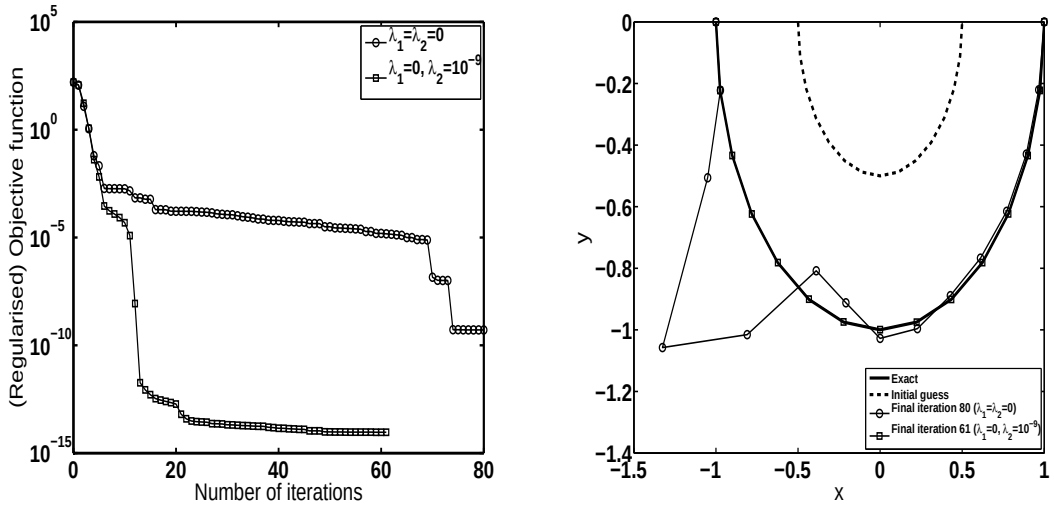

(a) (b)

Figure 6.9: (a) The objective and regularised objective functions and (b) Initial guess, exact and numerically reconstructed shapes of the boundary Γ_2, for Example 1, *Case III*, when there is no noise in the data (6.33), with regularisation $\lambda_1 = 0, \lambda_2 = 10^{-9}$, and without regularisation $\lambda_1 = \lambda_2 = 0$.

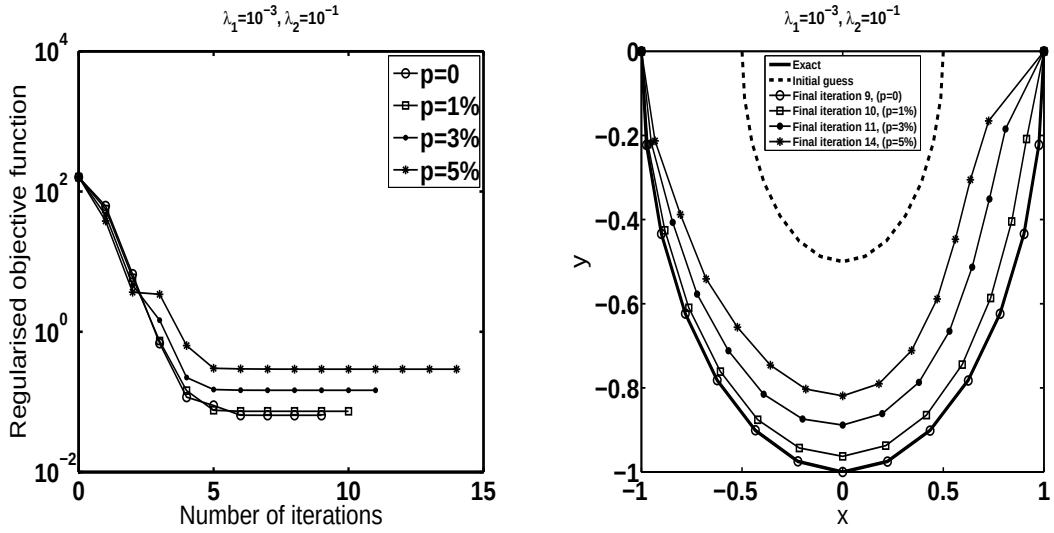

(a) (b)

Figure 6.10: (a) The regularised objective function and (b) Initial guess, exact and numerically reconstructed shapes of the boundary Γ_2, for Example 1, *Case III*, when there is $p = \{0, 1, 3, 5\}\%$ noise in the data (6.33) and $\lambda_1 = 10^{-3},\ \lambda_2 = 10^{-1}$.

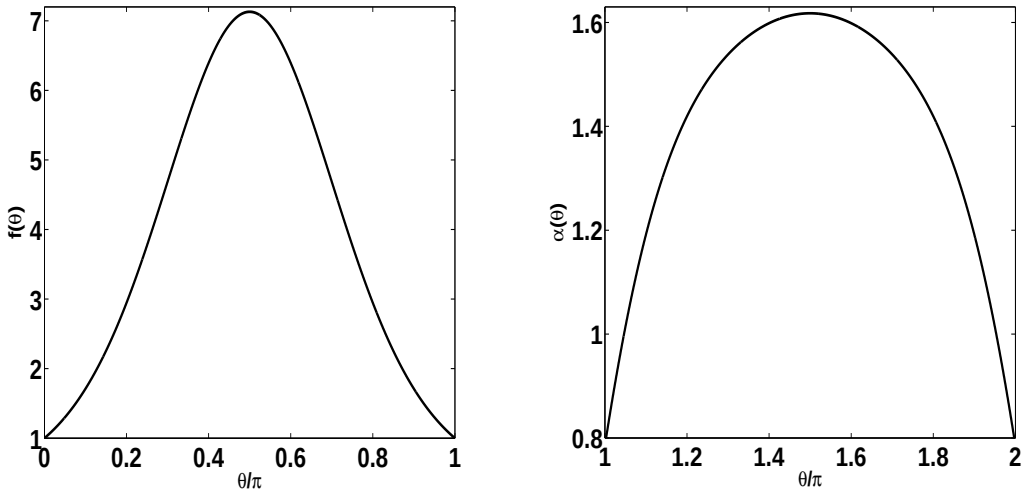

(a) (b)

Figure 6.11: (a) The Dirichlet boundary data (6.40) and (b) the Robin coefficient (6.43) for $\beta = 1$, $k = \sqrt{2}$, $\gamma = \sqrt{\frac{\pi^2}{16} + 2}$.

In the previous two examples we have considered non-homogeneous boundary conditions (6.34) or (6.37) on the unknown corroded boundary Γ_2.

In the next examples, we consider the more physical homogeneous Robin boundary condition, i.e. $h = 0$ in equation (6.3) on Γ_2.

6.4.3 Example 3

The unit disk domain $\Omega = B(\mathbf{0}; 1)$ is considered as in Example 1, and the boundary is divided into two parts as in (6.30) and (6.31). Take the Dirichlet data (6.2) on Γ_1 given by

$$u(1,\theta) = f(\theta) = \sqrt{2}e^{\gamma \sin(\theta)} \sin\Big(\frac{\pi}{4}(\beta\cos(\theta) + \beta + 1)\Big), \qquad \theta \in [0,\pi], \tag{6.40}$$

where $\gamma = \sqrt{\frac{\beta^2\pi^2}{16} + k^2}$ and the Neumann data (6.4) on Γ_1 given by

$$\frac{\partial u}{\partial n}(1,\theta) = \frac{\partial u}{\partial r}(1,\theta) = g(\theta) = \sqrt{2}e^{\gamma \sin(\theta)}\Big[\gamma \sin(\theta)\sin\Big(\frac{\pi}{4}(\beta\cos(\theta) + \beta + 1)\Big) + \frac{\beta\pi\cos(\theta)}{4}\cos\Big(\frac{\pi}{4}(\beta\cos(\theta) + \beta + 1)\Big)\Big], \qquad \theta \in [0,\pi]. \tag{6.41}$$

We also take homogeneous Robin boundary condition (6.3) on Γ_2, i.e. $h \equiv 0$, namely

$$\frac{\partial u}{\partial n}(1,\theta) + \alpha(\theta)u(1,\theta) = 0, \qquad \theta \in (\pi, 2\pi), \tag{6.42}$$

where α is the positive Robin coefficient given by

$$\alpha(\theta) = -\gamma \sin(\theta) - \frac{\beta\pi}{4} \cos(\theta) \cot\Big(\frac{\pi}{4}\Big(\beta\cos(\theta) + \beta + 1\Big)\Big), \qquad \theta \in (\pi, 2\pi). \quad (6.43)$$

Graphs of the Dirichlet data (6.40) and the Robin coefficient (6.43) for $\beta = 1$, $k = \sqrt{2}$, $\gamma = \sqrt{\frac{\pi^2}{16} + 2}$ are presented in Figures 6.11(a) and 6.11(b), respectively, showing that they are positive.

In this example, assuming that α is known and given by expression (6.43), the analytical solution for the modified Helmholtz equation (6.7) satisfying (6.40)-(6.43) is given by equation (6.6) and Γ_2 is given by expression (6.31). As in Example 1, the numerical results obtained using regularisation with and without noise in the input data (6.41) illustrated in Figures 6.12 and 6.13 show that the numerical solutions are accurate and stable.

For all the examples considered so far an analytical solution was available. In the next example such an analytical solution is not available.

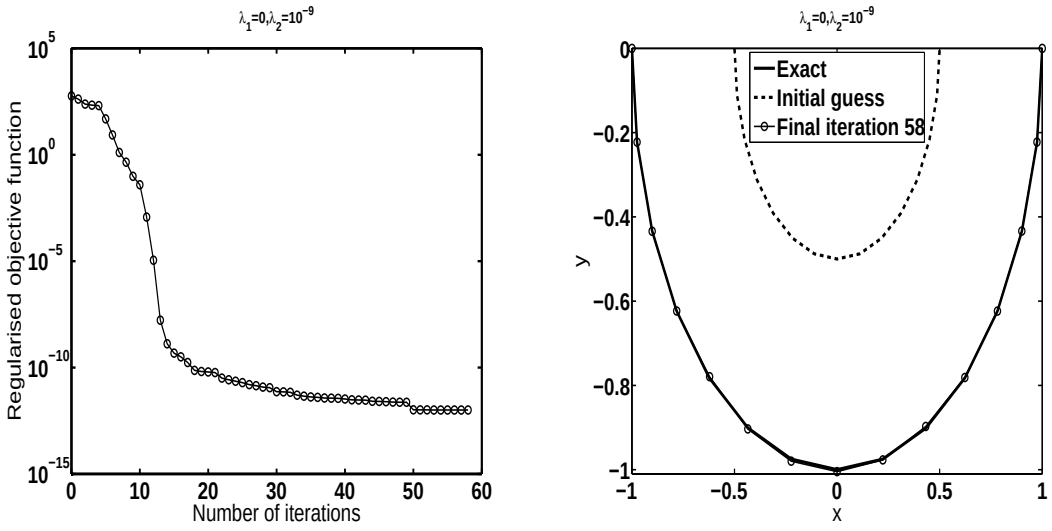

(a) (b)

Figure 6.12: (a) The regularised objective function and (b) Initial guess, exact and numerically reconstructed shapes of the boundary Γ_2, for Example 3, when there is no noise in the data (6.41) and $\lambda_1 = 0$, $\lambda_2 = 10^{-9}$.

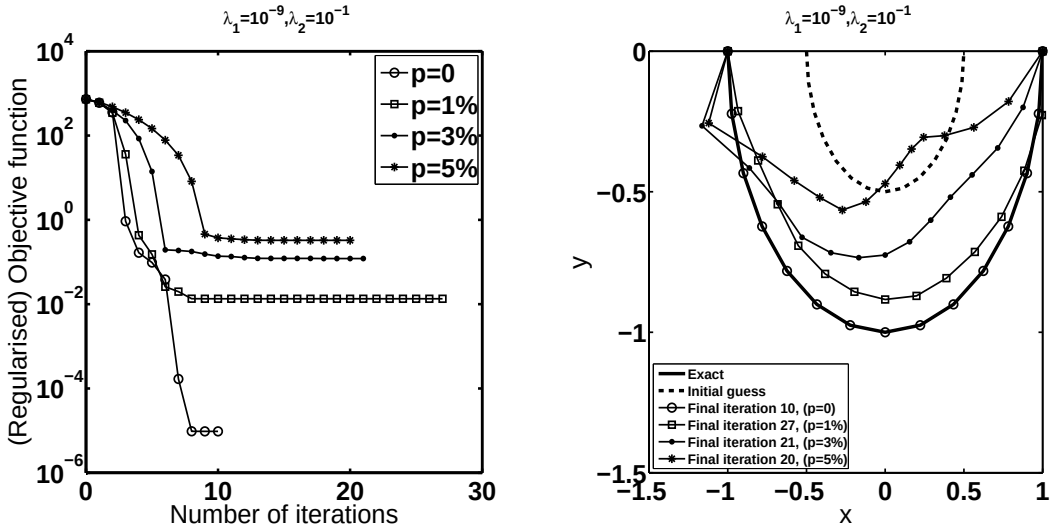

(a) (b)

Figure 6.13: (a) The regularised objective function and (b) Initial guess, exact and numerically reconstructed shapes of the boundary Γ_2, for Example 3 when there is $p = \{0, 1, 3, 5\}\%$ noise in the data (6.41) and $\lambda_1 = 10^{-9}, \lambda_2 = 10^{-1}$.

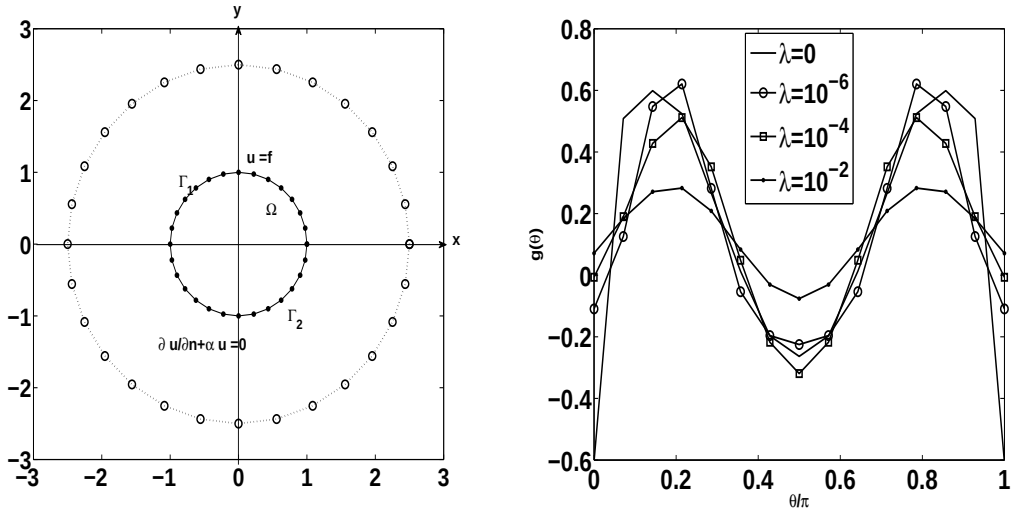

(a) (b)

Figure 6.14: (a) Distribution of source (∘) and boundary collocation (•) points, and (b) the numerical solutions for the normal derivative $g(\theta)$ obtained by solving the direct mixed problem with various regularisation parameters $\lambda \in \{0, 10^{-6}, 10^{-4}, 10^{-2}\}$, for Example 4.

6.4.4 Example 4

In this example, change the Dirichlet data (6.40) on Γ_1 to

$$u(1,\theta) = f(\theta) = \sin(\theta) - \sin^2(\theta), \qquad \theta \in [0,\pi], \tag{6.44}$$

and keep the same homogeneous Robin boundary condition (6.42) with the Robin coefficient given by (6.43), $\beta = 1$, $k = \sqrt{2}$, $\gamma = \sqrt{\frac{\pi^2}{16} + 2}$.

▶ Direct problem

Since in this case no analytical solution is available, the Neumann data (6.4) on Γ_1 is simulated numerically by solving, using the MFS, the direct mixed problem given by the modified Helmholtz equation (6.7), the homogeneous Robin boundary condition (6.42) on Γ_2, and the Dirichlet boundary condition (6.44) on Γ_1, when Γ_2 is known and given by the semicircle (6.31). The arrangement of the source and boundary collocation points are shown in Figure 6.14(a). The numerical solutions for the normal derivative $g(\theta) = \partial u/\partial n(1,\theta)$ on Γ_1, obtained with $R = 2.5$ for various regularisation parameters $\lambda \in \{0, 10^{-6}, 10^{-4}, 10^{-2}\}$ and $M = 14, N = 28$ are shown in Figure 6.14(b). The curve obtained for $\lambda = 10^{-4}$ in Figure 6.14(b) is chosen as the most accurate representation of the unavailable exact solution because, at least it satisfies the continuity of the flux at the end points $x = \pm 1$ where the Dirichlet and Robin boundary conditions meet. Indeed, from (6.44) we have that $u(1,0) = u(1,\pi) = 0$ and the homogeneous Robin condition (6.42) then also yields $\frac{\partial u}{\partial r}(1,0) = \frac{\partial u}{\partial r}(1,\pi) = 0$. Next, this curve corresponding to $\lambda = 10^{-4}$ in Figure 6.14(b) is used as input flux data (6.4) in the inverse problem.

▶ Inverse problem

Assuming now that Γ_2 is unknown, the inverse MFS is applied with a different R than 2.5, say $R = 3$, in order to avoid committing an inverse crime. The input Neumann data (6.4) is chosen out of the curve $\lambda = 10^{-4}$ of Figure 6.14(b), the Dirichlet data (6.3) is given by (6.44), and the homogeneous Robin boundary condition (6.42) on Γ_2 is considered.

The numerical results obtained using regularisation with and without noise in the input data, illustrated in Figure 6.15 show that the numerical solutions are accurate and stable even for a large amount of noise of up to $p = 20\%$.

The examples analysed so far considered the inverse problem in which the Robin coefficient α was assumed known. The next and final example considers the case when this coefficient is unknown.

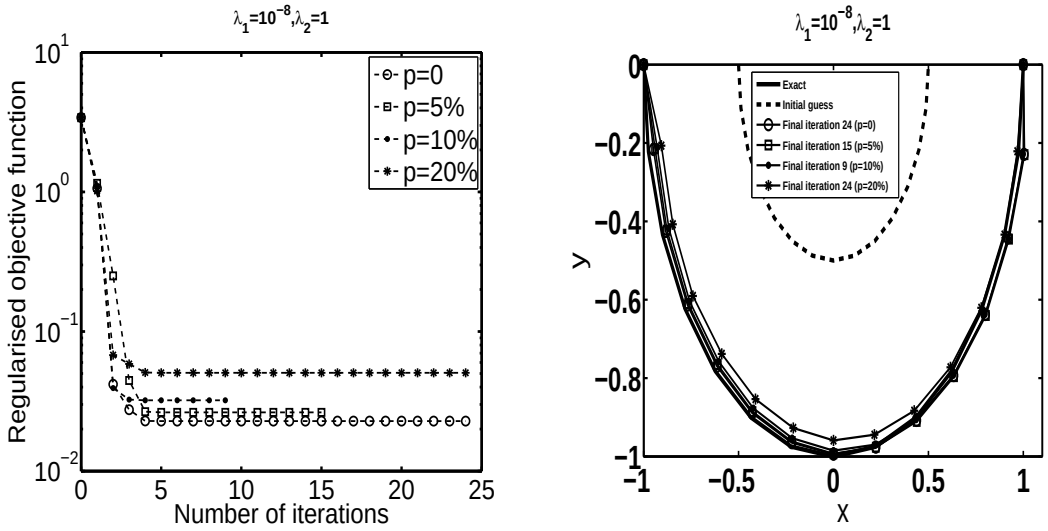

(a) (b)

Figure 6.15: (a) The regularised objective function and (b) Initial guess, exact and numerically reconstructed shapes of the boundary Γ_2, for Example 4, when there is $p = \{0, 5, 10, 20\}\%$ noise in the data (6.4) and $\lambda_1 = 10^{-8}, \lambda_2 = 1$.

6.4.5 Example 5

Assume now that both Γ_2 and α are unknown. The initial guess for the unknown Robin coefficient α is $\underline{0.1}$ for this and next examples. In order to ensure the uniqueness of solution we combine the Dirichlet data (6.40) and (6.44) on Γ_1 as

$$\begin{aligned} u_1(1,\theta) = f_1(\theta) = \sqrt{2}e^{\gamma\sin(\theta)}\sin\Big(\frac{\pi}{4}(\beta\cos(\theta)+\beta+1)\Big), \\ u_2(1,\theta) = f_2(\theta) = \sin(\theta) - \sin^2(\theta), \qquad \theta \in [0,\pi], \end{aligned} \tag{6.45}$$

with $k = \sqrt{2}$, $\beta = 1$, $\gamma = \sqrt{\frac{\pi^2}{16}+2}$. These Dirichlet boundary data are linearly independent with at least one of them positive, see Figure 6.11(a), and they induce the fluxes g_1 and g_2 via the operatorial relation (6.4). Since now the Robin coefficient α is also unknown, i.e. the functional T appearing in the left-hand side of (6.29) also depends on α, as $T(\underline{a}^{(1)}, \underline{a}^{(2)}, \underline{r}, \underline{\alpha})$, we add to it the zeroth-order regularisation term $\lambda_3\|\underline{\alpha}\|^2$ or, the first-order regularisation term $\lambda_3\|\underline{\alpha}'\|^2$. We also add noise in the flux g_2. The numerically obtained results for various amounts of noise are shown in Figures 6.16-6.18. From these figures it can be seen that the numerical solutions are stable with respect to the noise included in the input data. Moreover, the first-order regularisation in α improves the accuracy of the results over the zeroth-order regularisation. Finally, it can be remarked that the reconstruction of the Robin coefficient α is more difficult than the reconstruction of the corroded boundary Γ_2.

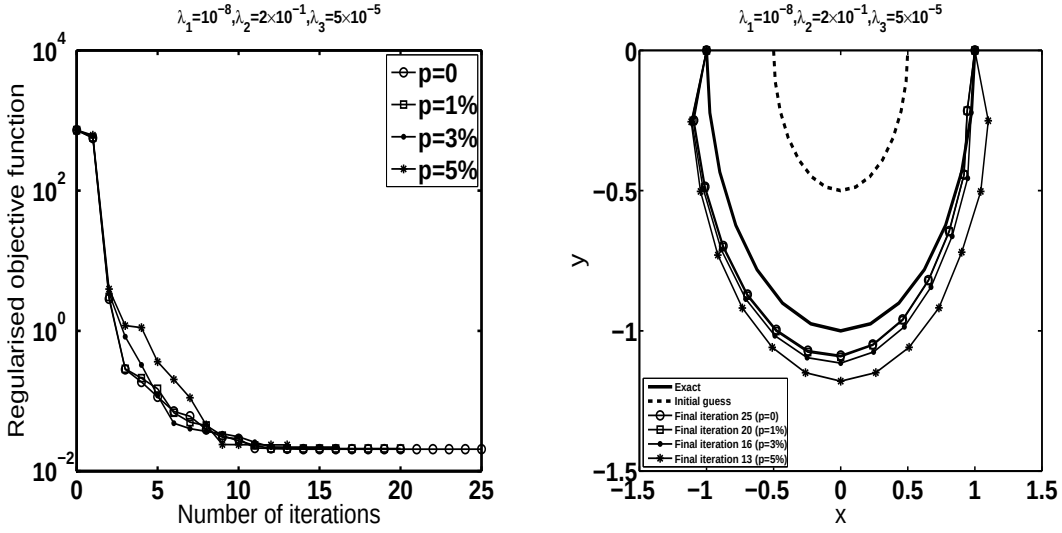

(a) (b)

Figure 6.16: (a) The regularised objective function and (b) Initial guess, exact and numerically zeroth-order regularisation (in α) reconstructed shapes of the boundary Γ_2, for Example 5, when there is $p = \{0, 1, 3, 5\}\%$ noise in the data (6.4) and $\lambda_1 = 10^{-8}, \lambda_2 = 10^{-1}$, $\lambda_3 = 10^{-5}$.

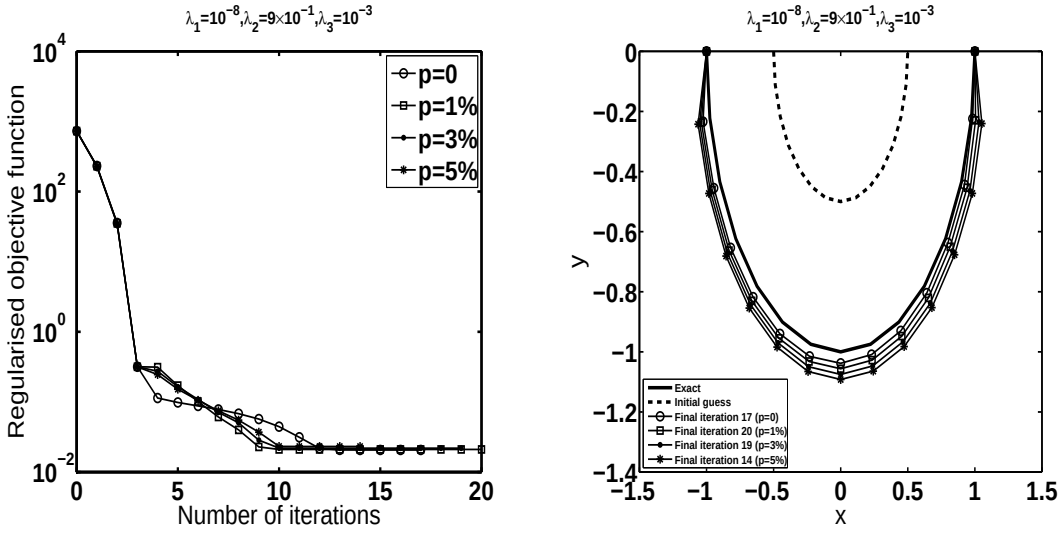

(a) (b)

Figure 6.17: (a) The regularised objective function and (b) Initial guess, exact and numerically first-order regularisation (in α) reconstructed shapes of the boundary Γ_2, for Example 5, when there is $p = \{0, 1, 3, 5\}\%$ noise in the data (6.4) and $\lambda_1 = 10^{-8}, \lambda_2 = 9 \times 10^{-1}$, $\lambda_3 = 10^{-3}$.

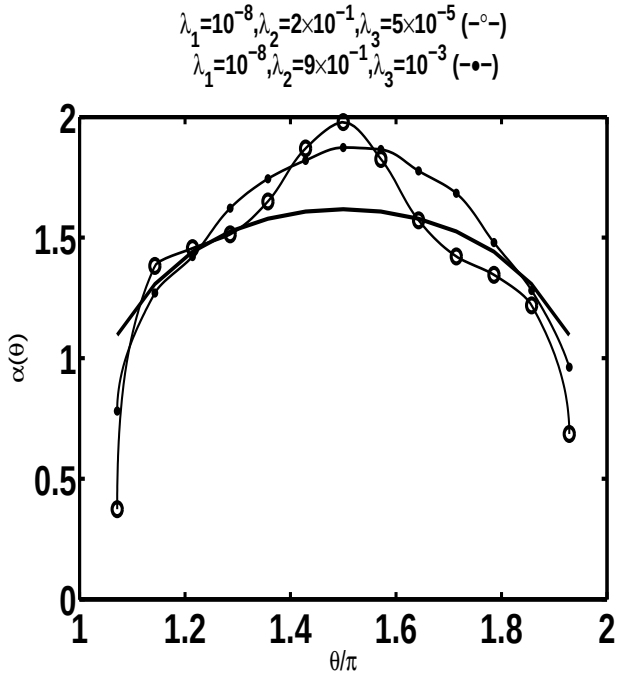

Figure 6.18: The numerical zeroth-order (-○-), first-order (-●-) and exact (——) solutions for the Robin coefficient α, for Example 5, when there is no noise in the data (6.4).

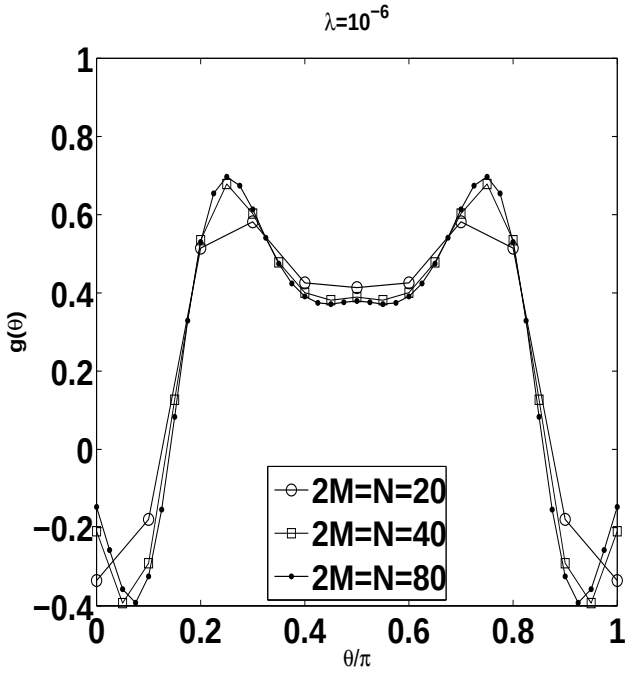

Figure 6.19: The numerical solutions for the normal derivative $g(\theta)$ obtained by solving the direct mixed problem for various values of $2M = N \in \{20, 40, 80\}$ with the regularisation parameter $\lambda = 10^{-6}$ for
Example 6.

6.4.6 Example 6

Finally, consider a complicated peanut shape domain $\Omega = \{(x, y) \in \mathbb{R}^2 |\ \sqrt{x^2 + y^2} < r(\theta) = \sqrt{\cos^2(\theta) + \frac{1}{4}\sin^2(\theta)};\ \theta \in [0, 2\pi]\}$, whose boundary is divided into two parts, namely

$$\Gamma_1 = \{(x, y) \in \mathbb{R}^2 |\ x = r(\theta)\cos(\theta);\ y = r(\theta)\sin(\theta);\ \theta \in [0, \pi]\}, \tag{6.46}$$

and

$$\Gamma_2 = \{(x, y) \in \mathbb{R}^2 |\ x = r(\theta)\cos(\theta);\ y = r(\theta)\sin(\theta);\ \theta \in (\pi, 2\pi)\}. \tag{6.47}$$

Take $k = \sqrt{2}$, the Dirichlet data (6.2) on Γ_1 given by

$$u(r(\theta), \theta) = f(\theta) = \Big(\cos^2(\theta) + \frac{1}{4}\sin^2(\theta)\Big)\sin^2(\theta), \qquad \theta \in [0, \pi], \tag{6.48}$$

and the homogeneous Robin boundary condition (6.3) on Γ_2 with $\alpha(\theta) = 1$ given by

$$\frac{\partial u}{\partial n}(r(\theta), \theta) + u(r(\theta), \theta) = 0, \quad \theta \in (\pi, 2\pi). \tag{6.49}$$

► **Direct problem**

Since no analytical solution is available, the Neumann data (6.4) on Γ_1 is simulated numerically by solving, using the MFS, the direct mixed problem given by the modified Helmholtz equation (6.1), the homogeneous Robin boundary condition (6.49) on Γ_2, and the Dirichlet boundary condition (6.48) on Γ_1, when Γ_2 is known and given by upper-half of the peanut shape (6.48). The numerical solutions for the normal derivative $g(\theta) = \partial u/\partial n(r(\theta), \theta)$ on Γ_1, obtained with $R = 2.5$ for various values of $2M = N \in \{20, 40, 80\}$ and the regularisation parameter $\lambda = 10^{-6}$ are shown in Figure 6.19. Form this figure it can be seen that the numerical results are convergent as the number of degrees of freedom increases. The curve numerical obtained for $2M = N = 40$ in Figure 6.19 is chosen as input flux data (6.4) in solving the inverse problem next.

► **Inverse problem**

Assuming now that Γ_2 is unknown, in the inverse problem the MFS is applied with a different R than 2.5, say $R = 3$, in order to avoid committing an inverse crime. The input Neumann data (6.4) is chosen out of the curve $\lambda = 10^{-6}$ of Figure 6.19, the Dirichlet data is given by (6.48), and the homogeneous Robin boundary condition (6.49) on Γ_2 is considered.

The numerical results are presented in Figures 6.20 and 6.21. First, from Figure 6.20 it can be observed that the numerical results obtained using the star-shaped approximation (6.18) for Γ_2, denoted by $K = \infty$, are far from the true peanut shape (6.47) and they rather maintain the circular feature being close to the initial guess. In order to improve the results we consider trigonometric polynomials as approximating radial function $r(\theta)$ in a finite-dimensional parametrisation space, see Chaji et al. (2008),

$$r(\theta) = a_0 + \sum_{j=1}^{K} a_j \cos(j\theta) + \sum_{j=1}^{K} b_j \sin(j\theta), \qquad \theta \in (\pi, 2\pi). \tag{6.50}$$

of degree K. We then perform the minimisation of (6.21) with respect to the parameteres $(a_j)_{j=\overline{0,K}}$ and $(b_j)_{j=\overline{1,K}}$ instead of the vector $\underline{r} = (r_j)_{j=\overline{2,M}}$. We take the initial guess for $a_0 = 1$, $(a_j)_{j=\overline{1,K}} = (b_j)_{j=\overline{1,K}} = 0$. The derivative r' in (6.27) is given by

$$r'(\theta) = -\sum_{j=1}^{K} j a_j \sin(j\theta) + \sum_{j=1}^{K} j b_j \cos(j\theta), \tag{6.51}$$

and the last term in (6.22) is replaced by $\lambda_2\Big(\sum_{j=0}^{K} a_j^2 + \sum_{j=1}^{K} b_j^2\Big)$. From Figure 6.20(b)

it can be clearly seen that there are very good improvements for the numerically reconstructed shape for $K \in \{4, 5\}$ in comparison with the true peanut shape (6.48). Figure 6.21 shows the numerical results obtained using various regularisation parameters $\lambda_1 = 10^{-8}, \lambda_2 \in \{10^{-3}, 10^{-6}\}$ without and with $p = 1\%$ noise in the input data (6.4) for $K = 5$. From this figure it can be seen that the numerical solutions are accurate and stable.

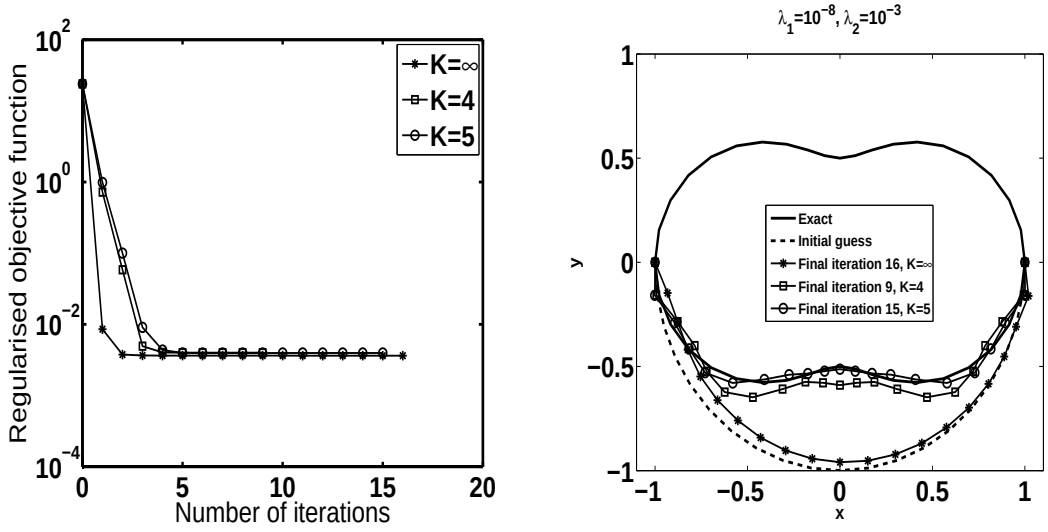

(a) (b)

Figure 6.20: (a) The regularised objective function and (b) $K \in \{4, 5, \infty\}$ Initial guess, exact and various numerically reconstructed shapes with of the boundary Γ_2 when there is no noise in the data (6.4) and $\lambda_1 = 10^{-8}, \lambda_2 = 10^{-3}$ for Example 6..

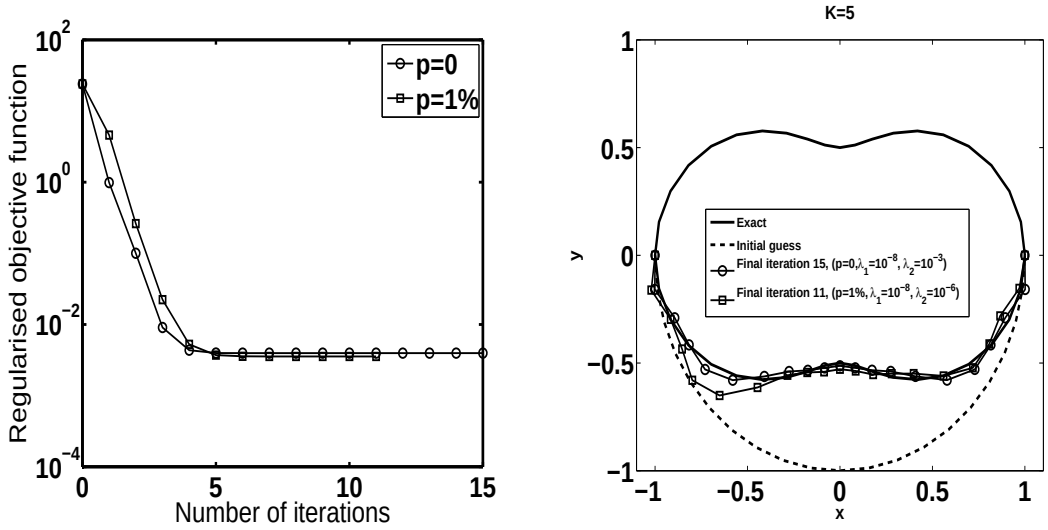

(a) (b)

Figure 6.21: (a) The regularised objective function and (b) Initial guess, exact and numerically reconstructed shapes of the boundary Γ_2 when there is $p = \{0, 1\%\}$ noise in the data (6.4) and $\lambda_1 = 10^{-8}, \lambda_2 = 10^{-3}$ and $10^{-6}, K = 5$ for Example 6.

6.5 Conclusions

In this chapter, two-dimensional Helmholtz-type inverse geometric problems, which consists of determining an unknown portion of the boundary Γ_2 and its Robin coefficient from one or two linearly independent pairs of Cauchy data on the known boundary $\Gamma_1 = \partial\Omega \setminus \Gamma_2$, have been investigated using the MFS. More precisely, a nonlinear regularized MFS has been used in order to obtain stable and accurate numerical results for the ill-posed inverse problem in question. Several examples have been investigated showing that the numerical results are satisfactory reconstructions for the corroded boundary and its Robin coefficient with reasonable stability against nosiy data.

Future work will consider extending the numerical method developed in this study to solving for the shape and impedance in inverse scattering governed by the Helmholtz equation in exterior unbounded domains, see Kress and Rundell (2001), Serranho (2006), and He et al. (2009).

Chapter 7

Reconstruction of an inhomogeneity

7.1 Introduction

Consider finally the determination of an inhomogeneity (anomaly) contained in a given domain from the knowledge of the imposed voltage (boundary temperature) and the measured current (heat) flux which arises in many non-destructive tomography testing of materials. In particular, in this chapter, Consider the inverse problem of determining an inhomogeneity Ω_2 (with Lipschitz boundary $\partial\Omega_2$) compactly contained in a bounded domain Ω (with smooth boundary $\partial\Omega$) entering in the modified Helmholtz elliptic equation

$$\nabla^2 u - k^2 u = 0 \qquad \text{in } \Omega, \tag{7.1}$$

where $k^2 = k_1^2 + (k_2^2 - k_1^2)\chi_{\Omega_2}$ is a given positive function with $k_2 > k_1 \geqslant 0$ and of class $C^2(\Omega)$, χ_{Ω_2} is the characteristic function of the domain Ω_2, and u is the potential (temperature). In heat transfer, equation (7.1) stands as the governing equation for a (two-dimensional) dry fin-tube heat exchanger, see Lin and Jang (2002). By defining

$$u := \begin{cases} u_1 & \text{in} \quad \Omega_1 := \Omega \setminus \Omega_2, \\ \\ u_2 & \text{in} \quad \Omega_2, \end{cases} \tag{7.2}$$

equation (7.1) can be rewritten as the following transmission problem:

$$\nabla^2 u_1 - k_1^2 u_1 = 0 \qquad \text{in} \quad \Omega_1, \tag{7.3}$$

$$\nabla^2 u_2 - k_2^2 u_2 = 0 \qquad \text{in} \quad \Omega_2, \tag{7.4}$$

$$u_1 = u_2, \qquad \text{on} \quad \partial\Omega_2, \tag{7.5}$$

$$\frac{\partial u_1}{\partial n} = \frac{\partial u_2}{\partial n} \qquad \text{on} \quad \partial\Omega_2. \tag{7.6}$$

Associated to the above problem (7.3)-(7.6) we also have the Cauchy boundary conditions on $\partial\Omega$ given by

$$u_1 = f \qquad \text{on} \qquad \partial\Omega, \tag{7.7}$$

$$\frac{\partial u_1}{\partial n} = g \qquad \text{on} \qquad \partial\Omega. \tag{7.8}$$

Such a problem arises in the determination of the contact resistivity of planar electronic devices, Fang and Cumberbatch (1992). Other formulations of inverse obstacle problems can be found in the topical review by Isakov (2009). Uniqueness of the inhomogeneity Ω_2 entering the inverse problem (7.3)-(7.8) has been established in the class of balls, star-shaped domains, convex hulls of polygons and other classes of subdomains in Kang et al. (2001); Hettlich and Rundell (1997); Kim and Yamamoto (2003); Kim (2002), respectively.

In the previous Chapters 4 and 5 inner rigid inclusions, cavities and absorbing obstacles in modified Helmholtz inverse geometric problems have been determined using the MFS. In this chapter, we provide yet another application of the MFS for solving the inverse transmission problem (7.3)-(7.8).

The outline of this chapter is as follows. In section 7.2, the MFS for the modified Helmholtz equation in composite bi-materials is presented. In section 7.3, the numerically obtained results are presented and discussed. In section 7.4, some conclusions and possible future work are given.

7.2 The Method of Fundamental Solutions (MFS)

In the MFS for a composite bi-material $\Omega = \Omega_1 \cup \Omega_2$, $\Omega_1 \cap \Omega_2 = \emptyset$, we approximate the solutions u_1 and u_2 of the modified Helmholtz equations (7.3) and (7.4) by a linear combination of fundamental solutions in the form, see Chapter 3,

$$u_{1,2N}(\underline{X}) = \sum_{j=1}^{2N} a_j G_-(\underline{X}, \underline{\xi}_1^j; k_1), \qquad \underline{X} \in \overline{\Omega}_1, \tag{7.9}$$

$$u_{2,N}(\underline{X}) = \sum_{j=1}^{N} b_j G_-(\underline{X}, \underline{\xi}_2^j; k_2), \qquad \underline{X} \in \overline{\Omega}_2, \tag{7.10}$$

where G_- is the fundamental solution for the modified Helmholtz equations which in two-dimensions for example is given by,

$$G_-(\underline{X},\underline{\xi};k_i)=K_0\Big(k_i\|\underline{X}-\underline{\xi}\|\Big),\quad i=1,2. \tag{7.11}$$

For simplicity, the constant $\frac{1}{2\pi}$, which does not appear in (7.11), has been embedded in the unknown coefficients $(b_j)_{j=\overline{1,N}}$ in (7.10). In the case that the background medium Ω_1 is harmonic, i.e. $k_1=0$, one should replace $G_-(\underline{X},\underline{\xi}_1;k_1)$ in (7.9) by the fundamental solution for the Laplace equation

$$\nabla^2 u_1=0 \qquad \text{in} \quad \Omega_1 \tag{7.12}$$

which in two-dimensions is given by

$$G_L(\underline{X},\underline{\xi})=-\frac{1}{2\pi}\ln\|\underline{X}-\underline{\xi}\|. \tag{7.13}$$

In this case, the MFS approximation for (7.12) is

$$u_{1,2N}(\underline{X})=\sum_{j=1}^{2N}a_j G_L(\underline{X},\underline{\xi}_1^j),\qquad \underline{X}\in\overline{\Omega}_1, \tag{7.14}$$

The source points $(\underline{\xi}_1^j)_{j=\overline{1,2N}}$ in (7.9) or (7.14) are located both outside the domain $\overline{\Omega}$ and inside the domain Ω_2, whilst the source points $(\underline{\xi}_2^j)_{j=\overline{1,N}}$ in (7.10) are located outside $\overline{\Omega}_2$. More precisely, $(\underline{\xi}_1^j)_{j=\overline{N+1,2N}}\in\Omega_2$ and $(\underline{\xi}_2^j)_{j=\overline{1,N}}\notin\Omega_2$ are placed on (moving) pseudo-boundaries $\partial\Omega_2^{'}$ and $\partial\Omega_2^{''}$ similar to $\partial\Omega_2$ at a distance $\delta>0$ inwards and outwards, respectively. The rest of source points $(\underline{\xi}_1^j)_{j=\overline{1,N}}\in\mathbb{R}^2\setminus\overline{\Omega}$ are placed on a (fixed) pseudo-boundary $\partial\Omega^{'}$ similar to $\partial\Omega$. A sketch of the fictitions curves $\partial\Omega_2^{'}$, $\partial\Omega_2^{''}$ and $\partial\Omega^{'}$ on which the source points are located is shown in Figure 7.1.

For simplicity, we assume that Ω is the unit circle $B(\mathbf{0};1)$ and that the unknown domain Ω_2 is star-shaped with respect to the origin, i.e.

$$\partial\Omega_2=\{(r(\theta)\cos(\theta),r(\theta)\sin(\theta))|\ \theta\in[0,2\pi)\},$$

where r is a 2π-periodic smooth function with values in the interval (0,1). We take

$$\underline{X}_i=(\cos(\theta_i),\sin(\theta_i)),\qquad i=\overline{1,N}$$

to be the outer boundary collocation points uniformly distributed on $\partial\Omega=\partial B(\mathbf{0};1)$,

where $\theta_i = 2\pi i/N$ for $i = \overline{1, N}$, and the source points

$$\underline{\xi}_1^j = (R\cos(\theta_j), R\sin(\theta_j)), \qquad j = \overline{1, N},$$

where $R > 1$ is fixed. We also take

$$\underline{X}_i = (r_{i-N}\cos(\vartheta_{i-N}), r_{i-N}\sin(\vartheta_{i-N})), \qquad i = \overline{N+1, 2N} \tag{7.15}$$

to be the inner unknown boundary collocation points on $\partial\Omega_2$, and the inner and outer source points

$$\underline{\xi}_1^j = (1-\delta)\underline{X}_j, \quad \underline{\xi}_2^{j-N} = (1+\delta)\underline{X}_j, \quad j = \overline{N+1, 2N},$$

where $\delta \in (0, 1)$. In equation (7.15), $r_i := r(\theta_i)$ for $i = \overline{1, N}$.

The MFS coefficient vectors $\underline{a} = (a_j)_{j=\overline{1,2N}}$, $\underline{b} = (b_j)_{j=\overline{1,N}}$ in (7.9) or (7.14), and (7.10), and the radii vector $\underline{r} = (r_i)_{i=\overline{1,N}}$ characterising the star-shaped inner boundary $\partial\Omega_2$ are determined by imposing the transmission conditions (7.5), (7.6) and the Cauchy data (7.7), (7.8) at the boundary collocation points $(\underline{X}_i)_{i=\overline{1,2N}}$ in a least-squares sense which recasts into minimising the nonlinear objective function

$$\begin{aligned} T(\underline{a}, \underline{b}, \underline{r}) \; &:= \Big\| u_1 - f \Big\|^2_{L^2(\partial\Omega)} + \Big\| \tfrac{\partial u_1}{\partial n} - g \Big\|^2_{L^2(\partial\Omega)} + \Big\| u_1 - u_2 \Big\|^2_{L^2(\partial\Omega_2)} \\ &\quad + \Big\| \tfrac{\partial u_1}{\partial n} - \tfrac{\partial u_2}{\partial n} \Big\|^2_{L^2(\partial\Omega_2)} + \lambda_1 \{ \|\underline{a}\|^2 + \|\underline{b}\|^2 \} + \lambda_2 \|\underline{r}'\|^2, \end{aligned} \tag{7.16}$$

where $\lambda_1, \lambda_2 \geq 0$ are regularisation parameters to be prescribed. Introducing the MFS approximations (7.10), and say (7.14) (with obvious modifications if (7.9) is used) into (7.16) yields

$$\begin{aligned} T(\underline{a}, \underline{b}, \underline{r}) &= \sum_{i=1}^{N} \Big[\sum_{j=1}^{2N} a_j G_L(\underline{X}_i, \underline{\xi}_1^j) - f(\underline{X}_i) \Big]^2 \\ &\quad + \sum_{i=N+1}^{2N} \Big[\sum_{j=1}^{2N} a_j \frac{\partial G_L}{\partial n}(\underline{X}_{i-N}, \underline{\xi}_1^j) - g(\underline{X}_{i-N}) \Big]^2 \\ &\quad + \sum_{i=2N+1}^{3N} \Big[\sum_{j=1}^{2N} a_j G_L(\underline{X}_{i-N}, \underline{\xi}_1^j) - \sum_{j=1}^{N} b_j G_-(\underline{X}_{i-N}, \underline{\xi}_2^j; k_2) \Big]^2 \\ &\quad + \sum_{i=3N+1}^{4N} \Big[\sum_{j=1}^{2N} a_j \frac{\partial G_L}{\partial n}(\underline{X}_{i-2N}, \underline{\xi}_1^j) - \sum_{j=1}^{N} b_j \frac{\partial G_-}{\partial n}(\underline{X}_{i-2N}, \underline{\xi}_2^j; k_2) \Big]^2 \\ &\quad + \lambda_1 \Big\{ \sum_{j=1}^{2N} a_j^2 + \sum_{j=1}^{N} b_j^2 \Big\} + \lambda_2 \sum_{j=1}^{N-1} (r_{j+1} - r_j)^2. \end{aligned} \tag{7.17}$$

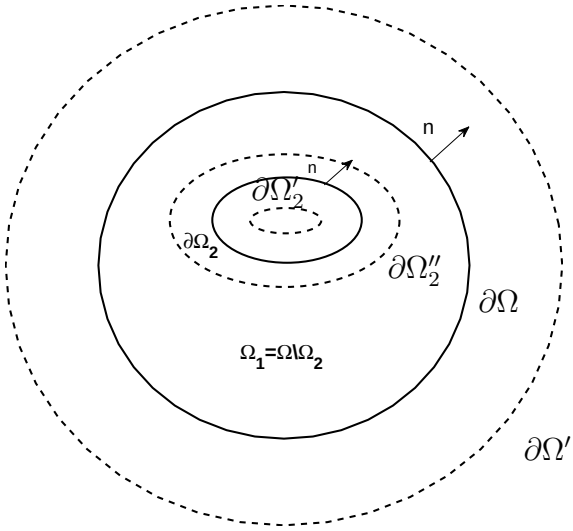

Figure 7.1: Sketch of the curves on which the source ($- - -$) and the boundary collocation (—) points are located in the MFS.

The minimisation of (7.17) imposes $4N$ nonlinear equations in the $4N$ unknowns $(\underline{a}, \underline{b}, \underline{r})$. We can obviously have more equations than unknowns if we take more boundary collocation points than sources. If there is noise in the measured data (7.8), we replace the exact g in (7.17) by the noisy g^ε given by (4.15). In equation (7.17), the normal derivative of G_L and G_{MH}, via (7.12) and (7.11), are given by

$$\begin{aligned}\frac{\partial G_L}{\partial n}(\underline{X}, \underline{\xi}) &= -\frac{(\underline{X} - \underline{\xi}) \cdot \underline{n}}{2\pi \|\underline{X} - \underline{\xi}\|^2}, \\ \frac{\partial G_-}{\partial n}(\underline{X}, \underline{\xi}; k_2) &= -\frac{k_2(\underline{X} - \underline{\xi}) \cdot \underline{n}}{\|\underline{X} - \underline{\xi}\|} K_1\Big(k_2 \|\underline{X} - \underline{\xi}\|\Big).\end{aligned} \tag{7.18}$$

The minimisation of the objective function (7.17) is accomplished computationally using the NAG routine E04FCF, as described in Chapter 4.

7.3 Numerical results and discussion

In this section, three examples in two-dimensions are presented in order to show the accuracy and stability of the MFS described in the previous section. We take $k_1 = 0$ and $k_2 = 1$.

In all numerical experiments, the initial guess for the unknown vectors $\underline{a}$, $\underline{b}$ are

$\underline{0}$ and the initial guess for the inner boundary is taken to be a circle located at the origin with radius 0.7, i.e. the initial guess for $\underline{r}$ is $\underline{0.7}$. Moreover, as required by the NAG routine E04FCF used, the tolerance XTOL was set to 10^{-6} and the maximum number of function evaluations, MAXCAL, was set to 1000. However, it is noted that by increasing the MAXCAL to be large, say 400 $\times$ (number of unknowns), as suggested by the NAG Fortran library manual, the computational time increases significantly and moreover, it does not produce more accurate numerical results. We also take $R = 2$, $M = N = 20$ for Examples 1 and 2, and $M = N = 40$ for Example 3.

7.3.1 Example 1

First consider an example for which the analytical solution is available and given by, see Hettlich and Rundell (1997),

$$u_1(r, \theta) = 1 + a_0 \ln(r), \qquad R_0 < r < 1, \tag{7.19}$$

where $a_0 = \frac{R_0 I_1(R_0)}{I_0(R_0) - R_0 I_1(R_0) \ln(R_0)}$,

$$u_2(r, \theta) = A_0 I_0(r), \qquad 0 < r < R_0, \tag{7.20}$$

where $A_0 = \frac{1}{I_0(R_0) - R_0 I_1(R_0) \ln(R_0)}$. The modified Bessel functions of first kind of order 0 and 1, namely I_0 and I_1 are computed using the NAG routines S18AEF and S18AFF, respectively.

In this example, the unknown inner boundary is the disk

$$\Omega_2 = B(\mathbf{0}; R_0) = \{(x, y) \in \mathbb{R}^2 |\ x^2 + y^2 < R_0^2\} \tag{7.21}$$

of radius $R_0 = 0.5$ and δ is taken to be 0.5. This analytical solution satisfies problem (7.4)-(7.8) and (7.12), with

$$f(\theta) = 1, \qquad \theta \in (0, 2\pi] \tag{7.22}$$

and

$$\frac{\partial u_1}{\partial n}(1, \theta) = g(\theta) = a_0, \qquad \theta \in (0, 2\pi]. \tag{7.23}$$

Figure 7.2 shows the objective function (7.17) with no regularisation, i.e. $\lambda_1 = \lambda_2 = 0$, when $p \in \{0, 1, 5, 10\}\%$ noise is added in the input data (7.23), as a function of the number of iterations. From this figure it can be seen that the unregularised

objective cost functional decreases rapidly within 6-8 iterations to either a very low value of $\mathbf{O}(10^{-29})$ for $p = 0$, or to a stationary level for $p > 0$. Moreover, as expected, this level of stationarity decreases with decreasing the level of noise p.

In Figure 7.3, we present the reconstructed inner boundary and the exact shape (7.21) with no regularisation for $p \in \{0, 1, 5, 10\}\%$. As expected, as the level of noise increases, since no regularisation is imposed, the reconstructed inner boundary becomes unstable.

Next, regularisation is used in (7.17) in order to stablise the numerical solutions. Figures 7.4 and 7.5 show the regularised objective function (7.17) and the reconstructed inner boundary, respectively, for $p = 10\%$ noise and various regularisation parameters $\lambda_1 = 0$, $\lambda_2 \in \{10^{-8}, 10^{-5}, 10^{-3}, 10^{-1}\}$. From Figure 7.5 it can be seen that accurate and stable numerical solutions are achieved for $\lambda_1 = 0$ and λ_2 in the range 10^{-3} to 10^{-1}, whilst clearly for $\lambda < 10^{-5}$ the obtained reconstructions become unstable.

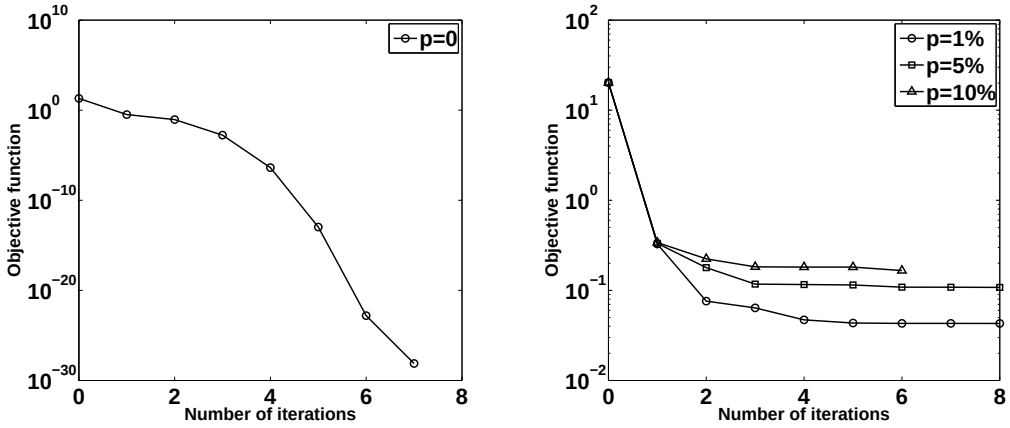

Figure 7.2: The unregularised objective function for $p \in \{0, 1, 5, 10\}\%$ noise, as a function of the number of iterations, for Example 1.

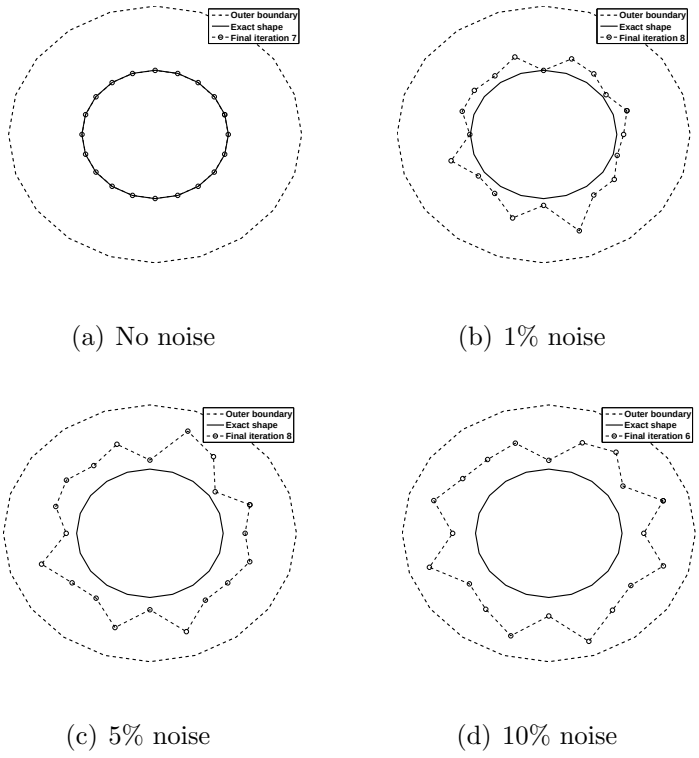

(a) No noise (b) 1% noise

(c) 5% noise (d) 10% noise

Figure 7.3: The reconstructed inner boundary with no regularisation for $p \in \{0, 1, 5, 10\}\%$ noise, for Example 1.

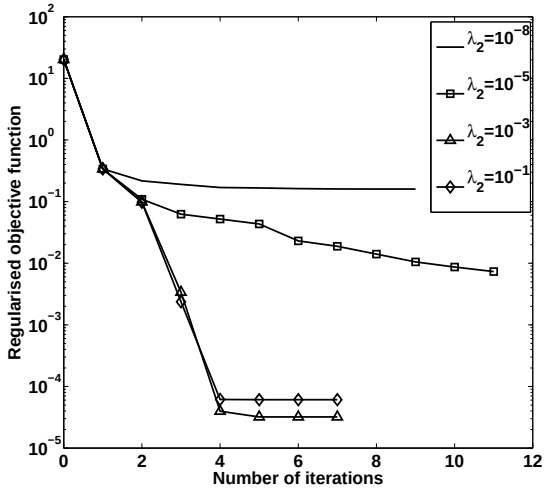

Figure 7.4: The regularised objective function with various regularisation parameters $\lambda_1 = 0, \lambda_2 \in \{10^{-8}, 10^{-5}, 10^{-3}, 10^{-1}\}$ for $p = 10\%$ noise, as a function of the number of iterations, for Example 1.

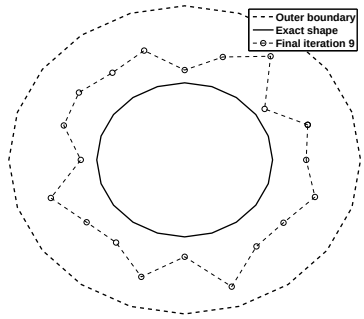

(a) $\lambda_2 = 10^{-8}$

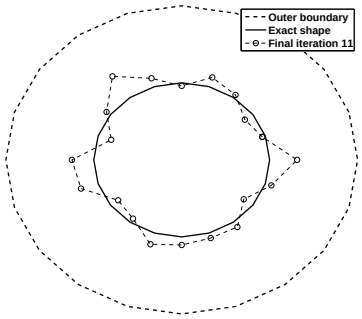

(b) $\lambda_2 = 10^{-5}$

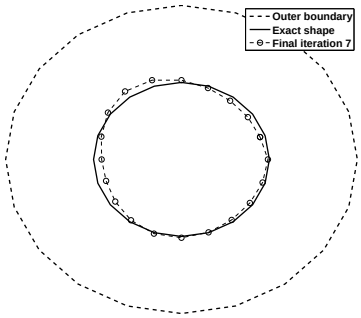

(c) $\lambda_2 = 10^{-3}$

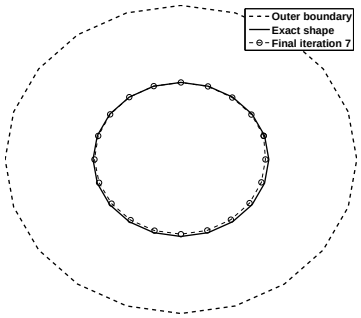

(d) $\lambda_2 = 10^{-1}$

Figure 7.5: The reconstructed inner boundary with various regularisation parameters $\lambda_1 = 0, \lambda_2 \in \{10^{-8}, 10^{-5}, 10^{-3}, 10^{-1}\}$ for $p = 10\%$ noise, for Example 1.

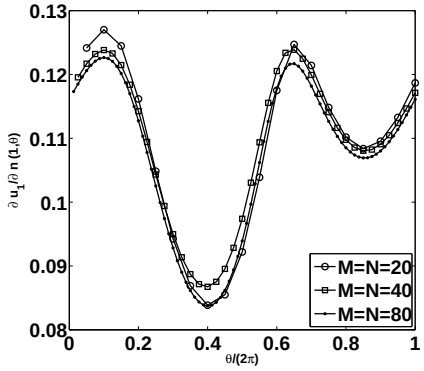

(a) $\lambda = 0$

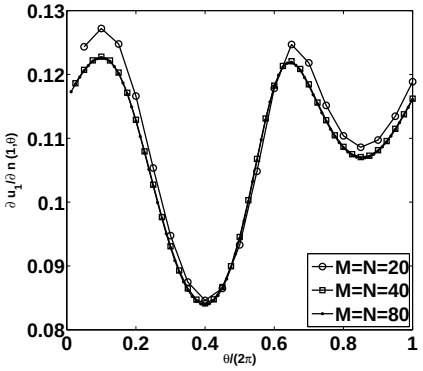

(b) $\lambda = 10^{-6}$

Figure 7.6: The numerical solutions for the normal derivative $\partial u_1/\partial n(1, \theta)$, obtained for various values of $M = N \in \{20, 40, 80\}$ with (a) no regularisation, and (b) regularisation parameter $\lambda = 10^{-6}$ for the direct problem associated to Example 2.

7.3.2 Example 2

In the second example, Consider a more complicated bean-shaped inclusion $\partial\Omega_2$ given by the radial parameterisation

$$r(\theta) = \frac{0.5 + 0.4\cos(\theta) + 0.1\sin(2\theta)}{1 + 0.7\cos(\theta)}, \qquad \theta \in (0, 2\pi] \tag{7.24}$$

within the unit circle $\Omega = B(\mathbf{0}, 1)$. The Dirichlet data (7.7) on $\partial\Omega$ is taken to be the same as in Example 1 and given by equation (7.22). Also choose $\delta = 0.3$.

Since in this case no analytical solution is available, the Neumann flux data (7.8) on $\partial\Omega$ is simulated numerically by solving, using the MFS, the direct problem given by equations (7.3)-(7.6) and (7.22), when $\partial\Omega_2$ is known and given by (7.24). In this case, the numerical solutions for the normal derivative $\partial u_1/\partial n(1, \theta)$ on $\partial\Omega$, obtained for various values of $M = N \in \{20, 40, 80\}$ with no regularisation $\lambda = 0$, and with regularisation $\lambda = 10^{-6}$ are shown in Figure 7.6. From Figure 7.6 it can be seen that the numerical results are convergent as the number of degrees of freedom increases. Furthermore, a small regularisation with $\lambda = 10^{-6}$ tends to improve the independance of the mesh between $M = N = 40$ and 80. Twenty evenly spread points out of the curve $M = N = 80$ with $\lambda = 10^{-6}$ of Figure 7.6(b) are chosen as input Neumann numerically simulated data (7.8) in the inverse problem. Next, in order to avoid committing an inverse crime we solve the inverse problem with $M = N = 20$.

Figures 7.7 and 7.8 for Example 2 are the anologous of Figures 7.2 and 7.3 for Example 1 and the same conclusions about the unstable nature of the unregularised solution, as the level of noise p increases, can be drawn. Figures 7.9 and 7.10 for Example 2 present similar characteristics to Figures 7.4 and 7.5 for Example 1. In order to investigate a different situation to that in Example 1 we regularise with $\lambda_1 > 0$ instead of $\lambda_2 > 0$. From Figure 7.10 it can be seen that a stable and reasonably accurate numerical solution is obtained for $\lambda_1 = 10^{-3}$ (and $\lambda_2 = 0$), whilst clearly for $\lambda < 10^{-4}$ the obtained reconstructions become unstable.

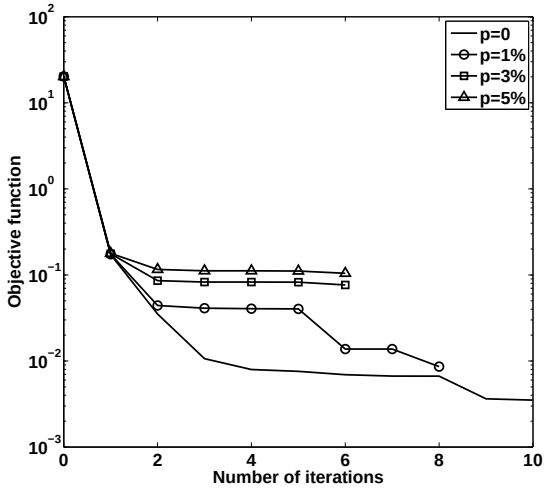

Figure 7.7: The unregularised objective function for $p \in \{0, 1, 3, 5\}\%$ noise, as a function of the number of iterations, for Example 2.

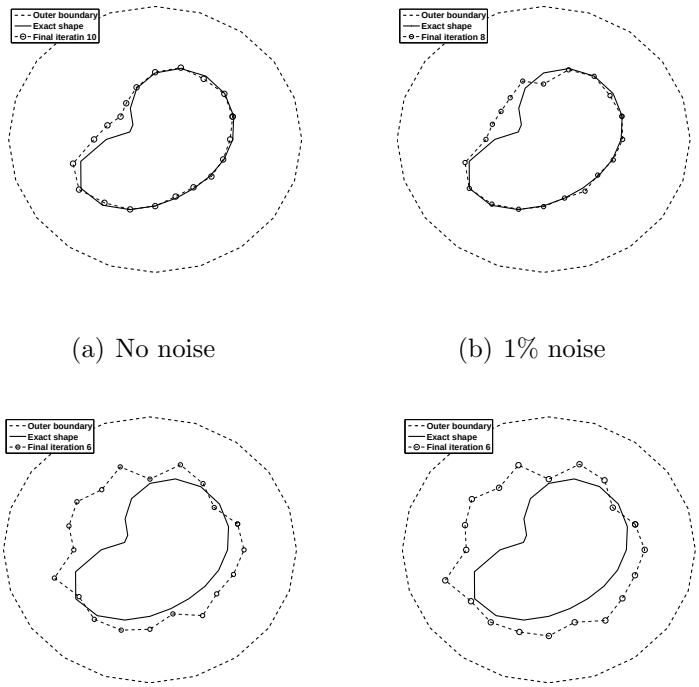

(a) No noise (b) 1% noise

(c) 5% noise (d) 10% noise

Figure 7.8: The reconstructed inner boundary with no regularisation for $p \in \{0, 1, 3, 5\}\%$ noise, for Example 2.

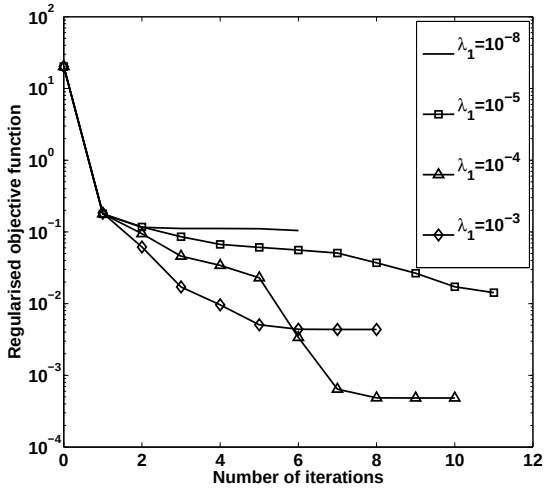

Figure 7.9: The regularised objective function with various regularisation parameters $\lambda_2 = 0$, $\lambda_1 \in \{10^{-8}, 10^{-5}, 10^{-3}, 10^{-1}\}$ for $p = 5\%$ noise, as a function of the number of iterations, for Example 2.

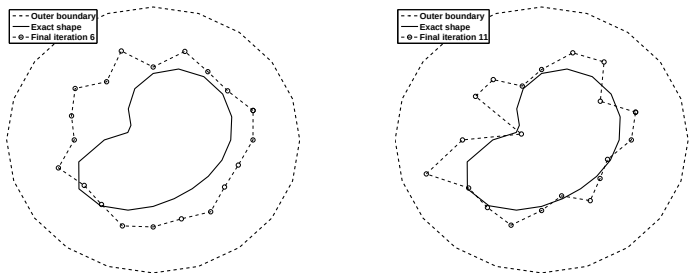

(a) $\lambda_1 = 10^{-8}$ (b) $\lambda_1 = 10^{-5}$

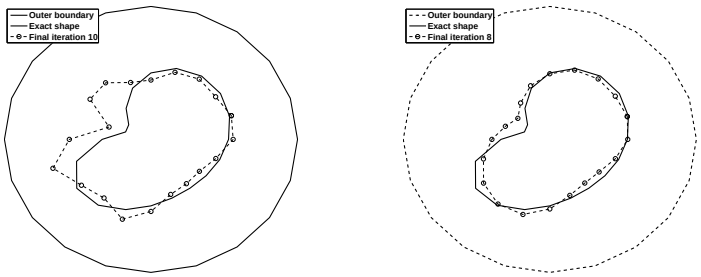

(c) $\lambda_1 = 10^{-4}$ (d) $\lambda_1 = 10^{-3}$

Figure 7.10: The reconstructed inner boundary with various regularisation parameters $\lambda_2 = 0$, $\lambda_1 \in \{10^{-8}, 10^{-5}, 10^{-4}, 10^{-3}\}$ for $p = 5\%$ noise, for Example 2.

7.3.3 Example 3

Finally consider reconstructing a complicated pear-shaped inclusion $\partial\Omega_2$ given by the radial parameterisation

$$r(\theta) = 0.6 + 0.125\cos(3\theta), \qquad \theta \in (0, 2\pi], \tag{7.25}$$

within the unit circle $\Omega = B(\mathbf{0}, 1)$. The Dirichlet voltage (7.7) on $\partial\Omega$ was taken to be the same as in Example 1 and given by equation (7.22). We also take $\delta = 0.3$. Since no analytical solution of this example is available, the Neumann flux data (7.8) on $\partial\Omega$ is simulated numerically by solving the direct problem (7.3)-(7.6) and (7.22), when $\partial\Omega_2$ is known and given by (7.25), using the MFS with $M = N = 80$ and $\lambda = 10^{-6}$. In order to avoid committing an inverse crime, use a different number $M = N = 40$ in the inverse problem. Next, two cases are considered for this example, as follows.

▶ Recovery from full angle data

Consider the first case when the full data of measurment of the flux g on the outer boundary $\partial\Omega$ is available. Figure 7.11 shows reconstructed inner boundary with $p = 5\%$, for various regularisation parameters $\lambda_1 \in \{10^{-8}, 10^{-5}, 10^{-3}, 10^{-1}\}$, $\lambda_2 = 0$. From this figure it can be seen that a stable and reasonably accurate numerical solution is obtained for λ_1 between 10^{-3} and 10^{-1} (and $\lambda_2 = 0$).

▶ Recovery from limited angle data

Finally, consider the case of limited flux measurment data g prescribed on the subportion $\{(1, \theta)|\ \theta \in [0, \pi]\}$ of the full outer boundary $\partial\Omega = \partial B(\mathbf{0}, 1)$. Figures 7.12 and 7.13 show the reconstructed inner boundary for both full and limited flux data with or without noise. From these figures it can be seen that, as expected, the reconstructed inner boundary from full angle data is much more accurate than that obtained from limited angle data.

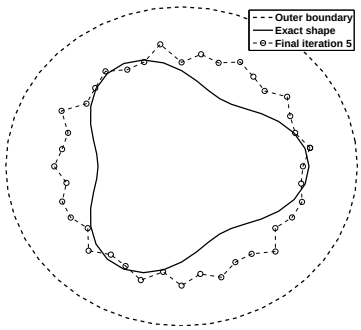

(a) $\lambda_1 = 10^{-8}$

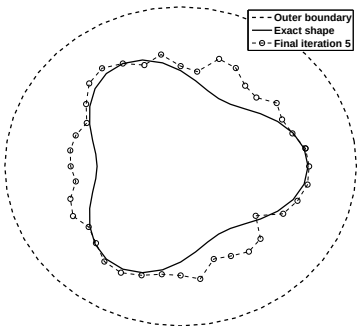

(b) $\lambda_1 = 10^{-5}$

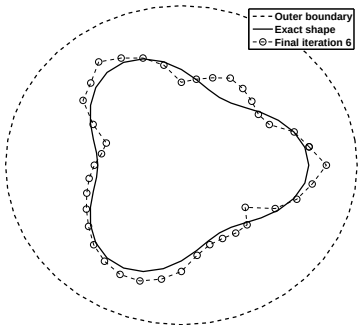

(c) $\lambda_1 = 10^{-3}$

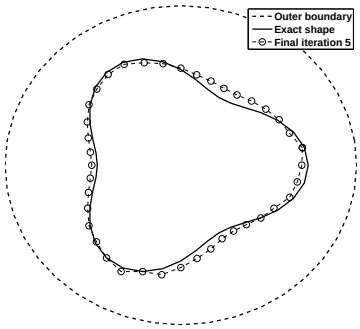

(d) $\lambda_1 = 10^{-1}$

Figure 7.11: The reconstructed inner boundary with various regularisation parameters $\lambda_2 = 0$, $\lambda_1 \in \{10^{-8}, 10^{-5}, 10^{-3}, 10^{-1}\}$ for $p = 5\%$ noise, for Example 3.

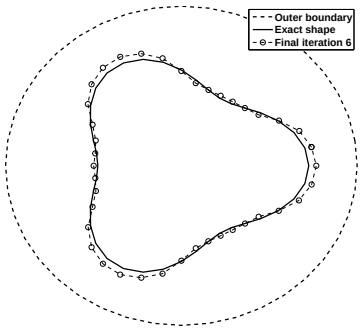

(a) Full angle data

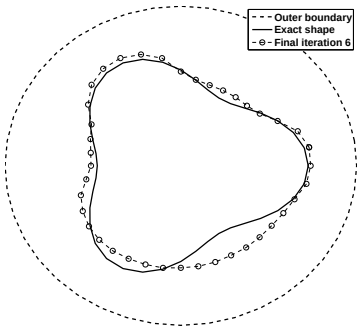

(b) Limited angle data

Figure 7.12: The reconstructed inner boundary for (a) full angle data for $\lambda_1 = 10^{-1}, \lambda_2 = 0$, and (b) limited angle data for $\lambda_1 = \lambda_2 = 10^{-9}$, for no noise, for Example 3.

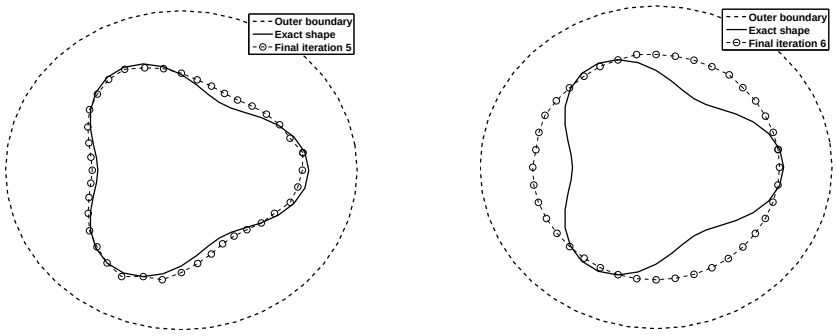

(a) Full angle data (b) Limited angle data

Figure 7.13: The reconstructed inner boundary for (a) full angle data for $\lambda_1 = 10^{-1}, \lambda_2 = 0$, and (b) limited angle data for $\lambda_1 = \lambda_2 = 10^{-9}$, for $p = 5\%$ noise, for Example 3.

7.4 Conclusions

In this chapter, a numerical method based on a regularised iterative MFS has been developed for the reconstruction of an inhomogeneity in an inverse problem for the modified Helmholtz equation. The choice of the two-family multiple regularisation parameters was based on trial and error. More rigorous choices of these parameters should be investigated in any future work. Several examples have been investigated showing that the MFS is accurate (for exact data) and stable (for noisy data). Future work will concern extending the MFS developed in this paper to the reconstruction of a source domain from Cauchy data, see Ikehata (1999).

Chapter 8

General conclusions and future work

8.1 Conclusions

The work presented in this thesis extends the range of application of the MFS to solve two types of problems, namely direct and inverse problems, for two- and three-dimensional Helmholtz-type equations. For inverse problems, the numerical results have been compared with their analytical solutions, where available, or with the numerical solution of the corresponding direct problem where no analytical solution is available.

In inverse geometric problems, the location and shape of part of the boundary of the solution domain under consideration is unknown. On the known part of the boundary, the conditions are over-specified. Therefore, in some cases, one needs to use extra information on an over-specified boundary. In practical situations, this extra information has to come from measurments and therefore, it is usually contaminated by random noise. Due to the ill-posed nature of the inverse problems, this random noise is frequently drastically magnified if standard solution procedures are used, as in direct problems, hence highly oscillatory and unbounded behaviour occurs in the solution. As a consequence, classical numerical methods are not capable of handling such inverse problems without being augmented by some stabilising techniques. This means that special corrective techniques are required to achieve an accurate and stable solution.

The MFS has been applied to solve inverse geometric problems for Helmholtz-type equations. The inverse geometric problems then have been reduced to ill-conditioned system of nonlinear equations which have been solved by the Tikhonov regularisation method. This method modifies the least-squares approach by adding smoothing factors which are dependent upon regularisation parameters in order

to reduce the influence of the measurement errors on the numerical results. One possible selection of the regularisation parameter is based on the L-curve method. The L-curve is one of the simplest and most popular methods for selecting a single regularisation parameter. This method plots the size of the solution (measured in appropriate norm) against the corresponding residual for many positive regularisation parameters. In many cases, the graph in an L-shaped curve and the value of the regularisation parameter that corresponds to the corner is considered to be nearly the optimal choice. If multiple regularisation parameters are encountered one has to generalize the L-curve concept to an L-hypersurface, see Belge et al. (2002), and the analysis of parameter selection becomes tedious and computationally expensive. In this thesis, emphasis is aimed more on the MFS and therefore, in a first attempt and for simplicity, the regularisation parameters have been chosen by simple trial and error, i.e. one gradually increases the regularisation parameters until the oscillations in the numerical solution start to smooth out and disappear. Some discussion on this has been provided in Section 7.3. But nevertheless more research has to be done in the future regarding the proper choice of the regularisation parameters for solving nonlinear and ill-posed problems.

In Chapter 1, a general introduction to direct and inverse problems has been presented, with the difficulties associated with these problems highlighted and a review of the previous work on this subject summarised. The MFS has several advantages when compared to the BEM and these advantages were discussed in detail in Section 1.4. The development of the MFS, which is a versatile meshless for approximating numerically various linear partial differential equations when the fundamental solution is known explicitly, have been surveyed. In the application of the MFS, unknowns were determined by enforcing the boundary conditions, this allows to obtain a system of linear/nonlinear equations. A well-conditioned system of linear algebraic equations can be solved using the Gaussian elimination method, whilst a highly ill-conditioned system of equations can be solved using a regularised least-squares method in order to achieve a stable and accurate solution. In this thesis, the Tikhonov regularisation method has been considered which is the most known stabilising technique. In this method, the influence of the measurement errors on the stability of results is reduced by adding smoothing terms in the least-squares functional.

In Chapter 2, direct problems for two- and three-dimensional Helmholtz-type equations in various geometries domains namely smooth domains, such as a circle, an annulus, exterior unbounded domains outside of a circle or a sphere, and non-smooth domains such as square have been investigated. Based on the MFS, the direct problem has been reduced to solving a system of linear algebraic equations

which has been solved using a Gaussian elimination approach. Convergence of the MFS has been analysed in Section 2.3. To validate the MFS technique, several tests examples have been investigated and the numerical results obtained show that the convergence of the MFS depends on increasing the number of source and boundary collocation points and the distance from the source points to the boundary of the solution domain.

In Chapter 3, direct Helmholtz-type problems in both two- and three-dimensional composite materials subject to boundary conditions and interface continuity conditions have been investigated. By employing the MFS, the system of linear equations has solved by the same approach as in Chapter 2. The degree of ill-conditioning of these direct formulations has been characterised by the condition number of the MFS matrix. Several examples involving Helmholtz-type equations in composite materials showed that the numerical results obtained by the MFS are accurate and in good agreement with the exact solutions, where available.

In Chapter 4, the inverse geometric problem for the modified Helmholtz in two-dimensions has been considered. The modified Helmholtz inverse geometric problem consists of determining an unknown inner boundary of an annular domain from a single pair of outer boundary Cauchy data. The inverse geometric problem has been discretised using the MFS which yields a system of nonlinear equations. Then, this system was solved by the least-squares approach using a standard NAG routine E04FCF. Different examples for two-dimensional simple-, bean- and peanut-shaped inner boundaries have investigated in order to see the performance of the proposed numerical technique. The stability of the solution was investigated by adding noise into the Neumann data, this yields unstable results if no regularisation was used. The Tikhonov regularisation method has been employed in order to obtain an accurate and stable solution. Overall, in all cases considered the numerical results illustrated the fact that the MFS is well-suited for the solution of inverse geometric problems. Furthermore, it is accurate for exact data and stable for noisy data.

Chapter 5 was concerned with the development of the MFS technique for solving the modified Helmholtz inverse geometric problem which consists of determining an unknown inner boundary and its surface heat transfer coefficient in an annular domain from one or two linearly independent pairs of outer boundary Cauchy data. After the application of the MFS, an ill-conditioned system of nonlinear equations is obtained, whose solution requires, as in the previous chapter, the use of Tikhonov regularisation method. While in this numerical study the regularisation parameters were chosen by trial and error, more rigorus criteria such as the L-curve or the L-(hyper) surface will be investigated in a future study. The numerical results show satisfactory reconstructions for the Robin coefficient and unknown inner boundary

with reasonable stability against noisy data.

Chapter 6 considered another class of inverse geometric problems governed by the Helmholtz-type equations in two-dimensions. This problem consists of determining an unknown portion of the boundary Γ_2 and its Robin coefficient from one or two linearly independent pairs of Cauchy data on the known boundary Γ_1. The MFS was applied to the governing equations and the resulting nonlinear system of algebraic equations was solved by the least-squares method. More precisely, a nonlinear regularised MFS was used for the ill-posed inverse problem in question. Several tests examples have been investigated showing that the MFS is able to find a very accurate and stable numerical reconstruction for the corroded boundary and its Robin coefficient with reasonable stability against noisy data.

Finally, Chapter 7 was concerned with the same type of inverse problem as in the Chapter 5, namely the inverse geometric problem. An MFS has been applied to the modified Helmholtz equation and the resulting ill-conditioned system of nonlinear equations solved using the regularised least-squares method. The MFS technique has been validated for some typical benchmark test examples in a (disk, bean and pear) inner boundaries and a situation where no analytical solution is available has been considered. It has been shown that this regularised MFS technique produces an accurate, (for exact data), and stable, (for noisy data), numerical solution.

In all the inverse geometric problems considered in this thesis, the convergence and the stability of the iterative MFS employed was thoroughly investigated for various boundary conditions formulations and various level of noise added into the input data, thus revealing several features of the method described. The iterative MFS was found to be accurate with respect to increasing the number of boundary collocation/source points and decreasing the level of noise. The numerical results obtained were found to be stable for both simple and complicated physical domains. Also, the numerical MFS implementation was found to be very efficient in terms of computational costs. Therefore, it may be concluded that the MFS is an efficient and reliable numerical method for solving inverse geometric problems.

8.2 Future work

Note that the numerical results presented in this thesis confirm the fact that efficient iterative MFS can be developed for the solution of inverse boundary value problems, inverse initial value problems or coefficient identification problems. Similar iterative MFS can be developed for determination of cracks and inclusions, for free surface identification or other inverse geometric problems.

As far as the future work is concerned, one can mention the following possible

investigations:
(i) Extending and developing the application of the MFS to deal with inverse geometric problems for time-dependent PDEs, such as the heat and wave equations.
(ii) Chapter 4 details numerical results concerning the modified Helmholtz inverse geometric problem in two-dimensions. It would be interesting to study the Helmholtz inverse scattering problem in both two- or three-dimensions, see the preliminary results of Karageorghis et al. (2012).
(iii) The regularisation parameters were chosen in this thesis by trial and error, one could employ the concept of the L-curve or the L-(hyper) surface criterion, see Belge et al. (2002), this is deferred to a future work.
(v) It is proposed in Chapter 6 to extend the numerical method developed to solving for the shape and impedance in inverse scattering governed by the Helmholtz equation in exterior unbounded domains, see Kress and Rundell (2001), Serranho (2006), and He et al. (2009).
(vi) Other possible work which may be considered in the future relates to the identification of multiple inclusions.
(vii) Continuing the work of Chapter 7, future work can also concern extending the MFS developed in this thesis to the numerical reconstruction of a source domain from Cauchy data, see Ikehata (1999).

Bibliography

Ahmed, M. T., Lavers, J. D., and Burke, P. E. (1989). An evaluation of the direct boundary element method and the method fundamental solutions. *IEEE Trans. Magn.*, **25**:3001–3006.

Alifanov, O. M. (1994). *Inverse Heat Transfer Problems*. Springer-Verlag, Berlin.

Alves, C. J. S. and Chen, C. S. (2005). A new method of fundamental solutions applied to nonhomogeneous elliptic problems. *Adv. Comput. Math.*, **23**:125–142.

Alves, C. J. S. and Martins, N. F. M. (2009). The direct method of fundamental solutions and the inverse Kirsch-Kress method for the reconstruction of elastic inclusions or cavities. *J. Integral Equations Appl.*, **21**:153–178.

Alves, C. J. S. and Valtchev, S. S. (2005). Numerical comparison of two meshfree methods for acoustic wave scattering. *Eng. Anal. Boundary Elements*, **29**:371–382.

Bacchelli, V. (2009). Uniqueness for the determination of unknown boundary and impedance with homogeneous Robin condition. *Inverse Problems*, **25**:015004 (4pp).

Balakrishnan, K. and Ramachandran, P. A. (2000). The method of fundamental solutions for linear diffusion-reaction equations. *Math. Comput. Modelling*, **31**:221–237.

Barnett, A. H. and Betcke, T. (2008). Stability and convergence of the method of fundamental solutions for Helmholtz problems on analytic domains. *J. Comput. Phys.*, **227**:7003–7026.

Beck, J. V. and Arnold, J. K. (1977). *Parameter Estimation in Engineering and Science*. John Wiley and Sons, New York.

Beck, J. V., Blackwell, B., and St-Clair Jr., C. R. (1985). *Inverse Heat Conduction*. J. Wiley-Intersc. Publ., New York.

Belge, M., Kilmer, M. E., and Miller, E. L. (2002). Efficient determination of multiple regularization parameters in a generalized L-curve framework. *Inverse Problems*, **18**:1161–1183.

Berger, J. R. and Karageorghis, A. (1999). The method fundamental solutions for heat conduction in layered materials. *Int. J. Numer. Method Engng.*, **45**:1681–1694.

Berger, J. R. and Karageorghis, A. (2001). The method fundamental solutions for layered elastic materials. *Eng. Anal. Boundary Elements*, **25**:877–886.

Bertero, M. and Boccacci, P. (1998). *Introduction to Inverse Problems in Imaging*. Institute of Physics Publishing, Bristol.

Beskos, D. E. (1997). Boundary element method in dynamic analysis: part II (1986-1996). *ASME Appl. Mech. Rev.*, **50**:149–197.

Bin-Mohsin, B. and Lesnic, D. (2012). Determination of inner boundaries in modified Helmholtz inverse geometric problems using the method of fundamental solutions. *Math. Comput. Simulation*, **82**:1445–1458.

Bogomolny, A. (1985). Fundamental solutions method for elliptic boundary value problems. *SIAM J. Numer. Anal.*, **22**:644–669.

Borman, D., Ingham, D. B., Johansson, B. T., and Lesnic, D. (2009). The method of fundamental solutions for detection of cavities in EIT. *J. Integral Equations Appl.*, **21**:381–404.

Burgess, G. and Mahajerin, A. (1984). A comparison of the boundary element method and superposition methods. *Comput. Struct.*, **19**:697–705.

Cabib, E., Fasino, D., and Sincich, E. (2011). Linearization of a free boundary problem in corrosion detection. *J. Math. Anal. Appl.*, **378**:700–709.

Cakoni, F. and Kress, R. (2007). Integral equations for inverse problems in corrosion detection from partial Cauchy data. *Inverse Problems and Imaging*, **1**:229–245.

Cakoni, F., Kress, R., and Schuft, C. (2010a). Integral equations for shape and impedance reconstruction in corrosion detection. *Inverse Problems*, **26**:095012 (24pp).

Cakoni, F., Nakamura, G., Sini, M., and Zeev, N. (2010b). The identification of a penetrable obstacle with mixed transmission conditions from far field measurements. *Applicable Analysis*, **89**:67–86.

Carpio, A. and Rapun, M. L. (2010). An iterative method for parameter identification and shape reconstruction. *Inverse Problems Sci. Eng.*, **18**:35–50.

Cattle, B. A. (2005). *Limited-access Remote-sensing using Inverse Problem Techniques*. PhD thesis, University of Leeds, UK.

Chaabane, S. and Jaoua, M. (1999). Identification of Robin coefficients by means of boundary measurements. *Inverse Problems*, **15**:1425–1438.

Chaji, K., Bagdouri, M. E., and Channa, R. (2008). A 2D domain boundary estimation. *Journal of Physics: Conference Series*, **135**:012039(8 pages).

Chandler-Wilde, S. N., Langdon, S., and Ritter, L. (2004). A high-wavenumber boundary-element method for an acoustic scattering problem. *Phil. Trans. R. Soc. Lond. A*, **362**:647–671.

Chen, C. S., Cho, H. A., and Golberg, M. A. (2006). Some comments on the ill-conditioning of the method of fundamental solutions. *Eng. Anal. Boundary Elements*, **30**:405–410.

Chen, J. T. and Wong, F. C. (1998). Dual formulation of multiple reciprocity method for acoustic mode of a cavity with a thin partition. *J. Sound Vib.*, **217**:75–95.

Chen, W. and Hon, Y. C. (2003). Numerical convergence of boundary knot method in the analysis of Helmholtz, modified Helmholtz, and convection-diffusion problems. *Computer. Methods Appl. Mech. Eng.*, **192**:1859–1875.

Colton, D. and Kress, R. (1983). *Integral Equation Methods in Scattering Theory*. Wiley, New York.

Colton, D. and Kress, R. (1998). *Inverse Acoustic and Electromagnetic Scattering Theory*. Springer, Berlin, 2nd edition.

Duraiswami, R., Chahine, G. L., and Sarkar, K. (1997). Boundary element techniques for efficient 2-D and 3-D electrical impedance tomography. *Chem. Eng. Sci.*, **52**:2185–2196.

Engl, H. W., Hanke, M., and Neubauer, A. (2000). *Regularization of Inverse Problems*. Springer, Netherlands.

Ennenbach, K. and Niemeyer, H. (1996). The inclusion of Dirichlet eigenvalues with singularity functions. *ZAMM*, **76**:377–383.

Fairweather, G. and Karageorghis, A. (1998). The method of fundamental solutions for elliptic boundary value problems. *Adv. Comput. Math.*, **9**:69–95.

Fang, W. and Cumberbatch, E. (1992). Inverse problems for metal oxide semiconductor field-effect transistor contact resistivity. *SIAM J. Appl. Math.*, **52**:699–709.

Fattorini, H. O. (1984). *The Cauchy Problem*. Cambridge University Press, Combridge.

Gill, P. E. and Murray, W. (1978). Algorithms for the solution of the nonlinear least-squares problem. *SIAM J. Numer. Anal.*, **15**:977–992.

Golberg, M. A. and Chen, C. S. (1999). The method of fundamental solutions for potential, Helmholtz and diffusion problems. *In: Boundary Integral Methods: Numerical and Mathematical Aspects, (ed. M.A. Golberg), Comput. Mech. Publ., Southampton*, pages 103–176.

Golub, G. H., Heath, M., and Wahba, G. (1979). Generalized cross-validation as a method for choosing a good ridge parameter. *Technometrics*, **21**:215–233.

Golub, G. H. and Van Loan, C. F. (1989). *Matrix Computations*. John Hopkins University Press, Baltimore.

Hadamard, J. (1923). *Lectures on Cauchy's Problem in Linear Partial Differential Equations*. Dover Publications, New York.

Hansen, P. C. (1990). Truncated singular value decomposition solutions to discrete ill-posed problems with ill-conditioned numerical rank. *SIAM J. Sci. Stat. Comput*, **11**:503–518.

He, L., Kindermann, S., and Sini, M. (2009). Reconstruction of shapes and impedance functions using few far-field measurements. *J. Comput. Phys.*, **228**:717–730.

Hettlich, F. and Rundell, W. (1997). Recovery of the support of a source term in an elliptic differential equation. *Inverse Problems*, **13**:959–976.

Hon, Y. C. and Chen, W. (2003). Boundary knot method for 2D and 3D Helmholtz and convection-diffusion problems under complicated geometry. *Int. J. Numer. Meth. Eng.*, **56**:1931–1948.

Hon, Y. C. and Li, M. (2008). A computational method for inverse free boundary determination problem. *Int. J. Numer. Meth. Eng.*, **73**:1291–1309.

Hui, W. and Qinghua, Q. (2007). Some problems with the method of fundamental solution using radial basis functions. *Acta Mechanica Solida*, **20**:1–9.

Ikehata, M. (1999). Reconstruction of a source domain from the Cauchy data. *Inverse Problems*, **15**:637–645.

Inglese, G. (1997). An inverse problem in corrosion detection. *Inverse Problems*, **13**:977–994.

Inglese, G. and Mariani, F. (2004). Corrosion detection in conducting boundaries. *Inverse Problems*, **20**:1207–1215.

Isakov, V. (2009). Inverse obstacle problems. *Inverse Problems*, **32**:123002 (18pp).

Ivanyshyn, O. and Kress, R. (2011). Inverse scattering for surface impedance from phase-less far field data. *J. Comput. Phys.*, **230**:3443–3452.

Kang, H., Kwon, K., and Yun, K. (2001). Recovery of an inhomogeneity in an elliptic equation. *Inverse Problems*, **17**:25–44.

Karageorghis, A. (2001). The method of fundamental solutions for the calculation of the eigenvalues of the Helmholtz equation. *Appl. Math. Lett.*, **14**:837–842.

Karageorghis, A., Johansson, B. T., and Lesnic, D. (2012). The method of fundamental solutions for the identification of the a sound-soft obstacle in inverse acoustic scattering. *Appl. Numer. Math.*, **62**:1767–1780.

Karageorghis, A. and Lesnic, D. (2008). Steady-state nonlinear heat conduction in composite materials using the method of fundamental solutions. *Computer Methods Appl. Mech. Engng.*, **197**:3122–3137.

Karageorghis, A. and Lesnic, D. (2009). Detection of cavities using the method of fundamental solutions. *Inverse Problems Sci. Eng.*, **17**:803–820.

Karageorghis, A. and Lesnic, D. (2010a). The method of fundamental solutions for the inverse conductivity problem. *Inverse Problems Sci. Eng.*, **18**:567–583.

Karageorghis, A. and Lesnic, D. (2010b). The pressure-stream function MFS formulation for the detection of an obstacle immersed in a two-dimensional Stokes flow. *Adv. Appl. Math. Mech.*, **2**:183–199.

Karageorghis, A. and Lesnic, D. (2011). Application of the MFS to inverse obstacle scattering problems. *Eng. Anal. Boundary Elements*, **35**:631–638.

Karageorghis, A., Lesnic, D., and Marin, L. (2011). A survey of applications of the MFS to inverse problems. *Inverse Problems Sci. Eng.*, **19**:309–336.

Katsurada, M. (1989). A mathematical study of the charge simulation method II. *J. Fac. Sci. Univ. Tokyo Sect. IA Math.*, **36**:135–162.

Katsurada, M. (1990). Asymptotic error analysis of the charge simulation method in a jordan region with an analytic boundary. *J. Fac. Sci. Univ. Tokyo Sect. IA Math.*, **37**:635–657.

Katsurada, M. and Okamoto, H. (1996). The collocation points of the fundamental solution method for the potential problem. *Comput. Math. Appl.*, **31**:123–137.

Kim, S. (2002). Uniqueness determination of inhomogeneity in an elliptic equation. *Inverse Problems*, **18**:1325–1332.

Kim, S. and Yamamoto, M. (2003). Uniqueness in identification of the support of a source term in an elliptic equation. *SIAM J. Math. Anal.*, **35**:148–159.

Kirsch, A. and Kress, R. (1987). An optimization method in inverse acoustic scattering. *In: Boundary Elements IX, (eds. C.A.Brebbia, W.L.Wendland and G.Kuhn), Comput. Mech. Publ., Southampton*, pages 3–18.

Kitagawa, T. (1988). On the numerical stability of the method of fundamental solution applied to the Dirichlet problem. *Japan. J. Appl. Math. Appl.*, **5**:123–133.

Kitagawa, T. (1991). Asymptotic stability of the fundamental solution method. *J. Comput. Appl. Math.*, **38**:263–269.

Kraus, A. D., Aziz, A., and Welty, J. (2001). *Extended Surface Heat Transfer*. Wiley, New York.

Kress, R. and Rundell, W. (2001). Inverse scattering for shape and impedance. *Inverse Problems*, **17**:1075–1058.

Kubo, S. (1988). Inverse problems related to the mechanics and fracture of solids and structures. *JSME International Journal*, **31**:157–166.

Kupradze, V. D. and Aleksidze, M. A. (1964). The method of functional equations for the approximate solution of certain boundary value problems. *USSR Comput. Math. Math. Phys.*, **4**:82–126.

Lesnic, D. (2001). A numerical investigation of the inverse potential conductivity problem in a circular inclusion. *Inverse Problems Eng.*, **9**:1–17.

Lesnic, D., Berger, J. R., and Martin, P. A. (2002). A boundary element regularization method for the boundary determination in potential corrosion damage. *Inverse Problems Eng.*, **10**:163–182.

Lesnic, D. and Bin-Mohsin, B. (2012). Inverse shape and heat transfer coefficient identification. *J. Comput. and Appl. Math.*, **236**:1876–1891.

Lin, C. N. and Jang, J. Y. (2002). A two-dimensional fin efficiency analysis of combined heat and mass transfer in elliptic fins. *Int. J. Heat Mass Transfer*, **45**:3839–3847.

Marin, L. (2005). A meshless method for the numerical solution of the Cauchy problem associated with three-dimensional Helmholtz-type equations. *Appl. Math. Comput.*, **165**:355–374.

Marin, L. (2006). Numerical boundary identification for Helmholtz-type equations. *Comput. Mech.*, **39**:25–40.

Marin, L. (2009). Boundary reconstruction in two-dimensional functionally graded materials using a regularized MFS. *CMES Comput. Model. Eng. Sci.*, **46**:221–253.

Marin, L. (2010a). Regularized method of fundamental solutions for boundary identification in two-dimensional isotropic linear elasticity. *Int. J. Solids Struct.*, **47**:3326–3340.

Marin, L. (2010b). Treatment of singularities in the method of fundamental solutions for two-dimensional Helmholtz-type equations. *Appl. Math. Modelling*, **34**:1615–1633.

Marin, L., Elliott, L., Ingham, D. B., and Lesnic, D. (2003). Identification of material properties and cavities in two-dimensional linear elasticity. *Comput. Mech.*, **31**:193–200.

Marin, L., Elliott, L., Ingham, D. B., and Lesnic, D. (2004). The boundary element method for the numerical recovery of a circular inhomogeneity in an elliptic equation. *Eng. Anal. Boundary Elements*, **28**:413–419.

Marin, L. and Karageorghis, A. (2009). Regularized MFS-based boundary identification in two-dimensional Helmholtz-type equations. *CMC Comput. Mater. Continua*, **10**:259–293.

Marin, L., Karageorghis, A., and Lesnic, D. (2011). The MFS for numerical boundary identification in two-dimensional harmonic problems. *Eng. Anal. Boundary Elements*, **35**:342–354.

Marin, L. and Lesnic, D. (2003). Numerical boundary identification in linear elasticity. In Amini, S., editor, *Fourth UK Conference on Boundary Integral Methods*, pages 21–30, Salford University, UK.

Marin, L. and Lesnic, D. (2005). The method of fundamental solutions for the Cauchy problem associated with two-dimensional Helmholtz-type equations. *Comput. Struct.*, **83**:267–278.

Marin, L. and Lesnic, D. (2007). The method of fundamental solutions for nonlinear functionally graded materials. *Int. J. Solids Structures*, **44**:6878–6890.

Marin, L. and Munteanu, L. (2010). Boundary identification in two-dimensional steady state anisotropic heat conduction using a regularized meshless method. *Int. J. Heat Mass Transfer*, **53**:5815–5826.

Martin, P. A. (2012). Two-dimensional acoustic scattering, conformal mapping, and the Rayleigh hypothesis. *J. Acoust. Soc. Am.*, **132**:2184–2188.

Martins, N. F. M. and Silvestre, A. (2008). An iterative MFS approach for the detection of immersed obstacles. *Eng. Anal. Boundary Elements*, **32**:517–524.

Mathon, R. and Johnston, R. L. (1977). The approximate solution of elliptic boundary value problems by fundamental solutions. *SIAM J. Numer. Anal.*, **14**:638–650.

Mera, N. S. and Lesnic, D. (2005). A three-dimensional boundary determination problem in potential corrosion damage. *Comput. Mech.*, **36**:129–138.

Mitic, P. and Rashed, Y. (2004). Convergence and stability of the method of meshless fundamental solutions using an array of randomly distributed sources. *Eng. Anal. Boundary Elements*, **28**:143–153.

Morozov, A. (1966). On the solution of fundamental equations by the method of regularization. *Soviet Math. Dokl.*, **7**:414–417.

Niwa, Y., Kobayashi, S., and Kitahura, M. (1982). Determination of eigenvalue by boundary element method. *In: Development in Boundary Element Methods 2, (ed. P.K. Banerjee and R. Shaw), Applied Science, Chapter 7, London*, pages 143–176.

Pagani, C. D. and Pierotti, D. (2009). Identifiability problems and defects with the Robin condition. *Inverse Problems*, **25**:055007 (12pp).

Philips, D. L. (1962). A technique for the numerical solution of certain integral equations of the first kind. *J. Assoc. Computing Machinery*, **9**:84–97.

Qin, H. H. and Cakoni, F. (2011). Nonlinear integral equations for shape reconstruction in the inverse interior scattering problem. *Inverse Problems*, **27**:035005 (17pp).

Ramachandran, P. A. (2002). Method of fundamental solutions: singular value decomposition analysis. *Commun. Numer. Methods. Engng.*, **18**:789–801.

Rap, A. (2005). *Inverse Contaminant Flow Problems using Boundary Element Methods*. PhD thesis, University of Leeds, UK.

Rundell, W. (2008). Recovering an obstacle and its impedance from Cauchy data. *Inverse Problems*, **24**:045003 (22pp).

Serranho, P. (2006). A hybrid method for inverse scattering for shape and impedance. *Inverse Problems*, **22**:663–680.

Serranho, P. (2007). A hybrid method for inverse scattering for sound-soft obstacles in $\mathbb{R}^3$. *Inverse Problems and Imaging*, **1**:691–712.

Sincich, E. (2010). Stability for the determination of unknown boundary and impedance with a Robin boundary condition. *SIAM J. Math. Anal.*, **42**:2922–2943.

Smyrlis, Y. S. (2009). Applicability and applications of the method of fundamental solutions. *Math. Comput.*, **78**:1399–1434.

Smyrlis, Y. S. and Karageorghis, A. (2010). The under-determined version of the MFS: Taking more sources than collocation points. *Appl. Numer. Math.*, **60**:337–357.

Tikhonov, A. N. and Arsenin, V. Y. (1977). *Solutions of Ill-posed Problems*. John Wiley and Sons, New York.

Ushijima, T. and Chiba, F. (2003). Error estimates for a fundamental solution method applied to reduced wave problems in a domain exterior to a disc. *J. Comput. Appl. Math.*, **159**:137–148.

Vauhkonen, P. J. (2004). *Image Reconstruction in Three-dimensional Electrical Impedance Tomography*. PhD thesis, University of Kuopio, Finland.

Xin, L. (2005). On convergence of the method of fundamental solutions for solving the Dirichlet problem of Poisson's equation. *Adv. Comput. Math.*, **23**:265–277.

Yang, F. L., Ling, L., and Wei, T. (2009). Reconstruction of part of boundary for the Laplace equation by using a regularized method of fundamental solutions. *Inverse Problems Sci. Eng.*, **17**:1113–1128.

Yang, F. L., Ling, L., and Wei, T. (2010). An adaptive greedy technique for inverse boundary determination problem. *J. Comput. Phys.*, **229**:8484–8490.

Zeb, A., Ingham, D. B., and Lesnic, D. (2008). The method of fundamental solutions for a biharmonic inverse boundary determination problem. *Comput. Mech.*, **42**:371–379.

Appendix A

The following counterexample relates to Example $1'$ of subsection 5.4.2.

A Counterexample

For a positive constant α, let us consider the following sequence of functions:

$$u_\nu(\rho,\vartheta) = \Big(I_\nu(k\rho) + C_\nu K_\nu(k\rho)\Big)\cos(n\vartheta), \quad \nu > 0, \tag{A.1}$$

where I_ν and K_ν are the modified Bessel functions of the first and second kind of order ν, respectively, and

$$C_\nu = \frac{krI_{\nu+1}(kr) + (\nu - \alpha r)I_\nu(kr)}{krK_{\nu+1}(kr) - (\nu - \alpha r)K_\nu(kr)}, \quad r > 0. \tag{A.2}$$

One may easily verify that u_ν satisfies the modified Helmholtz equation (4.1), and the Robin boundary condition (5.2) on the boundary of the circle $B(\mathbf{0};r)$ of radius $r > 0$. The Cauchy data (5.1) and (4.5) can easily be generated from equation (A.1) on a sufficiently large circle $\Omega = B(\mathbf{0};R)$ of radius $R > r$. Then the non-uniqueness of the inverse problem follows if we can show that given $k > 0$, for any $\alpha > 0$ there exists $\nu = \nu(\alpha) > 0$ such that the function $\phi : (0,\infty) \to \mathbb{R}$ defined by

$$\phi(r) = \frac{krI_{\nu+1}(kr) + (\nu - \alpha r)I_\nu(kr)}{krK_{\nu+1}(kr) - (\nu - \alpha r)K_\nu(kr)} \tag{A.3}$$

is not injective. One can easily obtain, using MAPLE for example, that $\lim_{r\to 0}\phi(r) = 0$, $\lim_{r\to\infty}\phi(r) = sgn(k-\alpha)\infty$, where sgn is the signum function. The derivative of ϕ is given by

$$\phi'(r) = \frac{k\Big(\nu^2 - \alpha r + (k^2 - \alpha^2)r^2\Big)\Big[I_{\nu+1}(kr)K_\nu(kr) + I_\nu(kr)K_{\nu+1}(kr)\Big]}{\Big[krK_{\nu+1}(kr) - (\nu - \alpha r)K_\nu(kr)\Big]^2}. \tag{A.4}$$

In order to investigate the non-injectivity of the function ϕ we consider the quadratic

$$(k^2 - \alpha^2)r^2 - \alpha r + \nu^2 = 0 \tag{A.5}$$

which is present in (A.4) and gives the stationary points of the function ϕ.
If $\alpha = k$ then ϕ is not injective in a neighbourhood of the point ν^2/α.
If $\alpha \neq k$ then (A.5) has the solutions

$$r_{1,2} = \frac{\alpha \pm \sqrt{\alpha^2 - 4(k^2 - \alpha^2)\nu^2}}{2(k^2 - \alpha^2)}.$$

If $\alpha > k$ then ϕ is not injective in a neighbourhood of the point

$$\frac{\alpha - \sqrt{\alpha^2 - 4(k^2 - \alpha^2)\nu^2}}{2(k^2 - \alpha^2)}.$$

If $0 < \alpha < k$ then one can take ν to be a subunitary fraction of $\frac{\alpha}{2\sqrt{k^2-\alpha^2}}$, i.e. $\nu = \frac{\alpha\chi}{2\sqrt{k^2-\alpha^2}}$ with $\chi \in (0, 1)$, and then ϕ will not be injective in a neighbourhood of the points

$$\frac{\alpha(1 \pm \sqrt{1 - \chi^2})}{2(k^2 - \alpha^2)}.$$

The above non-injectivity of the function ϕ shows that for any constant $\alpha \in (0, \infty)$ we can satisfy the Robin boundary condition (5.2) on circles of different radii, hence the inverse problem has a non-unique solution.